Universidad Autonoma de San Luis Potosí
Instituto de Física

Universidad de Valladolid
Facultad de Ciencias
Departamento de Física Teórica, Atómica y Optica

TESIS DOCTORAL

Structural and electronic properties of transition metal oxide clusters and their applications

Presentada por Rodrigo Humberto Aguilera Del Toro para optar por el grado de doctor por la Universidad de Valladolid, y el grado de doctor en ciencias (Física) por la Universidad Autónoma de San Luis Potosí

Dirigida por:

Dr. Andrés Vega Hierro
Dr. Juan Faustino Aguilera Granja

Andres Vega Hierro, Catedrático de Universidad, y Faustino Aguilera Granja, Catedrático de la Universidad Autonoma de San Luis Potosi, certifican que la presente memoria ha sido realizada, bajo su dirección, por Rodrigo Humberto Aguilera Del Toro en el Departamento de Fisica Teorica, Atomica y Optica de la Universidad de Valladolid y en el Instituto de Fisica de la Universidad Autonoma de San Luis Potosi..

Valladolid, 1 de Julio del 2019

Agradecimientos

En primer lugar, quiero agradecer a mis directores de tesis, los doctores Andrés Vega Hierro y Juan Faustino Aguilera Granja. El gran apoyo que he recibido por parte de ellos, ha hecho posible la realizaciń de esta tesis. He aprendido mucho de ellos, tanto académica como personalmente. De igual manera agradezco a los miembros del área de Atómica, Carlos Balbas, Andrés Aguado, David González, Luis Enrique González, Guillermo Vinuesa, Pablo Álvarez y en especial a José Manuel López, por comentarme la posibilidad de hacer un doble doctorado, algo que me cambio la vida.

La elaboración de esta tesis ha implicado a colaboradores de España, Francia, Chile y México, de más de 10 universidades o centros de investigación. Quiero dar las gracias a todos los investigadores de los que he aprendido cosas durante estos años, Amador García, Begoña Torres, Andrés Ayuela, Javier Gallego, Pedro Alvarado, José Luis Morán, Martín Montejano, Ricardo Guirado, Eugenio Vogel y en especial a Alexandre Lebon por apoyarme para realizar estancias de investigación en Brest, Francia.

Quiero agradecer a Marina Agulló, y a su familia, Paco padre, Paco hijo, y en especial a Ventura Antolín, fuiste como una madre para mi, y me hiciste sentir bienvenido en tu hogar en todo momento, siempre estarás en mi mente y en mi corazón, y en el de todos los que te quisimos.

A todos los becarios que compartimos muchas horas de comida, y solo unas pocas cervezas y vinos. A los de matemáticas, Marina, Bea, Azucena, Jesús, Osziel y Javi. A los de física, David, Vero, Bea, Alejandra, Pablo, Eduardo, Dani, Fernando y en especial a Estefanía German, por ser mi apoyo en mis peores horas. También a Eva Domingo y José Luis Nieto, por soportarme durante estos años y sacarme muchas risas cuando más lo necesitaba.

Durante estos años he conocido a muchas personas muy interesantes, y no podría mencionarlos a todos, pero me gustaría agradecer a un grupo de chicas que quiero mucho, que me ha hecho mucho bien en estos últimos meses, Nuria, Lorena, Raquel, Elena, Tina, Estefi, y en especial a Desi, que me soporto en mis noches de fiestas, y nunca me abandonó por más tarde que fuera.

De igual manera, quiero dar las gracias a mis amigos en México, Otilio, Esther, Itzel, Sofía, Alba, Blanca, Gerson (El Pana), Luz, Alejandra (Alesita), Agustin (El

guty), Itshamara y en especial a dos personas que más que amigos, son mis hermanos, Martín Pardo y Eliu Marín, los he abandonado durante mucho tiempo y aun asi siempre han estado para mi.

Quiero agradecer a toda mi familia, son muchos y no terminaría de nombrarlos. No los he visto mucho durante estos años, pero siempre que estoy con ustedes, es como si los hubiera visto todos los días.

A CONACyT por la beca del programa becas nacionales y a la UVa por el programa de contrataciones predoctorales, sin estos apoyos, no hubiera sido posible realizar esta tesis.

Muchas gracias a mis hermanos, aunque hemos discutido mucho, y no siempre nos entendemos, los quiero, y siempre los llevo conmigo a todos los lugares donde voy.

Finalmente, quiero agradecer a mis padres, Elvira y Faustino, toda la vida me han dado su apoyo, siempre he encontrado en ustedes las respuestas a todo, aunque muchas veces no me gusten esas respuestas, siempre han hecho todo por mi bien, y aunque a veces tenemos diferencias, al final logramos superar todo. Los quiero con todo mi corazón, nunca terminaría de agradecerles todo lo que han hecho por mi.

Quiza la clave para ser realmente libre sea
reir cuando puedas y llorar cuando lo necesites.
Luis Eduardo Aute

Resumen

El estudio de los óxidos de metales de transición es de gran relevancia en nuestros tiempo, debido a la diversidad de sus aplicaciones que tienen. En los ultimos años, la cantidad de estudios tanto teóricos como experimentales han ido en aumento. El interés de estos materiales viene de sus aplicaciones en nanomedicina, electrónica, catálisis, sustitución de materiales críticos, entre otros. En esta tesis, se presentan resultados teóricos para pequeños cúmulos de óxidos de metales de transición, prestando especial interés en las propiedades geométricas, electrónicas, magnéticas y catalíticas. Los resultados presentados en esta tesis, completan una serie de trabajos experimentales de fotofragmentacion, además de presentar resultados predictivos para diversos sistemas que podrían ser de interés para futuros trabajos experimentales.

Abstract

The study of transition metal oxides is of great relevance in our time, due to the diversity of their applications. In recent years, the amount of both theoretical and experimental studies have been increasing. The interest of these materials comes from their applications in nanomedicine, electronics, catalysis, substitution of critical materials, among others. In this thesis, theoretical results are presented for small cumulus of transition metal oxides, paying special attention to the geometrical, electronic, magnetic and catalytic properties. The results presented in this thesis complete a series of experimental photofragmentation works, besides presenting predictive results for diverse systems that could be of interest for future experimental works.

Contents

List of Tables

List of Figures

Chapter 1

Introduction

Cuántas veces la soledad nos acompaña.
Cuántas veces la compañía nos abandona.
Seamos justos al juzgarlas ...
Luis Eduardo Aute

The study of the properties of magnetic nanoparticles has been of scientific and technological interest since the 50s of the last century. However, only since the late 1990s have techniques been developed that enable the manufacture of nanoparticles with the required structural and chemical properties. The interest of the study of small atomic aggregates comes from that their properties are very different from those that have the extensive matter

1.1 Motivation and objectives

For a long time, transition-metal oxide (TMO) nanoparticles (NP) have been the matter of intense research due to their relevance in a large variety of technological applications, like those in medicine (1, 2, 3, 4, 5, 6, 7, 8, 9), new generation batteries (10, 11, 12), bactericidal agents (13, 14, 15), or catalytic processes (16, 17, 18, 19, 20, 21). TMO-NP are easy to obtain and cheap, and are being considered now as good candidates for the replacement of critical materials that are either harmful or scarce and expensive. Among their

electronic properties, magnetism is one of the most relevant one. TMO-NP exhibit superparamagnetic behavior and low blocking temperature even for sizes of tens of nanometers, due to their low magnetic anisotropy energy. Those characteristics make them useful, for instance, in magnetic resonance imaging and as magnetic markers, for which it is fundamental to avoid agglomeration within the environment where they have to act.

With the continuous trend of designing nanostructures to achieve unprecedent goals beyond the capabilities of macroscopic devices, transition-metal (TM) oxide nanoparticles (NPs) are becoming a desired target in many areas like nanomagnetism, nanocatalysis and nanomedicine. TM oxide NPs exhibit a variety of relevant properties in those contexts, depending on the TM component and stoichiometry. Besides, there is an increasing interest in replacing hazardous, costly or scarce materials (commonly classified as critical), and TM oxide NPs are good candidates also in this context. To give just a few concrete examples, Ti oxide NPs are among the most abundant with a global production of about 3000 tons per year (22, 23). They are commonly used in food products and against microorganisms (24, 25), and more particularly as growth inhibitors of oral bacteria (26). NPs of magnetite (Fe_3O_4) are widely used as a contrast agents in clinical magnetic resonance imaging, due to their magnetic properties, low toxicity and known pathways of metabolism(27). Co oxide NPs are useful in storage media and biomedical sensing (28, 29, 30). Fe oxide clusters can induce the conversion of nitric oxide to ammonia (31) Ni oxide NPs have been used in chemical sensors, and more particularly to construct a carbon composite electrode for the determination of paracetamol and some neurotransmitters (32). In fact, Ni oxide compounds are widely used in anodes in electrochemical cells (33), in chemical sensors (34) and in catalysts of reactions such as CO oxidation (35, 36), water splitting (37, 38) or $C - H$ bond activation of ethane (39). Therefore, the potential of Ni oxide NPs in those contexts must by enormous.

TMO-NP of late transition-metal elements (Fe, Co and Ni) have been extensively investigated both experimentally and theoretically (40, 41, 42, 43, 44,

45, 46, 47, 48, 49). Photoelectron spectroscopy (PES) (50, 51) allows to determine the most abundant stoichiometries and cluster products resulting after fragmentation of a parent cluster. Ion Mobility Mass Spectrometry (IMMS) (43, 52), allows to indirectly determine structural transition patterns as a function of cluster size. In the context of those type of experiments, DFT calculations have provided compelling evidence of which are the putative ground states (GS) of TMO-NP of different sizes. Our group has contributed to such knowledge by proposing GS of Co- and Ni-oxide cationic clusters (53, 54) after checking that those GS reproduce the most favourable fragmentation channels, the most abundant individuals in the mass spectra, and the structural patterns consistent with IMMS. We have also investigated the neutral and anionic counterparts of those TMO-NP (53, 54). Once the GS configurations were benchmarked against the experimental results, we analyzed in detail which configurations are optimal from the magnetic point of view for their potential use as nanomagnets.

One of the most interesting and long-standing research field in Materials Science is the design and characterization of alloys, and the seek of new routes to improve their properties in order to make them more efficient for specific purposes. Taking advantage of the cooperative effects of the constituent elements, one can envisage a large variety of applications depending on the composition and stoichiometry. Perhaps the most well known example is the combination of Fe and Cr to create stainless steel, whose properties can even be improved by the addition of other elements. At present, we have already collected a large amount of thermodynamic data, such as binary and ternary phase diagrams, chemical compositions and crystalline structures (55) and we understand the physical and chemical properties of many alloys (56). In the macroscopic regime, one can play with the constituent elements, stoichiometry and growth conditions in order to create alloys with specific properties. For example, Mpourmpakis *et al.* studied Fe-Co in bulk regime (57) and they found that alloys with Co concentration of 30% were those having the highest magnetic moment. However, the physical and chemical properties of a material

can be drastically modified at the nanoscale, as a consequence of quantum-confinement effects, and this is why nanoparticle research has become such a fascinating branch of Material Science. Therefore, in the context of alloys at the nanoscale, one can also play with the size as a new degree of freedom to fine tune a desired property, or to achieve new properties and functionalities that do not exist at the macroscopic regime.

The often unexpected and difficult to rationalize behavior of nanoalloys poses a great challenge, but at the same time is a breeding ground for surprising discoveries and innovative technological applications (58, 59). An intense effort has been devoted in the last years to investigate different kinds of nanoalloys, but the collected data is still scarce in comparison with what we have for macroscopic alloys. It is well known now that the most stable stoichiometries and chemical orders of nanoalloys do not correspond, in general, with those of their macroscopic counterparts. The relative position of the different atoms in a nanoalloy of a given composition leads to a large number of homotops that correspond to different chemical orders. Therefore, from a theoretical point of view, the determination of the low-energy isomers is a challenging task (60). In the case of magnetic nanoparticles, the low-energy spin states (spin isomers) have to be also characterized. In some cases, structure, chemical order and spin configuration are competitive from the energetic point of view. Bimetallic nanoparticles, made up of atoms of two different chemical species, are the simplest kind of nanoalloys.

There is one thing in common for the efficiency of any magnetic NP, independently of the application in which it will be used: it should be as strongly magnetic as possible for it to be turned into active actuators. Unfortunately, this is precisely the weak point of TMO-NP in general, since TM-O interactions induce antiparallel (AP) magnetic couplings which render them to be in a low-spin state, and consequently to have a small total magnetic moment. To overcome this issue, attempts have been made to increase the total moment of TMO-NP by their doping with another element (61, 62). In this context, Szczerba *et al.* have experimentally investigated the doping of iron oxide

nanoparticles with Zn with the goal of avoiding the spin missalignment, thus enhancing the total moment. The idea behind is that *Zn* substitutes Fe atoms at tetrahedral sites, which were the *Fe* atoms antiparallelly couplen with the rest in the original iron oxide NP. Although this doping works by eliminating the harmful Fe atoms, the substitutes Zn atoms do not contribute themselves to the total moment of the resulting doped NP, since they are nonmagnetic. However, if one could transform the AP couplings into P ones by means of a substitutional magnetic dopant instead of a nonmagnetic one, the total moment could be even larger. An interesting and surprising result was that, although AP couplings characterize in general the TMO, leading to a low-spin states, we identified several TMO-NP in a high-spin state with large total magnetic moment. There are even some TMO clusters with higher total moment than their non-oxidized transition-metal counterparts as a consequence of the robustness of the P magnetic couplings together with a non negligeable contribution of the spin-polarization of the oxygen atoms to the total moment. We also verified that as increasing the d-band filling in the transition metal (TM) series (that is as going from *Fe* to *Ni*), the paralell magnetic couplings become more robust against oxidation. But in general, the AP couplings prevail nevertheless, particularly at high oxidation rates.

1.2 Contributions of this thesis

This thesis is an advance in the area of metal oxide clusters, understanding of the geometrical, electronic, catalytic and magnetic properties. The present study complements a series of experimental results of ion mobility and fragmentation channels. We propose the possible structures for the clusters, in good agreement with the experimental measurements. Likewise, we propose a series of explanations of the way in which nickel, iron and indium oxide clusters are fragmented under the application of a photon laser, obtaining an excellent agreement with the relative abundance measurements obtained in different experiments. In addition, we propose various applications for the use

of transition metal oxide clusters, such as coating clusters with other materials, for the protection of their magnetic properties against oxidation. We also studied the catalytic properties of nickel oxide clusters, for the absorption of a carbon monoxide molecule, and the process of releasing an oxygen, forming carbon dioxide. Another application that we present is a possible route to preserve the magnetic moment of the metal clusters against oxidation, for this, we identify optimal mixtures between iron, nickel and cobalt. Moreover, we studied, structural, electronic and energetic properties of titanium oxide clusters and nanowires.

1.3 Structure of the thesis

In this first chapter, we give a general view of the previous works on the topic of metal oxides, the problems that the Scientific Community wants to solve, as well as the contribution of this thesis to those problems.

In Chapter 2 a brief introduction is made to the ab initio methodology used in structural and electronic studies, as well as to the codes used. Chapters 3 to 7 summarize some of the most relevant results obtained during the PhD. In chapter 3, are the principal results for systems based on nickel clusters, whilst in chapter 4 are compiled the ones for systems based o iron clusters. In Chapter 5 we discuss the behavior of mixtures of small transition metal oxide clusters. In chapter 6, we present results for titanium oxygen nanotubes, and impurities in titanium oxide clusters. In chapter 7, we have studied as applications, the properties of nanowires of titanium oxide clusters, built with TiO_2 clusters bricks, and the analysis of the change in the HOMO-LUMO gap, for the $(TiO_2)_{10}$ cluster with impurities. Finally, in chapter 8, are summarized the general conclusions of this thesis. The results obtained have given rise to several publications in international journals, whose references are listed at the end of the thesis.

Chapter 2

Theoretical model

Decir espera es un crimen, decir mañana
es igual que matar, ayer de nada nos sirve
las cicatrices no ayudan a andar.
Luis Eduardo Aute

2.1 Introduction

In this chapter a brief explanation will be given on the basic ingredients used in quantum mechanics for the solution of the electronic and atomic structure of molecular systems at present, as well as the computational method that we used for the calculation. In the origins of quantum mechanics the solution of the electronic and atomic structure was restricted to small systems that can be solved exactly like those of a non-multielectronic atom, or atomic systems, and in some cases highly symmetric systems. However, at present, the complexity of the systems that must be solved is such that trying to solve them analytically would be a very complicated task and with a very large time cost, this is where the computational development and numerical methods for the resolution intervene, for this type of problems. Thanks to the development of the computational methods, the complexity and quantity of problems that we can solved increased considerably, and now we can treat real physical problems

with a practical interest. All these numerical methods developed are based on approximations. In this thesis we will use some of them, and soon we will explain them. For the analysis of the structural and electronic properties of the clusters of this thesis we will use the functional density theory (DFT), as implemented in the numerical codes SIESTA (Spanish Initiative for Electronic Simulations with Thousands of Atoms) and VASP (Vienna ab-initio Simulation Package). In this chapter we will briefly explain the DFT theory, SIESTA and VASP codes.

2.2 Molecular Hamiltonian

In quantum mechanics, all the information regarding the properties of a system is contained in its wave function Ψ, which depends on 3N coordinates for a system without spin polarization (N being the number of particles in the system). We will do the development of the equations without including the degrees of freedom associated with the spin, since this development does not change when we include them. The wave function of a system can be obtained from the Schrödinger equation:

$$\hat{H}(R,t)\Psi(R,t) = i\hbar\frac{\partial\Psi(R,t)}{\partial t} \tag{2.1}$$

The total energy operator $\hat{\mathrm{H}}$(R,t) is known as the Hamiltonian operator by its analogy with its corresponding function in classical mechanics. In quantum mechanics it is defined in the space of the coordinates in the following way:

$$\hat{H}(R,t) = -\frac{\hbar^2}{2m}(\frac{\partial^2}{\partial x^2} + \frac{\partial^2}{\partial y^2} + \frac{\partial^2}{\partial z^2}) + V(R,t) \tag{2.2}$$

In such a way that the Schödringer equation takes the form:

$$[-\frac{\hbar^2}{2m}(\frac{\partial^2}{\partial x^2} + \frac{\partial^2}{\partial y^2} + \frac{\partial^2}{\partial z^2}) + V(R,t)]\Psi(R,t) = i\hbar\frac{\partial\Psi(R,t)}{\partial t} \tag{2.3}$$

Equation 2.3 describes a particle of mass m which moves through space under the influence of an external field $V(R,t)$. When we have the particular

case in which the external potential does not depend on time, the wave function can be described by the product of two wave functions, one that contains the temporal dependence and another the spatial part

$$\Psi(R,t) = \acute{\Psi}(R)T(t) \tag{2.4}$$

Therefore the equation 2.3 can be separated by the method of separation of variables, and thus in this way we can obtain a time-independent Schödringer equation:

$$[-\frac{\hbar^2}{2m}(\frac{\partial^2}{\partial x^2} + \frac{\partial^2}{\partial y^2} + \frac{\partial^2}{\partial z^2}) + V(R)]\Psi(R) = E\Psi(R) \tag{2.5}$$

where E is the energy of the particle.

Or expressed in terms of Hamiltonian operator:

$$\hat{H}\Psi = E\Psi \tag{2.6}$$

Equation 2.6 is clearly an quation of eigenvalues and it can be solved exactly only for simple potentials, such as: a free particle ($V = 0$), a box if infinite potential ($V = 0, -a \leq x \leq a$), harmonic oscillator ($V = \frac{1}{2}mw^2x^2$), among others. One of the most interesting cases is the solution of the Schödringer equation for the hydrogen-like atoms, since these have nucleus, of charge Ze and only one electron, so the potential energy will only depend on the distance from the electron to the nucleus, through the Coulomb interaction. So the Hamiltonian of equation 2 will take the form:

$$\hat{H} = -\frac{\hbar^2}{2m}(\frac{\partial^2}{\partial x^2} + \frac{\partial^2}{\partial y^2} + \frac{\partial^2}{\partial z^2}) - \frac{Ze^2}{4\pi\epsilon_0 r} \tag{2.7}$$

writing this in atomic units:

$$H = -\frac{1}{2}\nabla^2 - \frac{Z}{r} \tag{2.8}$$

where $\nabla^2 = \left(\frac{\partial^2}{\partial x^2} + \frac{\partial^2}{\partial y^2} + \frac{\partial^2}{\partial z^2}\right)$

However, our system can contain more and more these interactives with each other, so, assuming that the system of electrons and nuclei N, our Hamiltonian is going to have to include all these interactions between electrons and

nuclei to be correct When considering a Hamiltonian for a system of N cores (point masses of charge Z) and n electrons, is obtained:

$$H = \sum_{k=1}^{N} -\frac{1}{2M}\nabla_i^2 - \sum_{i=1}^{n} -\frac{1}{2}\nabla_i^2 - \sum_{k=1}^{N}\sum_{i=1}^{n}\frac{Z_k}{r_{ki}} + \sum_{i\neq j}^{n}\frac{1}{r_{ij}} + \sum_{k\neq l}^{N}\frac{Z_k Z_l}{R_{kl}} \tag{2.9}$$

where $m = |e| = \hbar = 1$, y $r_{ij} = |\vec{r}_i - \vec{r}_j|$

This Hamiltonian is known as multi-electron or molecular Hamiltonian [24], and is composed of different parts. The first term contains the kinetic energy of the nuclei, the second the kinetic energy of the electrons, the third the electron-nucleus interaction energy, the fourth the electron-electron repulsion and the fifth the core-core repulsion. k and l are a pair of nuclei and i and j a pair of electrons.

Solving the Schrödinger equation for this Hamiltonian in an exact way is impossible for realistic systems, even making use of computational methods, for this reason we must make use of certain approximations.

2.3 Born-Oppenheimer Approximation and Hellmann-Feynman theorem

We can simplify the equation (9) taking into account the large mass difference between nuclei and electrons, since the mass of the former is 10^3 times greater than the latter, and we can assume that the electrons will follow almost instantaneously the nuclear dynamics, since the variation in the time scale of the nuclei will be very slow in comparison with the nuclear movement.

In this way, we consider the nuclei fixed [25], and we can solve the electronic part of the equation using again the method of separation of variables, since our wave function can be written as the product of the electronic wave function $\phi(Q, q)$ and the nuclear wave function $\chi(Q)$:

$$\psi(Q, q) = \phi(Q, q)\chi(Q) \tag{2.10}$$

where Q are the coordinates of the nuclei, q of the electrons and $\chi(Q)$ is a wave function solution of the Schrödinger nuclear equation.

Being the nuclear Hamiltonian:

$$H_n = \left[\sum_{k=1}^{N} \frac{-1}{2M}\nabla_k^2 + \sum_{k\neq l}^{N} \frac{Z_k Z_l}{R_{kl}} + \epsilon_{elec}(Q)\right] \tag{2.11}$$

The nuclear Schrödinger equation is written:

$$H_n\, \chi(Q) = E\, \chi(Q) \tag{2.12}$$

where the electronic energy ϵ_{elec} acts as an effective potential dependent on the positions of the nuclei, since the interaction potential between the nuclei is constant ($V_{n-n} = \sum_{k\neq l}^{N} \frac{Z_k Z_l}{R_{kl}}$), we can override it for simplicity, so that the nuclear Schrödinger equation remains:

$$\left[\sum_{k=1}^{N} \frac{-1}{2M}\nabla_k^2 + \epsilon_{elec}(Q)\right] \chi(Q) = E\, \chi(Q) \tag{2.13}$$

Therefore the electronic Hamiltonian will be defined as:

$$H_{elec} = \sum_{i=1}^{n} -\frac{1}{2}\nabla_i^2 - \sum_{k=1}^{N}\sum_{i=1}^{n} \frac{Z_k}{r_{ki}} + \sum_{i\neq j}^{n} \frac{1}{r_{ij}} \tag{2.14}$$

As we can see, both the electronic wave function $\phi(Q,q)$ and the eigenvalues of this Hamiltonian ϵ_{elec} depend on the nuclear coordinates, which from now on we will consider as fixed parameters. Therefore we can determine the eigenvalues of a particular electronic state $\phi(Q,q)$ for known nuclear positions Q, so that we only have to solve the electronic Schrödinger equation:

$$H_{elec}\, \phi(Q,q) = \epsilon_{elec}(Q)\phi(Q,q) \tag{2.15}$$

thus, we can find the eigenvalues of the electronic energy such as:

$$\epsilon_{elec} = \int \phi^*(Q,q) H_{elec} \phi(Q,q) d\tau_q \tag{2.16}$$

where τ_q is the volume element in the space of the n electronic coordinates q.

it can be proved that:

$$\frac{\partial \epsilon_{elec}}{\partial Q} = \int \frac{\partial \phi^*}{\partial Q} H_{elec}\, \phi\, d\tau_q + \int \phi^* \frac{\partial H_{elec}}{\partial Q} \phi\, d\tau_q + \int \phi^* H_{elec} \frac{\partial \phi}{\partial Q} d\tau_q \tag{2.17}$$

And since H_{elec} is hermitic:

$$\int \phi^* H_{elec} \frac{\partial \phi}{\partial Q} d\tau_q = \int \frac{\partial \phi}{\partial Q} H_{elec} \phi^* d\tau_q = \epsilon_{elec} \int \frac{\partial \phi}{\partial Q} \phi^* d\tau_q \tag{2.18}$$

And due to this we can affirm:

$$\int \frac{\partial \phi^*}{\partial Q} H_{elec}\, \phi\, d\tau_q + \int \phi^* H_{elec} \frac{\partial \phi}{\partial Q}\, d\tau_q = \epsilon_{elec} \int \left(\frac{\partial \phi^*}{\partial Q} \phi + \phi^* \frac{\partial \phi}{\partial Q} \right) d\tau_q \tag{2.19}$$

$$\epsilon_{elec} \int \left(\frac{\partial \phi^*}{\partial Q} \phi + \phi^* \frac{\partial \phi}{\partial Q} \right) d\tau_q = \epsilon_{elec} \frac{\partial}{\partial Q} \int \phi^* \phi d\tau_q = 0 \tag{2.20}$$

and finally:

$$\frac{\partial \epsilon_{elec}}{\partial Q} = \int \phi^*(Q,q) \frac{\partial H_{elec}}{\partial Q} \phi(Q,q)\, d\tau_q \tag{2.21}$$

This is the Hellman-Feynman Theorem [26], which relates the derivative of the energy of a system with respect to a parameter (in this case the nuclear coordinates), with the expectation value of the derivative of the Hamiltonian with respect to the same parameter. The forces on the nuclei are then defined as:

$$F = -\left\langle \frac{\partial \epsilon_{elec}}{\partial Q} \right\rangle_{\phi(Q,q)} = - < \phi(Q,q) | \frac{\partial \epsilon_{elec}}{\partial Q} | \phi(Q,q) > \tag{2.22}$$

2.4 Calculation of the molecular electronic structure (DFT)

2.4.1 Kohn-Sham equations

Suppose that we know the correct wave function for the multielectronic system described in the previous sections, the energy of the system could be described as:

$$E = T + V + E_{ee} \tag{2.23}$$

where each term is defined as:

$$T =< \psi| \sum_i -\frac{1}{2}\nabla_i^2 |\psi > \tag{2.24}$$

$$V =< \psi| \sum_i \sum_k -\frac{Z_k}{r_{ik}} |\psi > =< \psi| \sum_i v(\vec{r_i}) |\psi > \tag{2.25}$$

$$E_{ee} =< \psi| \sum_{i \neq j} \frac{1}{r_{ij}} |\psi > \tag{2.26}$$

As we can see, the electron-electron interaction is contained in the last term we have called E_{ee}, while V contains the electron-core interaction and T is the kinetic energy of the interacting electron system.

We can write V as a function of the electronic density:

$$V[\rho] = \int v(\vec{r})\rho(\vec{r})d\vec{r} \tag{2.27}$$

where $\rho = |\psi|^2$

If we could express T and E_{ee} in terms of $\rho(\vec{r})$ we could write the total energy as a functional only dependent on electronic density. For a system with a determined number of electrons the only term that depends on the nature of the system is the potential of electron-core interaction, once defined the Hamiltonian is determined and therefore the wave function and the total energy, which are then functional of the mentioned potential.

This was demonstrated by P. Hohenberg and W.Kohn [27] in 1961 and was expressed in the following theorem:

Theorem 1. *The potential $v(\vec{r})$ is unambiguously determined by the electronic density $\rho(\vec{r})$ except for an additive constant. The potential is therefore a functional of electronic density.*

Since the potential determines the Hamiltonian and therefore the energy, the electronic density determines the energy of the system.

Theorem 2. *There is a functional $F[\rho]$ such that, for a given potential $v(\vec{r})$ and an electronic density $\rho(\vec{r})$ given, it minimizes the functional of the energy*:

$$E[\rho] = F[\rho] + \int v(\vec{r})\rho(\vec{r})dr \tag{2.28}$$

if, in addition, the given electronic density $\rho(\vec{r})$ is that of the fundamental state, this functional $E[\rho]$ is the corresponding one to the fundamental state of the system:

$$E_0[\rho] = F[\rho] + \int v(\vec{r})\rho(\vec{r})d\vec{r} \tag{2.29}$$

Obtaining thus the lowest possible value of energy.

$$F[\rho] = T[\rho] + E_{ee}[\rho] \tag{2.30}$$

The kinetic energy of the interacting electron system differs from that of the non-interacting electron system in the effect of electron correlations $T_c[\rho]$:

$$T[\rho] = T_s[\rho] + T_c[\rho] \tag{2.31}$$

The electrostatic energy E_{ee} is composed of two terms:

$$E_{ee}[\rho] = E_H[\rho] + U_{xc}[\rho] \tag{2.32}$$

where $E_H[\rho]$ is the Hartree energy:

$$E_H[\rho] = \frac{1}{2}\int\int \frac{\rho(\vec{r}_i)\rho(\vec{r}_j)}{r_{ij}} d\vec{r}_i d\vec{r}_j \tag{2.33}$$

representing the electrostatic interaction between an electron density ρ. And U_{xc} is the difference between the real electrostatic energy and the Hartree energy, due to correlation and exchange phenomena (Pauli exclusion principle).

From this we can define the functional of the exchange energy and correlation as:

$$E_{xc}2[\rho] = T[\rho] - T_s[\rho] + E_{ee}[\rho] - E_H[\rho] = T_c[\rho] + U_{xc}[\rho] \tag{2.34}$$

The functional of the total energy of the system will be:

$$E[\rho] = T_s[\rho] + E_H[\rho] + E_{xc}[\rho] + V[\rho] \tag{2.35}$$

Developing expressions:

$$E[\rho] = T_s[\rho] + \frac{1}{2}\int\int \frac{\rho(\vec{r}_i)\rho(\vec{r}_j)}{r_{ij}} d\vec{r}_i d\vec{r}_j + E_{xc}[\rho] + \int v(\vec{r})\rho(\vec{r})d\vec{r} \tag{2.36}$$

By minimizing this function with respect to electronic density we obtain the following Euler-Lagrange equation:

$$\frac{\delta E[\rho(\vec{r})]}{\delta\rho(\vec{r})} = \frac{\delta T_s[\rho(\vec{r})]}{\delta\rho(\vec{r})} + v_H(\vec{r}) + v_{xc} + v(\vec{r}) = 0 \tag{2.37}$$

where we have defined $v_{xc} = \frac{\delta E_{xc}[\rho(\vec{r})]}{\delta\rho(\vec{r})}$, and $v_H(\vec{r}) = \frac{\delta E_H[\rho(\vec{r})]}{\delta\rho(\vec{r})} = \int \frac{\rho(\vec{r})}{r_{ij}} d\vec{r}_j$, what is Hartree's potential.

This allows us to introduce a set of self-consistent equations, called Kohn-Sham equations[28]:

$$\left[-\frac{1}{2}\nabla_i^2 + v_{eff}(\vec{r})\right]\phi_i(\vec{r}) = \epsilon_i\phi_i(\vec{r}) \tag{2.38}$$

where $\phi(\vec{r})$ are our wave functions, known as Kohn-Sham orbitals, and the effective potential is $v_{eff} = v(\vec{r}) + v_H(\vec{r}) + v_{xc}$.

We still have a functional part of $F[\rho]$ that is unknown, the correlation and exchange functional energy $E_{xc}[\rho]$, which as we have seen in its definition, includes the kinetic correlation energy.

2.4.2 Local density approximation (LDA)

In their original work [28], Kohn and Sham indicated that solids can be treated as a homogeneous electron gas in first approximation. In this limit, the effects of exchange correlation are local and that is why an approximation of the local density (LDA) is proposed, in which the exchange correlation energy is an integral over the entire space where it is assumed that the energy density of correlation and exchange is identical to that of a homogeneous electronic gas.

$$E_{xc}^{LDA}[\rho(\vec{r})] = \int \rho(r)\epsilon_{xc}^{hom}(\rho(\vec{r}))d^3r \tag{2.39}$$

if we work out $\epsilon_{xc}^{hom}(\rho(\vec{r}))$:

$$E_{xc}^{LDA}[\rho(\vec{r})] = \int \rho(r)\left[\epsilon_{x}^{hom}(\rho(\vec{r})) + \epsilon_{c}^{hom}(\rho(\vec{r})\right]d^3r \tag{2.40}$$

This approach is very useful in the description of many systems, even though their electronic distribution is very different from that of a homogeneous electron gas. This is due to the cancellation of errors, since in the LDA approximation the effect of the exchange is overestimated and the effect of the correlation is underestimated, obtaining reasonable results for E_{xc}.

2.4.3 Generalized gradients approximation (GGA)

While this approach arises from the LDA, it goes one step further including a proportionality with respect to the gradient of the electronic density $\nabla\rho(\vec{r})$ in the functional exchange energy and correlation

$$E_{xc}^{GGA}[\rho(\vec{r})] = \int \rho(\vec{r})\epsilon_{xc}^{hom}(\rho(\vec{r}), \nabla\rho(\vec{r}))d^3r \tag{2.41}$$

And here we introduce a dimensionless functional that is proportional to $\nabla\rho(\vec{r})$[29,30]:

$$E_{xc}^{GGA}[\rho(\vec{r})] = \int \rho(\vec{r})\epsilon_{x}^{hom}(\rho)F_{xc}(\rho(\vec{r}), \nabla\rho(\vec{r}))d^3r \tag{2.42}$$

where F_{xc} is our dimensionless functional, and ϵ_x is the exchange energy of the homogenous unpolarized electronic gas [31]. This new functional will be

divided into two parts, one of exchange and another of correlation, which we can define by dimensioning the density gradients:

$$s_i = \frac{|\nabla^i \rho|}{(2k_F)^i \rho} = \frac{|\nabla^i r_s|}{2^i (2\pi/3)^{i/3} r_s} (\rho)^{1+i/3} \tag{2.43}$$

s_i is the i-th variation of the electron density with the average distance between electrons r_s y $k_F = (3\pi^2\rho)^{1/3}$ is the moment of Fermi.

So F_x[30,32] and F_c[33] are described with a serial expansion:

$$F_x = 1 + \frac{10}{81} s_1^2 + \frac{146}{2025} s_2^2 + ... \tag{2.44}$$

$$F_c = \frac{\epsilon_c^{LDA}(\rho)}{\epsilon_x^{LDA}(\rho)} (1 - 0,21951 s_1^2 + ...) \tag{2.45}$$

The contribution of the correlation to the total energy is much smaller than that of the exchange, in addition, as the order of the gradient of the electronic density increases, the correlation functional contributes less and ends up disappearing.

2.5 SIESTA Method

SIESTA (Spanish Initiative for Electronic Simulations with Thousands of Atoms) (63) is a DFT code (and a solution method) that allows the simulation of systems, both the periodic and isolated, from a few atoms up to the thousand order with good accuracy. SIESTA allows different LDA and GGA approaches to be used for the exchange and correlation potential. It also allows to use the creation of powerful hybrids; With variable mixture of several LDA and GGA. In the latest versions a new non-local potential is also included for the description of the Van der Waals interactions. SIESTA uses pseudopotentials of the Troullier-Martins (64) type constructed in a completely non-local way (Kleinman-Bylander)(65). As a base of states, it uses numeric functions located on the atoms based on the valence states. Additionally they can make N

order calculations, this means, with linear scaling, but not use them in this thesis. The calculations made in real space are made on a homogeneous network of points, which is defined through an energy criterion. In the simplest case of a cell. Cubic side L with an energy criterion E_c (in Rydberg) The network refers to:

$E = \frac{\pi^2 N^2}{L^2} > E_c$

The versatility of SIESTA makes it one of the most popular ab-initio-DFT codes among the scientific community, and it will be one of the codes used in the development of this thesis.

2.6 VASP Method

VASP, or Vienna Ab initio Simulation package (66, 67, 68), is a DFT code that allows the simulation of molecular system using the PAW method (69, 70, 71) (Projector Augmented Wave). Instead of pseudopotentials, the wave functions of the valence electrons tend to make rapid oscillations near the nucleus ions. This is due to the requirement that they be orthogonal to the states of the core electron. This brings problems since it requires many Fourier components to describe the wave functions correctly. The solution to this problem is to define a potential for core interactions, understanding by core the nucleus and the internal electrons. In the model that we are going to present, we only consider the interactions of the valence electrons with the core, with the aim that the calculations are simplified. VASP makes use of the PAW method. This method transforms wave functions into simpler ones (with softer oscillations and orthogonal with the core). The calculation is then simplified since the valence electrons are explicitly treated, allowing great efficiency when making calculations based on the DFT. VASP solves the Khon-Sham equations using a plane-waves basis set instead of numerical pseudoatomic orbitals, and the core interactions are treated be means of the projector-augmented wave (PAW) approach instead of pseudopotentials. This approach is consistent with the exact all-electron potential and provides a more accurate description of the

core interactions.

2.7 Theoretical approach and computational details

We performed fully self-consistent DFT calculations using the SIESTA code (63) (except for subsection 3.4, in which we used VAPS (66, 67, 68)). For the exchange and correlation potential we used the Perdew-Burke-Ernzerhof form of the generalized gradient approximation (GGA) (72). We employed norm-conserving scalar relativistic pseudopotentials (64) in their fully nonlocal form (65), generated from the atomic valence configuration, these are collected in Table 2.1, with their respective core radii. Non-linear partial core corrections (73), which are known to be important for transition metal pseudopotentials, are included at the core radius of 0.7 Å. Valence states were described using double-ζ basis sets for all atomic species. The energy cutoff used to define the real-space grid for numerical calculations involving the electron density was 250 Ry. The Fermi distribution function that enters in the calculation of the density matrix was smoothed with an electronic temperature of 15 meV. We used an energy criterium of 10^{-4} eV for converging the electronic density. In the calculations, the individual clusters were placed in a cubic supercell of $20 \times 20 \times 20$ Å^3, a size large enough to neglect the interaction between the cluster and its replicas in neighboring cells. It was considered only the Γ point ($k = 0$) when integrating over the Brillouin zone, as usual for finite systems.

The equilibrium geometries resulted from an unconstrained conjugate-gradient structural relaxation using the DFT forces. Structures were relaxed without any symmetry constraint until interatomic forces were smaller than 0.003 eV/Å. In all cases, different spin isomers were checked in order to ensure the correct ground state. For that search of spin isomers, the criterium for maximum interatomic forces was further reduced to 0.001eV/Å.

For selected compositions or homotops for which we found different states very close in energy, or untypical magnetic arrangements, additional calcula-

tions were performed using the VASP code (66, 67, 68) with the same GGA functional as that employed in SIESTA. However, VASP is more demanding than SIESTA from the computational point of view. In all cases tested, VASP and SIESTA yielded similar results.

Tabla 2.1: Electronic configuration (E. C.), and core radii (in a.u.) for s, p and d orbitals used in this thesis.

Element	E. C	s	p	d
Ti	$4s^2 3p^6 3d^2$	1.98	1.98	1.98
Fe	$3d^7 4s^1$	2.60	2.60	2.60
Co	$3d^8 4s^1$	2.50	2.50	2.50
Ni	$3d^8 4s^2$	2.00	2.32	2.44
Ag	$4d^{10} 5s^1$	2.17	2.82	2.40
In	$5s^2 4d^{10} 5p^1$	2.57	2.57	2.57
O	$2s^2 2p^4$	1.14	1.14	1.14

2.8 Definition of quantities in DFT

It is very useful to define some quantities that we use throughout this thesis. Adiabatic ionization potential and adiabatic electron affinity. Ionization potential is the energy necessary to remove an electron from the neutral system, whilst electron affinity is the energy necessary to add an electron to the neutral system, the adiabatic processes means that we calculate theses energies making a complete structural relaxation before measure these energies

$$I_P = E(N-1) - E(N) \tag{2.46}$$

and

$$E_A = E(N) - E(N+1) \tag{2.47}$$

where N is the number of electrons of the neutral cluster, $E(N)$ the energy of the neutral cluster and $E(N \pm 1)$ is the energy of the relaxed cluster with $N \pm 1$ electrons.

In order to characterize the global reactivity of the clusters, we calculate conceptual DFT based global reactivity descriptors (74, 75, 76, 77). In first place, the vertical ionization potential I and vertical electron affinity A are calculated, from total energy calculations on the N-1 and N+1 electron systems at the optimal neutral geometry:

$$I = E_0(N-1) - E(N) \tag{2.48}$$

and

$$A = E_0(N-1) - E(N) \tag{2.49}$$

where N is the number of electrons for the neutral cluster. $E(N)$ the energy of the neutral cluster and $E_0(N \pm 1)$ is the energy of the cluster with $N \pm 1$ electrons, with the neutral structure. From them, we can calculate the electronegativity (the negative of the electronic chemical potential μ):

$$\chi = -\mu = -(\frac{\partial E}{\partial N})_v = \frac{1}{2}(I + A) \tag{2.50}$$

and the chemical hardness (or fundamental gap, except for a constant factor):

$$\eta = \frac{1}{2}(\frac{\partial^2 E}{\partial N_v^2}) = \frac{1}{2}E_{gap} = \frac{1}{2}(I - A) \tag{2.51}$$

In these equations, the rightmost equality involves a finite difference approximation to the corresponding derivatives. An electrophilicity index (75) can then be defined as

$$\omega = \chi^2/2\eta = \chi^2/E_{gap} \tag{2.52}$$

The electronegativity quantifies the ability of the nanoalloys to attract and hold electrons.

The binding energy per atom of neutral and charged clusters, as well as the second total energy difference, as a function of the oxygen content m, are defined as follows:

$$E_b^0(n,m) = [nE(A) + mE(O) - E(n,m)^0]/(n+m) \tag{2.53}$$

$$E_b^{\pm}(n,m) = [E(A)^{\pm} + (n-1)E(A) + mE(O) - E(n,m)^{\pm}]/(n+m) \tag{2.54}$$

and

$$\Delta_2(n,m) = E(n,m-1)^{0/\pm} + E(n,m+1)^{0/\pm} - 2E(n,m)^{0/\pm} \tag{2.55}$$

where $E(n,m)^{0/\pm}$ are the total energy of the $A_nO_m^{0/\pm}$ clusters ($A = Ni, Fe$ and In, for chapter 3, 4 and 7 respectively). For a given n, the values $\Delta_2(n,m)$ as a function of m will show a prominent positive peak at those m values whose corresponding (n,m) clusters are more stable than their $(n,m-1)$ and $(n,m+1)$ neighbors against the addition or substraction of one oxygen atom.

In order to determine the most reactive sites according to purely electronic arguments, we have calculated the Fukui functions f^+ and f^- (78, 79, 80) defined as

$$f^{\pm}(\vec{r}) = (\frac{\partial\rho(\vec{r})}{\partial N_e})_v^{\pm} \tag{2.56}$$

where $\rho(\vec{r})$ is the spatial charge density, N_e the number of electrons, and the subscript indicates that the right/left derivatives have to be calculated at constant external potential, i.e. by keeping the atomic coordinates fixed. The scalar fields $f^{\pm}$ measure the local variations in electronic charge induced by the addition or removal of electrons, and so they can be used as useful local indices of electronic reactivity. f^+ refers to the electron density response upon addition of electrons, and so is an indicator of locally electrophilic regions which are more susceptible to nucleophilic attack; similarly, f^- locates the most nucleo-philic regions within the system, susceptible to an electro philic attack. Larger positive values of $f^{\pm}$ correspond to more reactive sites. Coupling the Fukui function with the Bader analysis, we can define atom-resolved condensed

Fukui functions, $f_i^{\pm}$ for each atom i , by calculating the variation in electronic charge inside each of the Bader atomic basins. Following the standard practice, we have approximated the derivatives by simple finite differences:

$$f_{N_e}^{+}(\vec{r}) = \rho_{N_e+1}(\vec{r}) - \rho_{N_e}(\vec{r}) \tag{2.57}$$

and

$$f_{N_e}^{-}(\vec{r}) = \rho_{N_e}(\vec{r}) - \rho_{N_e-1}(\vec{r}) \tag{2.58}$$

This involves converging the electronic structure of both cation and anion at the optimal geometry of the neutral structure for the different nanoalloys. Charged systems can be dealt with through the addition of a Madelung correction in the VASP calculations. Although the finite difference expressions provide the exact value for the derivative according to DFT (81), in practical calculations the expressions are not exact due to the self-interaction error of approximate exchange-correlation functionals. Nevertheless, the standard usage of those finite difference approximations is justified by the fact that approximate XC-functionals are much more accurate for integer numbers than for fractional numbers of electrons.

Chapter 3

Small nickel oxide clusters

La ciencia es una estrategia, es
una forma de atar la verdad.
Luis Eduardo Aute.

The aim of the present section is to characterize the fundamental properties of small Ni oxide clusters, in both the neutral and charged state and an exhaustive comparison with the photodissociation measurements of Dibble *at al.* (82). We calculate the putative ground states and the more favorable fragmentation channels. We calculate the spin-polarized electronic structure in order to analyze the magnetic properties as a function of relative oxygen concentration and charge states. We explore the isomeric map, from both the structural and spin configurations, in order to find metastable Ni oxide NPs that could be also of interest, as well as to compare with the isomeric map obtained by Ohshimo *et al.* (83) for the cationic clusters using a different DFT approach. We also present the calculated vibrational spectra of near degenerate isomers of $Ni_6O_6^{0/+}$ with different spin and/or geometry. This study illustrates how to resolve the true ground state of metal oxide clusters by comparing with infrared multiple photon dissociation (IR-MPD) experiments (84). As part of the applications of this chapter, we will study the absorption of carbon monoxide (CO) in nickel oxide clusters. We have studied all the possible sites of absorption of CO on the Ni_6O_m series, besides studying the carbon dioxide release of the

$Ni_6O_m - CO$ clusters, comparing our calculations with the experimental results of Sakuma *et al.* (85). Thus, the results of the present section complement the three previous experimental investigations with the final goal of giving a step forward in the knowledge of the fundamental properties of small Ni oxide clusters. Finally, we will conclude this chapter with the study of silver-nickel nanoalloys, and its possible application for protect the magnetic moment of the nickel clusters against the oxidation.

3.1 Geometrical configurations and electronic properties

We describe here the geometrical properties of the investigated $Ni_nO_m^{0/\pm}$ (n =3-8 and m =1-10) clusters. Before going into the structural details for each n series, we summarize those trends and growth patterns that are common to all or most of them. We focus on the cationic clusters, since it is the charge state of the clusters present in the experimental analysis. In the Fig. 3.1 are depicted the putative ground state geometry of these cations. In Fig. 3.2-3.7 of are depicted the putative ground state and first two low-energy isomers of the neutral clusters (n.m-I indicate the ground state for Ni_nO_m, n.m-II and n.m-III are the first and second isomers respectively). The ground state of their cationic and anionic counterparts, when not the same, corresponds to one of the two lowest-energy isomers, and it can be identified in Tables 1-12 of the Appendix A, where inter-atomic distances, binding energies and total spin-magnetic moment are also reported.

In the initial stages of oxidation, for all n, a compact Ni_n subcluster is formed, on which oxygen atoms start to bond preferentially in three-fold hollow sites, and then in bridge sites. This Ni_n motif is robust until $m \approx n$ and, up to this point, the growth pattern proceeds simply by capping Ni_n with O avoiding direct O-O bonding (oxygen atoms tend to distribute uniformly on the cluster). When $m \approx n$, a structural change takes place. The structure opens and the cluster adopts a low-coordinated arrangement, with a weakening of the

Ni-Ni bonding manifested in an increase of Ni-Ni inter-atomic distance and a lowering of the Ni-O one, as seen in the Fig. 3.8. The Ni-Ni coordination also reduces in general at this transition (Fig. 3.9). This is particularly notorious for clusters with $n < 6$, for which two-dimensional ring-like structures are formed at the stoichiometric or equiatomic oxidation rate ($m = n$). Those ring-like structures have, in general, a high relative stability in agreement with experiments, as well as exceptional magnetic properties (to be discussed in section 3.5.3). For $n \geq 6$, this opening of the geometrical structure as m approaches n becomes less dramatic (planar ring-like structures are not formed) though it is still recognizable (see the structures 6.5-I, 7.5-I, 8.8-I). After this reentrance of low-coordinated arrangements at $m \approx n$, the structure becomes again relatively compact at higher oxidation rates. This is again reflected in the average inter-atomic distances (Fig. 3.8) and coordination (Fig. 3.9). However, at higher oxidation rates, the structures become more complex. Although in most cases, similar Ni_n motifs as those formed for low oxidation rates can be still identified, other motifs based on the stable ring structures of smaller stoichiometric clusters can be also identified in some cases. The distribution of the Ni-O inter-atomic distances becomes narrow as the cluster size increases, regardless the charge state. As we will see, the reentrance of low coordinated structures close to the stoichiometric oxidation rate also correlates with the magnetic properties. Besides, the maximal value of the Ni-Ni inter-atomic distance corresponds with a minimal value in the magnetic moment, the only exception is observed for Ni_4O_4. The geometries of the neutral and anionic Ni oxide clusters are, in most cases, similar to those of their cationic counterparts; when different, a more open structure is formed as a general rule. The favorable site for O (hollow or bridge) changes, in some cases, with the charge state. Those cases can be identified in Fig. 3.8 through different Ni-O average inter-atomic distances reflecting a rearrangement of one or more oxygen atoms depending on the charge state. Note that this may happen even if the Ni subcluster is preserved. Changes in the Ni subcluster upon an electron deficit or excess are manifested in different Ni-Ni average interatomic distances and can

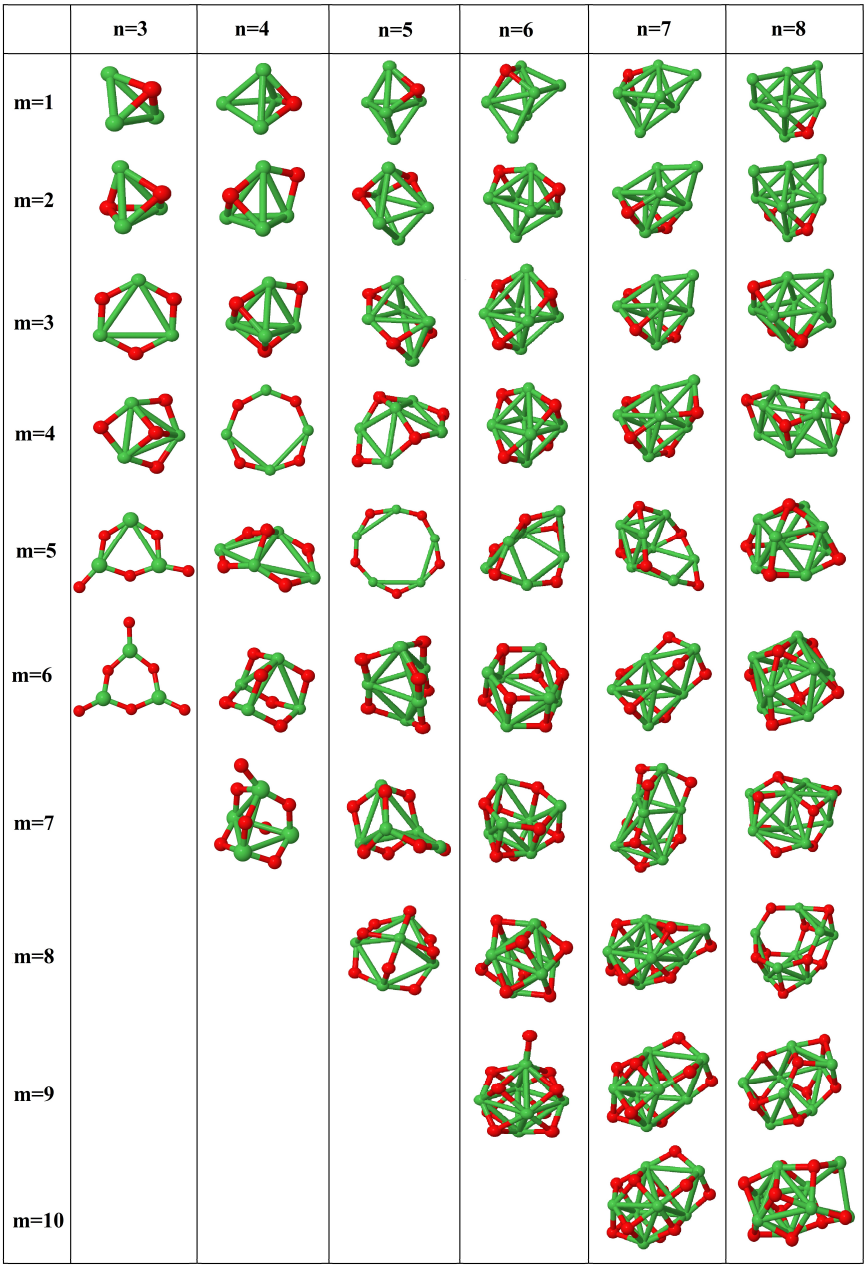

Figura 3.1: Putative ground state of $Ni_nO_m^+$ clusters.

be easily identified also in Fig. 3.8. Details of the corresponding ground states are collected in the tables of the appendix. Exceptions to the above rules are only Ni_6O and Ni_6O_5, with different Ni subcluster in different charge states but with the same average Ni-Ni and Ni-O distance.

The binding energy per atom of neutral and charged clusters, as well as the second total energy difference is plotted, as a function of the oxygen content m, in Fig. 3.10. These magnitudes are defined in Eqs. 2.53, 2.54 and 2.55 (with $A = Ni$), respectively. For a given n, the values $\Delta_2(n, m)$ (Fig. 3.10 right panels) as a function of m will show a prominent positive peak at those m values whose corresponding (n, m) clusters are more stable than their $(n, m-1)$ and $(n, m+1)$ neighbors against the addition or substraction of one oxygen atom. It is worth noticing that, in general, the picks in the second energy difference correspond to clusters that are formed by a fundamental building block made of two Ni and one oxygen atoms in an isosceles triangular arrangement, being the Ni-Ni the largest distance in the block. The fundamental block formed by Ni_2O is also present in larger unities with high stability, like the rhombus Ni_2O_2 and the Ni_3O_3 ring, that can be clearly identified in the putative ground states ($n.m.$-I) as illustrated in the Fig. 3.2 to 3.7. Some deviations in this trend are observed in the anionic clusters particularly for Ni_5 and Ni_6.

In the remaining of this section we describe the structural details for each n series. As we will see, the highest relative stability deduced from $\Delta_2(n, m)$ corresponds indeed to two-dimensional ring structures, or to structures in which rings of lower size clusters can be identified.

3.1.1 $Ni_3O_m{}^{0/\pm}, m = 1 - 6.$

Most clusters in this series (see Fig. 3.2) have a triangular core of nickel atoms, not only the putative ground states but also the lowest isomer, an exception being the linear 3.3-III. In poor oxygen clusters ($m \leq 2$), O atoms bind on hollow sites, while bridge positions are more favourable in rich oxygen clusters ($m \geq 3$).

Certain isomers have quite singular structural properties, only present in

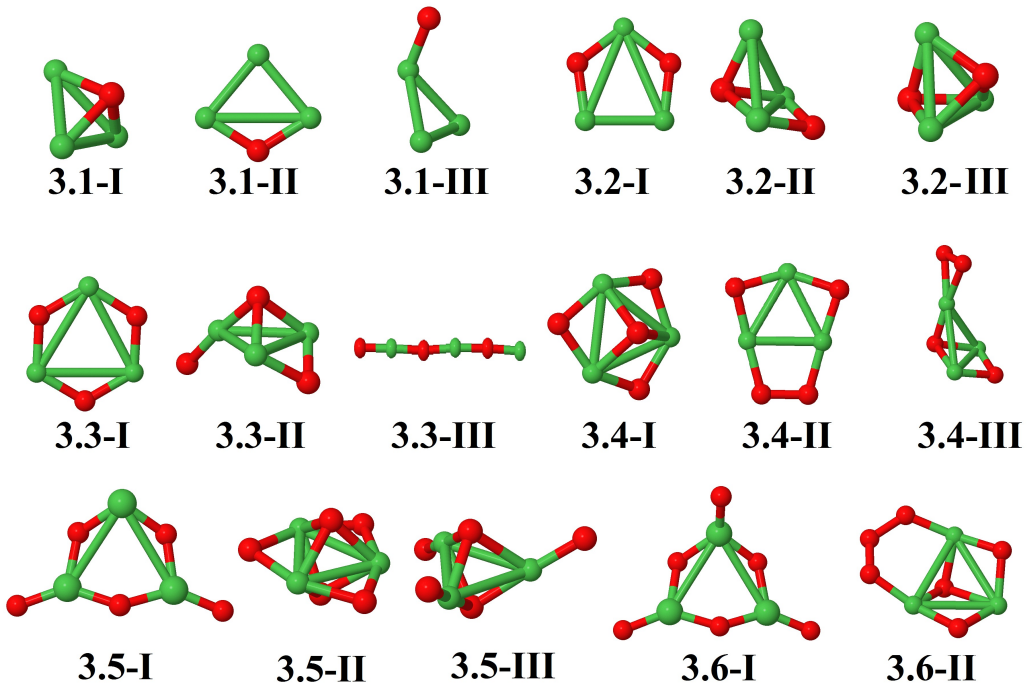

Figura 3.2: Putative ground state of Ni_3O_m neutral clusters.

this series; these are: 3.1-III, with the oxygen atom bonded on top position; 3.3-II, the only geometry with O atoms bonded in all kind of sites (hollow, bridge and top positions); 3.4-II, with a molecular oxygen bonded on bridge; 3.4-III, with two oxygen atoms molecularly bonded on top; 3.5-II and 3.6-I, with three atoms on top; and 3.6-I, with three oxygen atoms molecularly bonded to the nickel subcluster. The cluster 3.3-I has a planar ring-like structure, it has the largest binding energy per atom and the highest relative stability, manifested in the peak in the second energy difference (See Fig. 3.10), independently of the charge state, being the most stable one for this series. Furthermore, the average Ni-O inter-atomic distance (regardless of the charge state) has a minimal value as seen in Fig. 3.9. As we will see later, this is consistent with its abundance, as experimentally observed. This ring structure can be also identified in 3.4-I, 3.5-I and 3.6-I (see Fig. 3.2), where it is capped by one, two and three additional oxygen atoms, respectively.

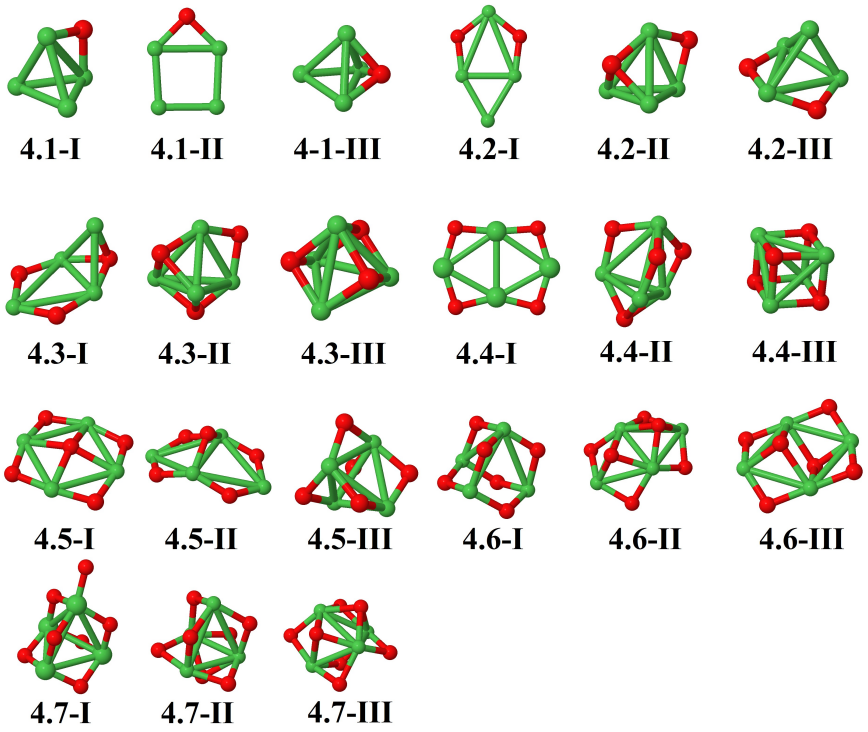

Figura 3.3: Putative ground state of Ni_4O_m neutral clusters.

3.1.2 $Ni_4O_m^{0/\pm}, m = 1 - 7.$

Most clusters have a tetrahedral Ni_4 core (See Fig. 3.3). The exception is 4.4.I with a planar ring-like structure (again for all charge states). This cluster has the largest binding energy per atom (Fig. 3.10) for the neutral and anionic states, while for the cationic one it has the same energy per atom as 4.5.II. On the other hand, the average Ni-O inter atomic distance for this cluster has a minimal value, while the Ni-Ni one has a maximum value only for the cationic cluster. Due to its relevance in the context of the experiments, we devote part of subsection 3.2 to a detailed discussion of the magnetic properties of $Ni_4O_4^{0/+}$. Planar structures are also found in certain low-energy isomers like 4.1-II and 4.2-I, both having the oxygen atoms bonded in bridge sites. 4.3-III is a Ni_3O_3 ring capped with a nickel atom; 4.5-I, 4.5-II, 4.6-II and 4.6-III can be also described as oxigen-capped ring-like structures.

3.1.3 $Ni_5O_m^{0/\pm}, m = 1 - 8.$

Clusters with low oxygen content (See Fig. 3.4) have an hexahedron-like core of nickel atoms. The cluster 5.4-I is a flat pyramid-like one, formed by two Ni_3O_3 rings sharing atoms. It has the largest relative stability, as reflected in the second energy difference (Fig. 3.10). Thus, the structure starts to open at this oxygen content and, with one just more O atom, 5.5-I already has a planar ring arrangement. This is the biggest planar Ni oxide cluster among all investigated ones. Unlike in the previous series, no peak appears in the second energy difference (Fig. 3.10) for this structure, but like in previous series, the average Ni-O inter-atomic distance has a minimal value (maximum for Ni-Ni inter-atomic distance) regardless the charge state. In fact, a transition from two dimensional structures to three-dimensional ones takes place for stoichiometric Ni oxide clusters at this particular size, in agreement with IMMS experiments (83). In clusters 5.6-I, 5.7-III, 5.8-I, a Ni_4O_4 ring motif can be identified, and a Ni_3O_3 ring motif in 5.4-I and 5.7-III.

3.1.4 $Ni_6O_m^{0/\pm}, m = 1 - 9.$

Almost all structures have an octahedral-like core of nickel atoms (See Fig. 3.5). Exceptions are 6.1-I with a capped hexahedral nickel core, which can be seen as the structure of 5.1-I with an additional Ni atom on a hollow site, and 6.5-I formed by a Ni_4O_4 ring capped with a Ni_2O. This last one is the open structure close to the stoichiometric oxidation rate for this series. Perfectly planar ring structures are no longer the putative ground state at the stoichiometric rate, but they exist as a low-lying isomer (6.6-III). The stoichiometric ground state, 6.6-I, is formed by two Ni_3O_3 rings one above the other in anti-site positions; it has a stability peak in the second energy difference (Fig. 3.10) and the largest binding energy per atom. This arrangement has a maximum value for the average Ni-Ni inter-atomic distance in the cationic and anionic states (See Fig. 3.8). Another particularly stable cluster, in both the cationic and neutral states, is 6.4-I (tetrahedral-like shape), which leads to the highest peak in the

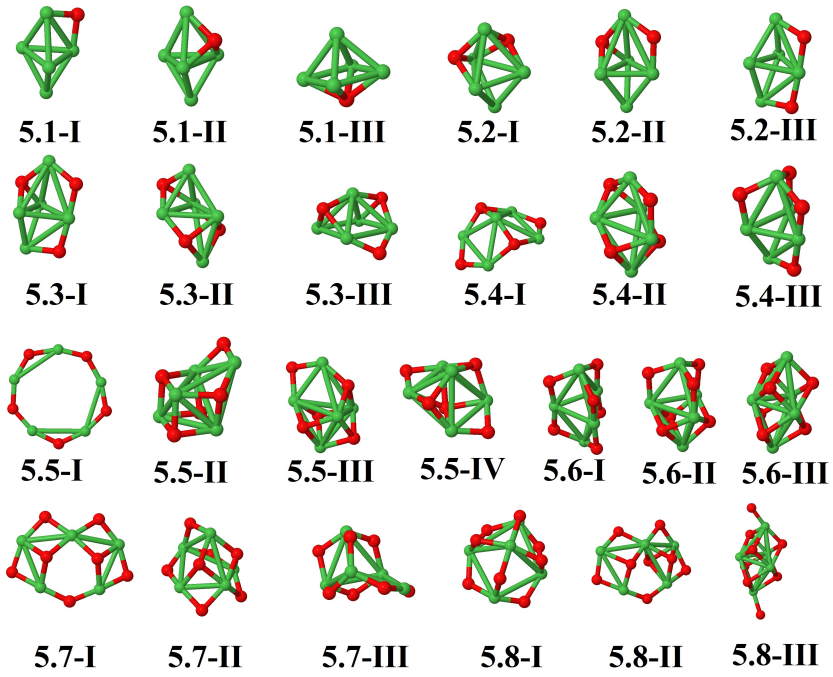

Figura 3.4: Putative ground state of Ni_5O_m neutral clusters.

second difference energy (See Fig. 3.10). Its structure is an octahedral core of nickel atoms with the oxygen atoms on hollow positions. This structure, of high symmetry (T_d), can also be seen as four interpenetrated Ni_3O_3 rings (located at the shared faces). In clusters 6.3-I, 6.4-I, 6.6-I, a Ni_3O_3 ring motif can be clearly identified (See Fig. 3.5).

3.1.5 $Ni_7O_m^{0/\pm}, m = 1 - 10.$

The ground state structures of this series (See Fig. 3.6) have a capped octahedral-like nickel core. The only exception is 7.5-I, which is formed by a Ni_4O_4 ring capped with a Ni_3O subcluster. This is the only open structure in this series close to the equiatomic oxidation rate and it has the largest relative stability (See Fig. 3.10). No planar structure appears anymore even among the low-energy isomers, but Ni_3O_3 rings can be identified in the surfaces of 7.3-I, 7.4-I, 7.5-I, 7.6-I and 7.8-I, and Ni_4O_4 rings in 7.5-I, 7.6-I, 7.7-I and 7.9-I. Those clusters minimize their energy by using Ni_3O_3 and Ni_4O_4 rings as building blocks.

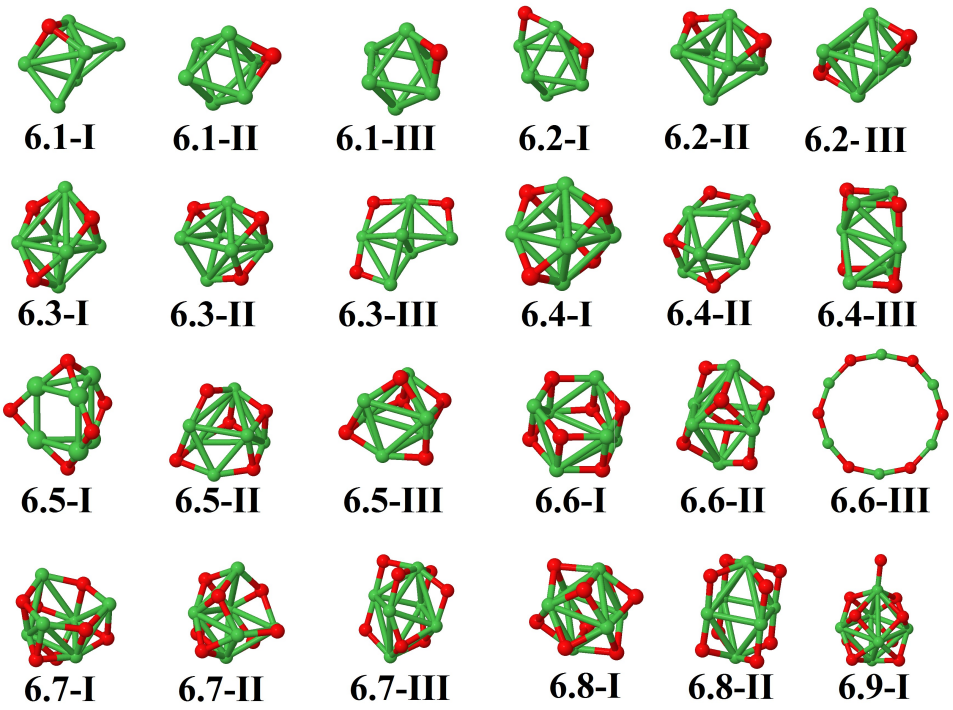

Figura 3.5: Putative ground state of Ni_6O_m neutral clusters.

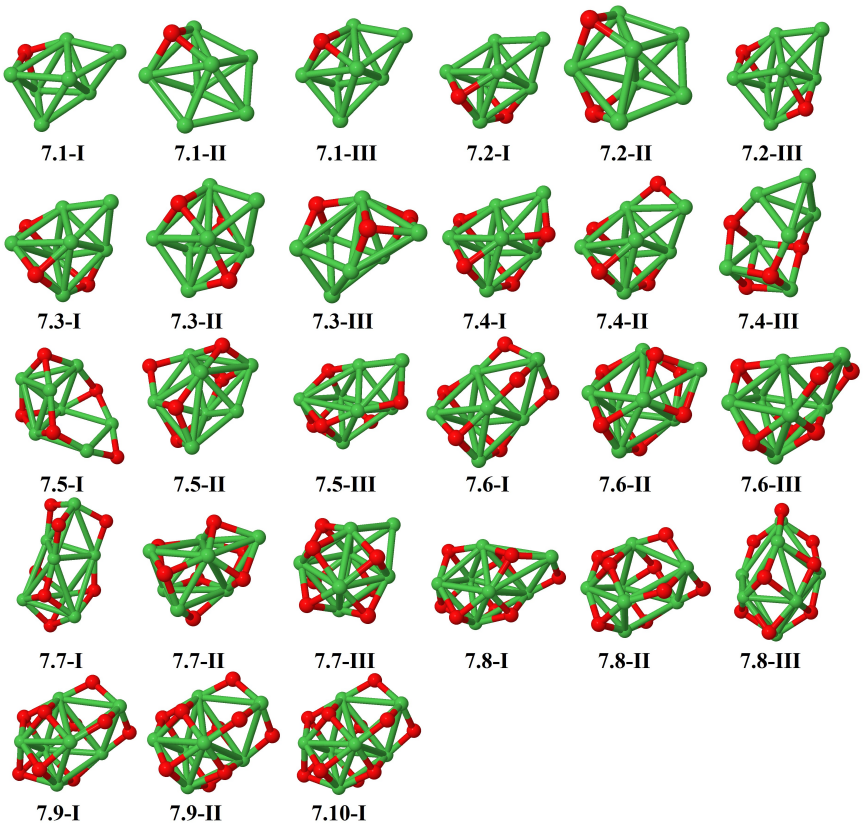

Figura 3.6: Putative ground state of Ni_7O_m neutral clusters.

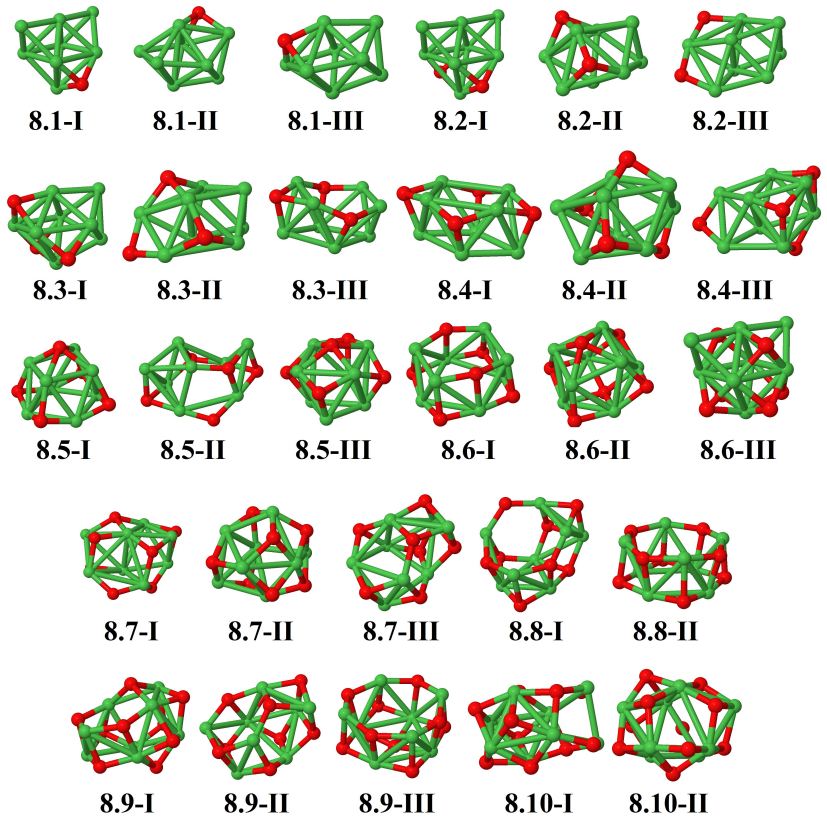

Figura 3.7: Putative ground state of Ni_8O_m neutral clusters.

The average Ni-Ni inter atomic distance (Fig. 3.8) increases with the number of oxygens atoms, except for the anionic cluster Ni_7O_8. The Ni-O average inter atomic distances enter in a narrow window of 1.84-1.94 Å. In this series for low O content, the second energy difference display an even-odd effect.

3.1.6 $Ni_8O_m^{0/\pm}, m = 1 - 10.$

Almost all ground states have a core of nickel atoms (See Fig. 3.7), being a bicapped octahedron for $m = 1, 2, 3$ and 10. Clusters with $m = 4, 5$ and 6 are tower-like, while those with $m = 8$ and 9 are amorphous. Like in other series, rings can be identified in some clusters. 8.5-I has a Ni_4O_4 ring merge to a Ni_4O sub-cluster, being the one with the highest relative stability (the largest pick in the second energy difference, Fig. 3.10); 8.3-I is a Ni_3O_3 ring merge to a Ni_5

(pyramid-like) sub-cluster; 8.4-I is a Ni_4O_4 ring merge to a Ni_4 (rhombus-like) sub-cluster; 8.8-I is an open structure formed by two Ni_3O_3 rings. It is nearly a hollow cage. In 8.9-I, five nickel atoms form a core and the other three are separated. The average Ni-Ni inter atomic distance increases with the number of O atoms, and the Ni-O average inter-atomic distances also enter in a narrow window of 1.84-1.94 Å.

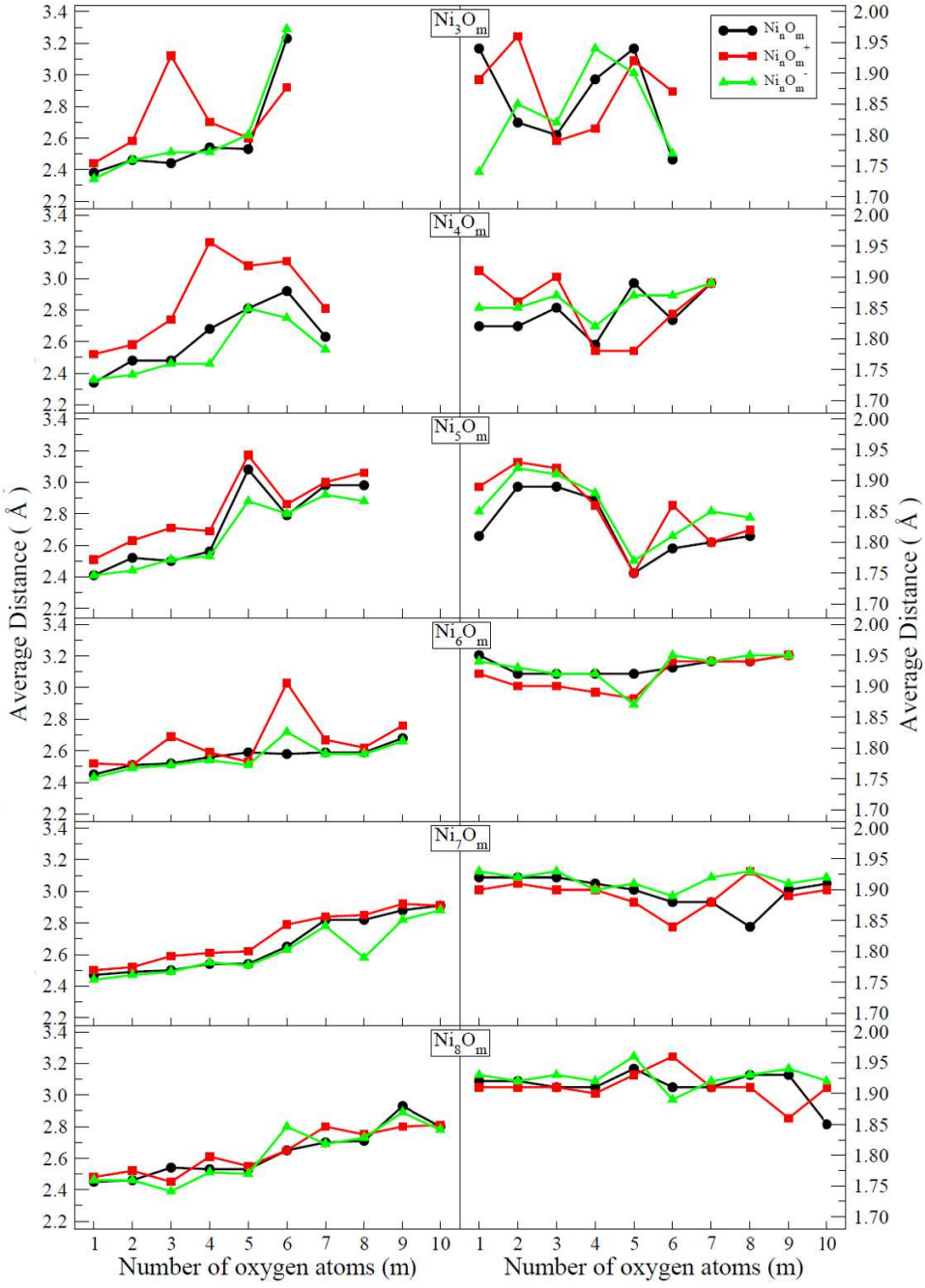

Figura 3.8: Ni-Ni (left panels) and Ni-O (right panels) average distance for $Ni_nO_m^{0/\pm}$ clusters as a function of the number of oxygen atoms (m).

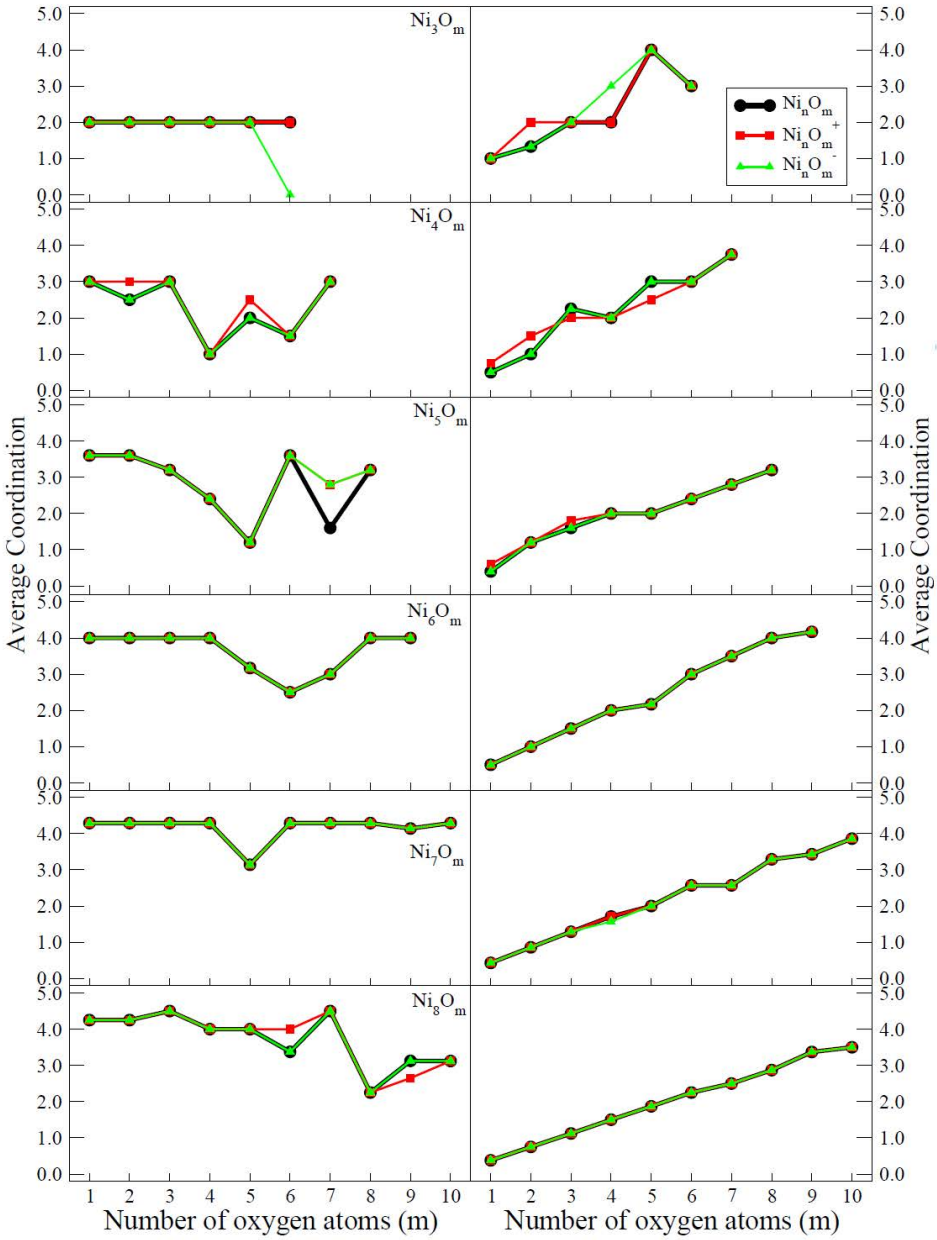

Figura 3.9: Average Ni-Ni (left) and Ni-O (right panels) coordination of the $Ni_nO_m^+$ clusters as a function of the number of oxygen atoms (m).

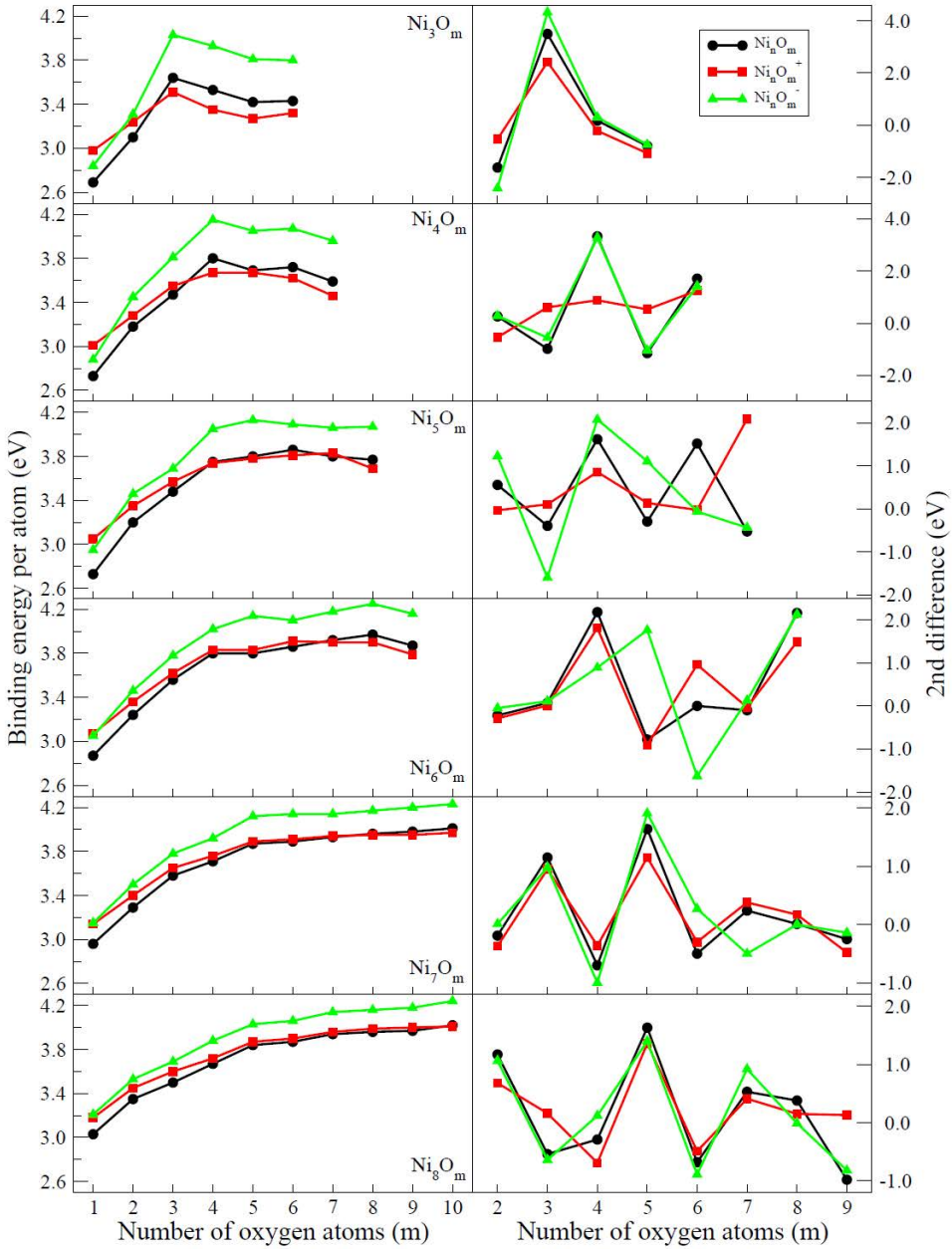

Figura 3.10: Binding energy per atom (left panels) and second difference of energy (right panels) of $Ni_nO_m^{0/\pm}$ clusters as a function of the number of oxygen atoms (m).

3.2 Magnetic properties

In Fig. 3.11 we summarize the results obtained for the total spin magnetic moment of the investigated Ni_nO_m clusters in their neutral and charged states. For most clusters, the change in the spin state upon ionization or upon an electron excess is consistent with a one electron process (reduction or increase of $1\mu_B$ with respect to neutral case). However, we note that Ni_4O_m is an exception in which for most oxidation rates, one electron more or less implies a strong spin-dependent charge redistribution leading to a large change of spin state. In this case, Ni_4O_6 is particularly relevant, since an electron excess increases the total spin moment from $2\mu_B$ (in the neutral state) to $11\mu_B$, that is a high spin state. It is interesting to note that the total moment of pure Ni_4 is $4\mu_B$ in our approach (in agreement with Gaussian results (86)), so that the oxidation at this rate ($m = 6$) did not significantly change the magnetic moment of Ni_4, but an electron excess in addition did it. This huge increase is not accompanied, in this case, by a noticeable change of the structural shape as in other clusters (see Tables 1-12 of the Appendix A). Therefore, in order to analyze the origin of such dramatic change in the total moment, we have calculated the atom-projected spin-polarized charge density and assigned local magnetic moments to the different atoms of the cluster, according to Mulliken populations (the same for the electronic occupation). The low spin state of the neutral Ni_4O_6 is due to antiparallel couplings which transform, upon the electron excess, into a ferromagnetic-like arrangement with Ni moments of $1.46\mu_B$ (more than twice the local moment of a Ni atom in the fcc bulk) and O moments of $0.86\mu_B$, and the resulting huge total moment. This cluster $Ni_4O_6^-$, as well as others like $Ni_6O_5^+$, Ni_7O_6 and Ni_8O_6, are specially interesting in the context of magnetic grains because of their large total magnetic moment (11 or $12\mu_B$). In particular, the last three ones are among the most abundant ones according to their stoichiometry in connection with mass spectrometry and photodissociation experiments (82). Moreover our results demonstrate that the unavoidable oxidation in environmental conditions does not necessarily quench the magnetic moment. On the contrary, the huge total moment of

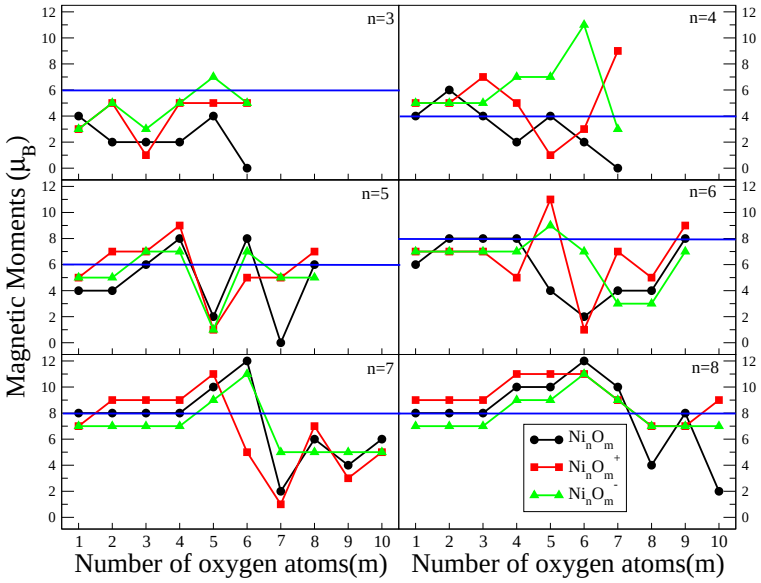

Figura 3.11: Total spin magnetic moment of $Ni_nO_m^{0/\pm}$ clusters as a function of the number of oxygen atoms (m). The horizontal (blue) line denotes the magnetic moment of the neutral Ni_n clusters.

Ni_7O_6 and Ni_8O_6 is due to oxidation, since the neutral Ni_7 and Ni_8 clusters have lower magnetic moment. And in the case of Ni_8O_6 the moment is even robust against both ionization and electron excess.

Fig. 3.11 demonstrates that oxidation does not quench, in general, the magnetic moment of small Ni clusters. From the local moments distribution within the clusters, we identified a high spin-polarization in many Ni atoms and a noticeable spin-polarization of O in general, which contributes the total magnetic moment. Other Ni atoms have low moments, close to the value in fcc bulk or even lower. We also find that changes in the spin state due to the charge state are not necessarily accompanied by a change of structural shape (an example being the cluster Ni_4O_6, already discussed) and no systematic trends are obtained from the data in this regard (see Tables 1-12 of the appendix). In general, most Ni oxide clusters exhibit antiparallel magnetic couplings in a more or less degree. Antiparallel couplings are a clear signature of strong

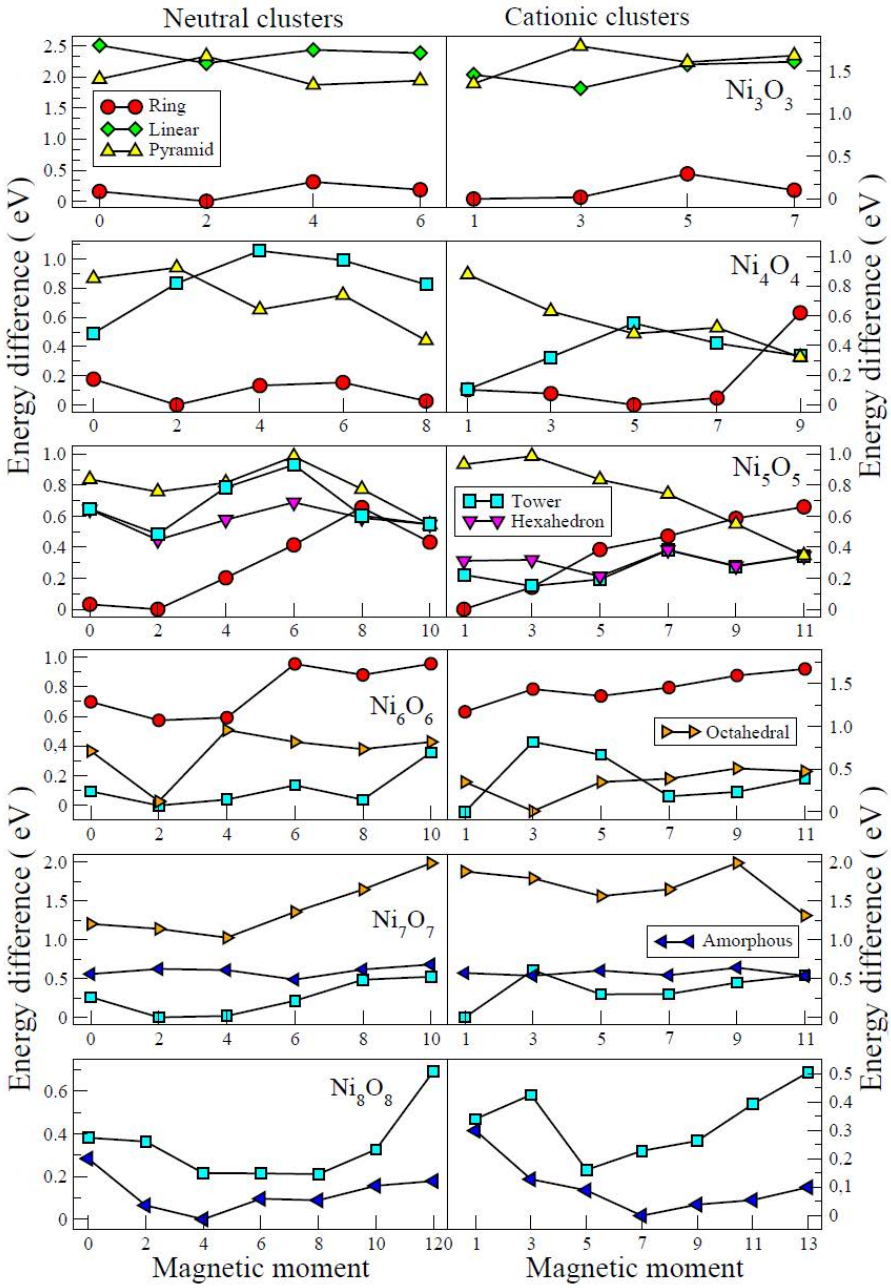

Figura 3.12: Energy difference (with respect to our putative ground state) as a function of the spin state of several structural arrangements of the stoichiometric clusters $Ni_nO_n^{0/+}$.

Ni-O interaction and oxygen-mediated Ni-Ni exchange, since pure Ni clusters are ferromagnetic-like. Clusters with larger total moment are those with less antiparallel couplings, thus closer to the ferromagnetic-like arrangement with high local spin-polarization. However, there exist few Ni oxide clusters with a small total moment (examples are Ni_6O_5, and Ni_nO_n with n =3 and 6 discussed later) but which exhibit a ferromagnetic-like configuration instead of antiparallel couplings, although with low local spin-polarization (Ni moments smaller than in the bulk). Analyzing the trend of the total spin moment as a function of the oxidation rate, we clearly see that it is non-monotonous, and that, in general, a minimum in the total moment is reached at the stoichiometric oxidation rate ($n = m$). This means that from the magnetic point of view, if a large magnetic moment is desired, oxidation at the stoichiometric rate must be avoided, but this seems difficult. In fact, mass spectrometry and photodissociation experiments (83) revealed that stoichiometric clusters are among the most abundant ones.

Ion mobility mass spectrometry (83) revealed a transition from two-dimensional ring- to tri-dimensional compact- structures in $Ni_nO_n^+$ and $\mathrm{Ni}_n\mathrm{O}_{n-1}^+$ at $n = 5$. They also found that both types of structures coexist for $Ni_5O_5^+$. Calculations of the same group (82) were consistent with the above facts in terms of cross sections which fitted the experimental values. However, for $Ni_4O_4^+$ the ring structure, although having the correct cross-section, is not their putative ground state; For $\mathrm{Ni}_5\mathrm{O}_5^+$ the ring structure is even at 0.36eV above the ground state which is relatively compact, but not the cluster with the correct cross section (the compact isomer with cross section closer to the experimental value is also quite high in energy, at 0.34eV above the ground state). Isomers at such high energy with respect to the ground state are not expected to be present for this size.

Since stoichiometric clusters are relevant due to their abundance (relative stability) and in view of the facts discussed above, it is pertinent to revisit them in some detail. We have analyzed the stoichiometric clusters found in our approach, in both the neutral (Ni_nO_n) and the cationic ($Ni_nO_n^+$) states

(the experiment deal with cations). In Fig. 3.12 we report the energy difference (with respect to our putative ground state) as a function of the spin state for all those clusters, considering several structure types. The main trends are: (i) two-dimensional ring structures are the putative ground state up to $n = 5$ for both charge states, which provides consistency with experiments of Ion mobility mass spectrometry (83) also from the energetic point of view. The compact structures calculated by Ohshimo *et al.* (83) as the putative ground state of $Ni_4O_4^+$ and $Ni_5O_5^+$ are now our first isomers. (ii) a transition to compact three-dimensional structures, based on an octahedron Ni subcluster, takes place at $n = 6$. Those compact structures are more competitive with the ring ones in the cationic clusters than in their neutral counterparts, as demonstrated by the fact that spin- and structural-isomers start to be accessible at the same energy window for smaller sizes in cationic clusters than in neutral ones. In Fig. 3.13 we present the calculated vibrational spectra of two structural isomers of Ni_6O_6, and of two spin and structural isomers of $Ni_6O_6^+$, which can aid to select the true ground state by comparing with future infrared spectroscopy experiments, like was recently done for the case of small $Co_xO_y^+$ clusters (84). (iii) A further structural transition takes place at $n = 8$, where the pattern based on an octahedron Ni subcluster evolves to a more open structure, again for the two charge states; (iv) a magnetic transition is found to occur just at $n = 8$ corresponding to the mentioned loss of the structural pattern based on the octahedron Ni subcluster. Thus, neutral clusters change from a total spin magnetic moment of $2\mu_B$ to $4\mu_B$, while cationic clusters change from $1\mu_B$ (being $Ni_4O_4^+$ the only exception with $5\mu_B$) to $7\mu_B$. Due to the relevance of Ni_4O_4 and to its being an exception in the magnetic trend, we discuss it in more detail at the end of this section.

Our results indicate that, for small Ni clusters oxidized at the stoichiometric rate, the geometrical shape does not essentially change upon ionization (just structural relaxations take place, as we will see in detail for Ni_4O_4 at the end of this section). From the data reported in Tables 1-12 of the Appendix A, we see that an electron excess does not affect essentially the structure either.

We note that the above can not be generalized to oxidation rates other than the stoichiometric one; on the contrary, the equi-atomic concentration seems to be an exception, since the ground state structures strongly depend on the charge state in a considerable number of non-stoichiometric Ni oxide clusters, particularly for those with $n < 7$ (see Tables of the appendix). In fact, stoichiometric clusters are an exception also in regard to the magnetic properties. These clusters, in their neutral and cationic states, bear the lowest total spin magnetic moment among the investigated compositions. They are in a low spin state before the second structural transition takes place. Note, however, that stoichiometric Ni oxides in the anionic state bear a higher spin magnetic moment. The change in the spin state upon ionization in stoichiometric Ni oxide clusters is consistent with a one electron process (reduction of $1\mu_B$), except for $n = 8$, being this cluster particularly interesting since ionization produces just the opposite effect, that is a spin-polarized electronic redistribution leading to a relatively high magnetic moment of $7\mu_B$. The same trend is obtained for the anionic state, indicating that an electron excess does produce a strong spin-dependent electronic charge redistribution, regardless the slight relaxation of the atomic structure.

Different spin-dependent electronic charge distribution can lead to the same total spin moment of the system. It is pertinent to explore the origin of the resulting total moment, in terms of magnetic couplings and local spin-polarizations. The origin of the low spin state in stoichiometric Ni_nO_n is not the same for all n. For $n = 3$ and 6, the clusters exhibit a ferromagnetic-like arrangement with all local moments pointing in the same orientation, but with a small spin-polarization in the Ni sites (0.32 and $0.22\mu_B$ for $n = 3$ and 6, respectively, about half the value in the fcc bulk) and an important contribution from the O sites (0.35 and $0.12\mu_B$ for $n = 3$ and 6, respectively). Interestingly, Ni_6O_6 is formed by two Ni_3O_3 rings. These are exceptional cases, since most of the clusters exhibit antiparallel magnetic couplings, in more or less degree, with some Ni local moments that can reach up to about $1.3\mu_B$, that is about twice the local moment of a Ni atom in the fcc bulk.

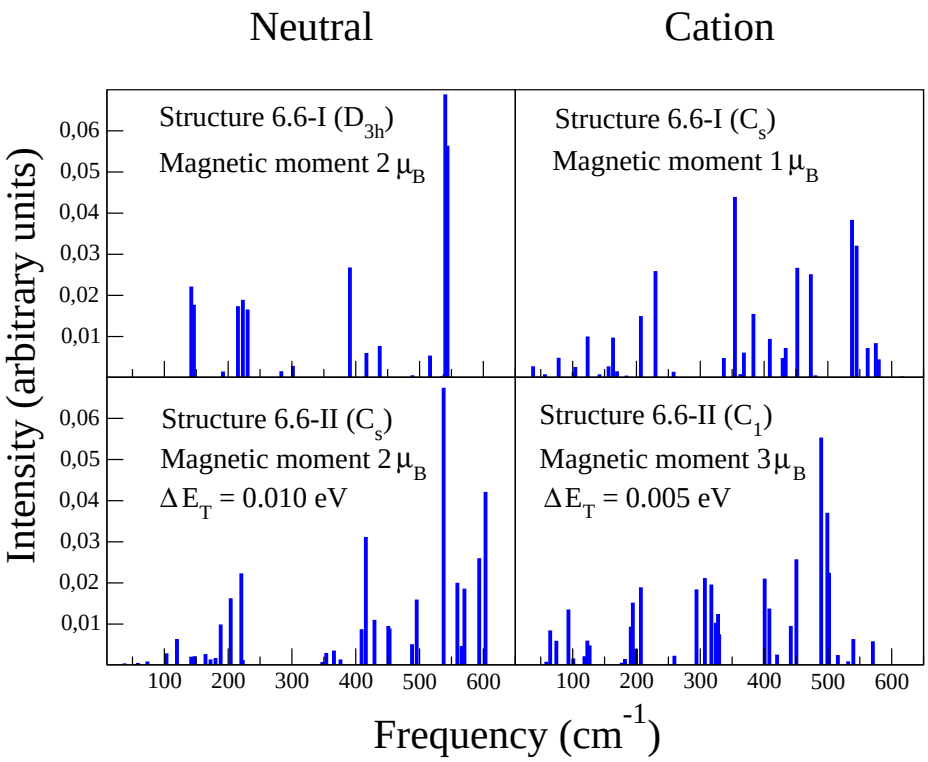

Figura 3.13: Vibrational spectra of the ground state (6.6-I) and first isomer (6.6-II) of Ni_6O_6 (left panels) and of $Ni_6O_6^+$ (right panels). The symmetry, magnetic moment, and excess total energy w.r.t. the ground state of each cluster are specified for comparison.

Finally, we analyze in detail the spin isomers of Ni_4O_4. For the sake of brevity, we do not present a similar analysis for other clusters. Fig. 3.14 illustrates the atomic structures, local magnetic moments distributions and magnetic couplings of the different spin isomers of Ni_4O_4, $Ni_4O_4^+$ and $Ni_4O_4^-$. As discussed above, the atomic structure is a two-dimensional ring, independently of the spin and charge states. Local relaxations are concomitant with the symmetry imposed by the spin-polarized charge distribution. Thus, ferromagnetic-like clusters (those with the higher total spin moment) are highly symmetric (see the high-spin states in all charge states). Symmetry breaking takes place as soon as antiparallel couplings arise. Marked antiferromagnetic-like config-

urations lead to low-spin states. These trends are common to all Ni oxide clusters investigated here, as discussed in previous paragraphs. We also find that different spin isomers with the same magnetic couplings exist, in which case the difference comes from the local spin-polarization (compare, for instance the local moments in the neutral Ni_4O_4 with total moments of 4, 6 and 8, all corresponding to ferromagnetic-like configurations). We can also identify spin-isomers whose energy difference essentially comes from the electronic redistribution, with atomic structure practically unchanged, while in other cases, part of this energy difference is contributed by the noticeable structural relaxation (the two lower-spin states of Ni_4O_4 and $Ni_4O_4^+$).

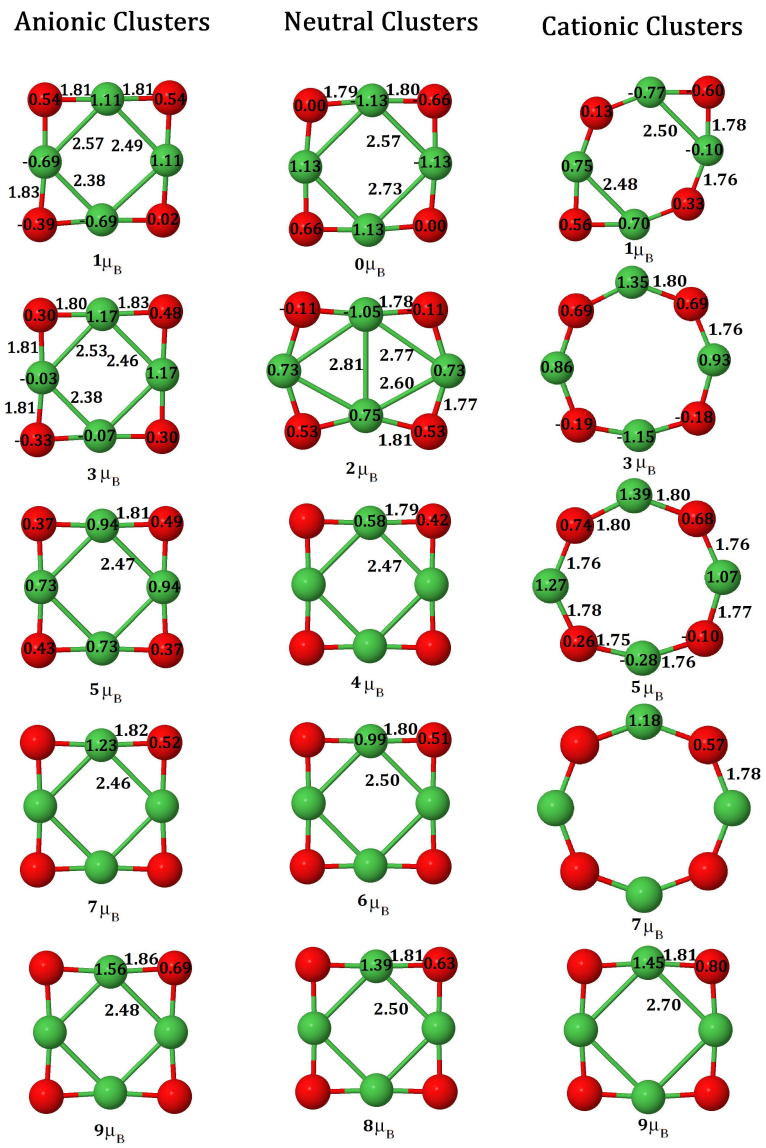

Figura 3.14: Atomic structures, total spin magnetic moment, local magnetic moments distributions and magnetic couplings of the different spin isomers of $Ni_4O_4^{0/\pm}$. Distances in $\mathring{A}$ and magnetic moments in μ_B.

3.3 Fragmentation channels of cationic clusters

The photo-dissociation of mass selected $Ni_nO_m^+$ cations is produced experimentally by multiple absorption of photons of 355 nm (3.49 eV) (82). Multiple photons are needed to break the nickel oxide clusters because, according to our calculations shown in Fig. 3.15, the binding energy per particle is in the range $\sim$ 3-4 eV. A comprehensive list of the photo-fragments produced by several mass selected clusters cations after multiple photon absorption is presented in Table 2 of the work of Duncan and coworkers (82). As discussed by these authors, the mechanism of fragmentation can be i) of parallel type, with the same parent cluster leading to two or more different fragments, ii) sequential, with a chain of parent-daughter fragments, or iii) a combination of i) and ii). Varying the laser power allows, in principle, to distinguish between the i) and ii) dissociation processes, but the experimental studies (82), which are consistent with mechanism i), cannot rule out with absolute certainty the sequential fragmentation scheme ii).

From the experimental fragmentation data, no direct information about the structure of the precursor cation can be obtained because extensive reorganization of the structures may occurs before fragmentation. In this section, we will compare the experimental fragments with those resulting from our total energy calculations, and taken into account both the parallel and sequential mechanisms. For a given step, we first subtract the calculated energies of the precursor and its possible fragments, and then we consider only the smaller values of these energy differences (excitation energies) within a narrow energy window. In some cases, due to the aforementioned structural reorganization before fragmentation, we will consider also the energies of the low lying energy isomers given in Tables 1-12 of the Appendix A. Then, our results in this sections give us only a qualitative link between our calculated structures and the observed photo-fragmentation of cationic nickel oxide clusters.

We consider now the fragmentation of a $Ni_nO_m^+$ cluster in a neutral frag-

ment plus a charged fragment according to the following channels (in parenthesis is given the symbol used in the Fig. 3.15):

i) Ni + $Ni_{n-1}O_m^+$; (brown diamonds)

ii) NiO + $Ni_{n-1}O_{m-1}^+$; (red squares)

iii) NiO_2 + $Ni_{n-1}O_{m-2}^+$; (green up triangles)

iv) Ni_2O_2 +$Ni_{n-2}O_{m-2}^+$; (purple down triangles)

v) O + $Ni_nO_{m-1}^+$; (blue left triangles)

and

vi) O_2 + $Ni_nO_{m-2}^+$ (black filled circles).

This process is endothermic so that the smaller $E_f(n,m)$ in absolute value, will be the more favorable the fragmentation along the corresponding channel. In Fig. 3.15 is plotted, as a function of the number of Nickel atoms, the calculated minimum energy needed to produce the fragmentation of $Ni_nO_m^+$ cations with $n = 3-8$ and $m = n-2$ (panel a), $m = n-1$ (panel b), $m = n$ (panel c), $m = n+1$ (panel d), and $m = n+2$ (panel e). These energies are defined as E($Ni_nO_m^+$) - E(Ni) - E($Ni_{n-1}O_m^+$), for channel i), and similarly for the other ii)-vi) fragmentation channels. In Table 3.1, we compile the fragmentation energies for these channels. In this thesis are not calculated possible fission barriers which may increase the energy needed for some fragmentation channels.

First we check our results against two general features which were highlighted in the experimental results of Duncan and coworkers (82):

I) Most of the photo-fragmentation series for $n.m$+2, $n.m$+1, and n.n (the series for $n.n$-1 clusters were not considered in the experiments) contain the $n.m$-2 fragment, which corresponds to the release of O_2. The few exceptions are the 3.6, 6.6, and 8.8 fragmentation series. That experimental feature is reproduced by our calculations, that is, the loss of O_2, is always the channel requiring minimum energy for the $n.m$+2, $n.m$+1, and $n.n$ fragmentation series, as seen in Fig. 3.15. The only exceptions are the fragmentation of 5.5, 4.4, and 8.8 parent cations. Note that 8.8 case is in agreement with experiments. For these cases, the fragments 4.4, 3.3, and 7.7, respectively, require

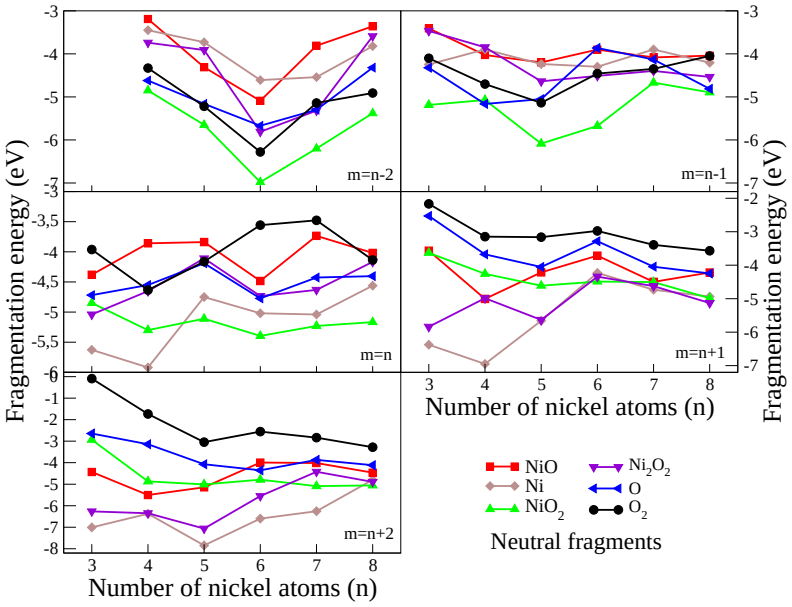

Figura 3.15: Calculated minimum energy needed to split a $Ni_nO_m^+$ cation ($m = n \pm 2, n \pm 1, n$) in a neutral and a charged fragment, being the neutral fragment as specified by the code in the lower right panel.

less energy than the fragments 5.3, 4.2, and 8.6, respectively (see panel $m = n$ of Fig. 3.15). Nevertheless, the preferred fragments, namely 4.4, 3.3, and 7.7, are also observed in the photo-fragmentation of 5.5, 4.4, and 8.8 cations (82).

II) The fragment 2.1 appears in all the experimental dissociation series, except for the 8.8 one. In our calculations, the fragment 2.1 is always obtained too, as we will see later when studding the sequential fragmentation of the several $n.m$ cations. On the other hand, the fragment 1.0 appears together with the fragment 2.1 in all the experimental $n.m$ series with $n < 7$ (except for 6.7 and 5.7), whereas the fragment 1.1 never is detected. In this respect, from our calculations we obtain that the minimum energy for the dissociation $Ni_2O^+ \rightarrow Ni^+ + NiO$ is 3.64 eV, to be compared with at least 5.06 eV needed for the reaction $Ni_2O^+ \rightarrow Ni_2^+ + O$, or with 5.09 eV for $Ni_2O^+ \rightarrow NiO^+ + Ni$ one.

In the following, for each initial parent cation $Ni_nO_m^+$ we trace the sequential

Tabla 3.1: Calculated fragmentation energies predicted in this thesis, where the biggest cluster conserve the charge. In bold are the most prevalent experimental channels obtained by Duncan *et al.* (82).

	Ni	NiO	NiO_2	Ni_2O	Ni_2O_2	O	O_2
$Ni_3O_2^+$	-4.25	-3.41	-5.19	-5.95	-3.47	-4.32	—
$Ni_3O_3^+$	-5.73	-4.48	**-4.95**	-9.04	-5.14	**-4.82**	-4.06
$Ni_3O_4^+$	**-6.38**	-3.57	**-3.63**	-9.25	-5.84	-2.43	**-2.17**
$Ni_3O_5^+$	-7.01	-4.43	-2.93	—	-6.26	-2.64	0.01
$Ni_3O_6^+$	-5.77	-6.14	-4.87	—	—	-3.72	-1.28
$Ni_4O_3^+$	-3.79	-4.03	-5.07	-5.73	-3.85	-5.16	-4.70
$Ni_4O_4^+$	-5.92	-3.76	-5.23	-6.94	-4.65	-4.55	-4.64
$Ni_4O_5^+$	-6.95	-5.01	**-4.15**	-8.84	-4.99	-3.68	**-3.15**
$Ni_4O_6^+$	-6.37	-5.50	-4.87	-9.97	-6.35	-3.14	**-1.74**
$Ni_5O_4^+$	-4.24	-4.20	-6.08	-5.45	-4.64	-5.05	-5.14
$Ni_5O_5^+$	-4.75	**-3.84**	**-5.11**	-7.21	-4.01	**-4.19**	**-4.16**
$Ni_5O_6^+$	-5.66	-4.21	**-4.61**	-8.62	-5.63	**-4.05**	**-3.16**
$Ni_5O_7^+$	-7.85	-5.15	-5.01	-8.97	-7.06	-4.07	**-3.05**
$Ni_6O_4^+$	-4.62	-5.09	-6.98	-6.28	-5.81	-5.67	-6.28
$Ni_6O_5^+$	-4.30	-3.90	-5.67	-5.59	-4.51	-3.86	-4.46
$Ni_6O_6^+$	-5.02	-4.48	**-5.39**	-6.69	**-4.73**	-4.77	**-3.56**
$Ni_6O_7^+$	-4.23	-3.71	-4.49	-6.83	-4.34	-3.28	**-2.98**
$Ni_6O_8^+$	-6.60	-3.99	-4.79	-9.29	-5.55	-4.30	-5.14
$Ni_7O_5^+$	-4.54	-3.81	-6.21	-5.89	-5.32	-5.30	-5.14
$Ni_7O_6^+$	-3.90	-4.08	-4.67	-5.83	-4.39	-4.13	-4.35
$Ni_7O_7^+$	-5.04	-3.73	**-5.23**	-6.21	-4.63	-4.43	**-3.48**
$Ni_7O_8^+$	-4.73	-4.50	-4.50	-6.18	-4.62	-4.05	**-3.39**
$Ni_7O_9^+$	-6.26	-4.01	-5.09	-8.07	-4.42	-3.87	-2.84
$Ni_8O_7^+$	-4.20	-4.04	-4.89	-5.39	-4.54	-4.81	-4.05
$Ni_8O_8^+$	-4.56	-4.02	-5.17	-6.51	-4.17	-4.40	-4.14
$Ni_8O_9^+$	-4.94	-4.22	-4.99	-6.41	-5.13	-4.25	**-3.57**
$Ni_8O_{10}^+$	-4.80	-4.46	-5.06	-8.17	-4.89	-4.11	-3.28

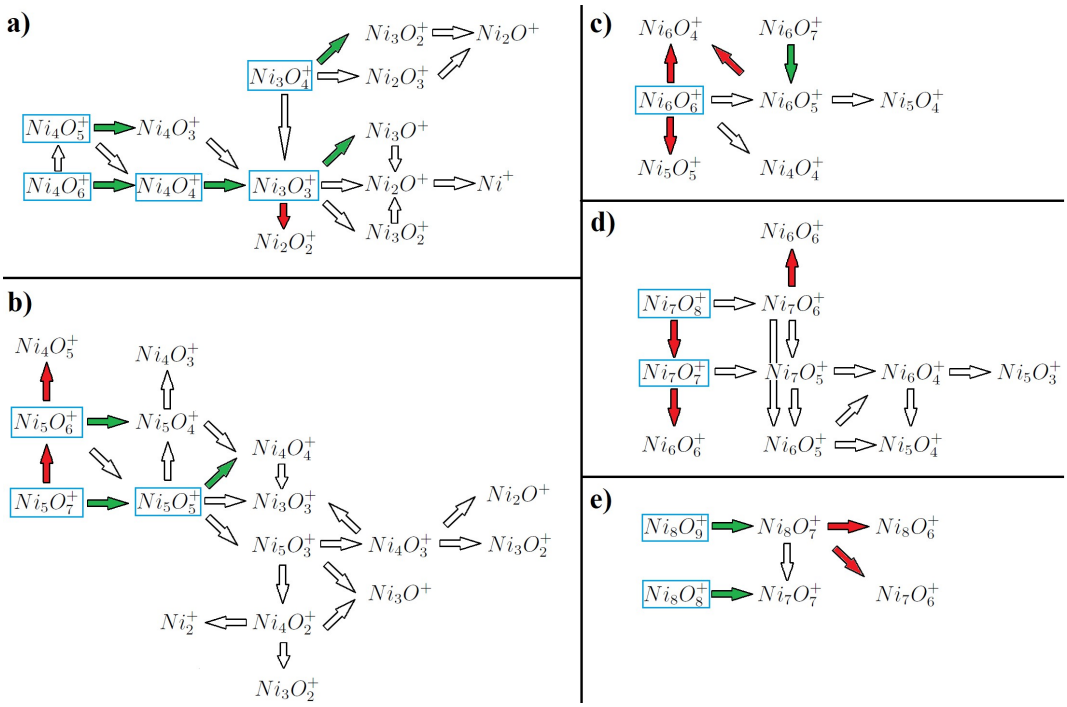

Figura 3.16: Multiple and sequential fragmentation channels for several clusters. In panel a), the fragmentation channels for $Ni_3O_m^+$ and $Ni_4O_m^+$ series, in panel b) for $Ni_5O_m^+$, in panel c) for $Ni_6O_m^+$, in panel d) for $Ni_7O_m^+$ and in panel e) for $Ni_8O_m^+$. Red arrows are forbidden experimental channels, and green arrows are the most favourable fragmentation channel, in our calculations.

series of fragmentation products by following the lower excitation energy paths along the corresponding panels of Fig. 3.15. Then, we compare these more probable fragments with those observed by Duncan and coworkers (82) (listed in their Table 2). We can follow the sequential and multiple fragmentation channels in Fig. 3.16. Selecting a initial cluster, it is possible going throw all possible fragment son clusters and get almost all clusters observed in the experimental measurements (82).

Let us start the above procedure by studying the fragmentation of some selected clusters. Analyzing the fragmentation of the cluster $Ni_6O_6^+$, we are able to obtain all the fragments obtained in experimentally (82) (except that

we also obtain the $Ni_5O_5^+$ and $Ni_6O_4^+$ clusters), in Fig. 3.17, we compile from the Fig. 3.15 and 3.16, and from Table 3.1, the fragmentation channels (both simultaneous and sequential):

$$Ni_6O_6^+ \rightarrow Ni_6O_5^+, \underline{Ni_6O_4^+}, \underline{Ni_5O_5^+}, Ni_5O_4^+, Ni_5O_3^+, Ni_4O_4^+, Ni_4O_3^+, Ni_4O_2^+, Ni_3O_3^+, Ni_3O_2^+, Ni_3O^+, Ni_2O_2^+, Ni_2O^+, Ni_2^+, Ni^+.$$

Almost all the clusters that we obtain in our calculations are observed experimentally, except for two clusters that according to our predictions should be obtained as a result of the fragmentation of the cluster $Ni_6O_6^+$, for this, we propose two reasons for not obtain experimentally these clusters.
I) The $Ni_6O_4^+$ and $Ni_5O_5^+$ cations are not observed because high energy barriers may occurs due to geometrical factors (compare the average bond distances in Tables Table-VI and Table-VII of the Appendix A). The observed *5.3* cation may be produced by exciting *6.5* or *5.4* fragments to energy higher than 5 eV.
II) $Ni_5O_5^+$ cation may not be observed because this cluster is fragmented into four clusters, all these channels in a very small energy window (0.35 eV), so, having so many possible ways to fragment, this cluster disappears almost completely and it is not observed experimentally.

In Fig. 3.18, the fragmentation for $Ni_7O_7^+$ cluster are shown. As in the previous example, most of the clusters that our calculations gives as result of the fragmentation of this cluster, are measurement in the experiment (82), except for $Ni_5O_5^+$ and Ni^+, and the reason that we propose why they are not observed in the experiment, is the same as in the $Ni_6O_6^+$ cluster.

$$Ni_7O_7^+ \rightarrow Ni_7O_5^+, Ni_6O_5^+, Ni_6O_4^+, \underline{Ni_5O_5^+}, Ni_5O_4^+, Ni_5O_3^+, Ni_4O_4^+, Ni_4O_3^+, Ni_4O_2^+, Ni_3O_3^+, Ni_3O2^+, Ni_3O^+, Ni_2O^+, Ni_2^+, \underline{Ni^+}.$$

In general, most of the fragmentations that require energies larger than 4.0 eV in our work do not appear in the experiment of Duncan *et al.* (82) Comparing our Table 3.1 and Table 2 of Duncan´s experiment(82), we observe that in general, most of the fragmentations that require energies larger than 4.5 eV in our work do not appear in the experiment. Although our overall agreement with the photodissociation experiments (82) is good, we note that there

are certain fragmentations that require energies lower than 4.5 eV (according to our calculations) but that do not appear in the experiment (for example $Ni_5O_5^+$). This could be indicative of the presence of a significative energy barrier, or simply of the fact that our ground state is not the structure present in the experiment.

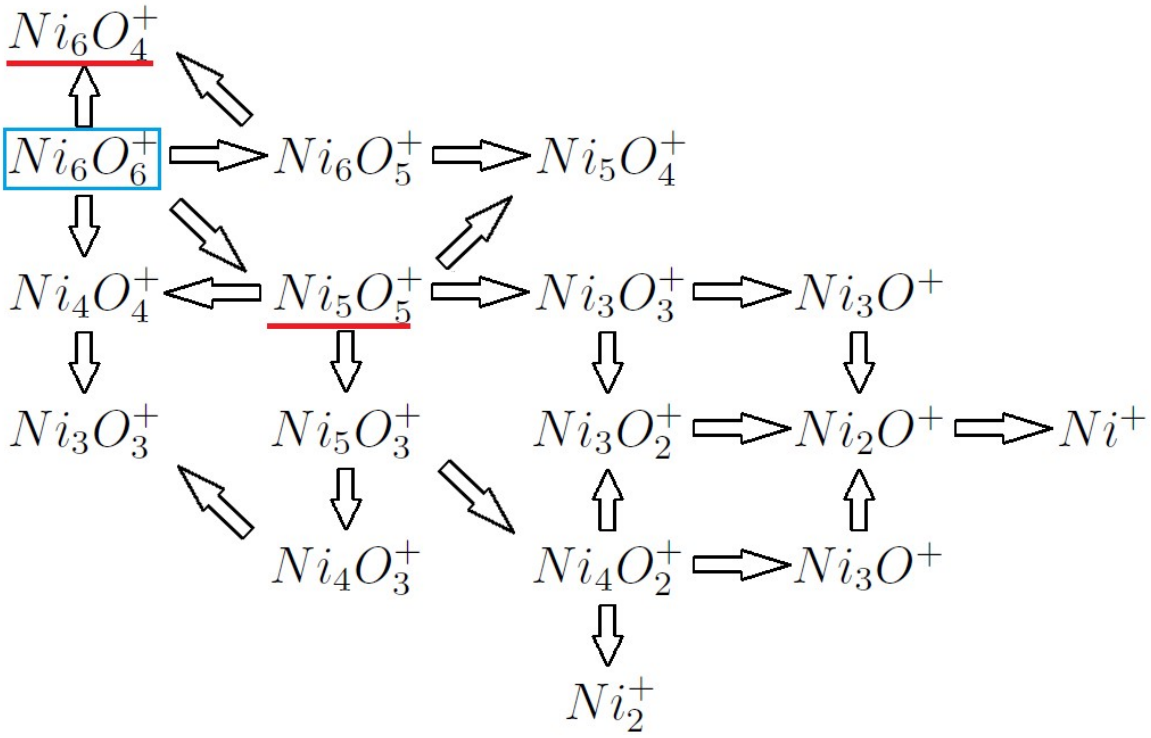

Figura 3.17: Multiple and sequential fragmentation channels for $Ni_6O_6^+$ cluster. Underlined are the clusters not observed experimentally.

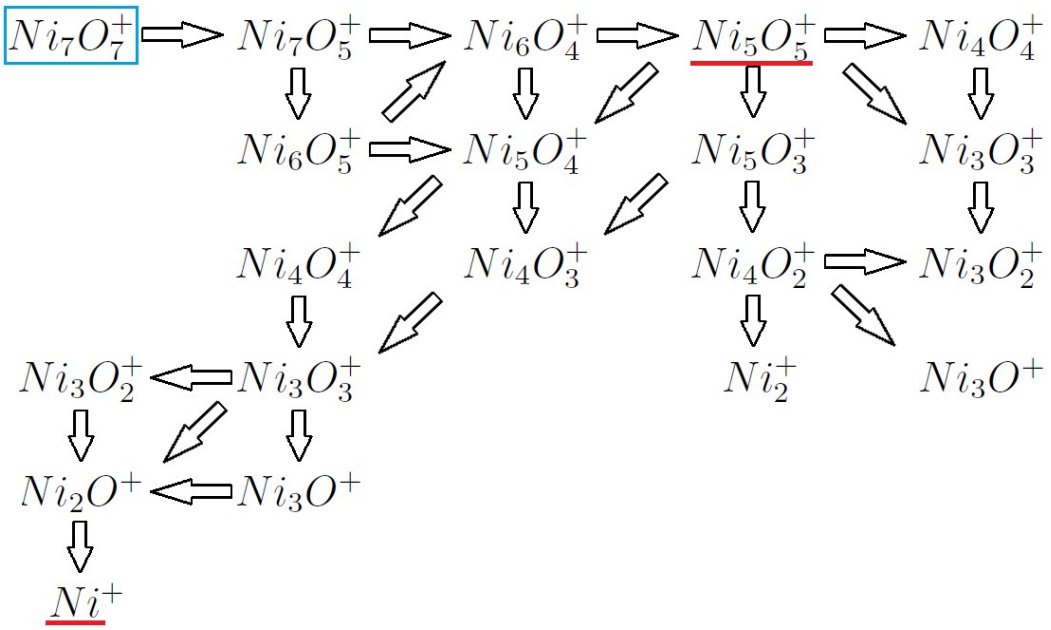

Figura 3.18: Multiple and sequential fragmentation channels for $Ni_7O_7^+$ cluster. Underlined are the clusters not observed experimentally.

3.4 Absorption of carbon monoxide in nickel oxide clusters

In this section the behavior of nickel oxide in presence of carbon monoxide (CO) will be discussed. Sakuma *et al.* (85) have studied the reaction of oxide nickel clusters cations $Ni_nO^+_{n+x}$ ($n = 4 - 10, x = -1 \sim +1$) with CO in a He buffer gas using mass spectroscopy. They have found that when cationic clusters react at room temperature, a CO molecule tends to attach immediately to NiO, for every cluster ion with different stoichiometry, although rate constants of the CO attachment reaction are more or less stoichiometry-dependent. However, CO was found to be released from cluster ions when these were heated up to 523 K after the reaction is completed. After these results, authors have concluded that CO molecule that physisorbs weakly to NiO at room temperature desorbs into the gas phase by the post heating. In addition, they have found that the reaction of two oxygen-rich clusters $Ni_6O^+_7$ and $Ni_8O^+_9$ produce one oxygen atom extraction, releasing carbon dioxide (CO_2). Since the oxygen extraction reaction is one order of magnitude slower than physisorption, it lies hidden in the mass spectrum, underneath the faster physisorption processes, nevertheless this oxygen extraction reaction can be revealed by post heating physisorption elimination.

Here, we discuss the reaction of $Ni_6O^+_m$ with CO, in order to determine how the CO molecule absorbs in these clusters. Also, the extraction of one oxygen atom (by means of CO_2 formation of the cluster $Ni_6O^+_7$ is studied. VASP calculations have been performed to verify the accuracy of our previous calculations made by using SIESTA code. Finally, we discuss and compare our results with those obtained experimentally by measurements of relative abundance as function of temperature.

3.4.1 Geometrical, electronic and magnetic properties of $Ni_6O_m^{0\pm}$ clusters

In Fig. 3.19 the structures for Ni_6O_m ($m = 1 - 9$) clusters are shown. They were calculated using VASP code. The ground states calculated by VASP and SIESTA match, as it can be seen in Fig. 3.19, except for Ni_6O_2. In Table A.13 and A.14 of Appendix A, several properties are resumed for neutral (Table A.13) and ionized (Table A.14) clusters. Some of these properties are shown in Fig. 3.20. A consistency has been found for calculations using VASP and SIESTA, for instance, for the binding energy per atom (Fig. 3.20 (a)), second energy difference (Fig. 3.20 (b)) and magnetic moment (Fig. 3.20 (c)). They follow the same trend for both codes. In Fig 3.20 (d) the global reactivity indicators are presented.

3.4.2 Global reactivity descriptors for Ni_6O_m clusters

In order to characterize the global reactivity of Ni_6O_m clusters, we calculate conceptual DFT based global reactivity descriptors (74, 75, 76, 77). In first place, the vertical ionization potential I (Eq. 2.48) and vertical electron affinity A (Eq. 2.49) are calculated for each nanoalloy composition. From them, we can calculate the electronegativity χ (Eq. 2.50) chemical hardness η (Eq. 2.51) and electrophilicity index ω (Eq. 2.52).

Results in Fig.3.20 endorse the expected trend, electronegativity increases with the number of oxygen atoms present in the clusters, the main conclusion would be that the addition of a small amount of oxygen atoms to a nickel surface does not change considerably the system electronegativity. However at m=5 a big shift on the electronegativity can be perceived, as a decrease for m=6, and finally an increase for a bigger rate of oxygen atoms. Ni_6O_5 shows a considerable change in electronegativity, which is an indicative of the facility of this cluster to absorb electrophilic external agents (like oxygen atoms, water or carbon monoxide). Therefore, it is expected that the surface oxidation be a faster and more exothermic process the more oxygen the system has until

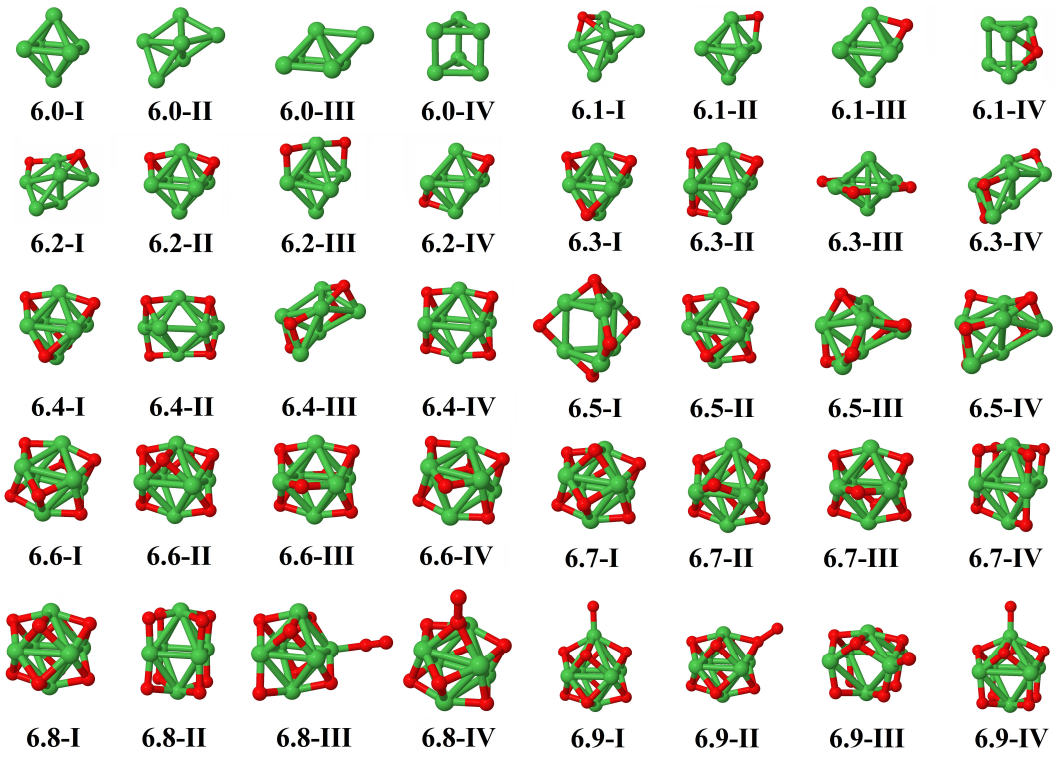

Figura 3.19: Ground state (I), first (II), second (III) and third (IV) lowest structural isomers of Ni_6O_m clusters. Green indicates Ni atoms, red oxygen atoms. Fist number denotes the number of Ni atoms and the second number denotes the number of oxygen atoms.

Ni_6O_5 cluster (see Fig. 3.20 panel (a)). On the other hand, the reactivity towards more nucleophilic agents will be reduced as the number of oxygen atoms increase. The chemical hardness quantifies the sensitivity of the chemical potential (of electronegativity) to change the number of electrons. The larger the hardness the more reluctant the material is to accept or donate electrons. Its inverse (the softness) correlates with the system polarizability. Results in Fig. 3.20 (d) show that the chemical hardness (η) does not change considerably, this means that the ability to absorb electrons from the system is not affected with the rate of oxidation.

The electrophilicity ω measures the energy change of a system upon maximum uptake of electrons (i.e. to the point where the electronegativity vanishes)

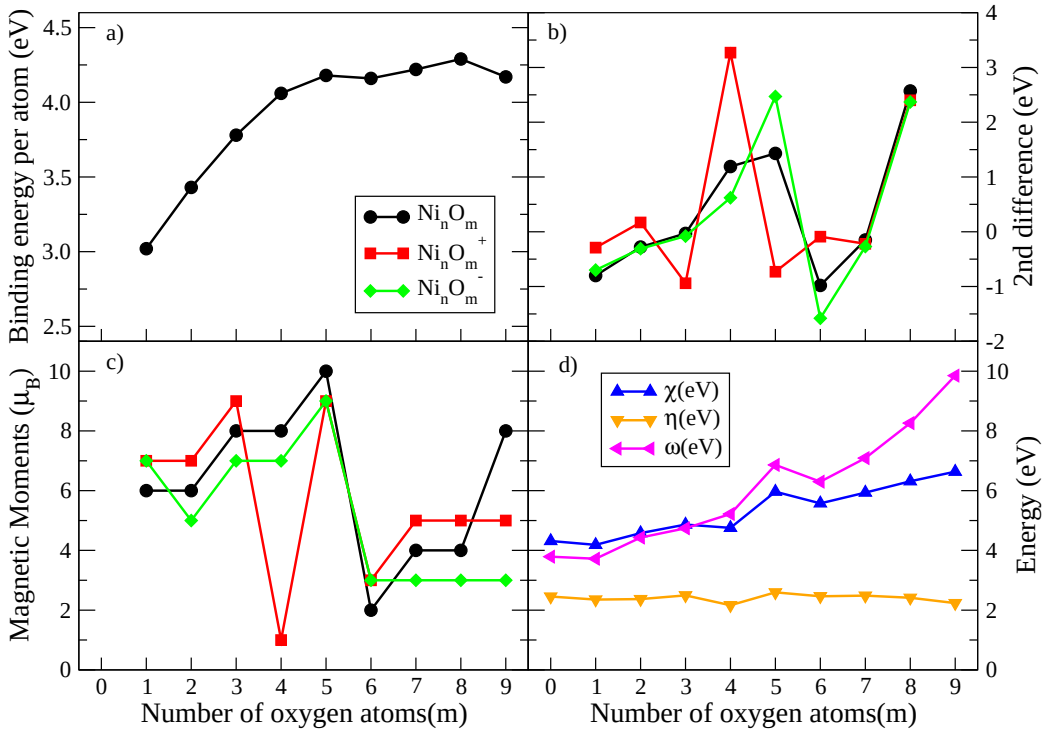

Figura 3.20

(75). Therefore, it is related to the electron affinity, which measures the energy change when an electron is added. In fact, we have observed that the composition dependence of ω exactly parallels that of A. The average tendency of ω to increase with the rate of oxygen indicates that the absorbtion of oxygen facilitates the absorption of more oxygen

3.4.3 Absorbtion of CO on $Ni_6O_m^+$ clusters

In order to determine how is the carbon monoxide absorption process in clusters $Ni_6O_m^+$ and which are the reaction barriers (work in progress), we must determine the local minima of the reaction paths. It is possible to give an idea of the dynamics process using the information of the local minima, with no need to see the behavior of absorption barriers for CO and CO_2 dissociation.

In Fig. 3.21 and 3.22 the local minimums for the reaction paths of clusters Ni_6^+ and $Ni_6O_7^+$ are presented (respectively).

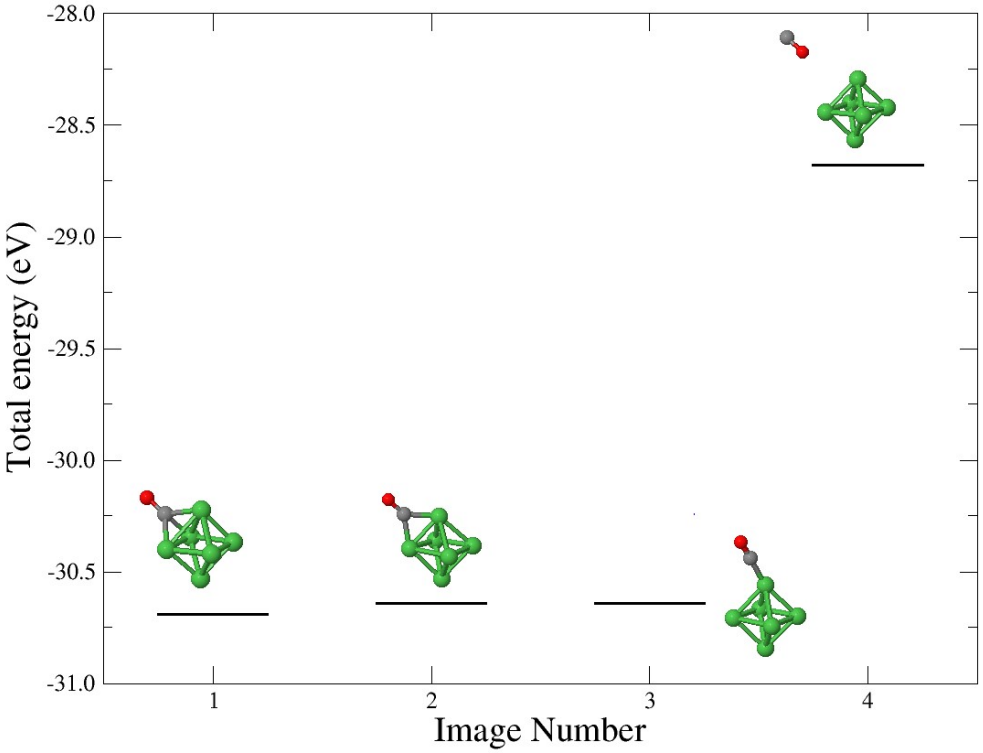

Figura 3.21: local minimos of the reaction path of Ni_6^+ with CO.

In Fig. 3.21 the local minima for Ni_6^+ cluster, with a chemically and physically CO molecule absorbed are shown. We can see that the energy difference between the first three states is small, so, energetically the system has no preference for a way to absorb the CO molecule, but, when CO is released, the system loses a lot of energy, and clearly a great amount of energy would be needed to be injected into the system to go from a chemical to a physical absorption (image 4 of Fig. 3.21). In Fig. 3.22, there is the local minimum of the $Ni_6O_6^+ + CO$ reaction, unlike the previous reaction, we do not obtain any local minimum where the CO molecule is physically absorbed into the system. As the nickel cluster containing oxygen atoms is so saturated, the CO molecule is absorbed on top, after this, the molecule sticks to one of the oxygen atoms, breaking two of the bonds with the nickel atoms. Finally, a molecule of CO_2 is

released from the system, leaving a $Ni_6O_6^+$ cluster, which is energetically more favorable than its neighbors $Ni_6O_5^+$ and $Ni_6O_7^+$ (as seen in the second energy difference Fig. 3.20 b)).

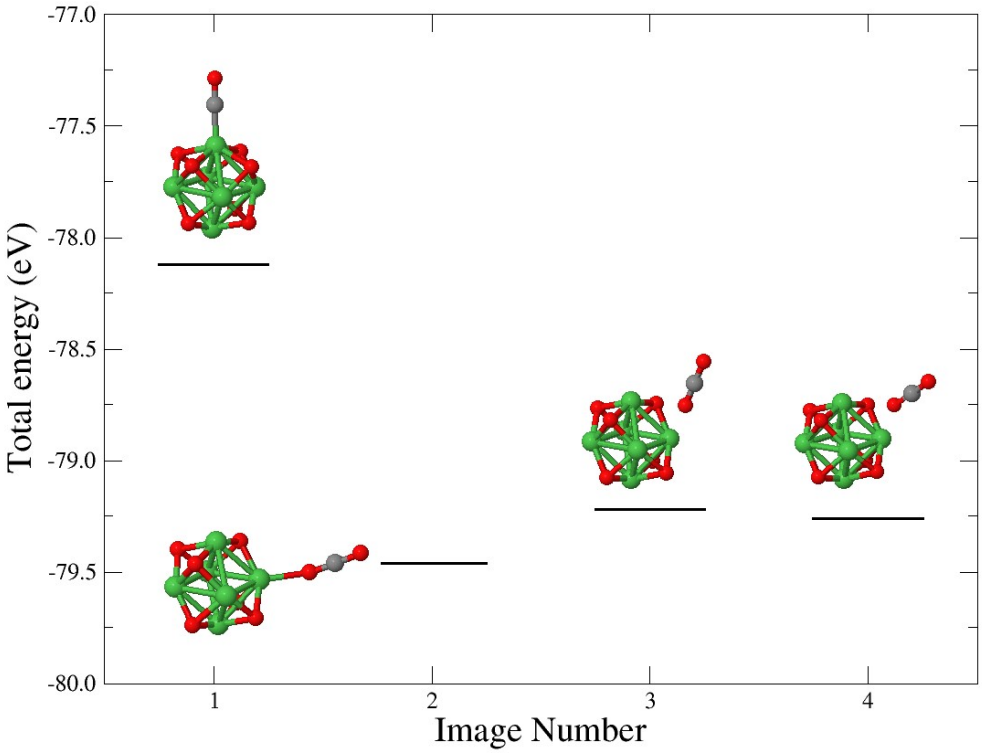

Figura 3.22: Local minimums of the reaction path of $Ni_6O_6^+$ with CO_2.

3.5 Oxidation of nickel-silver nanoalloys.

As we have seen previously, the oxidation of nickel, brings as a consequence decrease in the magnetic moment for certain oxidation rates, with a dependence that is difficult to rationalize (See Fig. 3.11), but for certain applications, it is necessary that the magnetic moment of the clusters preserved the values shown in the gas phase, for this reason, we need to find the way to protect nickel clusters form action of the environment, without modifying their magnetic behavior, but at the same time, provide a physical protection to prevent oxidation as exposure to the environment ambient. One of the characteristics we need in the material that we will use to protect nickel is that this will be immiscible, and also that the diffusion of the nickel towards the superficial layer be limited energetically. This makes silver one of the possible candidates for this propose. There are a lot of results in the literature indicating that nickel-silver alloys are characterized by being immiscible on all scales (volumetric and nanometrics), getting core-shell structures in the nanometric scale, where the nickel atoms are located in the core. Silver, besides being a good candidate for protect the magnetic properties of nickel clusters, also has antibacterial properties, which could provide a protection against other types of harmful molecules. The fact of having a particle that in addition to having antibacterial properties, and also present magnetic behavior (provided by nickel core), would allow us to move it easy through the application of magnetic fields. Due to these reasons, the use of silver to protect nickel clusters would be of great scientific and technological interest.

Nickel and silver are metals with interesting properties of technological relevance: nickel is a well known ferromagnetic and silver has antibacterial properties. Both exist in the face centered cubic phase but are immiscible. In the context of alloys at the nanoscale, one can play with the size to fine tune a desired property, or to achieve new properties and functionalities that do not exist at the macroscopic regime. In this subsection, we explore how the subtle interaction between Ni and Ag triggers the chemical order, the electronic structure, and the magnetic properties of a AgNi nanoalloy of 55 atoms, a size that

can accommodate core/shell configurations with sizable parts. We determine, in the whole composition range, the chemical order, absolute and relative stabilities by means of binding energy, excess energy and second energy difference, as well as total and part-projected spin-polarized electronic densities of states and local charge and spin magnetic moments distribution. Ni-core/Ag-shell structures are particularly stable, but contrary to what one would expect by simply extrapolating the properties of the pure Ag and Ni clusters or of pure fcc bulks, we find unexpected behaviors along the composition range, such as quenched magnetic moments in Ni, total magnetic moments essentially contributed in some cases by Ag, or electronic charge transfer that changes its sign depending on the stoichiometry. These behaviors lead to magnetic transitions as a function of the composition, and differ, in some cases, from those of the smaller 13-atoms AgNi nanoalloys of the same symmetry with which we compare, a further demonstration of the complex nature of nanostructures. The above trends are robust against ionization and electron capture.

The aim of the present section is to characterize, in the framework of the density functional theory, the chemical order, electronic structure, and related properties like structural parameters, thermodynamical stability, relative stoichiometric stability and magnetism, of Ag_xNi_y icosahedral nanoalloys of 55 atoms, in which core/shell structures with sizable Ni subclusters can be achieved along the composition range. Pure Ag_{55} and Ni_{55}, that are the limits of compositions, have been shown to stabilize in the icosahedral ground state (87, 88, 89), contrary to what happens in the smaller nanoalloy of 13 atoms for which Pereiro and co-workers found the icosahedron as the global minimum energy (90), whereas Fernández *et al.*, found a BBP-like structure (91). The size of this 55-atoms nanoalloy is, on the other hand, closer to what can be experimentally attained. For simplicity, we assume the Mackay icosahedral structure along the full composition range. Although icosahedral structures are more plausible in the 55-atoms nanoalloy than in the 13-atoms one, we note that due to the large Ag and Ni size mismatch and resulting stress, poli-icosahedral structures, irregular or antimackay icosahedral structures could appear at in-

termediate sizes instead of Mackay ones. These facts have been already shown for NiAg nanoalloys, mostly for larger ones where quiral shells can be also formed (92, 93, 94, 95). We have considered all possible homotops, as well as the different spin isomers, so that metastable chemical orders and spin excitations are also characterized. We complement our investigation with the study of the effects of an electron deficit or excess, which is important upon ionization or electron capture. In order to determinate the effect of the oxygen over the silver-nickel nanoparticles we also investigate the absorbtion of oxygen atoms on some selected alloys, studding the differences of oxidizing the pure nickel clusters and the silver-nickel core-shell nanoparticles.

3.5.1 Pure $Ag_xNi_y^{0/\pm}$ ($x + y = 13$ and 55) nanoalloy

To establish the behavior of core-shell nanoparticles of nickel-silver alloys with oxygen, we must determine how the magnetic properties of nickel clusters change in the presence of silver. To this aim, we have studied two cluster sizes alloys, 13 and 55 atoms in whole composition range, we choose these sizes because closed shell geometrical structures are presented, having well defined the core-shell structure, making it easier to separate the effects of each of one the elements.

We also determine, in the whole composition range, the chemical order, absolute and relative stabilities by means of binding energy, excess energy and second energy difference, as well as total and part-projected spin-polarized electronic densities of states and local charge and spin magnetic moments distribution. Ni-core/Ag-shell structures are particularly stable, but contrary to what one would expect by simply extrapolating the properties of the pure Ag and Ni clusters or of pure fcc bulks, we find unexpected behaviors along the composition range, such as quenched magnetic moments in Ni, total magnetic moments essentially contributed in some cases by Ag, or electronic charge transfer that changes its sign depending on the stoichiometry. These behaviors lead to magnetic transitions as a function of the composition, and differ, in some cases, from those of the smaller 13-atoms AgNi nanoalloys of the same

symmetry with which we compare, a further demonstration of the complex nature of nanostructures. As a first step, we calculated the AgNi nanoalloy of 13 atoms with icosahedral structure for two purposes. One was to benchmark our theoretical approach against previous results for the same system in the Ag rich phase by Harb and co-workers (96) using the Gaussian code with GGA-PB86 and LANL2DZ relativistic effective core potential. In Fig. 3.23 we provide several low-energy homotops. The second purpose of this calculation was to have a reference to compare with the 13-atoms core of the larger 55-atoms nanoalloy with compositions up to 13 Ni atoms, in order to assess the role played by the interaction with the remaining 42 Ag atoms at the shell. This will be discussed in the following sections. Our ground states (see Fig. 3.23) are the same as theirs, except for $Ag_{10}Ni_3$, for which our predicted ground state corresponds to their first isomer (nearly degenerated with the ground state). We complete the study of the AgNi nanoalloy of 13 atoms to cover all the composition range, not reported so far. In Fig. 3.24 we shown the local transfer of charge and magnetic moment.

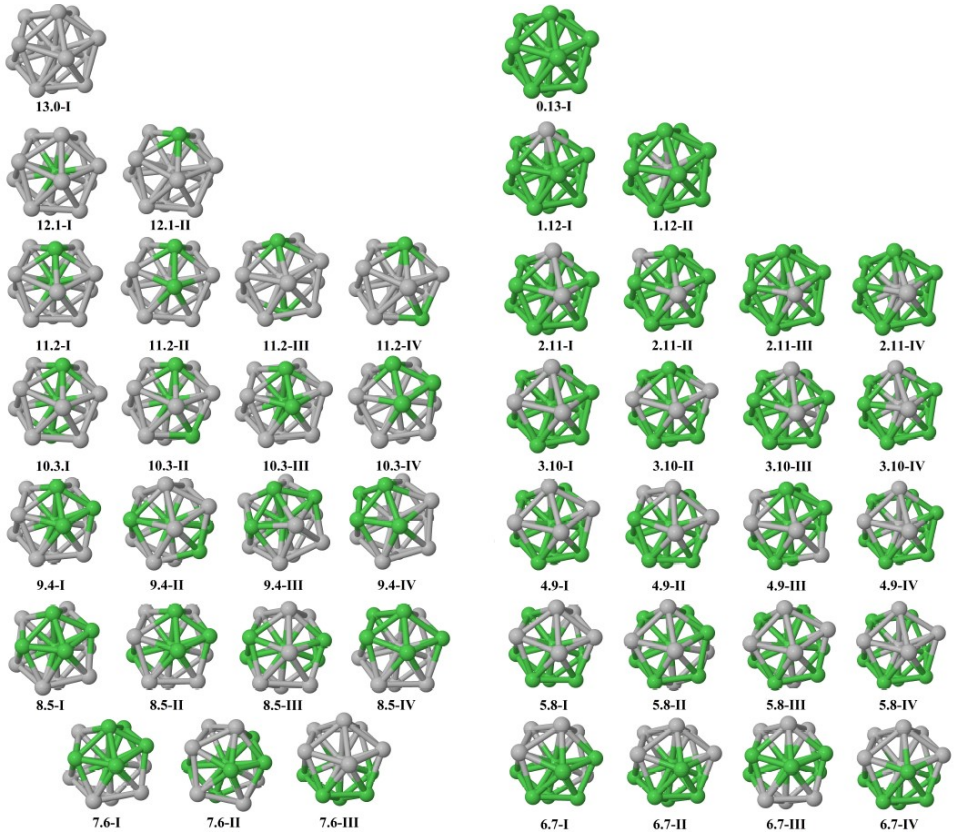

Figura 3.23: Putative ground state and up to first three low-energy homotops of Ag_xNi_y clusters with $x + y = 13$. The cluster $x.y-$I is the putative ground state with x silver atoms (grey) and y nickel atoms (green), $x.y-$II, $x.y-$III and $x.y-$IV are the first, second and third isomers respectively.

The local electronic charge and magnetic moments distribution within the nanoalloys were determined from the Mulliken population (see Fig. 3.24), although in those same cases where additional VASP calculations were conducted, we performed this analysis using Bader's method (97, 98) which divides the nanoalloy into atomic volumes by locating the zero-flux surfaces of the electron density field. A comparison of the magnetic moment obtained from both approaches in three of those selected compositions of the 13-atoms nanoalloy are shown in Fig. 3.25.

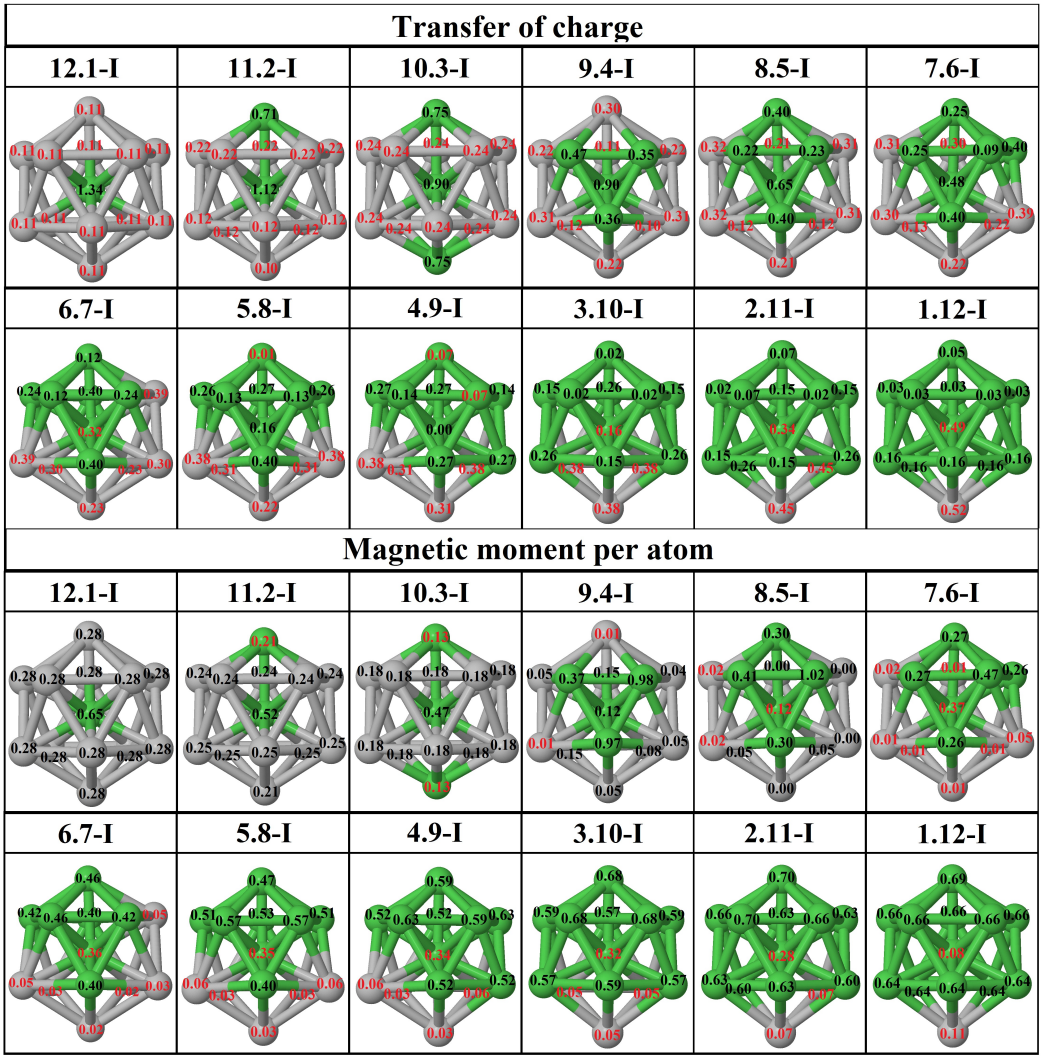

Figura 3.24: Local electronic charge transfer and magnetic moment of the ground state of Ag_xNi_y clusters with $x + y = 13$. For charge transfer, numbers in black (red) indicate gain (loss) of charge; for the magnetic moment, numbers in black (red) indicate spin up (down).

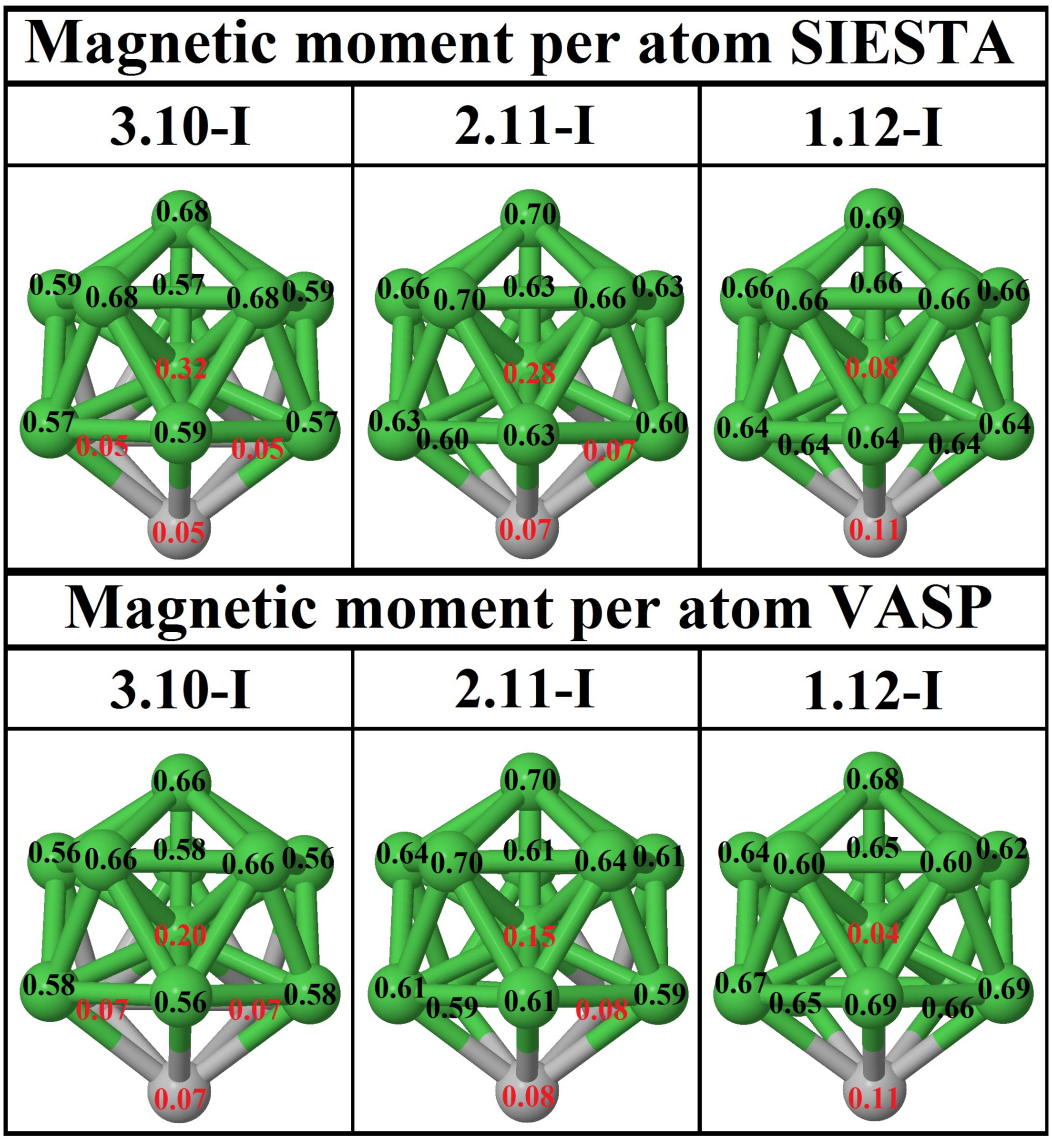

Figura 3.25: Local magnetic moment of $AgNi_{12}$, Ag_2Ni_{11} and Ag_3Ni_{10} clusters as calculated with SIESTA and VASP codes. Numbers in black (red) indicate spin up (down).

Tabla 3.2: Several properties of the ground state and low-energy homotops of Ag_xNi_y nanoalloys with $x + y = 13$: $\triangle$ = Energy difference (in eV) with respect to the ground state; I_p = adiabatic ionization potential (in eV); E_A = adiabatic electron affinity (in eV); μ = total spin magnetic moment (in μ_B); D(x-y) = Average x-y distance in Å(x, y= Ag, Ni).

n.m-isomer	$\triangle$	I_P	E_A	μ	D(Ag-Ag)	D(Ni-Ni)	D(Ag-Ni)
13.0-I	0.00	4.89	0.83	5	2.78	—	—
12.1-I	0.00	4.68	1.07	4	2.76	—	2.62
12.1-II	1.59	3.77	1.21	4	2.79	—	2.76
11.2-I	0.00	4.63	0.88	3	2.75	2.45	2.64
11.2-II	1.56	4.77	1.23	5	2.77	2.47	2.74
11.2-III	1.58	4.69	1.10	3	2.77	2.69	—
11.2-IV	1.62	4.74	1.10	5	2.76	2.75	—
10.3-I	0.00	4.68	0.86	2	2.76	2.46	2.63
10.3-II	0.10	4.61	0.89	2	2.76	2.46	2.63
10.3-III	0.10	4.55	1.06	2	2.75	2.44	2.65
10.3-IV	1.60	4.83	1.23	4	2.76	2.52	2.74
9.4-I	0.00	4.57	1.00	3	2.76	2.47	2.65
9.4-II	0.04	4.58	0.97	3	2.76	2.43	2.64
9.4-III	0.05	4.58	0.97	1	2.75	2.47	2.64
9.4-IV	1.63	4.76	1.36	7	2.75	2.50	2.75
8.5-I	0.00	4.62	1.00	2	2.76	2.47	2.64
8.5-II	0.01	4.65	0.97	0	2.75	2.44	2.65
8.5-III	0.07	4.67	0.98	0	2.74	2.44	2.64
8.5-IV	1.80	4.65	1.39	0	2.75	2.59	2.68
7.6-I	0.00	4.73	0.99	1	2.76	2.47	2.64
7.6-II	0.16	4.79	0.97	1	2.73	2.43	2.65
7.6-III	1.79	4.84	1.27	3	2.75	2.57	2.68
6.7-I	0.00	4.82	1.05	2	2.75	2.47	2.65
6.7-II	0.05	4.95	1.02	2	2.74	2.45	2.65
6.7-III	0.14	4.95	1.02	2	2.74	2.45	2.64
6.7-IV	1.87	4.87	1.33	2	2.74	2.58	2.66
5.8-I	0.00	5.02	1.06	3	2.75	2.47	2.64
5.8-II	0.12	5.11	1.12	3	2.74	2.46	2.65
5.8-III	0.13	5.03	1.13	3	2.75	2.46	2.64
5.8-IV	1.94	5.07	1.27	3	2.74	2.58	2.64
4.9-I	0.00	5.16	1.14	4	2.75	2.47	2.64
4.9-II	0.05	5.14	1.19	4	2.74	2.47	2.65
4.9-III	0.13	5.17	1.23	4	2.72	2.46	2.66
4.9-IV	2.01	5.17	1.30	4	2.71	2.59	2.49
3.10-I	0.00	5.32	1.29	5	2.75	2.47	2.65
3.10-II	0.03	5.32	1.31	5	2.73	2.46	2.66
3.10-III	0.10	5.35	1.34	5	2.72	2.47	2.65
3.10-IV	2.06	5.33	1.40	5	2.67	2.58	2.49
2.11-I	0.00	5.51	1.42	6	2.73	2.47	2.66
2.11-II	0.06	5.54	1.45	6	—	2.47	2.65
2.11-III	0.11	5.55	1.47	6	2.61	2.59	2.56
2.11-IV	2.10	5.55	1.47	6	2.61	2.59	2.56
1.12-I	0.00	5.68	1.66	7	—	2.47	2.65
1.12-II	2.19	5.67	1.73	7	—	2.60	2.47
0.13-I	0.00	5.81	1.80	8	—	2.47	—

3.5.2 Chemical order, stability and electronic properties

The ground state configurations of Ag_xNi_y ($x + y = 55$) nanoalloys are shown in Fig. 3.26. In the Appendix A, are collected several low-energy homotops for each composition (Figs. A.1 to A.5), corresponding to metastable chemical orders, and in Tables A.15 to A.19, are collected several properties for these clusters. Regarding the inter-atomic distances of the nanoalloys, we find that Ni-Ni bonds are shorter than Ag-Ni bonds, and these are shorter than Ag-Ag ones. The average inter-atomic distances remain almost constant as a function of stoichiometry (2.75 Å for Ag-Ag, 2.65 Å for Ag-Ni, and 2.46 Å for Ni-Ni). An electron excess or deficit does not modify the chemical order, since the corresponding ground state homotops are the same as in the neutral nanoalloy. The chemical order pattern is clear. Ni atoms tend to occupy the internal positions, building up a Ni subcluster. This is consistent the lower atomic volume and the larger cohesive energy of Ni as compared to Ag. The lower average inter-atomic distances in Ni_{55} than in Ag_{55} creates a size mismatch when the nanoalloy is formed, causing a steric effect that tends to favor segregation of the bigger atomic species (Ag) to the surface positions. The larger cohesive energy of Ni as compared to Ag favor segregation of Ni to the interior positions so that a larger number of the more cohesive Ni-Ni bonds can be generated. Therefore, segregation always occurs, and a core/shell structure tends to be formed, in agreement with the experimental findings (99, 100) and calculations of smaller AgNi nanoalloys (92, 101, 96, 102) and larger ones (93, 94, 95). When the number of Ni atoms is lower than 14, all them occupy the most internal positions. $Ag_{42}Ni_{13}$ is a perfect core/shell cluster, and the next Ni atom in $Ag_{41}Ni_{14}$ starts occupying the outer shell of the 55-atoms icosahedral structure in positions as close as possible to the already formed Ni_{13} core. The chemical order pattern is, thus, the one that maximizes the number of Ni-Ni bonds with a Ni subcluster surrounded by Ag atoms. The robustness of this chemical order pattern is demonstrated by the fact that for all 55-atoms nanoalloys with less that 14 Ni atoms, except $Ag_{52}Ni_3$ and $Ag_{48}Ni_7$, their 13-atoms core has the same chemical order (corresponds to the same

homotop) as the ground state of the 13 atoms nanoalloy of the corresponding stoichiometry.

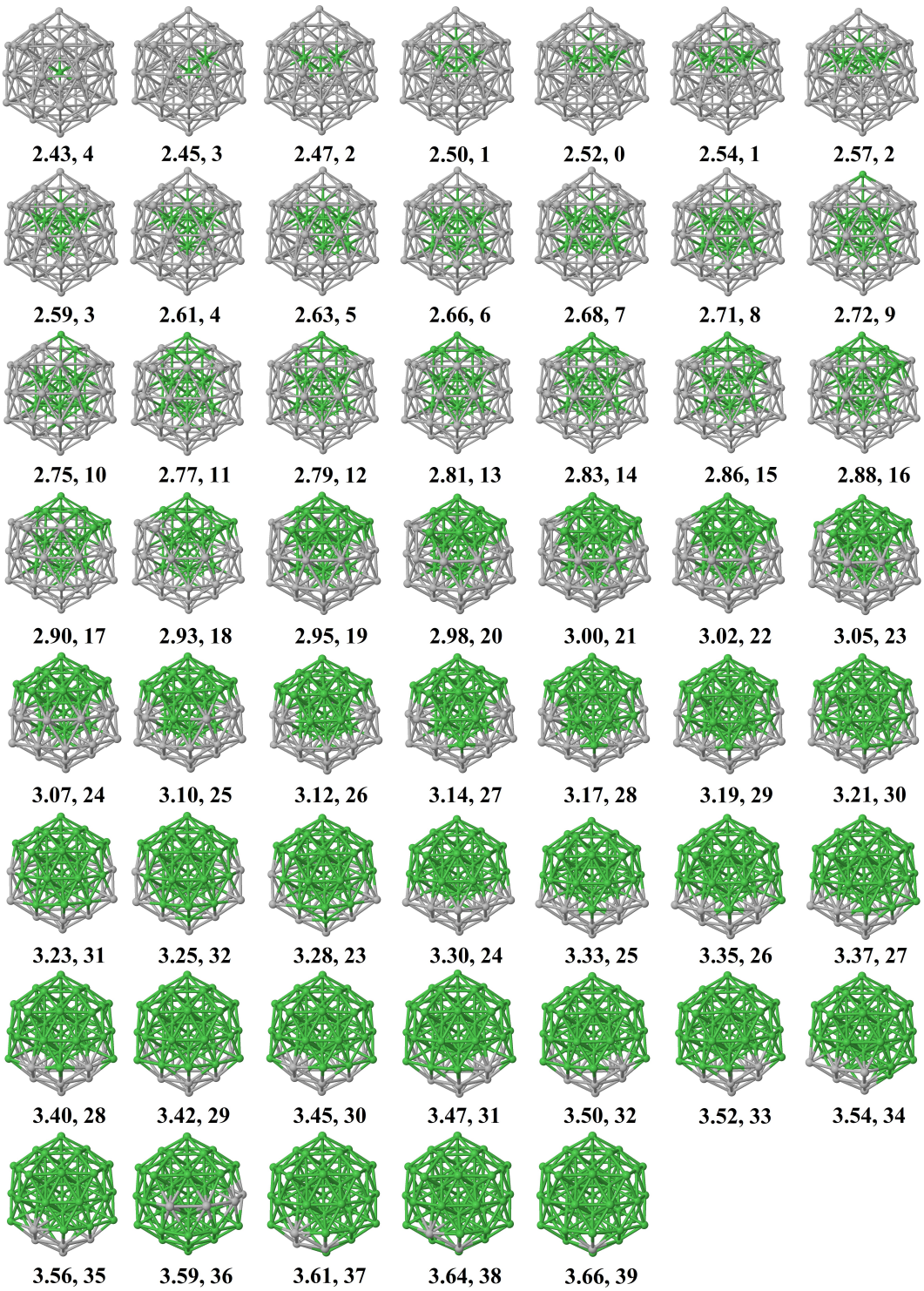

Figura 3.26: Ground state geometries of $[Ag_xNi_y]$ clusters with $x + y = 55$. The numbers below the structures are the binding energy per atom (in eV) and the total spin magnetic moment (in μ_B), respectively.

This also points to the fact that the outer 42 Ag atoms may provide protection to the core. We will come to this point later. Another result showing the robustness of the described chemical order pattern is that the $Ag_{12}Ni_{43}$ homotop with the 12 Ag atom at the 12 vertices of the shell results 1.8 eV less stable than the putative ground state (both fully relaxed).

The high cohesive energy of Ni favors the Ni-Ni bonds, as discussed above. On the other hand, this result could be seen, in some sense, as a manifestation of the tendency to off-center cores as increasing the core size (94). We calculated the second energy difference ($\Delta_2 E$) to determine the relative stabilities of the different stoichiometries with respect to their neighboring ones. This magnitude is defined as follows:

$$\Delta_2 E(x,y)^{0/\pm} = E(x+1,y-1)^{0/\pm} + E(x-1,y+1)^{0/\pm} - 2 \times E(x,y)^{0/\pm}$$

In order to compare the nanoalloy with an ideal mixture of the pure clusters, we evaluated the excess energy (E_{exc}) (105)

$$E_{exc}(x,y) = E(x,y) - x\frac{E(\mathrm{Ag}_{x+y})}{x+y} - y\frac{E(\mathrm{Ni}_{x+y})}{x+y}$$

where $E(\mathrm{Ag}_{x+y})$ and $E(\mathrm{Ni}_{x+y})$ are the energies of the pure clusters in their ground states. A negative excess energy indicates that formation of the corresponding nanoalloy is energetically favorable as compared to an ideal mixture. The ideal mixture would follow a simple Vegard law, according to which the total energy of the nanoalloys follows a linear behavior connecting the energies of the pure clusters. Fig. 3.27 collects the data of $\Delta_2 E$ and E_{exc} for the different stoichiometries.

The excess energy (Fig. 3.27 upper panel) shows that, although all the nanoalloys are stable, only the formation of few of them, corresponding to certain stoichiometries with less than 14 Ni atoms, is favourable with respect to

an ideal mixing of Ag_{55} and Ni_{55}, reflecting the strong tendency to segregation, instead of to maximize the number of Ni-Ag bonds. In all those stoichiometries, the Ni subcluster is completely covered by Ag. E_{exc} exhibits marked minima for $Ag_{54}Ni$, $Ag_{48}Ni_7$, $Ag_{42}Ni_{13}$, $Ag_{26}Ni_{29}$, $Ag_{23}Ni_{32}$. The first one, $Ag_{54}Ni$, corresponds to the smallest perfect core/shell configuration with the Ni atom in the center of the 55-atoms icosahedron. $Ag_{42}Ni_{13}$ is the next perfect core/shell structure with a perfect 13-atoms Ni core. This is the most representative perfect core/shell Ni@Ag nanoparticle with both core and shell of considerable size, and will be analyzed in more detail later. The other three correspond to very symmetrical arrangements. $Ag_{48}Ni_7$ has a decahedral nickel subcluster, which is a closed structure, forming a quasi perfect core/shell structure. In $Ag_{26}Ni_{29}$ and $Ag_{23}Ni_{32}$, the nickel sub-cluster has an almost closed structure, with a mushroom-like structure.

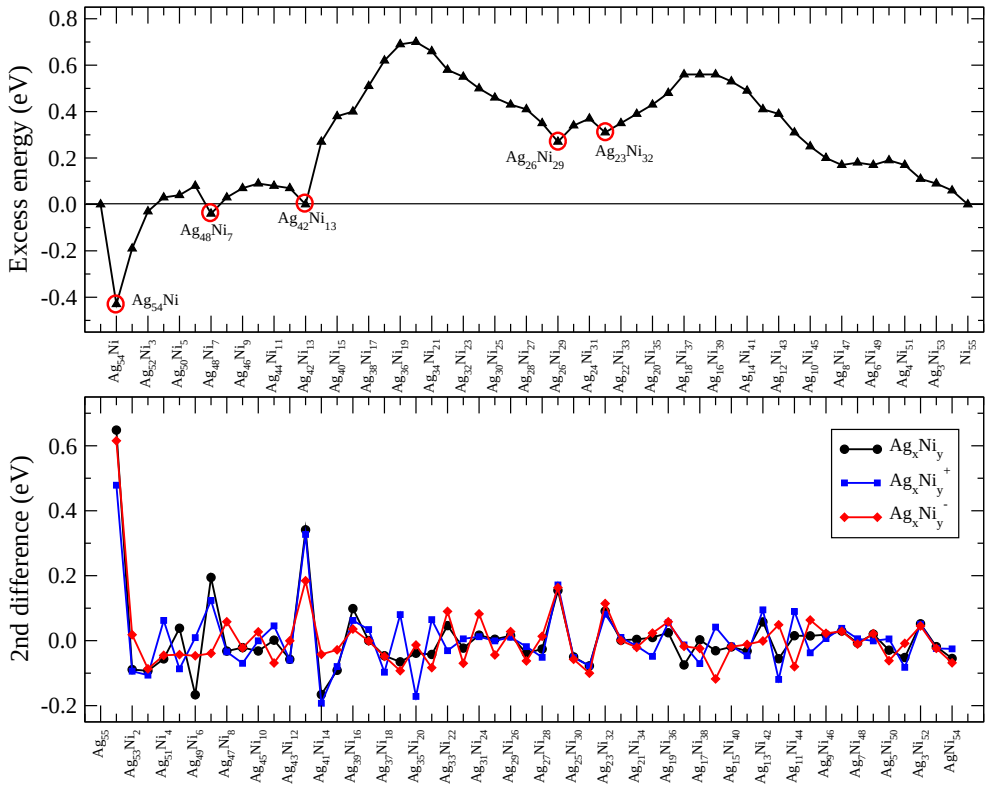

Figura 3.27: Excess energy (upper panel) and second energy difference (lower panel) of $[Ag_xNi_y]$ clusters with $x+y=55$. The local minima of excess energy are highlighted.

The second energy difference (Fig. 3.27 lower panel) shows marked peaks at exactly the same stoichiometries, which is an indicator of their relative stability with respect to neighboring stoichiometries, and of their abundance if grown from their constituent atoms in a thermodynamical bath. Those stoichiometries can be considered as magic compositions for this nanoalloy. Besides, all except $Ag_{48}Ni_7$ remain magic compositions upon ionization or electron capture. $Ag_{48}Ni_7$ has no peak of Δ_2E in the anionic state, being the peak shifted to $Ag_{47}Ni_8$. The highest peak of Δ_2E corresponds to $Ag_{54}Ni$ (the first core/shell structure). We note that among the smaller 13-atoms nanoalloys, $Ag_{12}Ni$ with a central Ni atom gives the highest peak in Δ_2E, reflecting the high relative stability of this arrangement also in the smaller nanoalloy. The reason of the

high stability of $Ag_{54}Ni$ in the Mackay icosahedral structure has been already analyzed by Mottet et al. (103) who also shown that in the icosahedral Ag_{55} cluster, the single impurity of Ni located at the central site even increases the melting temperature. As these authors point out, the icosahedral structure results more stable in these clusters than a crystal fragment because it optimizes the surface energy (more compact facets are exposed at the surface in an icosahedron). However, the strong distortion produced of the lattice creates strain and compression at the center of the icosahedron because inter-shell distances are contracted. Introducing a smaller atom (like Ni) at the central site of the icosahedron relaxes this strain thus reducing the compression at the center. Therefore, from the energetic point of view, the central site is the optimal position for the Ni impurity. It is interesting to analyze how the Ag-Ni hybridization evolves as varying the Ag/Ni ratio starting from one of the stoichiometric limits. In the Appendix A are collected the total and element-projected Density of Electronic States (DOS), as going from $Ag_{54}Ni$ to $AgNi_{54}$ (Figs. A.6 to A.14 The overall shape of the DOS is similar, provided that the atomic arrangement is icosahedral in all cases, and that at this Ni concentration regime all the nanoalloys are in low-spin states as we will discuss in the next section (we will see that in the high Ni-concentration the nanoalloys are, on the contrary, strongly spin-polarized and sustain a considerable magnetic moment). The Ag-Ni hybridization takes place close to the Fermi energy, down to 2 eV below E_F, being the lower energy states essentially contributed by Ag. The HOMO progressively acquires Ni character as increasing the Ni content, reaching the nearly pure Ni character already at a low Ni content. The Ni character of the HOMO, even for those nanoalloys for which all Ni atoms are located in a core surrounded by Ag indicates that, although the Ag-Ni is relatively weak and Ag provides physical protection to the core, Ni states should play an important role in the reactivity of these nanoalloys, as well as in other processes like ionization. Thus, upon ionization, the electron is mainly extracted from the Ni states. Other electronic properties like the adiabatic ionization potential and electron affinity of both the ground state

and low-energy homotops of these nanoalloys can be found in the Appendix A.

3.5.3 Magnetic properties

The total spin magnetic moment of the predicted ground states of the 55-atoms AgNi nanoalloys is plotted in Fig. 3.28 in the whole composition range. Several magnetic phase transitions take place. Let us focus first on the neutral nanoalloys, starting from the low Ni concentration limit. We note that small pure Ag clusters can sustain a magnetic moment in contrast to the Ag bulk; Ag_{55} is in a low spin state ($3\mu_B$) while Ni_{55} is in a high spin state ($40\mu_B$) characterized by parallel magnetic couplings (reminiscent from the ferromagnetic Ni fcc) and per atom magnetic moment of $0.7\mu_B$/atom (slightly larger than that in the bulk). $Ag_{54}Ni$ is the first perfect core/shell cluster with the Ni atom in the center. The moment of $Ag_{54}Ni$ is $4\mu_B$, that is one μ_B larger than that of Ag_{55}, although this increase is, unexpectedly, contributed by the Ag atoms and not by the Ni one. Fig. 3.29 shows the local charge and magnetic moment distribution in this cluster. An electronic charge transfer from the outer 42-atoms to the inner 13-atoms takes place. This is a general trend in the 55-atoms nanoalloy. The Ni atom gains 0.35 electrons and its moment is quenched ($0.08\mu_B$) and antiparallel to those of Ag. The quenching of the magnetic moment in the Ni atom is consistent with the loss of the moment in magnetic impurities embedded in a nonmagnetic matrix. The reason is the electron delocalization and hybridization with the host states, as illustrated in the DOS shown in the Appendix A and manifested by the noticeable electronic charge gained by the Ni atom due to charge transfer from Ag. We note that in a system with more than half-band filling (like Ni) an increase of charge tends, in general, to reduce the spin-polarization. Therefore the magnetic moment of this cluster is essentially contributed by the Ag atoms, and in particular by those located at the surface shell. The 42-atoms outer shell of Ag plays here an important role that can be assessed by comparing the local charge and moment distribution in the inner 13-atoms core of $Ag_{54}Ni$ (Fig. 3.29) with the distribution in the smaller $Ag_{12}Ni$ nanoalloy (See Fig. 3.24).

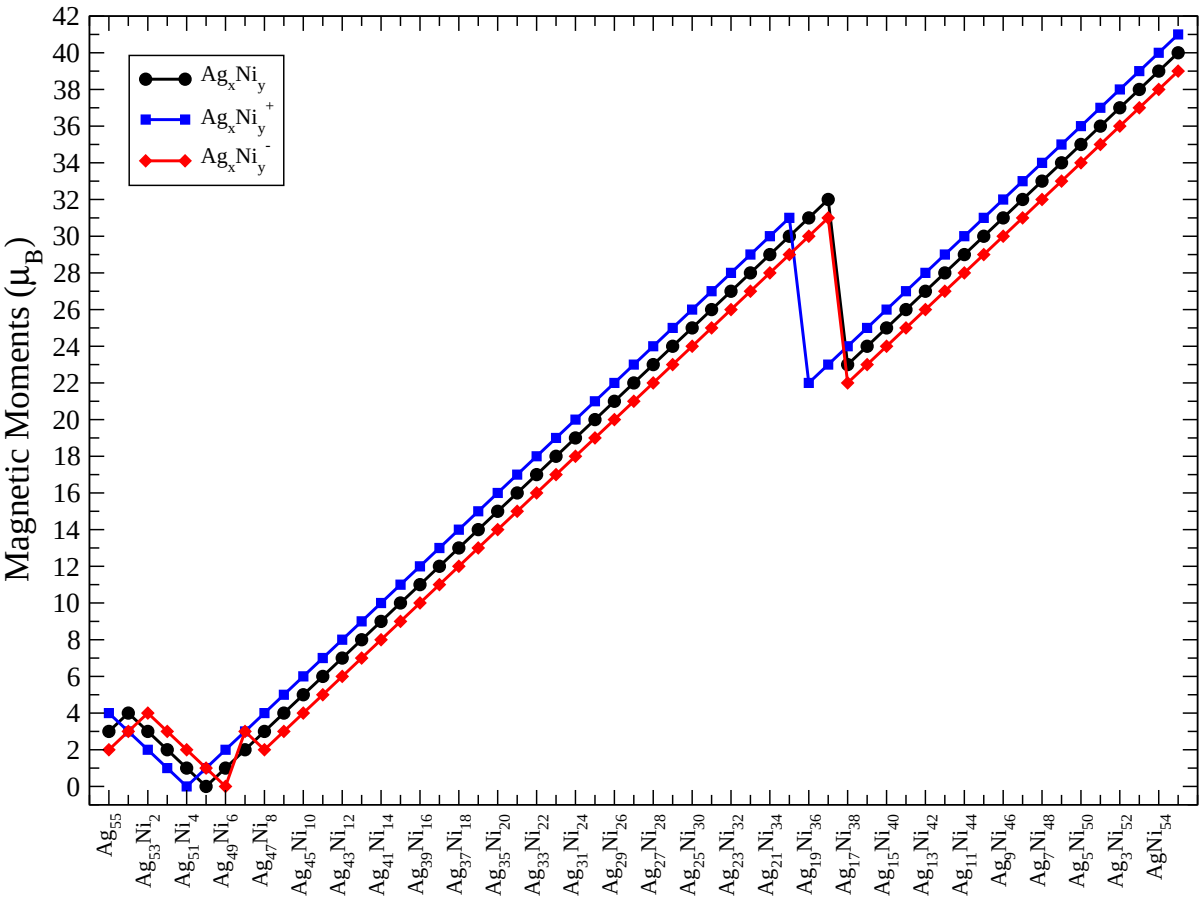

Figura 3.28: Total spin magnetic moment of the $[(Ag_xNi_y)^{0/\pm}]$ clusters with $x + y = 55$ as a function of the composition.

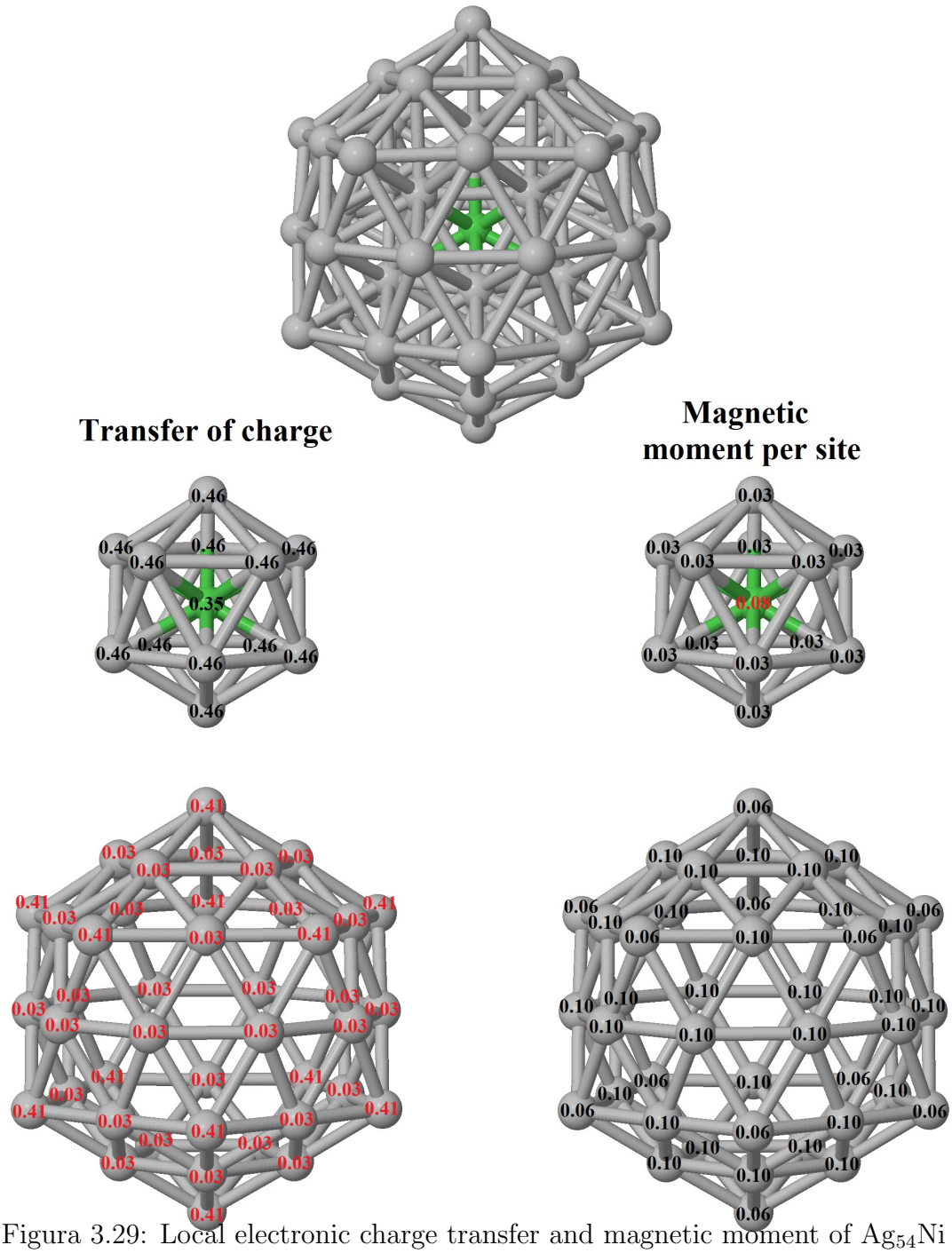

Figura 3.29: Local electronic charge transfer and magnetic moment of $Ag_{54}Ni$ cluster. For charge transfer, numbers in black (red) indicate gain (loss) of charge; for the magnetic moment, numbers in black (red) indicate spin up (down). Contributions of the inner 13 atoms and the outer 42 are separated for the sake of clarity.

In Fig. 3.30 we plot the total magnetic moment of the 55-atoms AgNi nanoalloys for compositions up to $Ag_{42}Ni_{13}$ together with that of the 13-atoms AgNi nanoalloy for the sake of comparison. We also separate, in the case of the 55-atoms nanoalloy, the contributions of the 42 outer atoms and of the 13 inner ones (see Fig. 3.24). 13-atoms cluster. In contrast, the inner 13 atoms of $Ag_{54}Ni$ contribute together less than $0.5\mu_B$ to the total moment. Despite the fact that $Ag_{12}Ni$ has $4\mu_B$ like $Ag_{54}Ni$, the Ni atom contributes $0.65\mu_B$ in the smaller

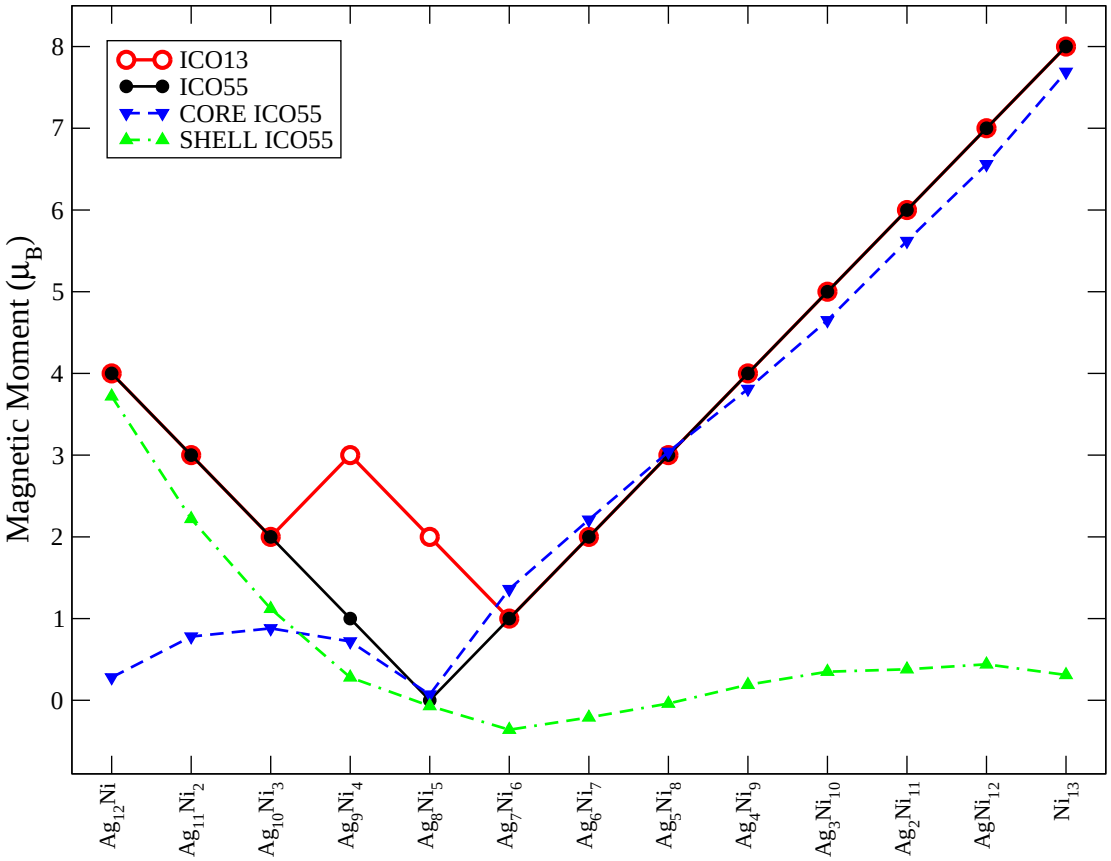

Figura 3.30: Total magnetic moment of the 55-atoms AgNi nanoalloys for compositions of Ni content up to $Ag_{42}Ni_{13}$ (black circles). Total magnetic moment of the 13-atoms AgNi nanoalloys in the whole composition range (open circles). Contribution of the 42 outer atoms (up green triangles) and of the 13 inner ones (down blue triangles) of the 55-atoms AgNi nanoalloys to their total moment.

The outer Ag atoms lose charge in favor of the central Ni atom. Therefore, the spin-polarized electronic charge distribution within the 13 atoms cluster dramatically changes upon its capping with the 42 Ag atoms of the outer shell, and this holds along the low Ni content regime of the nanoalloys. The charge transfer is triggered by the atomic environment to a large extent. We note that although the electronegativities of Ag and Ni are similar, in the 55 atoms

nanoalloy with less than 14 Ni atoms, the charge transfer takes place from the outer Ag atoms to all the inner 13 ones, included the Ag inner atoms. However, in the smaller 13 atoms nanoalloy, no Ag atom gains electronic charge.

Contrary to what one would expect based on an extrapolation between the values of the magnetic moments of the pure Ag_{55} and Ni_{55} clusters, the total moment of the nanoalloy in the high Ag concentration limit decreases as increasing Ni concentration up to $Ag_{50}Ni_5$, an exception being the discussed $Ag_{54}Ni$ case. Up to $Ag_{50}Ni_5$, the inner 13 atoms contribute less than $1\mu_B$, the decrease in the total moment being, therefore, due to a decrease in the spin-polarization of Ag. The lowest moment (singlet state) is reached at $Ag_{50}Ni_5$ in which the spin polarization is completely quenched. We note that the singlet state here is due to antiparallel magnetic couplings and low local magnetic moments (see Fig. 3.31). An interesting magnetic trend concerns the coupling between Ni atoms when the Ni subcluster is small. This coupling is sensitive to the atomic environment and to the interaction with Ag. We have already seen in the previous paragraph that when a Ni subcluster of less than 6 atoms is covered by Ag in the 55-atoms nanoalloy, the Ni moment is quenched. If we compare the magnetic couplings of the Ni subclusters (up to 13 Ni atoms) in the 55-atoms with the 13-atoms nanoalloys, we find that in the absence of the 42 Ag atoms of the shell, few Ag atoms in the smaller nanoalloy are enough to promote antiparallel couplings between Ni atoms. Even one Ag atom in the $AgNi_{12}$ nanoalloy promotes antiparallel couplings within the Ni subcluster. In general, The same Ni subclusters that were magnetically quenched in the 55-atoms nanoalloy, but preserving parallel couplings, have antiparallel magnetic couplings in the 13-atoms nanoalloy, which lead to an unusual and unexpected magnetic arrangement for a system made of a late transition metal element like Ni, and it is a manifestation of the complex and rich magnetic arrangements that can be found at the nanoscale, depending on the size, and on the atomic and chemical environments. In this composition range, the Ni subcluster is very small, and due to the high average Ni-Ag coordination and corresponding strong Ni-Ag hybridization (see Fig. 3.32) and noticeable charge transfer, the

spin polarization is strongly reduced (although not as much as in the single embedded impurity). Consequently, the Ni-Ni bonding weakens and the tendency to develop parallel magnetic couplings characteristic of pure Ni systems decreases.

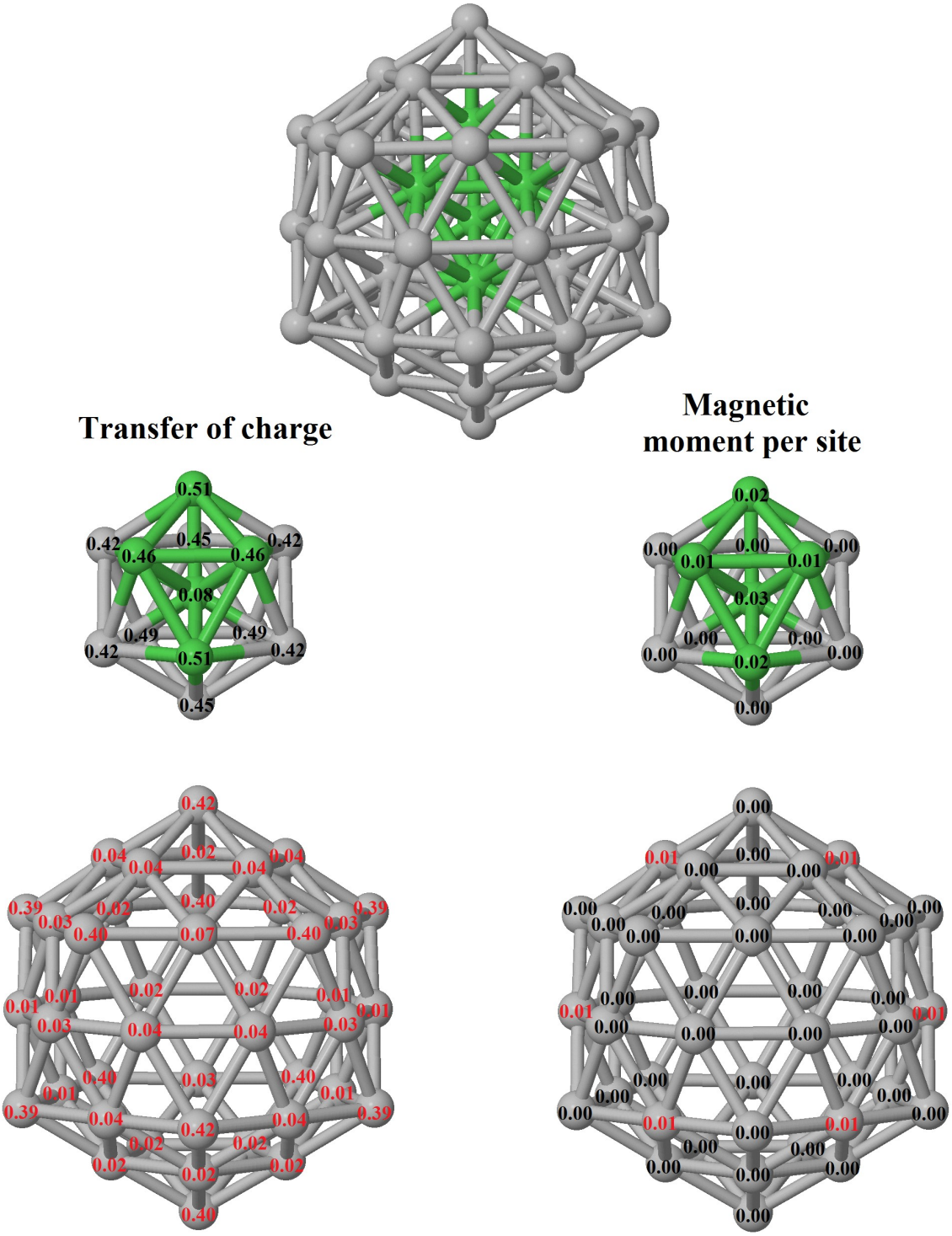

Figura 3.31: Local electronic charge transfer and magnetic moment of $Ag_{50}Ni_5$ cluster. For charge transfer, numbers in black (red) indicate gain (loss) of charge; for the magnetic moment, numbers in black (red) indicate spin up (down). Contributions of the inner 13 atoms and the outer 42 are separated for the sake of clarity.

A manifestation of the weakening of the Ni-Ni bonding is the large average Ni-Ni interatomic distance in the Ni subcluster, particularly in the low Ni concentration regime. This distance is larger than that of the relaxed freestanding Ni cluster extracted from the nanoalloy. The Ni dimer in $Ag_{53}Ni_2$ has an interatomic distance that exceeds in 20% that of the free-standing Ni_2. As soon as the Ni content exceeds a critical value, and a sufficiently big Ni core is formed, this distance tends to equal the one in the pure Ni cluster, but the increase is still noticeable up to $Ag_{45}Ni_{10}$ where the Ni subcluster is still expanded by about 7%.

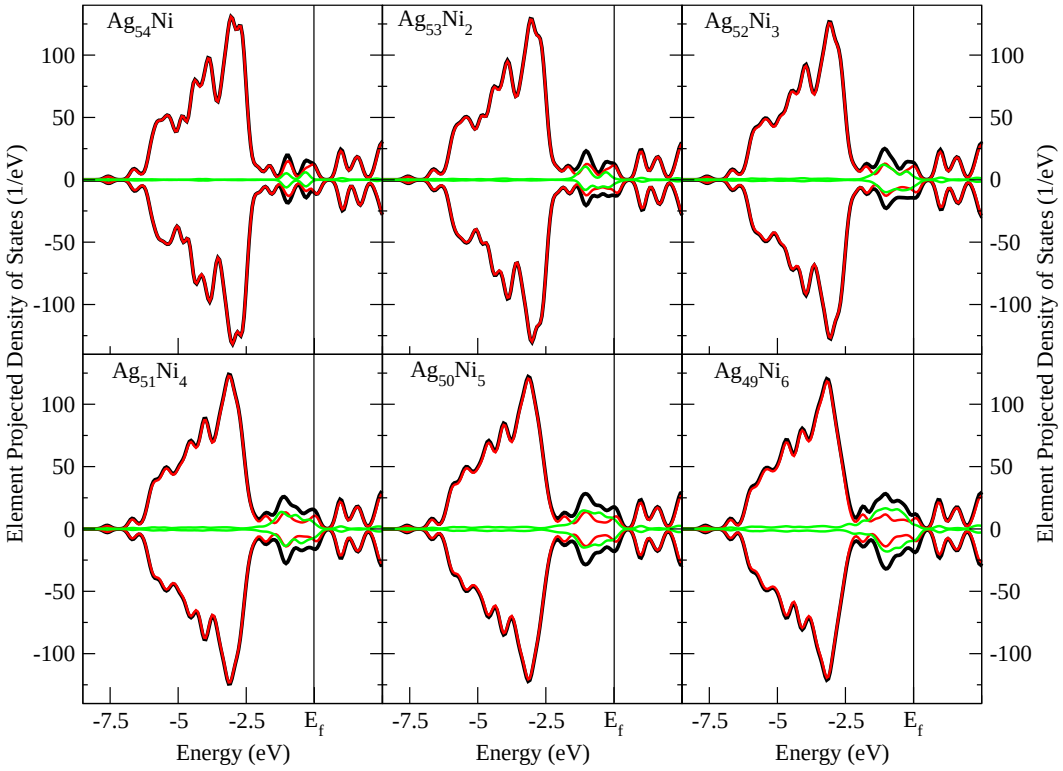

Figura 3.32: (Color online) Total DOS (black line), partial contribution of silver (red line) and nickel atoms (green line) of $Ag_{54}Ni$ to $Ag_{49}Ni_6$ clusters.

Further support to the assessment that Ni-Ag hybridization and charge transfer is fundamental in governing the magnetic properties here is the fact that a pure Ni cluster has larger magnetic moments if it is expanded. We have checked this in our case by repeating calculations for several Ni subclusters extracted from the nanoalloy. Beyond this Ni concentration ($Ag_{50}Ni_5$) the total moment linearly increases as increasing the Ni content, with a sudden drop of $9\mu_B$ at $Ag_{18}Ni_{37}$, to continue the linear increase with the same slope as before till the pure Ni_{55} limit. The linear increase is associated with the formation of a compact Ni subcluster with a net magnetic moment that contributes most of the moment of the nanoalloy in this composition regime. Fig. 3.31 shows that beyond $Ag_{50}Ni_5$, the moment of the inner 13 atoms of the nanoalloy is now similar to the moment of the 13-atoms nanoalloy of the corresponding stoichiometry, and that the contribution of the outer 42-atoms shell becomes negligible, although it points in the same direction as the Ni moment (this Ag-Ni coupling holds for larger Ni content until the sudden drop at $Ag_{18}Ni_{37}$ occurs). The above results demonstrate that the formation of a sizable Ni subcluster allows it to preserve its magnetic identity to a large extent when covered or interfaced by Ag, with a weak core-shell interaction, and that the magnetic moment of the nanoalloy is, thus, localized in the Ni subcluster. In the previous section, we have discussed how the electronic density of states evolves as increasing the Ni content in the nanoalloy, and how the increase in the total moment is consistent with the enhancement of the spin-polarization of the molecular orbitals with most Ni character, which are those located close to E_F. The magnetic ordering in Ni is parallel, in contrast with the few antiparallel couplings of the smaller 13-atoms nanoalloy (see Fig. 3.24).

At the stoichiometry $Ag_{18}Ni_{37}$, the nanoalloy reaches a total moment of $32\mu_B$, with per Ni-atom moment of $0.85\mu_B$. This spin polarization in Ni exceeds by 30% the one in the Ni fcc bulk. It is expected that as increasing the size of a Ni cluster its magnetic moment converges to the bulk value. The sudden drop of the magnetic moment occurring at $Ag_{18}Ni_{37}$ is mainly due to a reduction of the spin polarization in the Ni subcluster while keeping the parallel magnetic couplings reminiscent of the ferromagnetic order of the bulk. Beyond this magnetic phase transition, the rather small moment of Ag points in opposite direction to the Ni moment, but it is negligible. This drop of spin polarization in Ni ensures a per atom magnetic moment

in Ni_{55} similar to the bulk one. The mentioned antiparallel coupling between the magnetic moments of Ag and Ni is also found in the 13-atoms nanoalloy, particularly in the rich Ni regime.

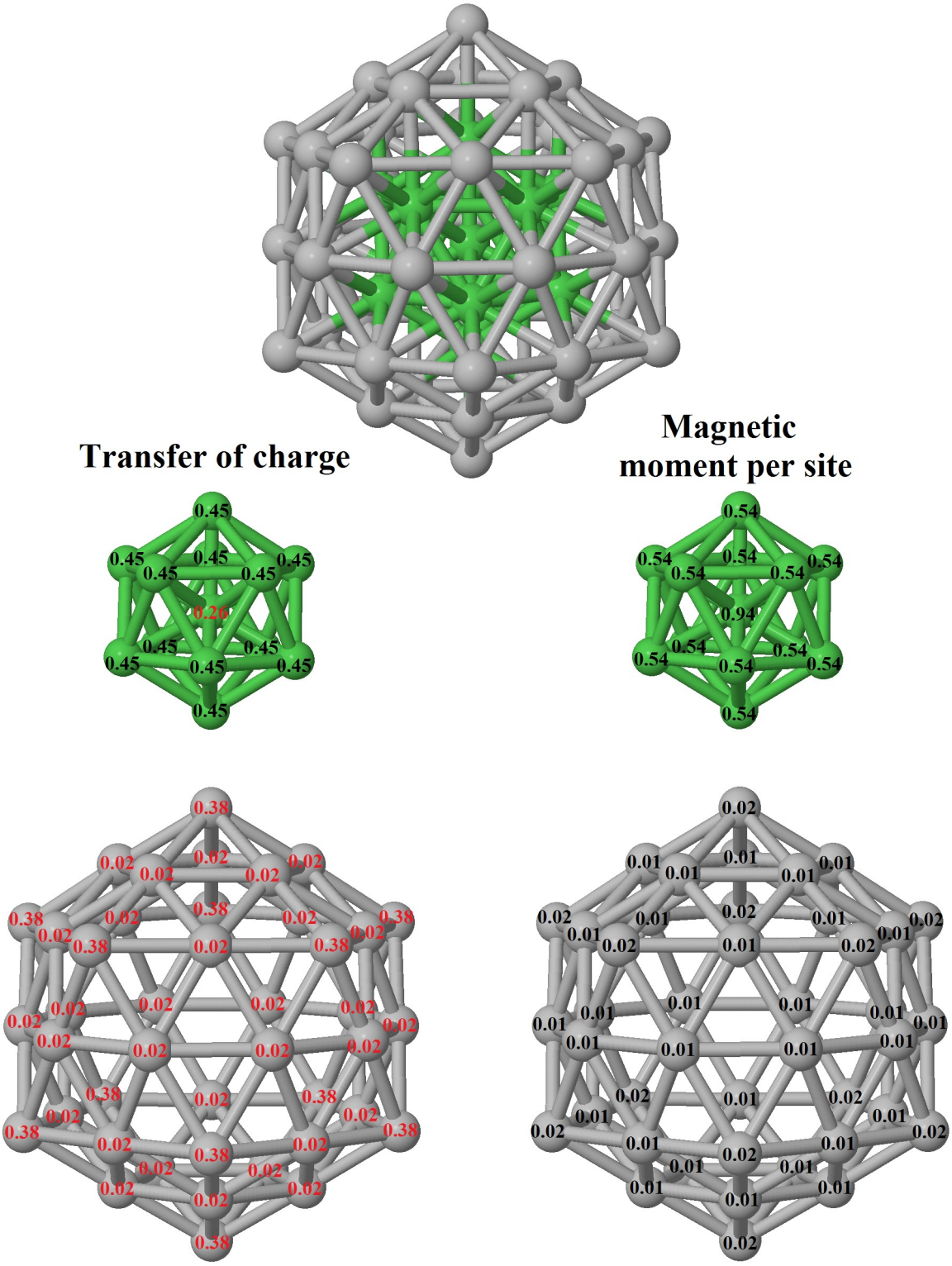

Figura 3.33: Local electronic charge transfer and magnetic moment of $Ag_{42}Ni_{13}$ cluster. For charge transfer, numbers in black (red) indicate gain (loss) of charge; for the magnetic moment, numbers in black (red) indicate spin up (down). Contributions of the inner 13 atoms and the outer 42 are separated for the sake of clarity.

We also see that the total magnetic moment of a 55 atoms nanoalloy with a given composition is more robust against the chemical order than that of the 13-atoms nanoalloy. This can be inferred by comparing the magnetic moment of the low-energy homotops in the nanoalloys of both sizes. The rest of this section is devoted to the analysis of the other perfect core/shell cluster, $Ag_{42}Ni_{13}$ with a 13-atoms icosahedral Ni core. This 55-atoms core/shell cluster has $8\mu_B$, exactly the same as Ni_{13}, most of which ($7.42\mu_B$) is localized in the Ni core. This situation is also present in CoCu and CoAu nanoalloys, where Co atoms are totally covered by Cu and Au atoms respectively(104). Fig. 3.33 illustrates the local charge and magnetic moment distribution in this cluster. The central Ni atom loses 0.26 electrons, so that a radial oscillation of charge transfer takes place. This electronic deficit leads the inner atom to have a large moment of $0.94\mu_B$. The magnetic couplings are parallel. The density of states of $Ag_{42}Ni_{13}$ is plotted in the Fig. 3.34 for the three charge states.

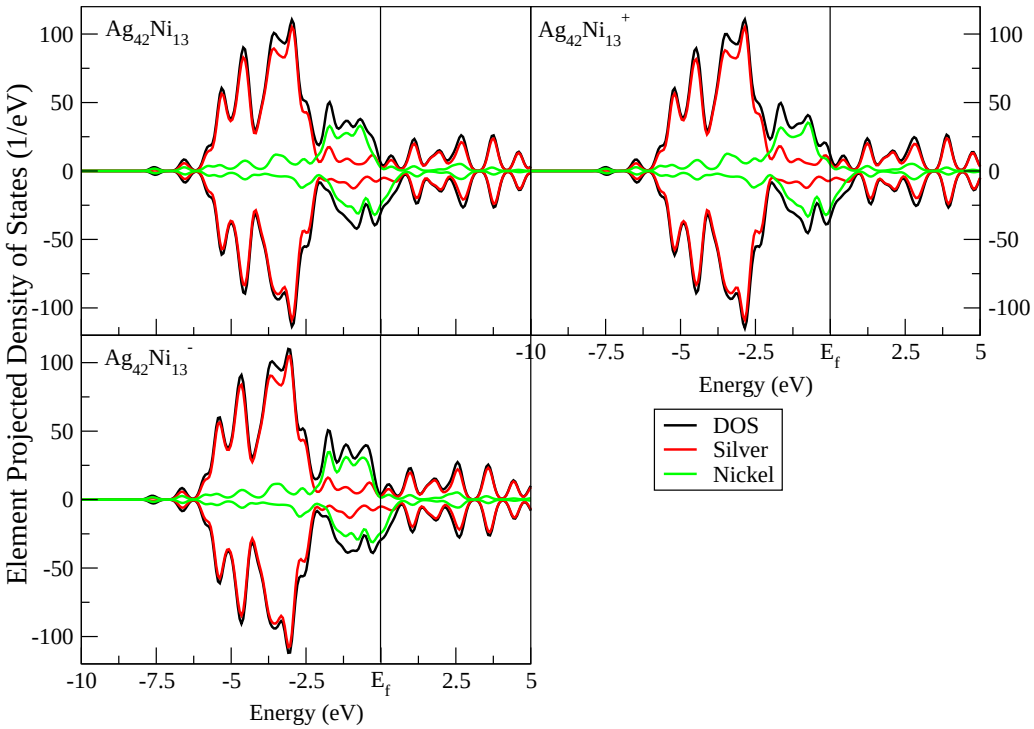

Figura 3.34: Total DOS (black line), partial contribution of silver (red line) and nickel atoms (green line) of $Ag_{42}Ni_{13}$ cluster. The vertical line marks the Fermi energy.

The Ag and Ni contribution to the molecular orbitals along the spectrum in clear and illustrates a weak Ag-Ni interaction and a high spin-polarization, particularly in the states mostly contributed by Ni. The HOMO of the neutral cluster is of minority spin. This explains why upon ionization the magnetic moment increases $1\mu_B$ as shown in Fig. 3.28 (the electron is extracted from minority spin states) while the opposite happens upon an electron capture. This is a general trend in most of the composition range except in the rich Ag limit (up to $Ag_{48}Ni_7$) where the above trend is reversed in several stoichiometries. The DOS of the neutral clusters in this region, plotted in the SI, do not allow such a clear interpretation; the HOMO character has also a large Ag contribution and the overall spin polarization is much weaker. We note that another exception to this rule can be found at the magnetic phase transition at $Ag_{18}Ni_{37}$ which, in the case of the cationic nanoalloys, occurs earlier

(at $Ag_{20}Ni_{35}$ instead) and, consequently, in the intermediate concentrations the total moment changes upon ionization by $9\mu_B$. The drop in the cationic nanoalloys to restore the per atom moment in Ni occurs at a lower Ni content since ionization further increases the Ni moment as a consequence of the aforementioned spin- and element-character of the HOMO.

3.5.4 Oxidation of $Ag_{42}Ni_{13}$

Once the nickel-silver nanoalloys have been described, and having selected the best stoichiometries from the energy and stability point of view, we will now study how the nanoparticle $Ag_{42}Ni_{13}$ behaves, under oxidation. In Fig. 3.35 are collected the ground state and the first two structural isomers of the $Ag_{42}Ni_{13}O_m$ clusters with $m = 1 - 8$ and 20 (for $m = 20$ we only calculate one cluster). The oxidation process is the addition of atomic oxygen one by one to the surface of this cluster. Adding an oxygen atom (Fig. 3.36), we can see that it absorbs a large amount of charge from the silver atoms (shell), and in a less degree from the nickel atoms (core). As we showed in the previous section, in the graph of the density of state of $Ag_{42}Ni_{13}$ (Fig. 3.34), we notice that the HOMO is mostly formed by nickel electrons of minority state, for this reason when electrons are removed from the core of the system (nickel atoms), the magnetic moment of the core increases, from 7.42 μ_B to 7.73 μ_B, this is consistent with the density of states. While the magnetic moment of the core increases, the corresponding of the shell decreases, going from 0.58 μ_B to 0.34 μ_B, appearing antiferromagnetic couplings on the surface of the system, in the same way, we can see that the oxygen atom is absorbed on a triangular face next to one of the vertices of the icosahedron with antiferromagnetic coupling. This process does not imply the total change of the magnetic moment of the system ($8\mu_B$), but concentrates it even more in the core of the nanoparticle. This behavior continues for more oxidation rates (Fig. 3.37-3.39). Adding more oxygen atoms, the magnetic moment of the core increases, decreasing the magnetic moment of the shell, and keeping the system´s magnetic moment constant (8 μ_B). When four oxygen atoms are absorbed in the surface (Fig. 3.39), the magnetic moment of the core (8.02 μ_B) is approximately the total of the nanoparticle, whilst the corresponding to the shell decreases to 0.15 μ_B (due to the antiferromagnetic couplings), and the total magnetic moment for the oxygen atoms drop to -0.17 μ_B.

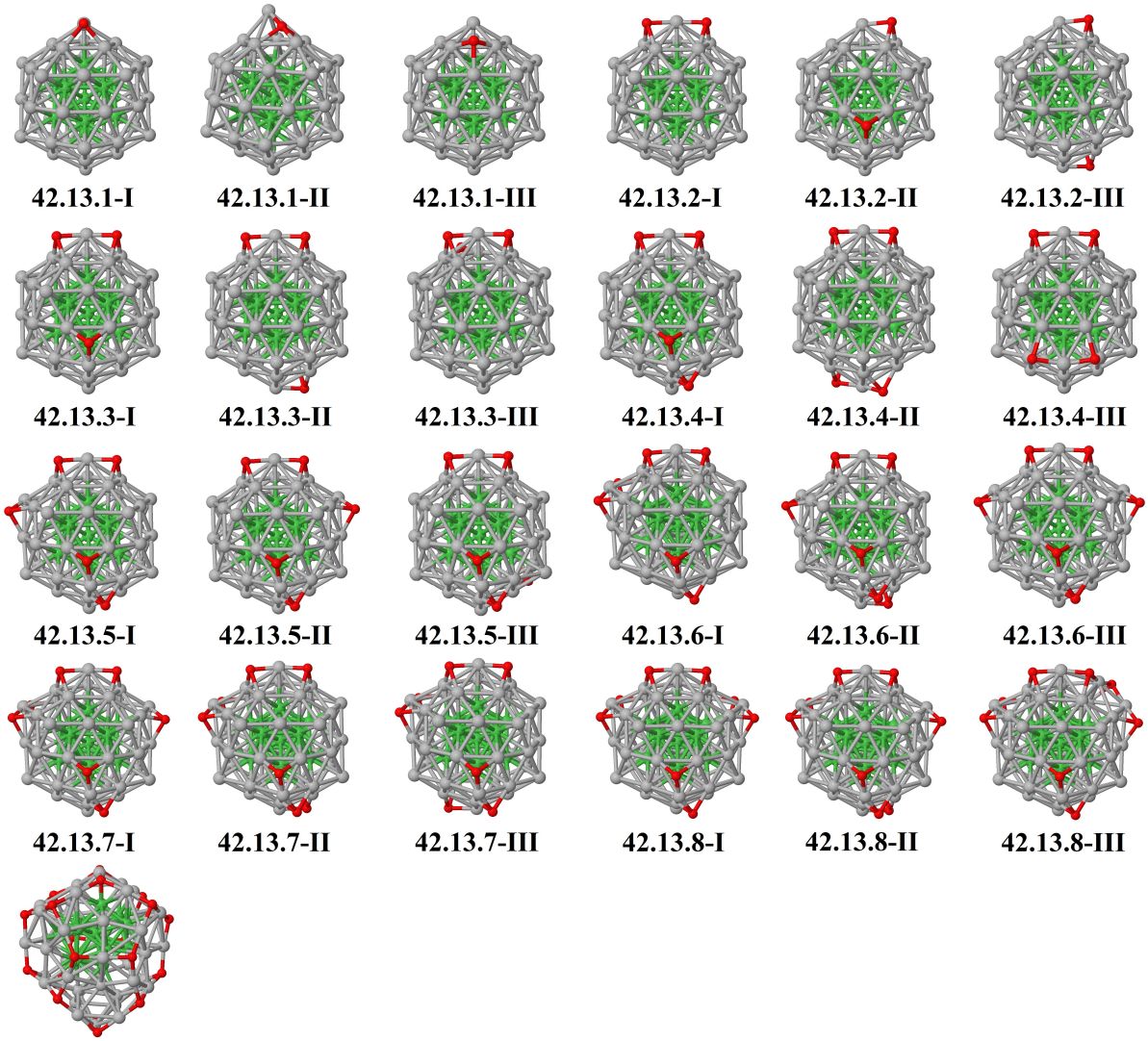

Figura 3.35: Putative ground state and up to first three low-energy homotops of $Ag_{13}Ni_{42}O_m$ clusters with $m = 1 - 8$ and 20.

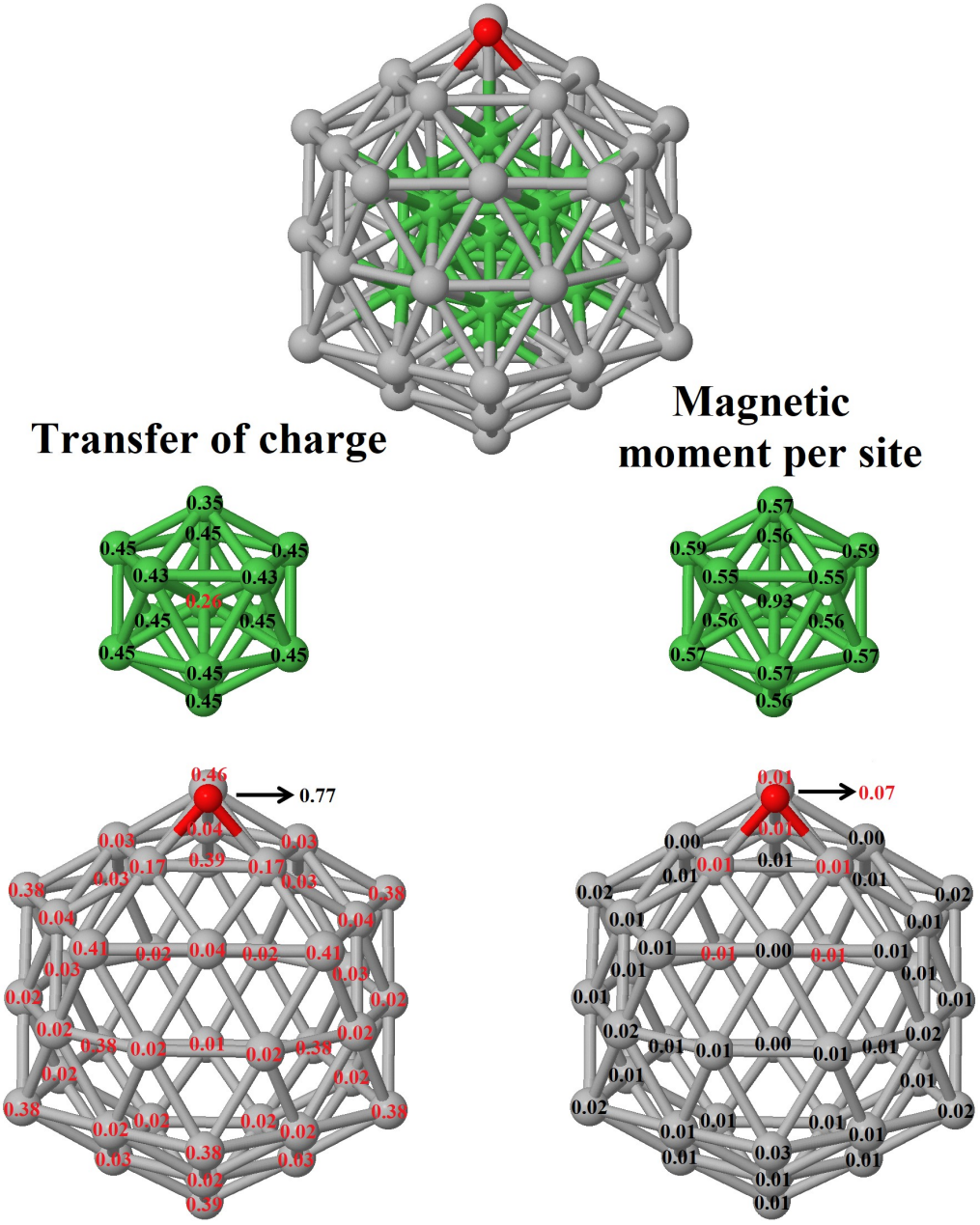

Figura 3.36: Local electronic charge transfer and magnetic moment of $Ag_{13}Ni_{42}O$ cluster. For charge transfer, numbers in black (red) indicate gain (loss) of charge; for the magnetic moment, numbers in black (red) indicate spin up (down). Contributions of the inner 13 atoms and the outer 42 are separated for the sake of clarity.

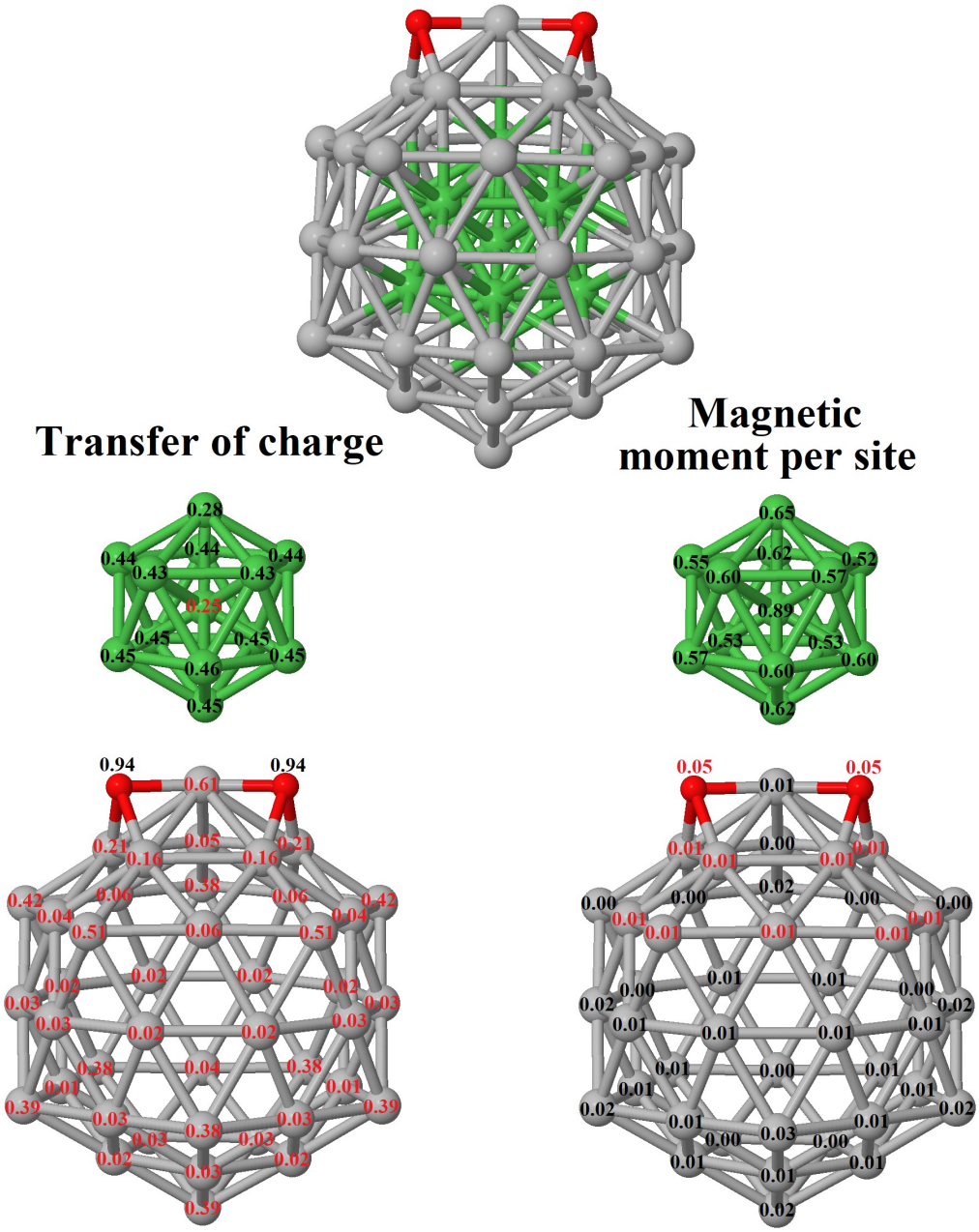

Figura 3.37: Local electronic charge transfer and magnetic moment of $Ag_{13}Ni_{42}O_2$ cluster. For charge transfer, numbers in black (red) indicate gain (loss) of charge; for the magnetic moment, numbers in black (red) indicate spin up (down). Contributions of the inner 13 atoms and the outer 42 are separated for the sake of clarity.

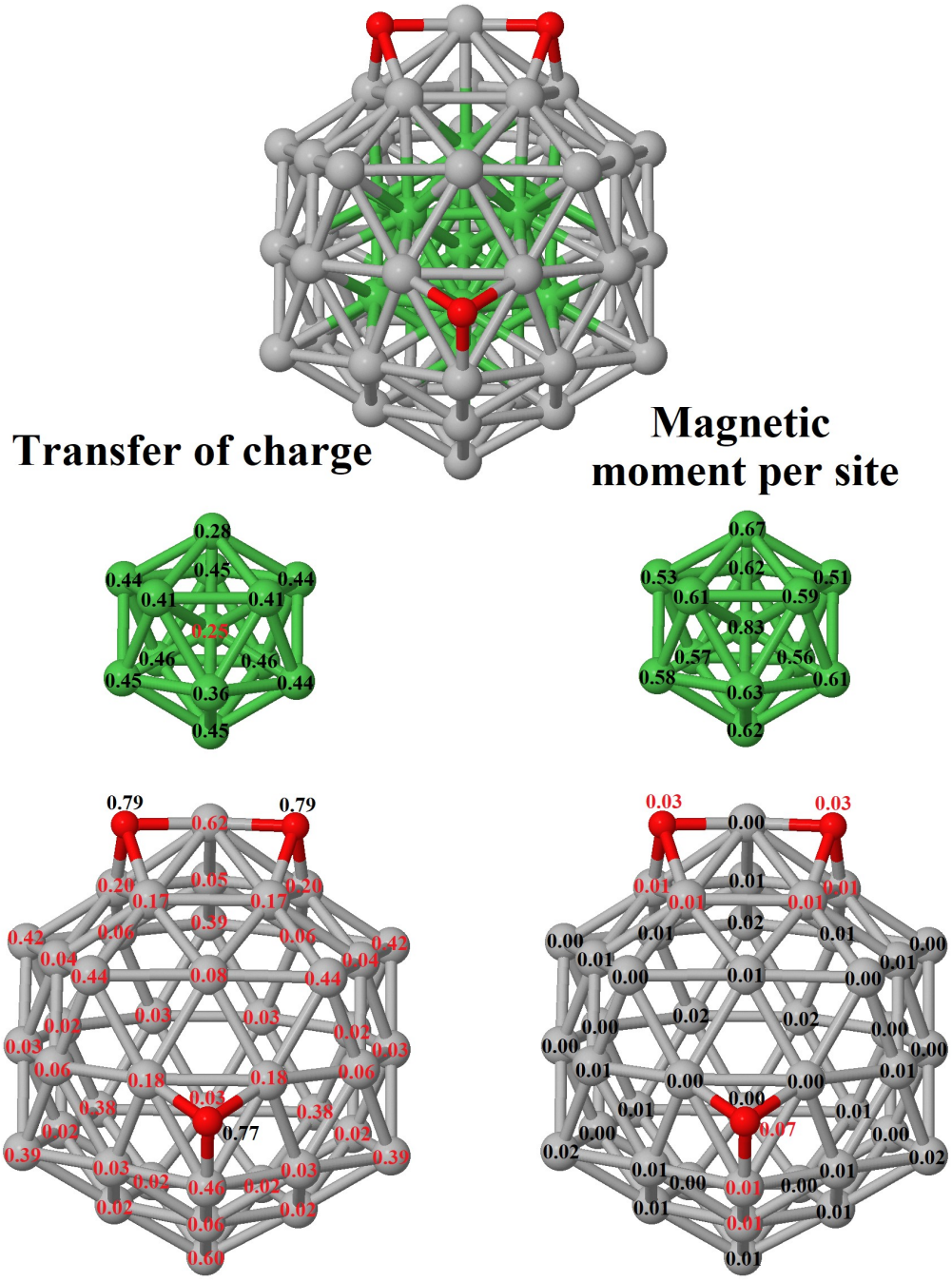

Figura 3.38: Local electronic charge transfer and magnetic moment of $Ag_{13}Ni_{42}O_3$ cluster. For charge transfer, numbers in black (red) indicate gain (loss) of charge; for the magnetic moment, numbers in black (red) indicate spin up (down). Contributions of the inner 13 atoms and the outer 42 are separated for the sake of clarity.

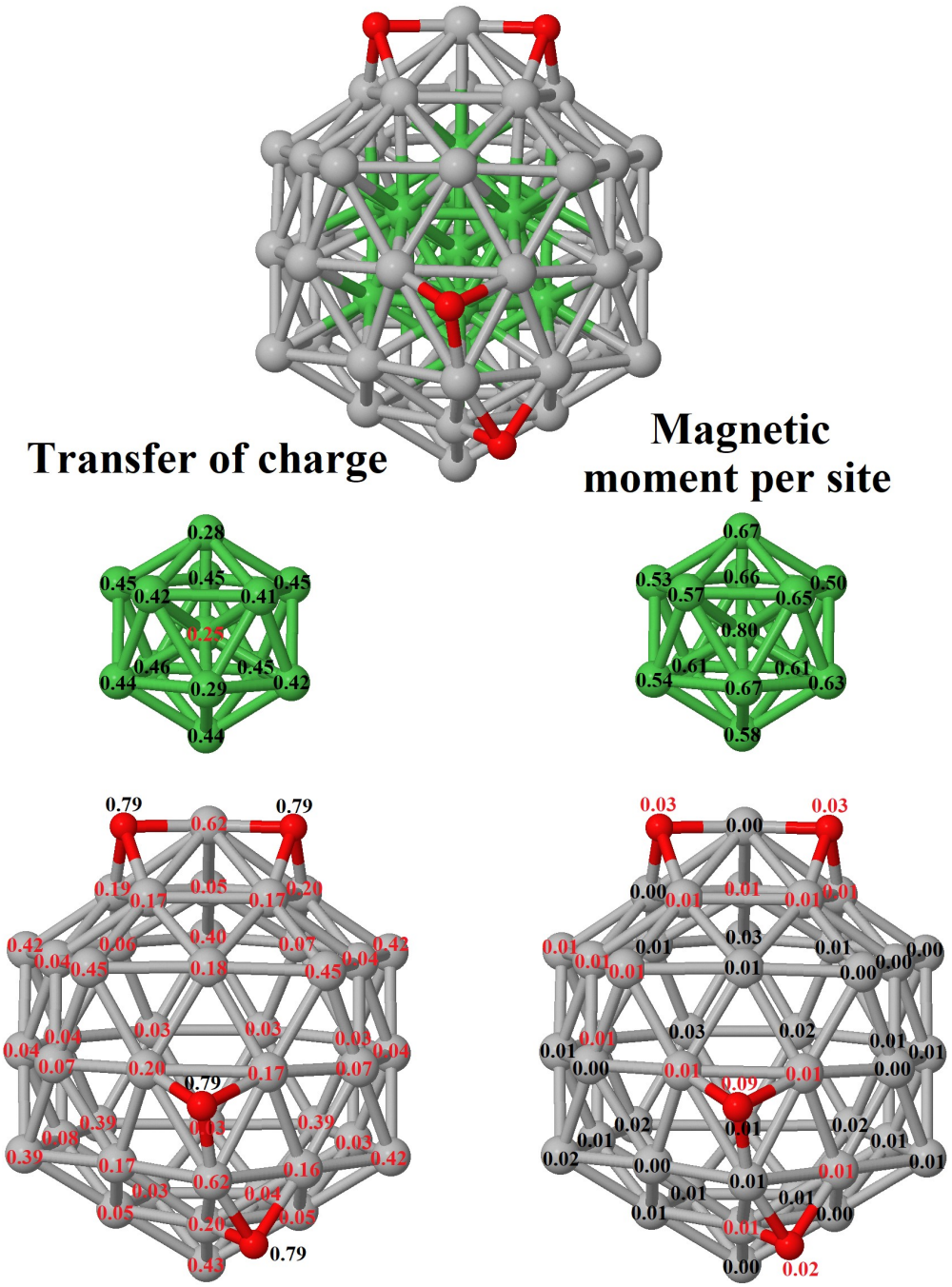

Figura 3.39: Local electronic charge transfer and magnetic moment of $Ag_{13}Ni_{42}O_4$ cluster. For charge transfer, numbers in black (red) indicate gain (loss) of charge; for the magnetic moment, numbers in black (red) indicate spin up (down). Contributions of the inner 13 atoms and the outer 42 are separated for the sake of clarity.

Tabla 3.3: Magnetic moment in μ_B per component (core, shell and oxygen atoms) for putative low energy clusters.

Cluster	μ core	μ shell	μ oxigen
$Ag_{42}Ni_{13}$	7.42	0.58	—
$Ag_{42}Ni_{13}O$	7.73	0.34	-0.07
$Ag_{42}Ni_{13}O_2$	7.85	0.25	-0.10
$Ag_{42}Ni_{13}O_3$	7.93	0.20	-0.13
$Ag_{42}Ni_{13}O_4$	8.02	0.15	-0.17
$Ag_{42}Ni_{13}O_5$	8.02	0.15	-0.17
$Ag_{42}Ni_{13}O_6$	8.09	0.05	-0.14
$Ag_{42}Ni_{13}O_7$	8.09	0.13	-0.22
$Ag_{42}Ni_{13}O_8$	8.11	0.22	-0.33
$Ag_{42}Ni_{13}O_{20}$	6.60	-0.44	-0.16

In Table 3.3, are compiled the magnetic moment of the ground states per component of $Ag_{42}Ni_{13}O_m$ clusters with $m = 1-8$ and 20. As we showed in last subsection, for cluster $Ag_{42}Ni_{13}$, the magnetic moment is concentrated in the core of the system ($\sim$ 93% of the total μ), when we add oxygen atoms, the magnetic moment of the core increases, whilst the corresponding for the shell decreases up to $Ag_{42}Ni_{13}O_6$, and after that increases for $Ag_{42}Ni_{13}O_7$ and $Ag_{42}Ni_{13}O_8$. The oxygen atoms always couple antiparallel with respect to the core atoms, decreasing the magnetic moment of those atoms as the rate of oxygens increase. When the oxidation of the nanoparticle, reader a high rate (structure 42.13.20-I, Fig. 3.35), we observe that the structure of the system becomes completely deformed. Due to this deformation, one of the oxygen atoms penetrate the silver shell, bonding with core atoms, decreasing the magnetic moment of the nickel atom bonded to oxygen, lowering, as consequence, the total magnetic moment of the system up to 6 μ_B. Despite this, the magnetic moment of the core is still higher (6.6 μ_B) than the total system (6 μ_B). The above results show that silver is a good protector for the magnetic moment of the nickel cluster, and once this coating is corrupted, the system decreases its magnetic moment. Comparing the density of states for $Ag_{42}Ni_{13}$ without and with oxygen atoms (Fig. 3.40), we observe a decrease int the minority electrons (nickel´s electrons), for this reason the magnetic moment of the nickel (core) contribution increases, as we had predicted in the magnetism section.

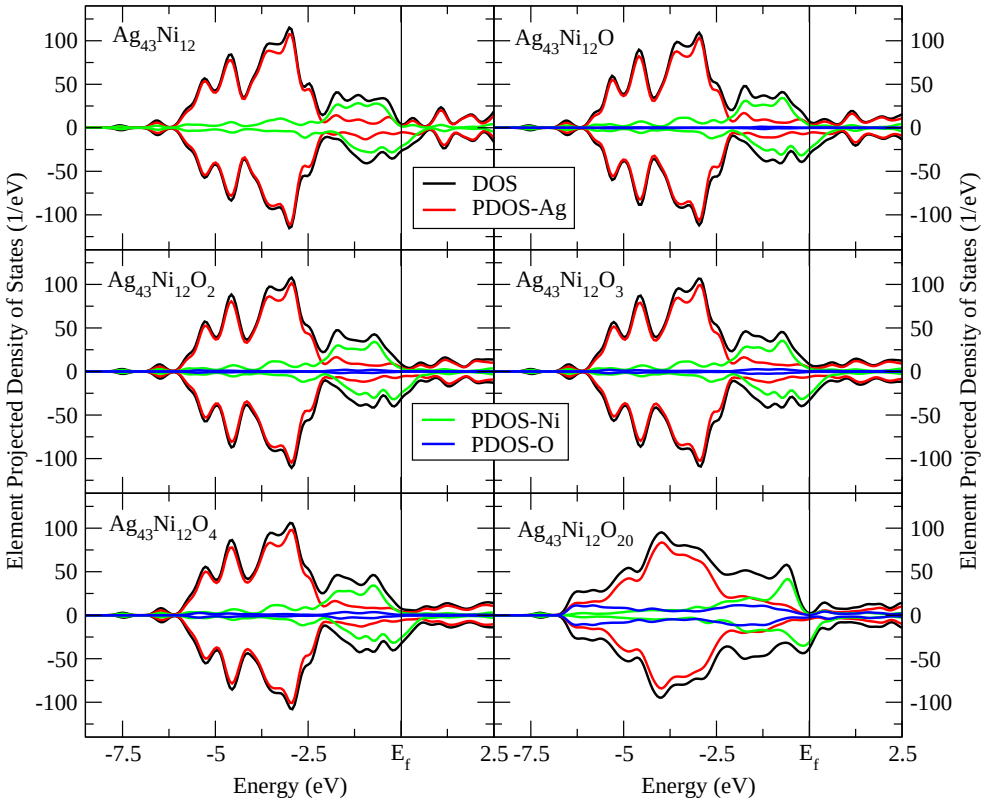

Figura 3.40: Total DOS (black line), partial contribution of silver (red line), nickel atoms (green line) and oxigen atoms (blue line) of $Ag_{42}Ni_{13}O_m$ cluster with $m = 0 - 4$ and 20. The vertical line marks the Fermi energy.

3.6 conclusions and perspectives

The minimum energy structure of nickel oxide clusters, $Ni_nO_m^{\pm/0}$ (n = 3-8; m = 1-9), is obtained in this section by testing a large number of plausible geometries and optimizing the several candidates by means of DFT calculations. These initial geometries were constructed i) as planar and three dimensional arrangements of NiO units, and ii) as small pure nickel clusters covered with consecutive oxygen atoms. For the n=$m \leq 5$ cases the ground state is formed by planar ring structures, with alternating Ni and O atoms, independently of the charge state, which agrees with recent ion mobility experiments. For larger sizes the ground state structures show three dimensional (3D) structures with pyramidal, hexahedral, and octahedral-like geometry, respectively, as the cluster size increases. These 3D structures are composed of a nickel subcluster core covered by oxygen at three fold hollow sites (at low oxygen coverage) or bridge sites (at high oxygen coverage).

We studied the trend of the binding energy and the second total energy difference of $Ni_nO_m^{\pm/0}$ clusters as a function of the number m of oxygen atoms, resulting in many cases that the clusters with $n = m$ or $n = m + 1$ are more stable than those with $m > n$, which is in agrement with recent time of flight mass spectrometry experimental results for nickel oxide cluster cations. We used our total energy calculations in order to rationalize the patterns in the photo-fragments observed in the mentioned experiments after multiple photon dissociation of mass selected clusters, namely that the loss of O_2 is the preferential dissociation channel, and that Ni_2O^+ fragment is a product of the dissociation series of most parent ions. Thus, we are able to explain how most of the observed n.m photo-fragments are produced on the basis of simple final state energy considerations, the few exceptions being due to plausible high energy barriers.

We also investigated the magnetic properties of $Ni_nO_m^{\pm/0}$ clusters as a function of the oxygen content. The total spin magnetic moment exhibits a drop close to the equiatomic concentration ($n = m$), reflecting the reentrance of planar or quasiplanar structures whose magnetic arrangement is characterized in general by the maximum number of antiparallel couplings among all compositions. As a general trend, antiparallel couplings are found, in more or less degree depending on the composition, size and charge state. However, we have identified certain niquel oxide clusters, like $Ni_6O_5^+$, Ni_7O_6 and Ni_8O_6, with a considerably large total moment (11 or 12μ_B) as

well as with a high relative stability, an interesting result in the context of magnetic grains design. The large moment of these magnetic grains is due to the promotion of parallel magnetic couplings, despite their significative oxidation rate, an unavoidable fact in environmental conditions.

As far as a well established manner to experimentally discriminate cluster isomers which present differences in their atomic structure is the inspection of their infrared vibrational spectra, we have calculated the vibrational spectra of certain clusters that resulted nearly degenerate in our calculations, namely Ni_6O_6 and $Ni_6O_6^+$ isomers with different geometries and spin multiplicities. We hope that this information may help to elucidate the true ground state by means of infrared multiple photon dissociation measurements.

In this chapter we also, we investigated, the energetic stability, chemical order, electronic structure, and magnetic properties, of Ag_xNi_y nanoalloys of 13 and 55 atoms with icosahedral shape. We also studied the effects of an electron deficit or excess.

Ni atoms tend to occupy the internal positions, building up a Ni subcluster, and developing segregated atomic configurations among which core/shell structures are particularly stable, in qualitative agreement with the experimental findings and calculations of smaller AgNi nanoalloys. Although binding energies demonstrate that these nanoalloys are thermodynamically stable independently of the composition, the excess energy indicates that only the formation of $Ag_{54}Ni$, $Ag_{48}Ni_7$ and $Ag_{42}Ni_{13}$ is favourable with respect to an ideal mixing of Ag_{55} and Ni_{55}. Among those, Ag_{54}Ni and $Ag_{42}Ni_{13}$ are perfect core/shell configurations. $Ag_{26}Ni_{29}$ and $Ag_{23}Ni_{32}$ also exhibit marked minima of the excess energy. Those five stoichiometries also correspond to maxima of the second energy difference, so that they can be considered as magic compositions of the nanoalloy.

The magnetic phase diagram of these nanoalloys is complex. Contrary to what one would expect, the total moment of the nanoalloy in the high Ag concentration limit tends to decrease as increasing Ni concentration up to $Ag_{50}Ni_5$, due to the quenching of the Ni moment associated to the charge transfer from the outer 42 Ag atoms to the inner 13 ones. Beyond this Ni concentration, the total moment linearly increases as increasing Ni content up to $Ag_{18}Ni_{37}$, where a sudden drop of $9\mu_B$ takes

place, to continue the linear increase with the same slope till the pure Ni limit. This linear increase is associated to the formation of a sizable Ni subcluster with non quenched spin polarization and parallel magnetic couplings, being the contribution of the outer Ag atoms to the total moment of the nanoalloy negligible now. Therefore, the formation of a sizable Ni subcluster allows it to preserve its magnetic identity to a large extent when covered or interfaced by Ag, providing the nanoparticle with a magnetic moment localized in the core. The projected densities of states show that the HOMO rapidly acquires Ni character as increasing the Ni content. The clear Ni character of the HOMO for most stoichiometries indicates that, although the $Ag - Ni$ interaction is weak and Ag provides a physical protection to the Ni core, Ni states should play an important role in the reactivity of these nanoalloys, as they indeed do in processes like ionization. The HOMO of the neutral cluster is of minority spin which explains why upon ionization the magnetic moment increases $1\mu_B$. The opposite happens upon an electron capture. Finally, many of the above magnetic trends have not an analog in the smaller nanoalloy of 13 atoms with the same icosahedral shape, a manifestation of the richness of behaviors at the nanoscale.

Using silver as a protective cover for the nickel cluster magnetic moment has shown very promising results. When the $Ag_{42}Ni_{13}$ cluster is oxidized, the total magnetic moment of the system is conserved, presenting an increase in the local magnetic moment of the nickel atoms, and antiferromagnetic couplings in the cluster surface. When the clusters are super oxidized, the shell is penetrated by the oxygen atoms, decreasing the total magnetic moment of the cluster. In spite of this, the magnetic moment of the core is greater than the total of the system (due to antiferromagnetic couplings on the surface).

Chapter 4

Small iron oxide clusters.

La ciencia y el amor son iguales. Ambos son una suma de errores que conducen a la verdad.
Luis Eduardo Aute.

The aim of the present section is to characterize the fundamental properties of small Fe oxide clusters, paying special interest on their magnetic properties. To determine the reliability of our results, we made an exhaustive comparison with the photodissociation measurements of Molek *et al.* (109) for cationic clusters. We study a great variety of oxidation rates, from the absorption of a single oxygen atom, to the saturation limit. As a function of the oxidation rate, we have analyzed various geometrical, electronic and magnetic properties, obtaining interesting trends never reported before for the magnetic properties. We explore the isometric map from both the structural and spin configurations, in order to be sure that we obtain the fundamental geometric and magnetic moment ground states. We also present an exhaustive study of the magnetic moment of the series Fe_4O_m, finding a resurgence in the magnetic moment for high oxidation rates. We also present a spin map for the Fe_6O_8 cluster, besides an analysis of the density of states for several interesting cases.

4.1 Geometrical configurations and electronic properties

In this subsection we present the geometrical, electronic and stability properties, as well as fragmentation paths of the $Fe_nO_m^{0/\pm}$ (n =1-7 and m =1-16) clusters (Fig. 4.1-4.5). In Fig. 4.6 we show Fe-Fe and Fe-O average distances. For stability analysis, we graph the binding energy per atom (Eqs. 2.53 and 2.54, with $A = Fe$) and the second energy difference (Eq. 2.50), these magnitudes are shown in Fig. 4.7 and 4.8.

The binding energy increases in general to a maximal value, beyond which a smooth decrease is observed (except for Fe_3O_m, where two maxima are presented), this behavior is obtained regardless the state of charge, coinciding the maximum value for the neutral and charged clusters. The biggest peaks in the second energy difference coincide with the maximum binding energy per atom (others peaks are also observed). For odd number of iron atoms, the oxygen atoms bond in bridge and hollow position, whilst for even number of iron atoms, they are bonded only in bridge positions.

4.1.1 ${Fe_3O_m}^{0/\pm}, m = 1 - 9.$

The preferred position of the oxygen in this series (see Fig. 4.1) are the bridge sites. As long as we have a bridge available the oxygen tends to occupy it, with the only exception of Fe_3O_2, where we have oxygens in bridge and face. The next position to fill are the top, but when there are no top available, the oxygen locates in face position.

The binding energy per particle (see Fig. 4.5) presents a maximal value at m =6. In this cluster all the top and bridges have been occupied by oxygen, and after m =6 the energy decreases. When we add an oxygen atom to the cluster 3.5-I, a reconstruction is observed, from having a sub-cluster of iron to a structure build by FeO bonds, the energy difference between this reconstructed cluster (Fig. 4.1) and the 3.5-I adding an oxygen on top, is 0.23 eV/atom, which give us an idea of why the reconstruction is observed.

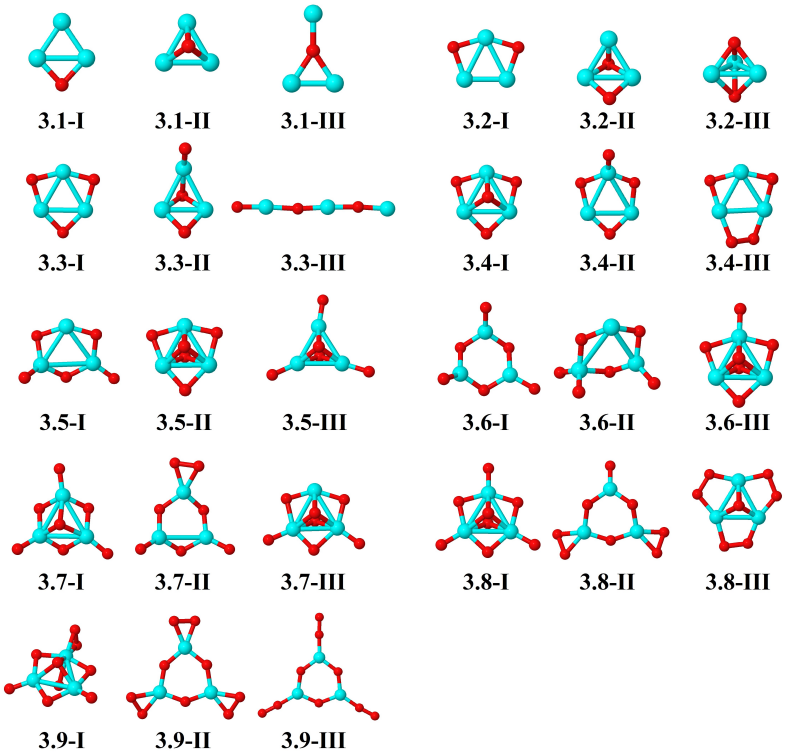

Figura 4.1: Putative ground state of Fe_3O_m clusters.

Due to the reconstruction of the cluster 3.4-I to 3.5-I, both faces of the clusters became available, and at these sites the oxygen atoms are bonded in the next clusters (3.7-I and 3.8-I), after this, there are no available sites to place the oxygens without a molecular absorption which is what happens in 3.9-I. The Fe-Fe distances increase almost monotonously to a maximum in Fe_3O_6, and beyond that decreases. The Fe-O average distance oscillates between 1.92 and 1.75 Å, having its minimum value where the average Fe-Fe distances have its maximum value (Fe_3O_6 cluster).

4.1.2 $Fe_4O_m{}^{0/\pm}, m = 1 - 14.$

All the ground states of this series have a Fe tetrahedral-like sub-clusters, except Fe_4O_4 which is has a ring-like planar structure (see Fig. 4.2). Most of the clusters of this series have the same structures as the neutral clusters regard-

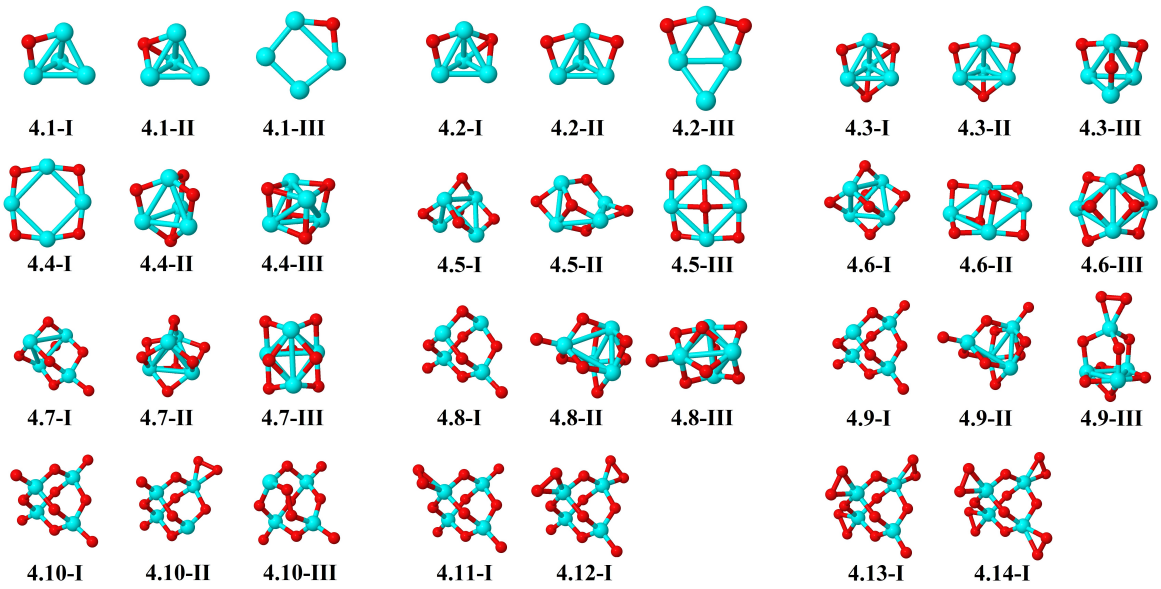

Figura 4.2: Putative ground state of Fe_4O_m clusters.

less of the state of charge, except for the smallest clusters ($Fe_4O^{\pm}$, $Fe_4O_2^{-}$, $Fe_4O_3^{-}$). As in the previous series, the more likely position for the oxygen atoms is in bridge, the absorbtion trend of the oxygen atoms is in bridge position if available (except for 4.2-I and 4.3-I), when all the bridge position are occupied, the oxygen atoms becomes to bonded in top position. No molecular absorbtion has been observed in the ground states until Fe_4O_{11}. The binding energy per particle increases up to Fe_4O_6 (see Fig. 4.8), regardless of the state of charge, and after that, decreases. The most stable clusters of this series are Fe_4O_4, Fe_4O_6 and Fe_4O_{10} where a maximum value in the second energy difference are observed regardless of the state of charge (see Fig. 4.7), except for $Fe_4O_{10}^{-}$.

The average Fe-Fe and Fe-O distances show an interesting behavior, the Fe-Fe distances increase up to Fe_4O_4, with a big step between Fe_4O_3 and Fe_4O_4 (associated with a structural transition), beyond that, the Fe-Fe average

distances decrease up to 4.6-I, where all possible bridge position have been occupied (this clusters show the highest peak of stability in the second energy difference, Fig. 4.8, and the largest value for the binding energy per atom, Fig. 4.7). When no more bridge position are available, the oxygen atoms start to bond in top position (4.7-I), increasing the Fe-Fe average distances till all Fe-Fe bonds were broken (4.9-I and 4.10-I), and the interaction in the clusters becomes through Fe-O bonds. The structures from 4.7-I to 4.10-I, have and zincblenda like structures mainly due to the presence of Fe-O bonds.

4.1.3 $Fe_5{O_m}^{0/\pm}, m = 1 - 15.$

In this series (as present in Fig. 4.3), we have mainly two families of clusters, the hexahedron-like and square pyramid-like approximately appearing in the same amount, we observe some degree of deformation depending on the oxygen contain. If there are available bridge position, the oxygen atoms trend to bond in them, as in the previous series, the exception are 5.3-I, 5.4-I and 5.7-I, where two oxygen are bonded in hollow position. All the structures are three dimensional, the only exception is 5.5-II which has a ring-like planar structure. The inter atomic Fe-Fe distances increase as function of the number of oxygen atoms, up to 5.9-I, after that, the Fe-Fe bonds start to breaking. For 5.10-I, 5.11-I and 5.12-I clusters, we observe that the Fe atoms begin to separate each others. The Fe-O average interatomic distance oscillate between 1.77 and 1.92 Å. The energy per atom, increase up to 5.7-I, after that, decrease monotonously, regardless of the state of charge (as illustrated in Fig. 4.5). For the second energy difference several maximal values are observed at 5.4-I, 5.7-I and 5.11-I, each one of these maxima are in a different magnetic zone (see Fig. 4.9).

4.1.4 $Fe_6{O_m}^{0/\pm}, m = 1 - 16.$

Unlikely the past series, where the absorbtion of the oxygen atoms is through bridges positions, for this series (see Fig. 4.4), the hollow positions are observed up to 6.8-I cluster, beyond this size are bridge and top position the favorable

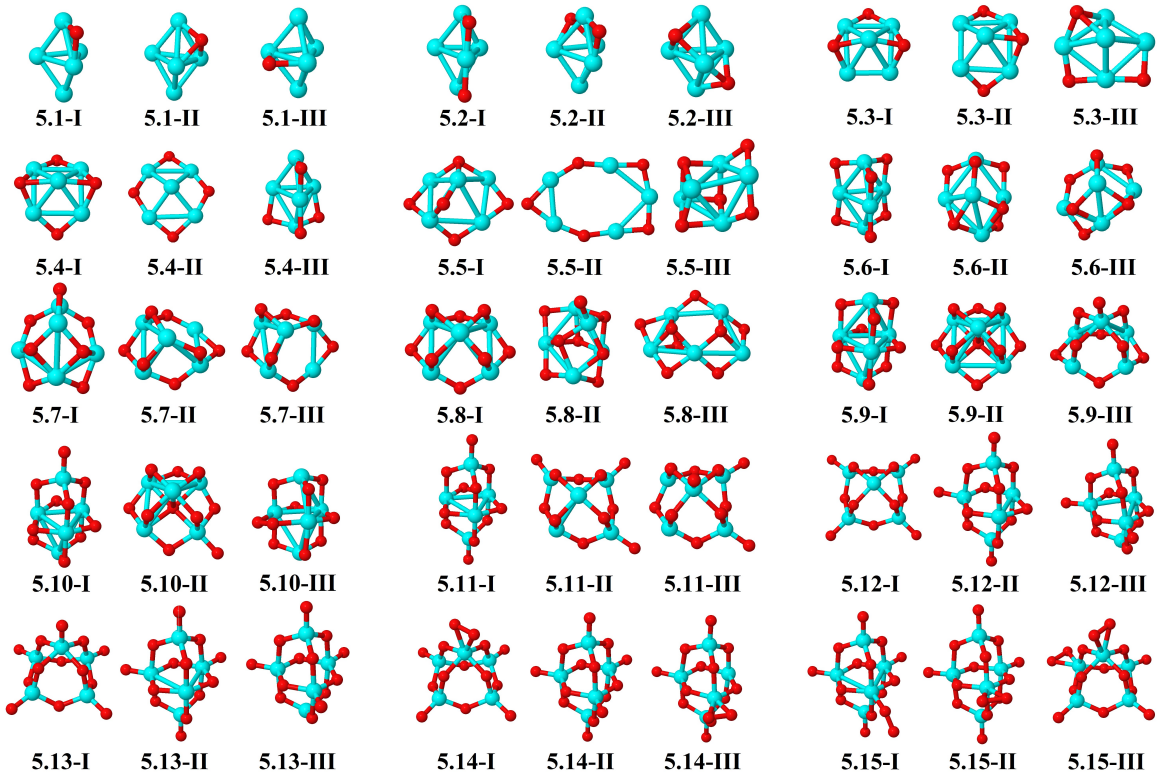

Figura 4.3: Putative ground state of Fe_5O_m clusters.

ones.

Two different structural families are obtained in this series, the octahedral one (6.1-I to 6.8-I), and open triangular prism (6.9-I to 6.15-I). The average Fe-O inter atomic distance for the octahedral family are bigger than the corresponding to the triangular prism (See Fig. 4.4), whilst the Fe-Fe average distance increase with the number of oxygen atoms up to 6.8-I, after that, no Fe-Fe bonds are observed (except for 6.10-I, where only two Fe atoms are bonded). Worth notice is that for super rich oxygen clusters, the oxygen atoms that surround the Fe atoms show local tetrahedral symmetry, remind a diamond-like structure or the zincblenda-like. The binding energy per atom increase as function of the oxygen atoms up to 6.9-I, after that, decrease monotously, regardless the state of charge (See Fig. 4.7). The figure of second energy dif-

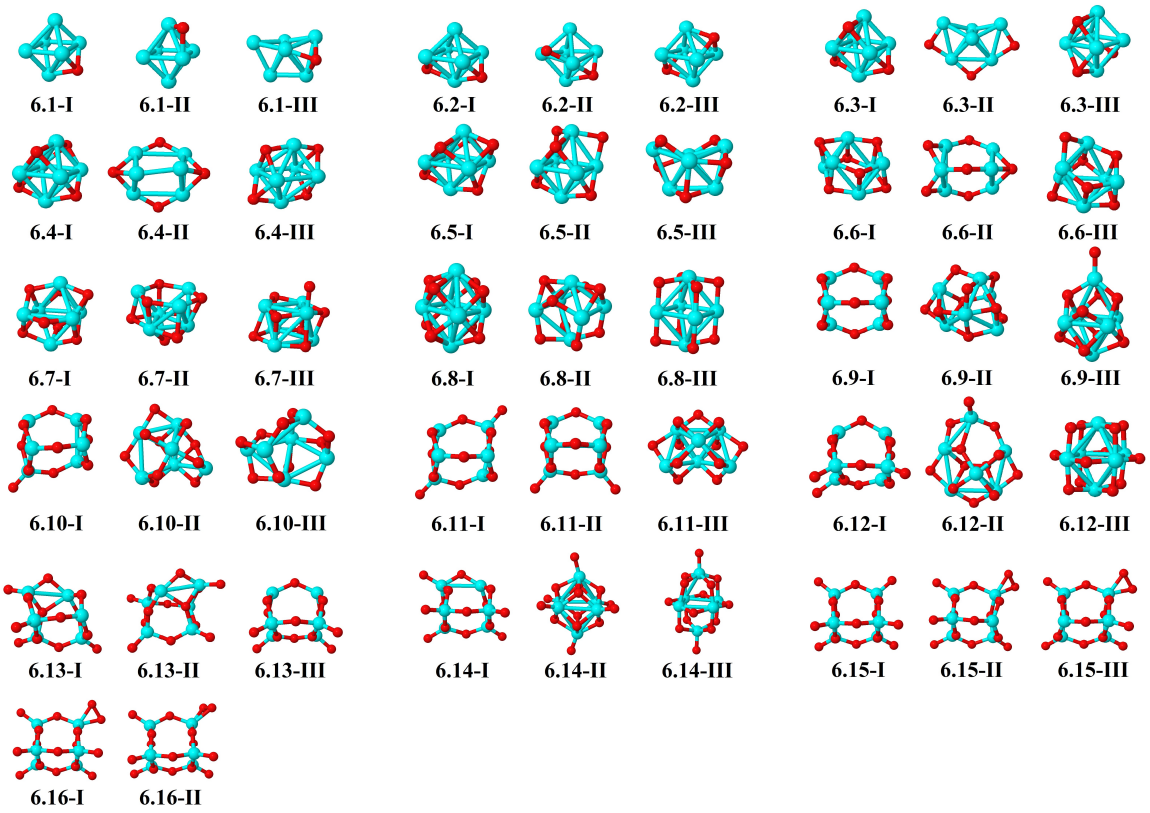

Figura 4.4: Putative ground state of Fe_6O_m clusters.

ference (See Fig. 4.8), have the biggest peak at 6.9-I, this is the first structure where all the Fe-Fe bonds are broken. Other maxima is observed at 6.4-I, with a octahedral Fe sub-cluster, a overall tetrahedral symmetry is observed in the whole cluster.

4.1.5 $Fe_7O_m{}^{0/\pm}, m = 1 - 15.$

As in the Fe_6O_m series, the oxygen atoms prefers hollow position for absorbtion up to Fe_7O_9 (See Fig. 4.5), after this cluster, the most favourable positions are bridges, and finally when there are not available bridges, the oxygens atoms become to absorbed on top positions. The most abundant geometry in this series is the decahedral one from Fe_7O to Fe_7O_8 (except Fe_7O_3). As in previous series, me average Fe-Fe inter atomic distance increase up to Fe_7O_{12}, after

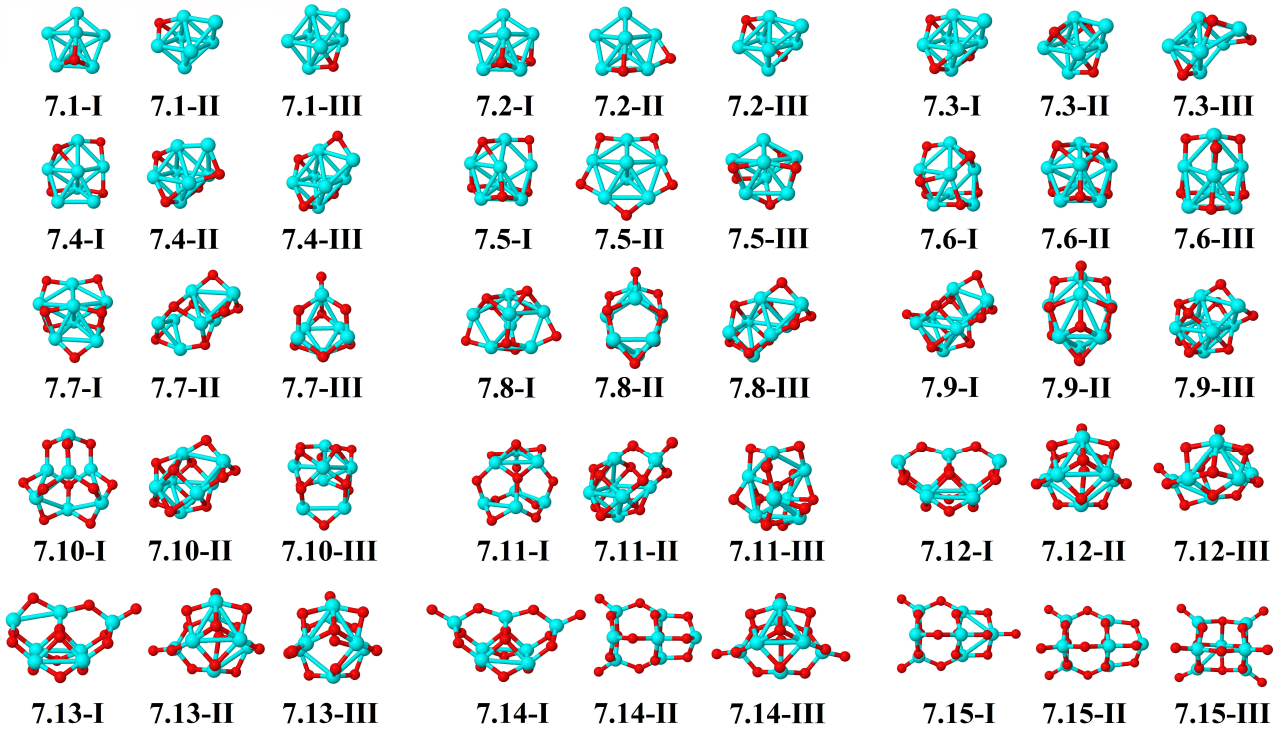

Figura 4.5: Putative ground state of Fe_7O_m clusters.

that, no Fe-Fe bonds are observed (See Fig. 4.5). The binding energy (see Fig. 4.6) increase up to Fe_7O_{10}, after that, decrease slowly. The most stable clusters according to the second energy difference (see Fig. 4.8) are the clusters Fe_7O_3, Fe_7O_5, Fe_7O_7 and Fe_7O_{10}.

4.2 Magnetic properties

The magnetic moment behavior of the clusters present two different phases depending on the oxygen concentration as illustrated in Fig. 4.9 for all the families of clusters. The first one (low oxygen concentration) is a high magnetic phase, where the high magnetic moment comes from high local magnetic moment of the iron atoms, and parallel couplings. The second one (oxygen saturation), is a low magnetic phase, where the low magnetic moment comes from antiparallel couplings.

The magnetic moment of the Fe_nO_m clusters are ferromagnetic from $m = 1$ to $m = n - 1$, regardless of the state of charge (exception is observed for Fe_7O_m, where the change is at $m = 5$). From $m = n$ the clusters become antiferromagnetic, however for Fe_4O_m and Fe_5O_m, we observed two additional phases, the third one consists of a resurgence of the magnetic moment in $m = n+5$, in the third phase the high magnetic moment of the clusters comes from low local magnetic moment of the iron atoms, now coupling ferromagnetically. Finally, in the fourth phase an antiferromagnetic behavior is observed again.

Now, we will discus the magnetic behavior of the $Fe_4O_m^{0/\pm}$ series in more detail. In Fig. 4.10 are observed four phases in the magnetic moment for the series $Fe_4O_m^{0/\pm}$. For $m = 1 - 3$ the magnetic moment of the system is ferromagnetic, for $m = 4 - 8$ the clusters are antiferromagnetic (for $Fe_4O_m^0$ this zone is $m = 4 - 7$). From Fe_4O_9 to Fe_4O_{11} the clusters are ferromagnetic again, and finally, after this, we have another antiferromagnetic zone. To be sure of the fundamental state of the magnetic moment in Fig. 4.10 we took the ground state structure for each stochiometry, and we calculated from these structures (only for the Fe_4O_m neutral clusters), all possible values of the magnetic moment, and determined the energy difference with respect to the ground state magnetic moment. For a low oxygen concentration, the ground state has clearly a high magnetic moment, and as the number of oxygen atoms increases, the energy difference between the high and low magnetic spin isomers is becoming smaller. From Fe_4O_4 up to Fe_4O_8, the ground state has a low magnetic moment, due to antiferromagnetic couplings (See Fig. 4.12). The

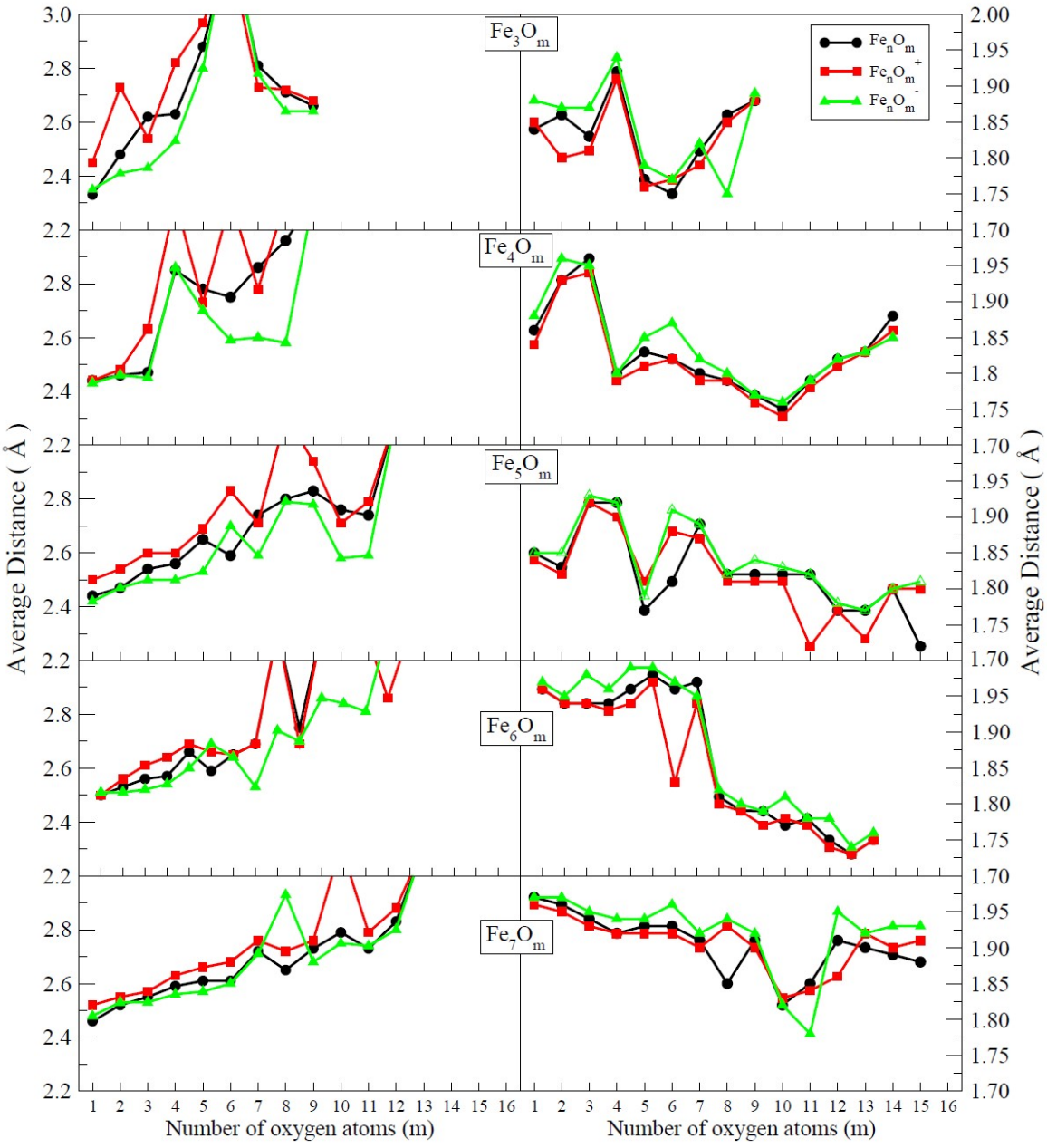

Figura 4.6: Fe-Fe (left panels) and $Fe-O$ (right panels) average distance for $Fe_nO_m^{0/\pm}$ clusters as a function of the number of oxygen atoms (m).

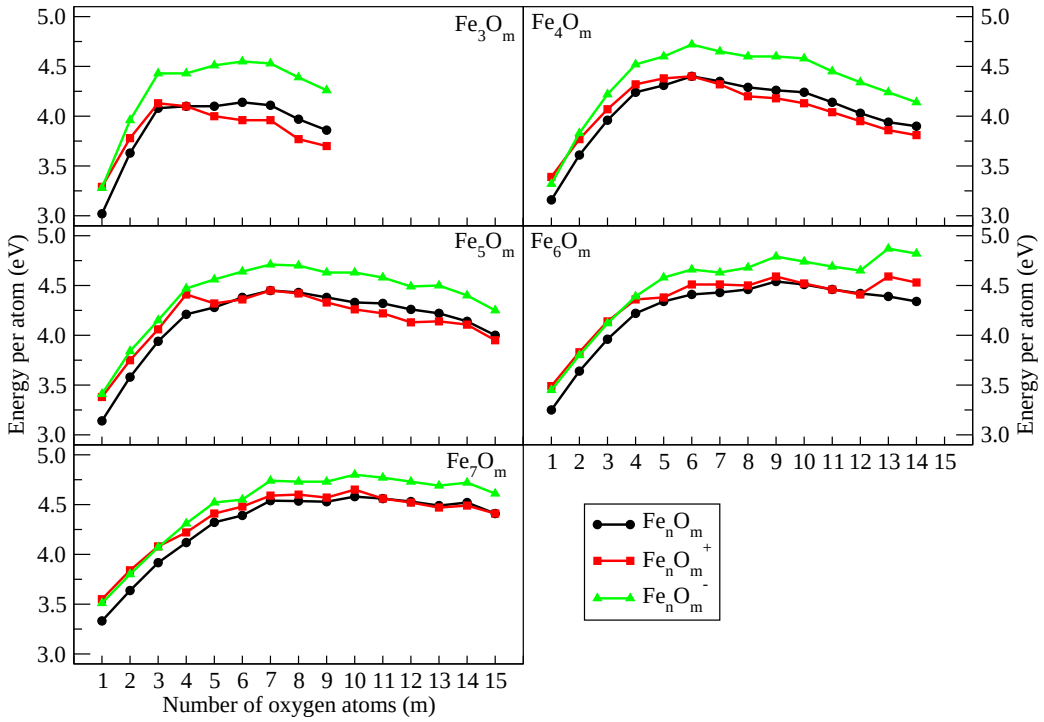

Figura 4.7: Binding energy per atom of $[Fe_nO_m]$ with n = 3-7 and m = 1-15.

third magnetic phase observed at the super oxygen saturated region is located from Fe_4O_9 to Fe_4O_{11}, the magnetic moment increase again in agreement with the reentrance of the magnetic moment previously discussed in Fig. 4.10.

Another way in which we built the initial structures was through the Fukui functions. For example, we calculated the Fukui function for the ground state of Fe_4O, and where the Fukui function is maximum (or the sum of these), we place the next oxygen atom in this position. We repeat this process for all other clusters. In general, this way of building the clusters is very effective, since when we calculate the Fukui function for Fe_nO_m and determine the place where the sum of the Fukui function is maximum, the ground state of the Fe_nO_{m+1} cluster, is the structure that was built in this way. In Fig. 4.11, we can see the Fukui function for the Fe_4O_m series. We notice that it is possible build the ground state structure Fe_4O_{m+1} from the Fukui function

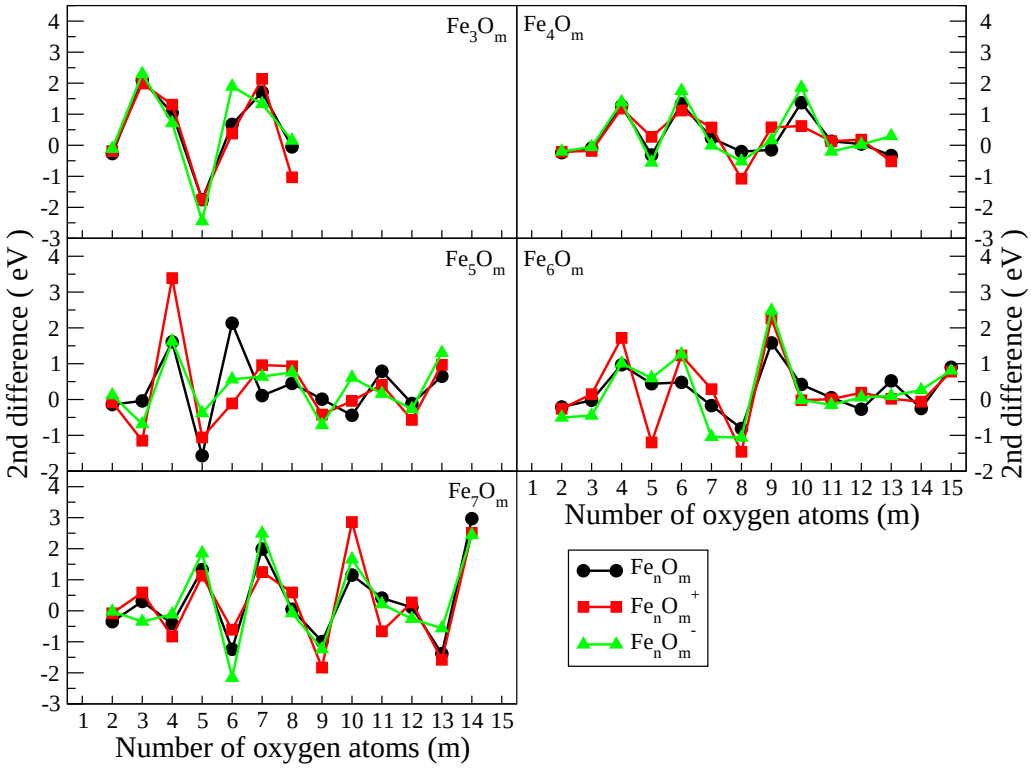

Figura 4.8: Second energy difference of $[Fe_nO_m]$ with n = 3-7 and m = 1-15.

except for Fe_4O_4 and Fe_4O_5, the construction of the geometry of the ground states is following this process by means of the Fukui function of the previous cluster.

Analyzing the local magnetic moment of this series (Fig. 4.12) we see that in the first phase the magnetic couplings are parallel (Fe_4O to Fe_4O_3), and the high total magnetic moment of the clusters is due to the high local magnetic moment of the atoms. In the second phase (Fe_4O_4 to Fe_4O_8) the low magnetic moment is due to high local magnetic moment but with antiferromagnetic couplings. These antiferromagnetic clusters are characterized due to the fact that the clusters can be sub-divided into two parts, one of the parts with spin up and the other with spin down, the oxygen that are between these two sub-parts have zero or almost zero magnetic moment. In the third phase (Fe_4O_9 to Fe_4O_{11}) the high magnetic moment comes from parallel couplings, but low

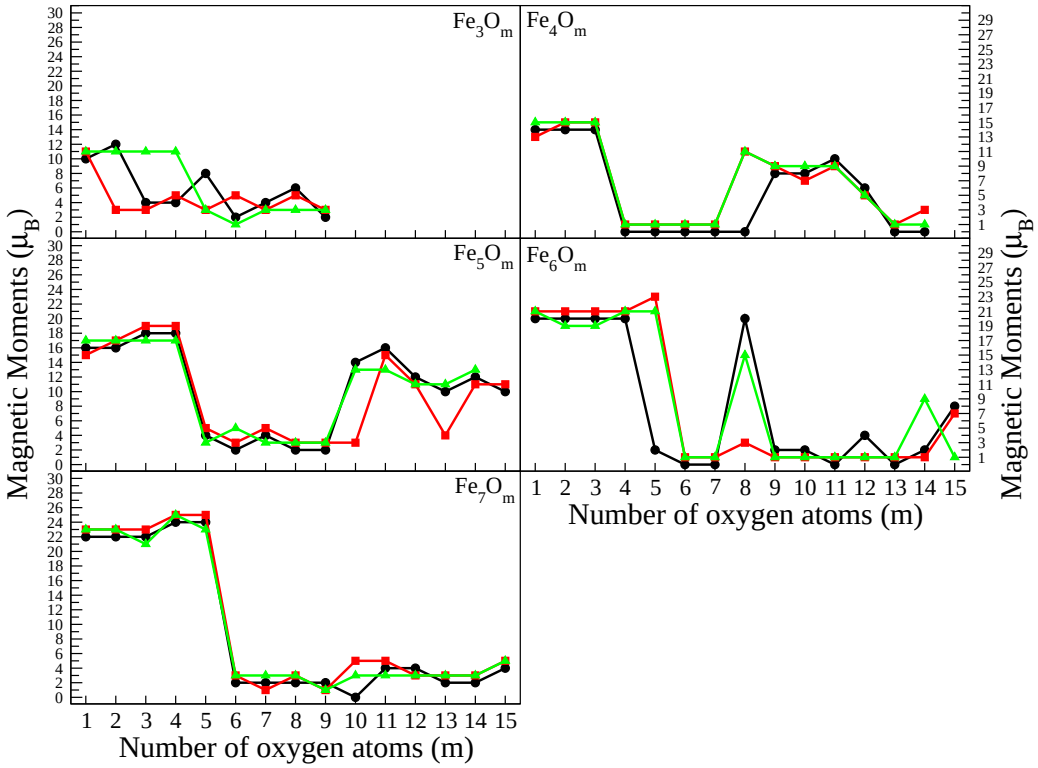

Figura 4.9: Magnetic moment of $[Fe_nO_m]$ with n = 3-7 and m = 1-15.

local magnetic moment are presented (low spin polarization region).

Comparing the local magnetic moment of the iron atoms in the first phase, where the values are between $3.2\mu_B$ and $3.4\mu_B$, in the third phase the local magnetic moments of iron atoms are between $1.3\mu_B$ and $3.1\mu_B$, the iron atoms that are coordinated with three oxygen atoms have a magnetic moment of $\sim 3\mu_B$ and those that are coordinated with four oxygen atoms have $\sim 1.3\mu_B$. In the fourth phase (Fe_4O_{12} to Fe_4O_{14}) we have similar behavior for the couplings as in the second one, two antiferromagnetic sub-clusters can be identified, with magnetic moments in opposite directions, and the oxygen atoms in between these sub-clusters with zero or almost zero magnetic moment (magnetically frustrated). The contribution of iron to the total magnetic moment of the cluster decreases with the addition of oxygen. As the number of oxygen increases the iron-iron bonds weakens, this is observed in the average iron-iron

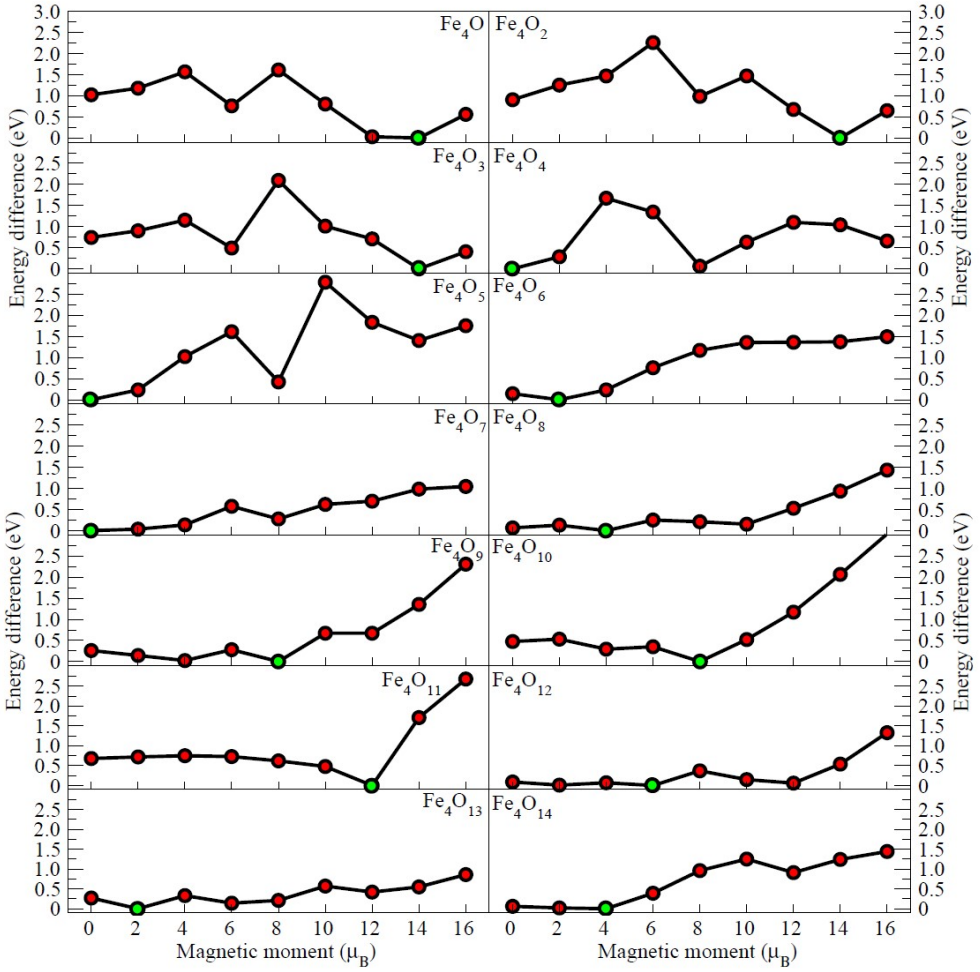

Figura 4.10: Energy difference between the spin isomers and possible to the ground state solution (green circle) as a function of the total magnetic moment for all the Fe_4O_m with m =1-14. Each frame corresponds to a fix oxygen composition.

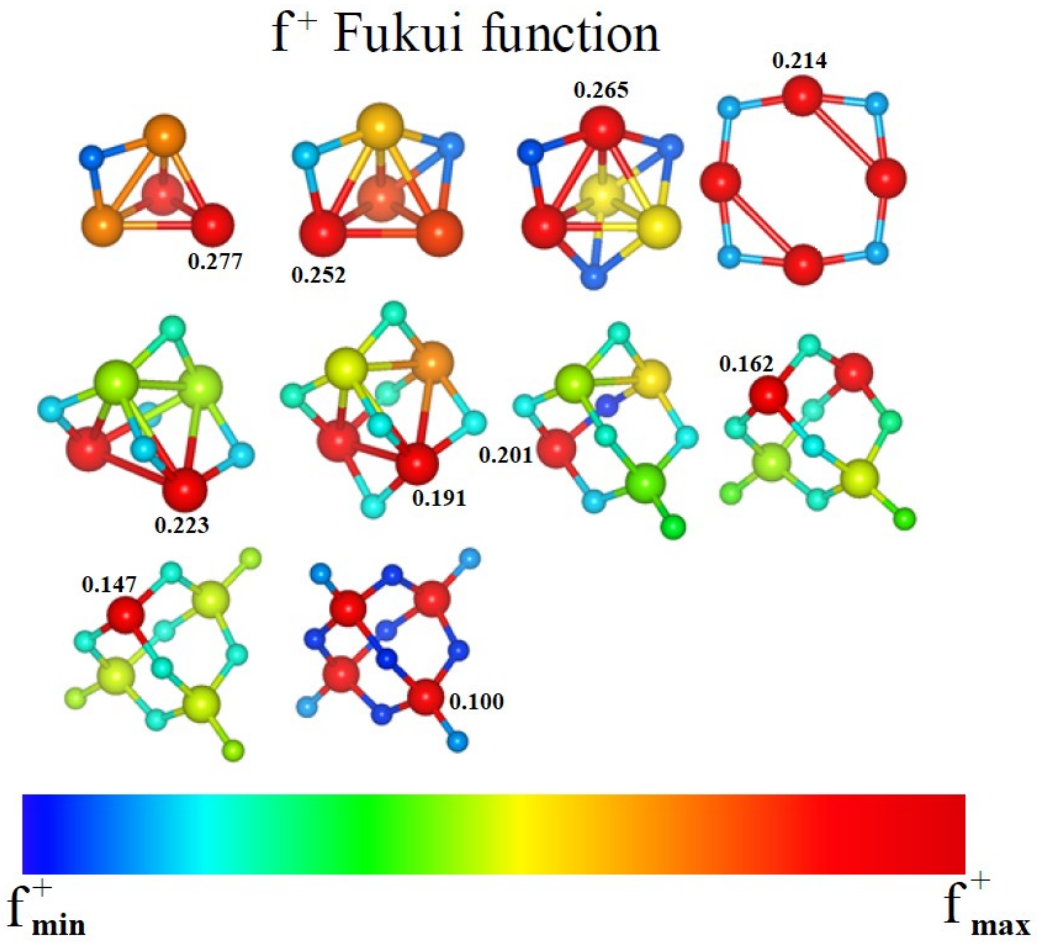

Figura 4.11: Elctrophilic Fukui function f^+ for a representative sample of Fe_4O_m clusters. Small spheres represent O atoms, large spheres represent Fe atoms. Red spheres correspond to the maximum and blue spheres for minimun value of the Fukui function f^+. The maximun value of f^+ is explicitly annoted next to the corresponding atom.

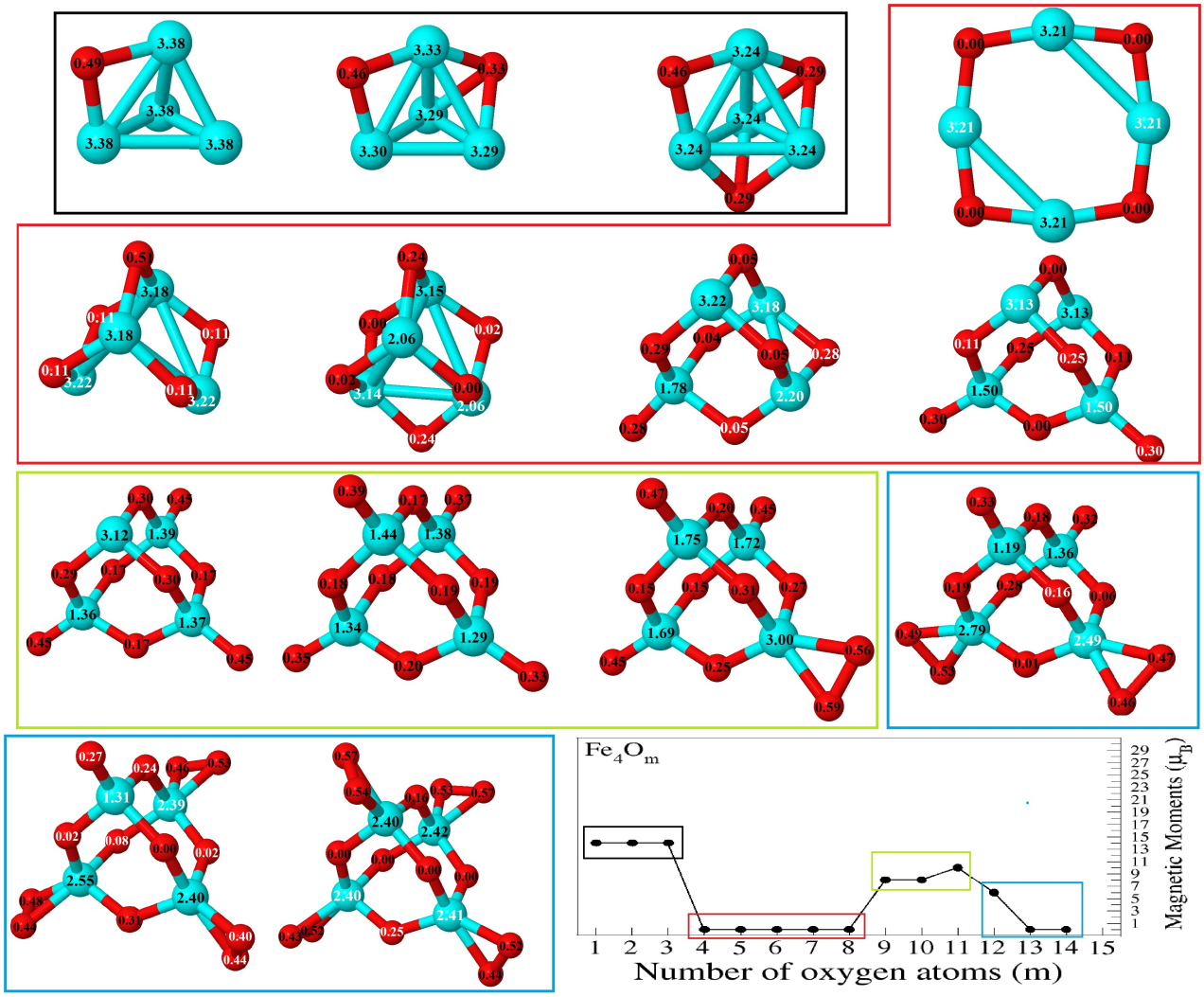

Figura 4.12: Local magnetic moment of Fe_4O_m clusters. Numbers in black (white) indicate spin up (spin down).

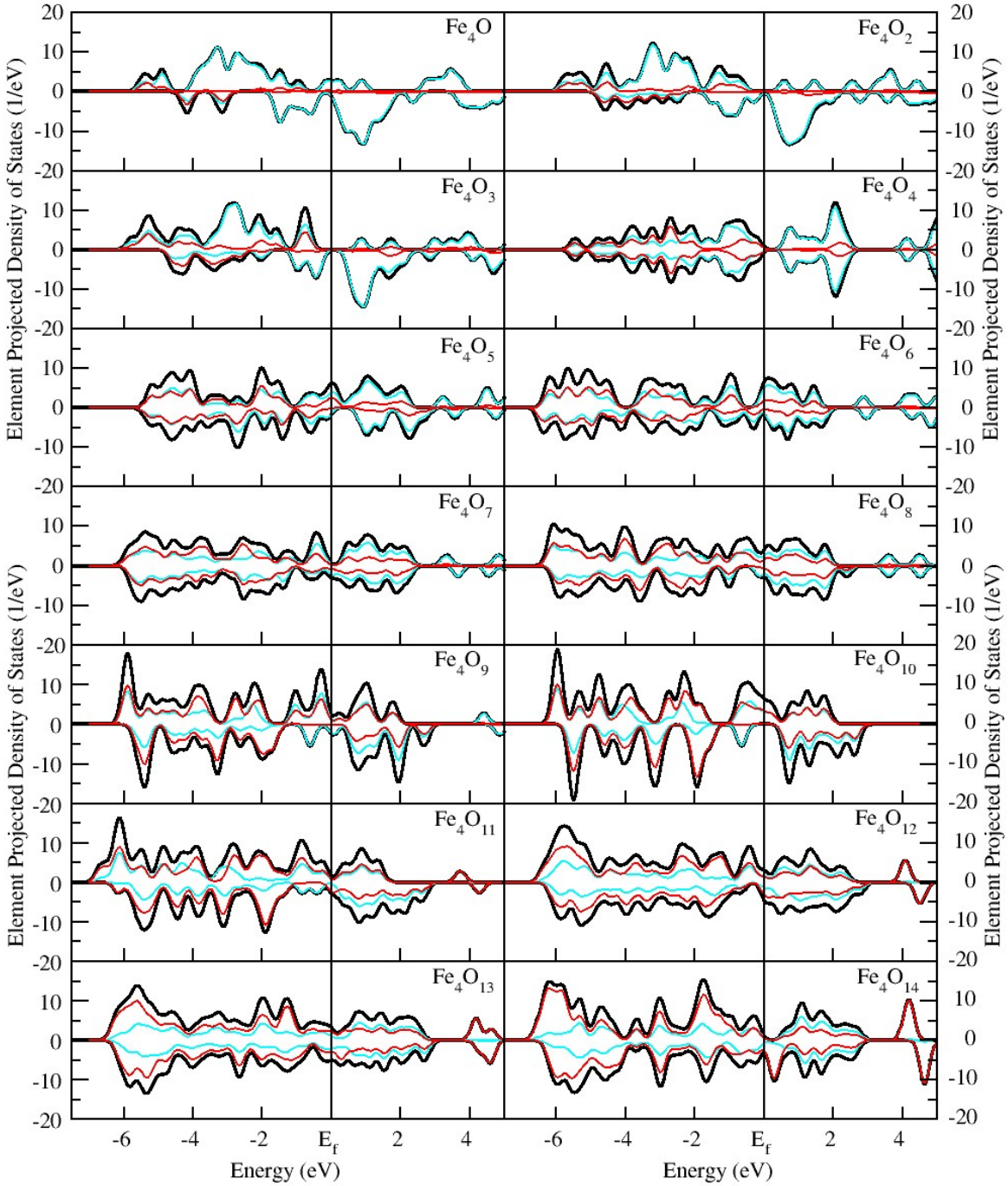

Figura 4.13: Total DOS (black line), partial contribution of iron (cian line) and oxygen atoms (red line) of Fe_4O_m cluster. The vertical line marks the Fermi energy.

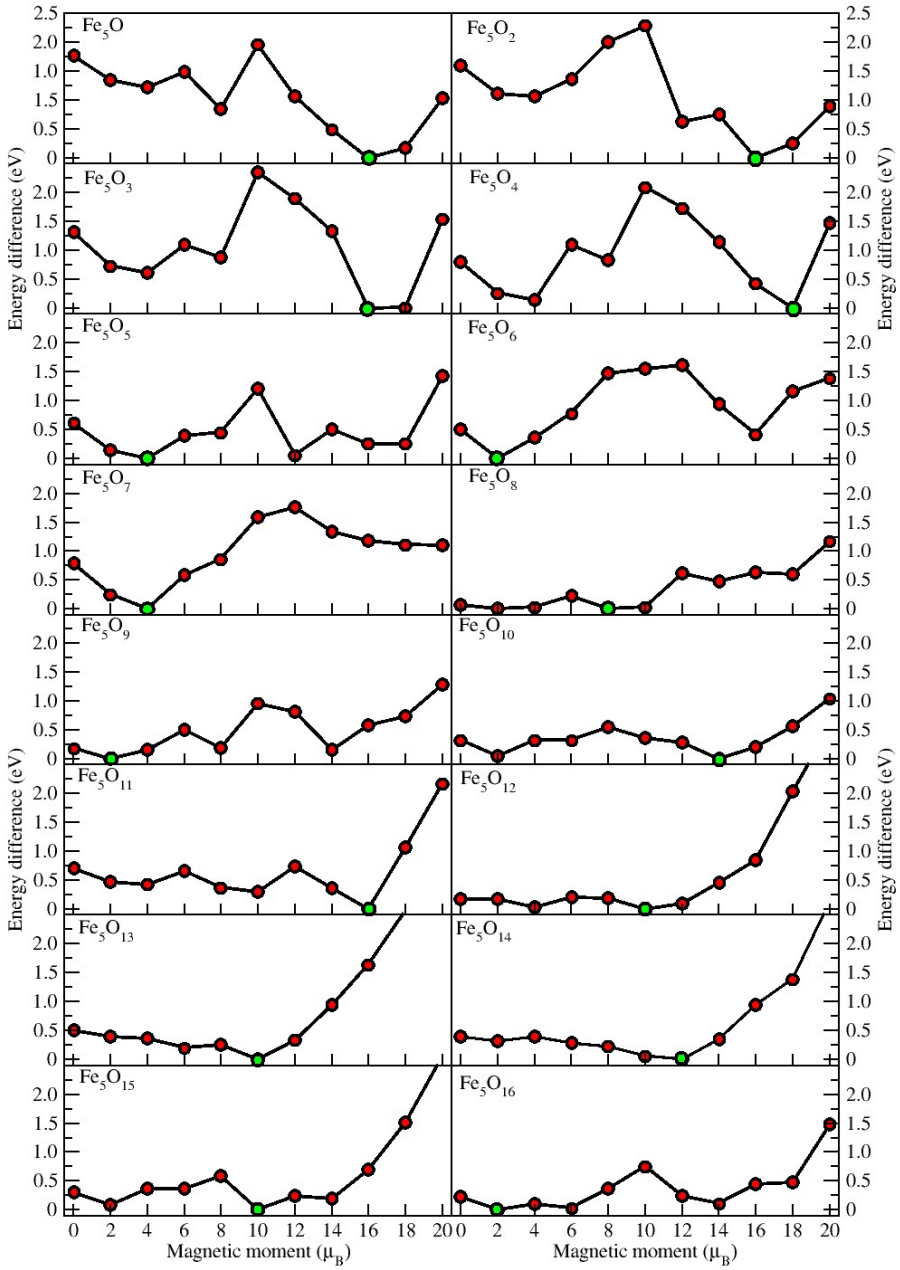

Figura 4.14: Energy difference between the spin isomers and possible to the ground state solution (green circle) as a function of the total magnetic moment for all the Fe_5O_m with m =1-16. Each frame corresponds to a fix oxygen composition.

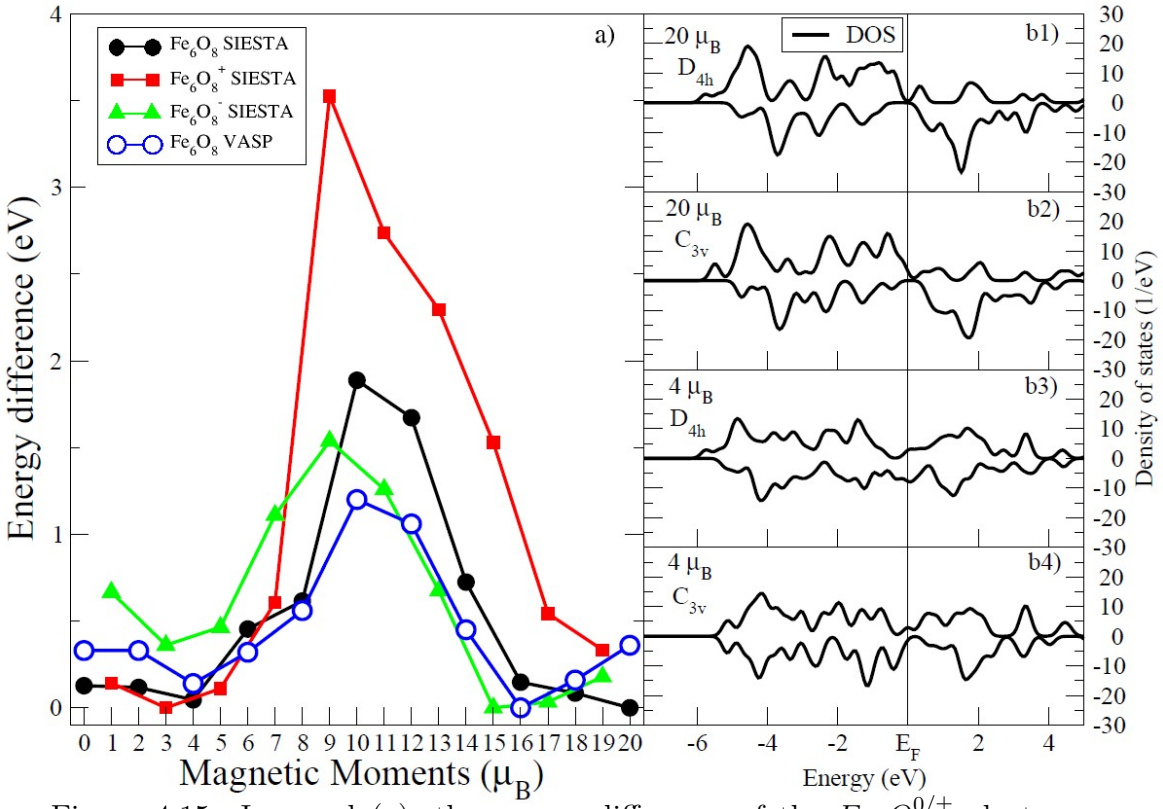

Figura 4.15: In panel (a), the energy difference of the $Fe_8O_6^{0/\pm}$ clusters as function of the magnetic moment is show. In panes (b1) to (b4), are shown the density of states for the cluster Fe_6O_8 with magnetic moment of $20\mu_B$ (with symmetries D_{4h} and C_{3v}, Fig. 4.15 (b1) and (b2) respectively), and $4\mu_B$ (with symmetries D_{4h} and C_{3v}, Fig. 4.15 (b3) and (b4) respectively)

interatomic distances, which increases from 2.44$\mathring{A}$ for Fe_4O to 2.75$\mathring{A}$ in Fe_4O_7 (see Fig. 4.6), after which the iron-iron bonds disappear and clusters are totally formed by Fe-O bonds. The magnetic behavior of the Fe_4O_m series is reflected in the density of states (see Fig. 4.13).

This behavior of the resurgence of the magnetic moment is only observed for the Fe_4O_m and Fe_5O_m (Fig. 4.14) and in a less degree for Fe_6O_m (only for $Fe_6O_8^{0/-}$ clusters). To clarify the behavior in the particular case of the Fe_6O_m cluster, we performed additional calculations in the spin sweep. In Fig. 4.15a) we have the graphic of the magnetic moment of the $Fe_6O_{8^{0/\pm}}$ clusters,

where we notice that the neutral and anion have a high magnetic moment solution, whereas the cation has low magnetic moment (due to antiferromagnetic couplings). Although the structure of the systems are similar for the different spin states, the symmetry changes throughout the entire magnetic moment spectrum. The ground state for the neutral case has a magnetic moment of $20\mu_B$ with D_{4h} symmetry (Fig 14 b1)), and the first isomer has a low magnetic moment ($4\mu_B$) and C_{3v} symmetry (Fig. 4.15 b4)).

With the aim of seeing what plays the main role in the stabilization of this solution (electron density or structural symmetry), we performed two calculations with fixed geometry relaxing only the electronic structure (single point calculations).

In order to determine which of the effects is more important in the determination of the magnetic moment of the fundamental state of the cluster, if the geometry or the electronic density, we perform the following calculations: using the geometry of $4\mu_B$, we set the magnetic moment of $20\mu_B$ (Fig. 4.15 b2)) and with the geometry of $20\mu_B$ we fix the magnetic moment of $4\mu_B$ (Fig. 4.15 b3)). The results show that the electronic density of states (Fig. 15 b2) and b3)) does not change considerably with respect to the solutions b1) and b4) respectively. Moreover, when we did this symmetry change, the clusters with $20\mu_B$ increase its energy in 0.67eV whilst the cluster with $4\mu_B$ increase in 1.13eV, this means that the $20\mu_B$ cluster with the C_{3v} symmetry is better than the $4\mu_B$ one with D_{4h} symmetry . For these reasons, we conclude that the magnetic moment depends more in the electronic density than in the symmetry.

In Fig. 4.15 a) we have done similar analysis of the magnetic moment using now the VASP code in order to corroborate the solutions obtained with SIESTA. Both codes shown similar tendencies in the magnetic solution, although different values in the magnetic moments are obtained for SIESTA ($20\mu_B$) and VASP ($16\mu_B$).

4.3 Fragmentation channels of cationic clusters

In order to study the fragmentation channels, we calculated the fragmentation energy, defined as follows:

$E_f(n,m) = [E(n,m)^+] - [E(x,y)^+] - [E(n-x, m-y)]$

where the first term is the energy of the parent cationic cluster and the rest are the energies of the product-clusters sons, one of which results positively charged. Note that our definition is based on total energies of initial and final states and no energy barriers are considered which could be important in certain cases (if structural rearrangement of the parent-cluster occurs prior to fragmentation, for instance). We consider a large number of possible fragmentation channels, although we only report the most favorable ones:

(i) ${Fe_{n-1}O_m}^{+/0} + Fe^{+/0}$,

(ii) ${Fe_{n-1}O_{m-1}}^{+/0} + FeO^{+/0}$,

(iii) ${Fe_{n-1}O_{m-2}}^{+/0} + FeO_2^{+/0}$,

(iv) ${Fe_{n-2}O_m}^{+/0} + Fe_2^{+/0}$,

(v) ${Fe_{n-2}O_{m-1}}^{+/0} + Fe_2O^{+/0}$,

(vi) ${Fe_{n-2}O_{m-2}}^{+/0} + Fe_2O_2^{+/0}$,

(vii) $Fe_nO_{m-1}^+ + O$,

(viii) $Fe_nO_{m-2}^+ + O_2$,

In Tables 4.1 and 4.2 we can find the fragmentation energies of the previous channels. In Table 4.1 the energies of the channels are collected in which the largest fragment is the one that conserves the charge, while Table 4.2 contains the energy of the channels where the one that conserves the charge is the smallest cluster. We can see that in general, the most likely fragmentation channel is in which the largest cluster conserve the charge, except for the cluster $Fe_5O_3^+$, which is fragmented into $Fe_2^+ + Fe_3O_3$ (see table 2).

In Molek's work (109), they have studied the fragmentation channels for the iron oxide clusters (${Fe_nO_m}^+$ with n =1-17 and m =2-19). Molek *et al.* concluded that the fragmentation of these clusters, are carried out sequentially,

Table 4.1: Calculated fragmentation energies predicted in this work, where the biggest cluster conserve the charge. In bold are the most prevalent experimental channels obtained by Molek *et al.* (109), and underlined is the stronger experimental signal (when available from ref. (109)) among these channels.

	Fe	FeO	FeO_2	Fe_2	Fe_2O	Fe_2O_2	O	O_2
Fe_3O^+	-3.77	-3.36	—	-5.51	-4.68	—	-5.52	—
$Fe_3O_2{}^+$	-4.57	-3.99	-5.05	-8.93	-5.86	-4.59	-5.71	-6.16
$Fe_3O_3{}^+$	-6.60	**-4.97**	**-5.86**	-11.39	-9.47	-5.95	-5.90	-6.53
$Fe_3O_4{}^+$	-6.94	-5.02	**-4.86**	-12.93	-9.93	-7.57	**-3.91**	-4.73
$Fe_3O_5{}^+$	-6.13	-4.05	-3.60	—	-10.17	-6.73	-2.60	**-1.43**
$Fe_3O_6{}^+$	-7.34	-5.14	-4.52	—	—	-8.86	-4.50	**-2.02**
Fe_4O^+	-3.82	-3.85	—	-4.47	-4.19	—	-5.96	—
$Fe_4O_2{}^+$	-3.76	-3.98	-5.48	-5.20	-4.76	-4.04	-5.65	-6.53
$Fe_4O_3{}^+$	-3.72	-4.13	-5.82	-7.20	-5.70	-4.81	-5.86	-6.44
$Fe_4O_4{}^+$	-5.86	**-4.27**	-6.15	-9.67	-7.88	**-5.94**	-6.04	-6.83
$Fe_4O_5{}^+$	-8.12	-5.23	**-5.11**	-11.13	-9.17	-6.94	**-4.86**	-5.83
$Fe_4O_6{}^+$	-8.21	-7.21	-5.79	-12.42	-10.35	-7.95	-4.59	**-4.37**
$Fe_4O_7{}^+$	-7.84	-6.18	-6.66	—	-10.53	-8.02	-3.47	-2.98
Fe_5O^+	-3.43	-3.90	—	-4.13	-4.29	—	-5.79	—
$Fe_5O_2{}^+$	-3.79	-3.95	-5.88	-4.42	-4.77	-4.49	-6.01	-6.72
$Fe_5O_3{}^+$	-3.97	-4.34	-5.97	-4.57	-5.11	-5.02	-6.05	-6.97
$Fe_5O_4{}^+$	-5.14	-5.69	-7.53	-7.87	-6.42	-6.51	-7.21	-8.18
$Fe_5O_5{}^+$	-4.10	**-3.47**	-5.49	-9.09	-6.33	**-4.44**	-3.82	-5.96
$Fe_5O_6{}^+$	-4.40	-3.49	-4.33	-9.48	-8.62	-5.41	-4.89	-3.63
$Fe_5O_7{}^+$	-5.93	-3.90	-4.47	-10.64	-9.12	-7.81	-5.00	**-4.81**
$Fe_5O_8{}^+$	-7.70	-4.48	-3.92	-12.36	-9.32	-7.36	**-4.04**	**-3.96**
Fe_6O^+	-4.03	-4.32	—	-4.34	-4.93	—	-5.63	—
$Fe_6O_2{}^+$	-4.27	-4.79	-6.55	-4.94	-5.22	-5.38	-6.25	-6.81
$Fe_6O_3{}^+$	-4.74	-5.29	-7.27	-5.59	-6.08	-5.93	-6.51	-7.68
$Fe_6O_4{}^+$	-3.89	-5.60	-7.63	-5.90	-6.58	-6.64	-6.36	-7.79
$Fe_6O_5{}^+$	-5.49	-3.82	-7.00	-6.47	-5.96	-6.20	-5.42	-6.70
$Fe_6O_6{}^+$	**-5.66**	**-5.05**	-4.85	-6.93	-6.16	**-5.22**	**-5.06**	-5.40
$Fe_6O_7{}^+$	-5.27	-4.78	-5.64	-8.08	**-6.19**	**-4.97**	-4.62	-4.60
$Fe_6O_8{}^+$	-5.56	-4.11	-5.08	-10.13	-7.04	-4.71	-4.33	-3.86
$Fe_6O_9{}^+$	-8.23	-5.85	-5.87	-11.31	-10.55	-7.02	-5.78	-5.03
Fe_7O^+	-3.95	-4.09	—	-4.86	-5.28	—	-5.66	—
$Fe_7O_2{}^+$	-3.86	-4.62	-6.23	-5.01	-5.65	-5.64	-6.16	-6.74
$Fe_7O_3{}^+$	-3.59	-4.61	-6.83	-5.20	-5.89	-6.09	-6.24	-7.32
$Fe_7O_4{}^+$	-3.03	-3.90	-6.39	-3.80	-5.64	-5.89	-5.81	-6.97
$Fe_7O_5{}^+$	-3.92	-3.85	-6.19	-6.29	-4.75	-6.15	-6.31	-7.04
$Fe_7O_6{}^+$	-4.51	-4.08	-5.48	-7.05	-6.57	-4.59	-5.65	-6.88
$Fe_7O_7{}^+$	-5.62	-4.75	-5.78	-7.78	-7.41	-6.49	-5.73	-6.30
$Fe_7O_8{}^+$	-5.92	-4.76	**-5.35**	-8.36	**-7.04**	**-6.23**	-4.62	-5.27
$Fe_7O_9{}^+$	-4.25	-4.54	-4.84	-9.36	-7.11	-5.35	-4.12	-3.66
$Fe_70_{10}{}^+$	-6.68	-4.71	-6.47	-11.78	-9.94	-7.25	-5.95	-4.99

Table 4.2: Calculated fragmentation energies predicted in this work, where the smallest cluster conserve the charge. In bold are the most prevalent experimental channels obtained by Molek *et al.* (109), and underlined is the stronger experimental signal (when available from ref. (109)) among these channels.

	Fe^+	FeO^+	FeO_2^+	Fe_2^+	Fe_2O^+	$Fe_2O_2^+$
Fe_3O^+	-4.68	—	—	-3.49	—	—
$Fe_3O_2{}^+$	-4.59	-5.86	—	-5.18	-4.17	—
$Fe_3O_3{}^+$	-5.78	-5.95	-9.47	-6.42	-6.04	-4.97
$Fe_3O_4{}^+$	**-4.87**	-5.15	-7.57	-6.98	**-5.30**	**-4.86**
$Fe_3O_5{}^+$	**-3.70**	-2.93	**-5.47**	—	**-4.54**	**-2.80**
$Fe_3O_6{}^+$	-4.44	-3.66	-5.14	—	—	**-3.95**
Fe_4O^+	-4.91	—	—	-4.32	—	—
$Fe_4O_2{}^+$	-4.50	-6.02	—	-4.17	-4.93	—
$Fe_4O_3{}^+$	-4.03	-5.82	-9.59	-5.32	-4.99	-5.70
$Fe_4O_4{}^+$	**-5.83**	-5.53	-9.57	-6.54	**-6.33**	**-5.94**
$Fe_4O_5{}^+$	**-7.50**	-6.16	-8.10	-7.63	**-6.37**	**-6.10**
$Fe_4O_6{}^+$	**-7.14**	-7.55	-8.45	-8.46	**-7.18**	**-5.86**
$Fe_4O_7{}^+$	-7.47	-6.07	-8.73	—	-6.90	-5.56
Fe_5O^+	-4.63	—	—	-4.15	—	—
$Fe_5O_2{}^+$	-4.80	-6.10	—	-4.10	-5.12	—
$Fe_5O_3{}^+$	-4.77	-6.30	-9.85	-3.81	-5.11	-6.07
$Fe_5O_4{}^+$	-5.81	-7.44	-11.23	-6.79	-5.98	-7.22
$Fe_5O_5{}^+$	**-4.73**	-5.09	-8.97	-7.41	**-5.57**	**-4.71**
$Fe_5O_6{}^+$	-4.40	-5.08	-7.69	-7.35	-7.26	—
$Fe_5O_7{}^+$	**-5.52**	-4.86	-7.79	-9.21	**-7.31**	**-7.17**
$Fe_5O_8{}^+$	**-5.91**	-5.02	-6.61	-10.07	**-8.22**	**-6.26**
Fe_6O^+	-5.63	—	—	-4.47	—	—
$Fe_6O_2{}^+$	-5.62	-7.34	—	-4.88	-5.69	—
$Fe_6O_3{}^+$	-5.74	-7.59	-11.56	-5.32	-6.36	-7.10
$Fe_6O_4{}^+$	-5.66	-7.55	-11.66	-5.51	-6.64	-7.62
$Fe_6O_5{}^+$	-6.25	-6.54	-10.69	-6.03	-5.89	-6.97
$Fe_6O_6{}^+$	**-5.85**	-6.77	-9.31	-5.88	**-6.05**	**-5.86**
$Fe_6O_7{}^+$	-5.25	-5.92	-9.09	-6.61	**-5.45**	**-5.57**
$Fe_6O_8{}^+$	-5.42	-5.04	-7.96	-7.28	**-5.90**	**-4.69**
$Fe_6O_9{}^+$	-7.51	-6.67	-8.53	-9.21	-8.03	-6.59
Fe_7O^+	-5.65	—	—	-5.39	—	—
$Fe_7O_2{}^+$	-5.47	-7.26	—	-5.30	-6.52	—
$Fe_7O_3{}^+$	-5.17	-7.17	-11.21	-5.14	-6.50	-7.66
$Fe_7O_4{}^+$	-4.41	-6.44	-10.69	-4.50	-5.91	-7.21
$Fe_7O_5{}^+$	-5.13	-6.19	-10.46	-5.99	-5.78	-7.12
$Fe_7O_6{}^+$	-5.62	-6.24	-9.54	-6.17	-6.60	-6.33
$Fe_7O_7{}^+$	-6.66	-6.80	-9.67	-6.69	-6.86	-7.23
$Fe_7O_8{}^+$	-6.44	-6.75	-9.14	-7.16	**-6.28**	**-6.39**
$Fe_7O_9{}^+$	-4.89	-6.01	-8.57	-7.57	**-6.24**	**-5.30**
$Fe_70_{10}{}^+$	-6.76	-6.30	-9.67	-9.83	**-8.49**	**-7.09**

that is, the cluster parent $Fe_nO_m{}^+$ is fragmented into $Fe_{n-x}O_{m-y}{}^+ + Fe_xO_y$, and this in turn in $Fe_{n-(x+x')}O_{m-(y+y')}{}^+ + Fe_{x'}O_{y'}$, so they obtain a path that goes from the largest to the smallest clusters. However, these sequential paths do not explain the presence of all clusters in some of these sequential fragmentations. They also mention that fragmentation can not exist in parallel, that is, that the $Fe_nO_m{}^+$ cluster can not be fragmented simultaneously in $Fe_{n-a}O_{m-b}{}^+$ and $Fe_{n-c}O_{m-d}{}^+$, however, there are some cases, in particular that of the cluster $Fe_6O_6{}^+$, which would be better explained with both types of fragmentations, this is simultaneous fragmentation into two channels, and then in sequential fragmentation. Another option is that the fragments neutrals that remain as a result of sequential fragmentation, add to some charged clusters, this possibility, explains most of those clusters that in principle do not seem to come from a sequential fragmentation.

Now, we will compare our calculations (Fig. 4.16) with the data available in the experiment of Molek and co-workers (109), from $Fe_2O_2^+$ to $Fe_7O_{10}{}^+$. In Fig. 17 a), we have compiled from Table 1 of the Molek *et al.* work (109), the possible fragmentation channels, which do not conflict with the sequential way to fragment clusters, and Fig. 4.17 b), they are placed the fragmentation channels that are not explained with a sequential fragmentation. Most of the fragmentations are explained by a sequence fragmentation, except for some clusters that result of fragmentation of the clusters $Fe_6O_6{}^+$, $Fe_7O_8{}^+$, $Fe_7O_9{}^+$ and $Fe_7O_{10}{}^+$, now we will explain the first of these fragmentations.

$Fe_6O_6{}^+$: The fragmentation of this cluster is a clear indication that the neutral and charged products bond each other, and not only fragmentations are present. As a result of the fragmentation of $Fe_6O_6{}^+$ they obtain $Fe_6O_7{}^+$, it is clear that this cluster can not be obtained only from the fragmentation, so the cluster $Fe_6O_7{}^+$, is obtained from the bond of neutral and charged clusters. Since Molek *et al.* (109) showed that it is not possible to obtain parallel fragmentations, not all the products of this fragmentation are explicable. The fragmentation b1) (In Fig. 4.17 b1)), has two channels that are mutually exclusive (because there can not be simultaneous fragmentations), in case that

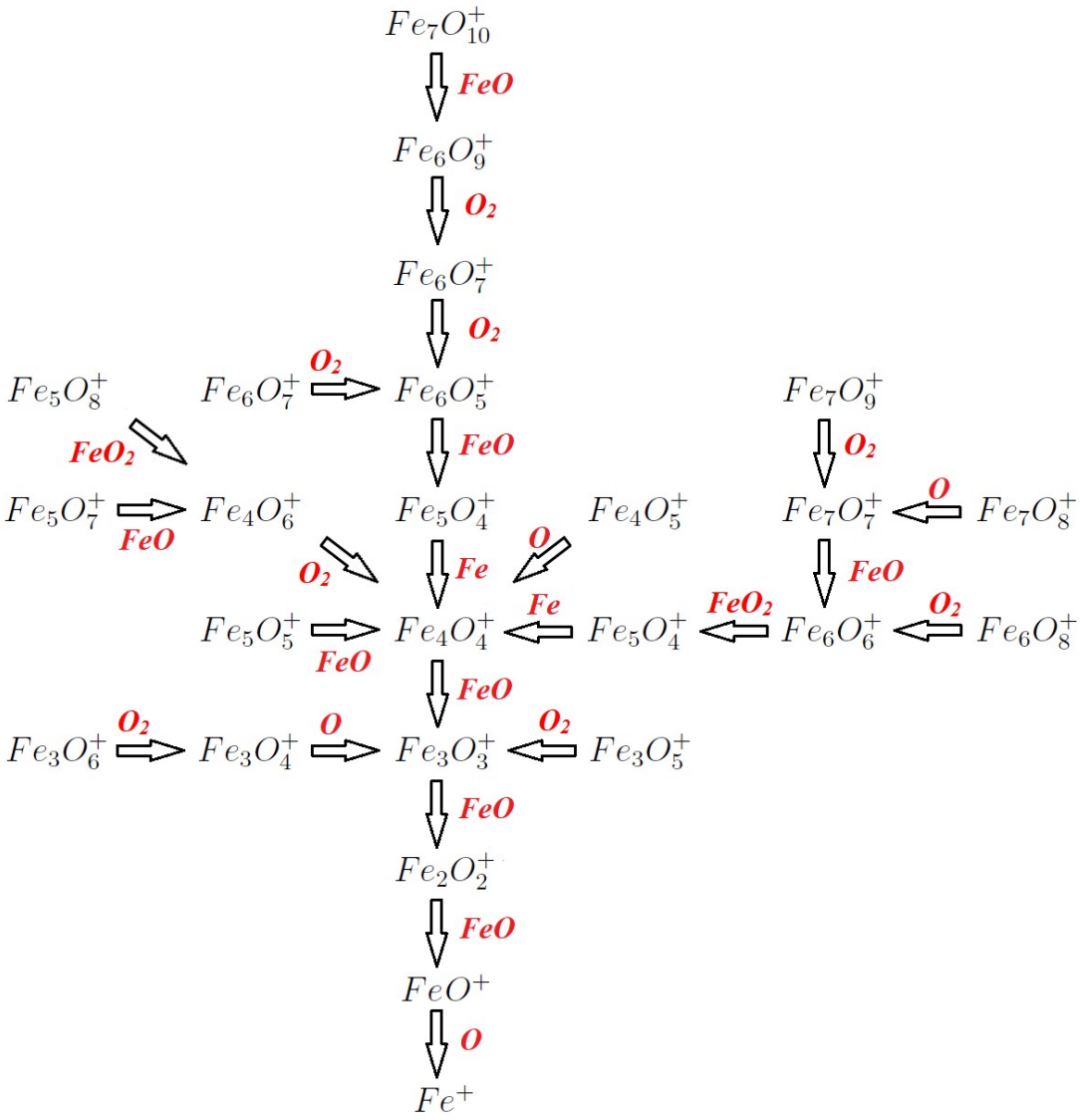

Figura 4.16: Theoretical sequential fragmentation channels predicted in our calculation. Below every arrow, it is presented the neutral subcluster (red color) detached from parent clusters.

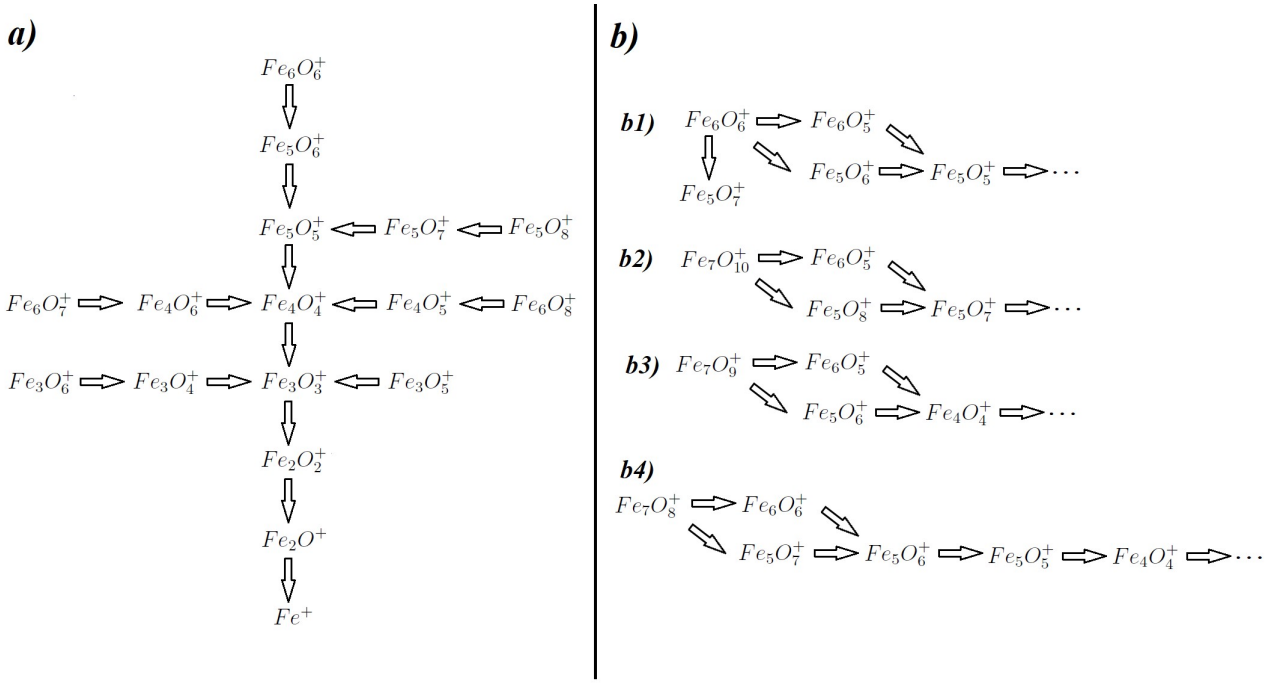

Figura 4.17: Experimental fragmentation channels obtained by Molek *et al* (109). In panel (a) (left hand side) sequential fragmentations that do not get in conflict with the sequential fragmentation proposed in their work. In panel (b) (right hand side) fragmented clusters that get in conflict with the sequential fragmentation paths.

the fragmentation was $Fe_6O_6^+ \longrightarrow Fe_6O_5^+$, it is not possible to reach from $Fe_6O_5^+$ to $Fe_5O_6^+$ and vice versa, so the only way to get both products, is that the small neutral fragments are attached to charged fragments.

Due to this, we can not be completely sure of which are the ways that clusters continue to fragment, that is why we propose with our calculations, the possible paths in which the clusters are fragmented. In Fig. 4.16, we have made a diagram of the more favorable fragmentation channels than we get with our calculations. For most of the small clusters, our data agree with the experiment (from $Fe_2O_2^+$ up to $Fe_5O_5^+$, except for the fragmentation of $Fe_2O_2^+$), but for the larger clusters, we have some differences.

4.4 conclusions and perspectives

The minimum energy structure of iron oxide clusters, $Fe_nO_m^{\pm/0}$ (n = 3-7; m = 1-15), is obtained in this paper by testing a large number of plausible geometries and optimizing the several candidates by means of DFT calculations. These initial geometries were constructed i) as planar and three dimensional arrangements of FeO units, ii) as small pure iron clusters covered with consecutive oxygen atoms and iii) for the bigger oxidation rates molecular oxygen absortion. For the n=m = 3 and 4 cases the ground state is formed by planar ring structures, with alternating Fe and O atoms, independently of the charge state, which agrees with recent ion mobility experiments. For larger sizes the ground state structures show three dimensional (3D) structures with pyramidal, hexahedral, decahedral, octahedral-like and zincblenda-like geometry, respectively, as the cluster size increases.

We investigated the properties of $Fe_nO_m^{\pm/0}$ clusters as a function of the oxygen content. The total spin magnetic moment exhibits a drop close to the equiatomic concentration ($n = m$), reflecting the reentrance of planar or quasi-planar structures whose magnetic arrangement is characterized in general by the maximum number of antiparallel couplings among all compositions. As a general trend, antiparallel couplings are found, in more or less degree depending

on the composition, size and charge state. However, we have identified certain niquel oxide clusters, like $Ni_6O_5^+$, Ni_7O_6 and Ni_8O_6, with a considerably large total moment (11 or $12\mu_B$) as well as with a high relative stability, an interesting result in the context of magnetic grains design. The large moment of these magnetic grains is due to the promotion of parallel magnetic couplings, despite their significative oxidation rate, an unavoidable fact in environmental conditions.

We have found a resurgence magnetic behavior never before reported for iron oxide clusters. It is known that the magnetic moment of the iron clusters is quenched when they are oxidized, due to antiferromagnetic couplings. For the Fe_4O_m and Fe_5O_m series, we found that for large oxidation rates, the antiferromagnetic couplings disappear and the magnetic moment of the system increases, due to low local magnetic moments of the iron, but with parallel couplings. We also made a scan of the magnetic moment for the cluster Fe_6O_8, because this is the only cluster of the Fe_6O_m series with a high oxidation rate that presents high magnetic moment. Finally, we studied the fragmentation channels of this clusters, compared with experimental measurements of photofragmentation. We have a great agreement for small clusters, but for larger clusters we have a difference with the experimental measures of relative abundance, despite this, we provide a satisfactory explanation of the difference with our calculations.

Chapter 5

Mixed transition metal oxide clusters.

Hay algunos que dicen, que todos los caminos
conducen a roma, y es verdad por que el mio,
me lleva cada noche al hueco que te nombra.
Luis Eduardo Aute.

In a systematical way, we study the possibility of inducing ferromagnetic-like order and to promote a high-spin state in TMO-NP (TM= Fe, Co and Ni) by their doping with a different TM element of the list. For this purpose, we extended previous calculations preformed by Torres *et al.* (108) for $FeCo$ dimers to all possible pure and bimetallic dimers (the smallest size), trimers and tetrameres allowing us to have a variety of stoichiometries and geometrical arrangements in the range of small sizes. The goal was to identify optimal mixed TM oxides from the magnetic point of view, as well as to extract qualitative trends, if possible, that might help to choose the best dopant for larger magnetic TMO-NP. Taking into account the database of geometries of the putative ground states and low-energy isomers of Co (51), Ni (52)(chapter 3), and Fe-oxide (chapter 4) oxide clusters, we determined the putative ground states of the mixed TM oxide clusters $A_{n-x}B_xO_m$ ($A, B = Fe, Co, Ni$; n=2, 3, 4; $0 \leq x \leq n$) with different oxidation rates, m.

We will discuss first their structural properties and stability. These properties are connected with their electronic structure and magnetic properties

that will be discussed in a second subsection. There are several factors that contribute in determining the structural properties and stability in these binary TM oxide clusters, in particular the difference in binding energy of Fe, Co and Ni and the relative strength of the metal-metal and metal-oxygen bonds. The Pauling scale electronegativities of O, Fe, Co, Ni are 3.4, 1.83, 1.88, 1.91, respectively, so it is expected a non negligible electronic charge transfer from the metal atoms towards O atoms in these systems. This effect will strengthen metal-oxygen bonds due to the partial ionic contribution while weakening the metal-metal bonds. Concerning the magnetic properties, it is known that clusters of Fe, Co and Ni have large parallel magnetic moments per atom than their respective bulk counterparts (due to electron localization). However, due to the expected loss of charge in the metal atoms, and the weakening of the metal-metal interaction, weakening in the tendency to parallel magnetic couplings is expected. Moreover, the contribution of the spin-polarization of the oxygen atoms to the total moment may not be negligible. The interplay between all those factors depends on the composition and size so that it is very difficult to anticipate which of the oxidized nanoalloys will exhibit the best performance from the point of view of the magnetic properties without carrying out explicit calculations for each particular system.

5.1 Geometrical configurations and electronic properties

The putative global minimum structures of $A_{n-x}B_xO_m$ ($A, B = Fe, Co, Ni$; $0 \leq x \leq n$), with m up to oxygen saturation, are shown in Figs. 5.1, 5.2 and 5.3-5.4 for n =2, 3 and 4, respectively. In Fig. 5.5 we plot the average binding energy per atom of the corresponding binary TM oxide clusters, calculated as:

$$E_b(A_{n-x}B_xO_m) = \frac{(n-x)E(A) + xE(B) + mE(O) - E(A_{n-x}B_xO_m)}{n+m} \quad (5.1)$$

where $E(S)$ is the total energy of system S. (Moreover, the values of binding

energies per atom are given below the putative global minimum structures shown in Figs. 5.1-5.4).

The following general trends can be inferred from all these results:
i) The oxygen atoms tend to occupy bridge sites between the TM atoms, and when bridge sites are saturated, O atoms tend to occupy top sites (except for Ni_3O_4 and Fe_3O_4).
ii) The oxygen bonds preferentially with Fe atoms. When the oxygen rate increases, the next preferential atoms are Co and finally Ni.
iii) The net electronic charge in the O atoms, resulting from the charge transfer from the metal atoms, favors an uniform distribution of the O atoms throughout the cluster.
iv) At oxidation rates where the number of O atoms equals the number of metal atoms, ring-like structures are formed for all sizes considered in this chapter. In this atomic configuration all metal-metal bonds are mediated by oxygen. This trend was already discussed in previous chapters for the pure Ni (chapter 3 (52)) and Fe (chapter 4) clusters, and in our previous work of Co(51) clusters, and it has been also discussed by other groups for other systems (83, 107). We now see that these ring-like structures are preserved in the TM oxide nanoalloys at least for the 3d elements here considered.
v) We considered up to m= 6 or 7 oxygen atoms which is enough to analyze the transition from atomic to molecular adsorption in the case of the TM dimers (still not in the trimmers and tetrameres). When the oxygen concentration is high enough, oxygen starts to be adsorbed molecularly, that is with short $O-O$ inter-atomic distances. The critical oxygen concentration for molecular adsorption to occur lowers as going from Fe to Co and Ni as it can be clearly seen in the structures of the oxidized dimers in Fig. 5.1: while in Fe_2O_m no molecular adsorption takes place for $m \leq 6$, in Co_2O_m and Ni_2O_m it occurs for $m = 5$; and for $m = 5$ and 6, respectively. Concern mixed oxide clusters, in $FeCo_m$ no molecular adsorption takes place for $m = 6$, in $CoNiO_m$ and $FeNiO_m$ it occurs for $m = 5$ and 6; and for $m = 4$, 5, 6, respectively. The molecular adsorption is a manifestation of oxygen saturation of the system and

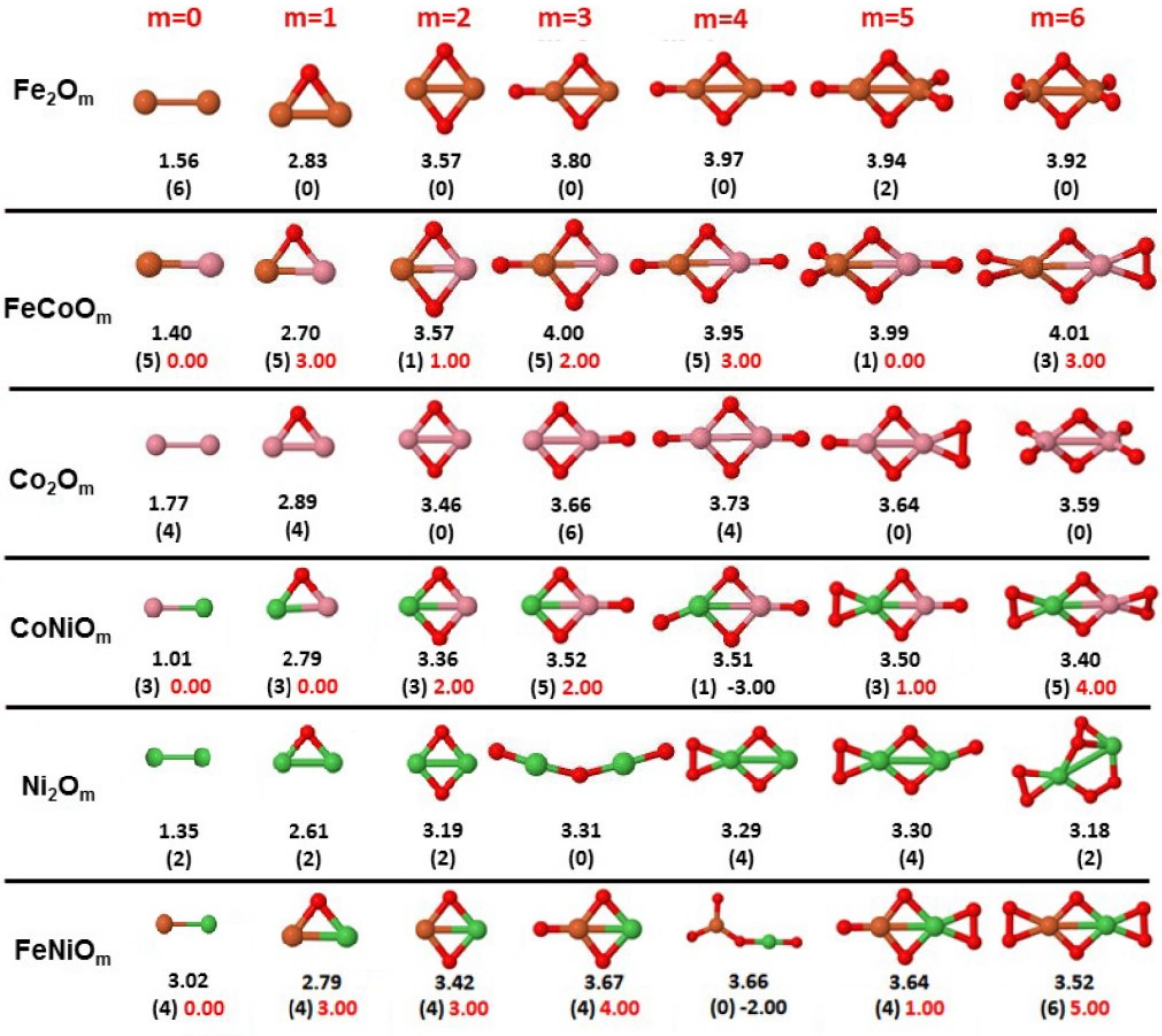

Figura 5.1: Putative global minimum structures of pure and mixed oxide clusters dimers. Numbers below structures are the binding energy per atom (in eV), numbers in parenthesis are the magnetic moment (in μ_B), and the third number (in the case that appear) is the excess magnetic moment (in μ_B) defined in Eq. 5.1.

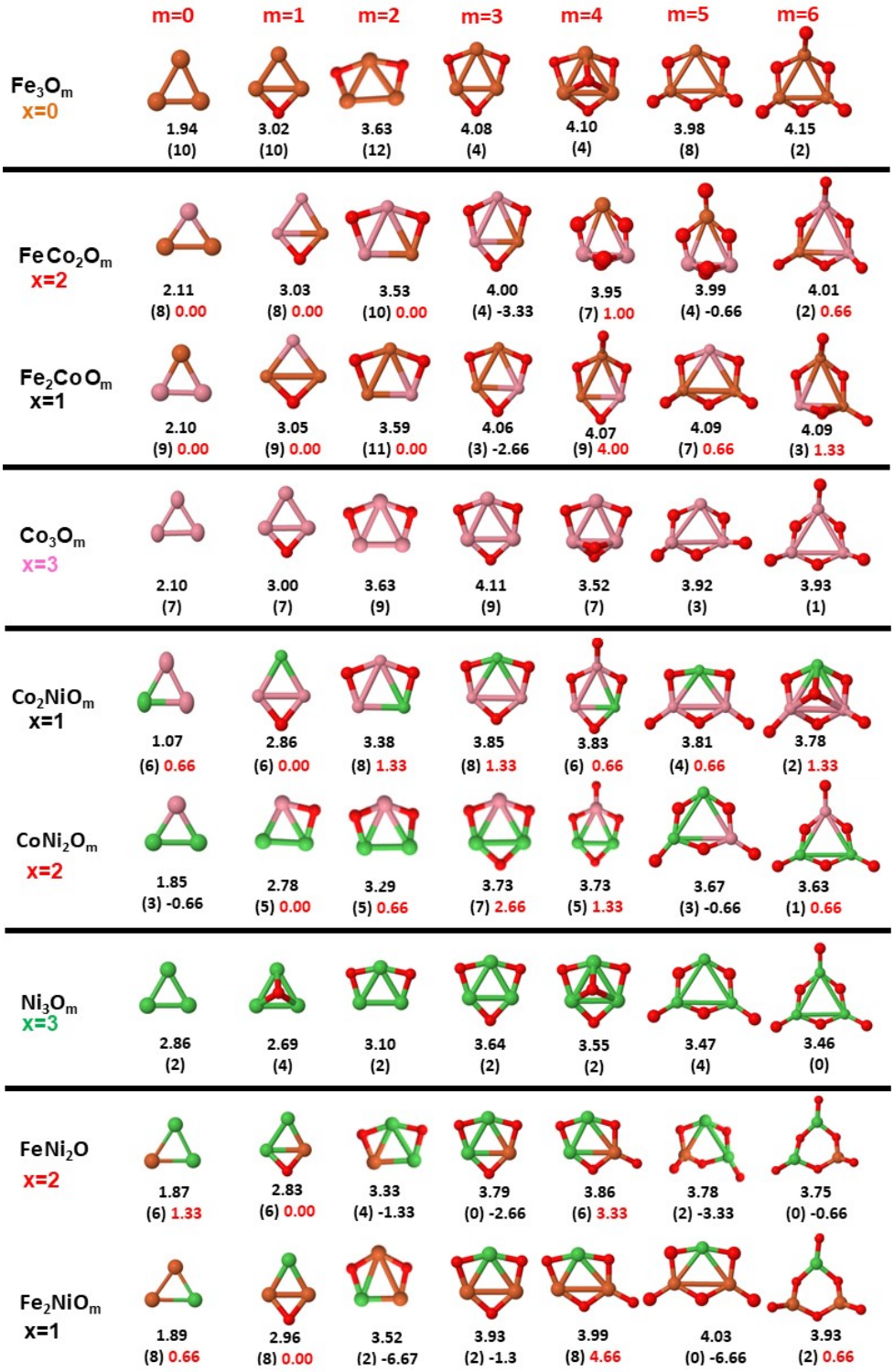

Figura 5.2: Putative global minimum structures of pure and mixed oxide clusters trimmers. Numbers below structures are the binding energy per atom (in eV), numbers in parenthesis are the magnetic moment (in μ_B), and the third number (in the case that appear) is the excess magnetic moment (in μ_B) defined in Eq. 5.1.

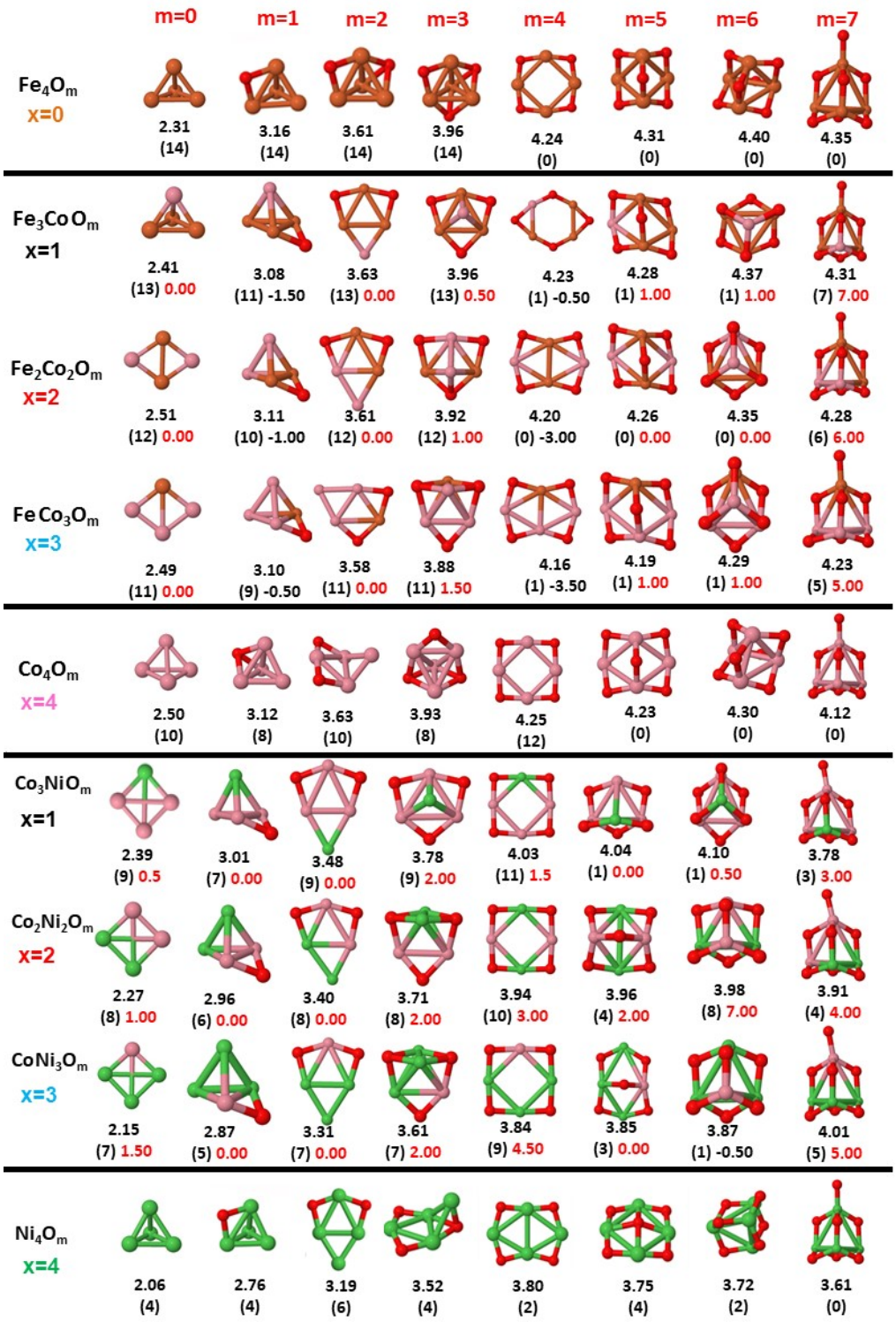

Figura 5.3: Putative global minimum structures of pure and mixed oxide clusters tetrameres. Numbers below structures are the binding energy per atom (in eV), numbers in parenthesis are the magnetic moment (in μ_B), and the third number (in the case that appear) is the excess magnetic moment (in μ_B) defined in Eq. 5.1.

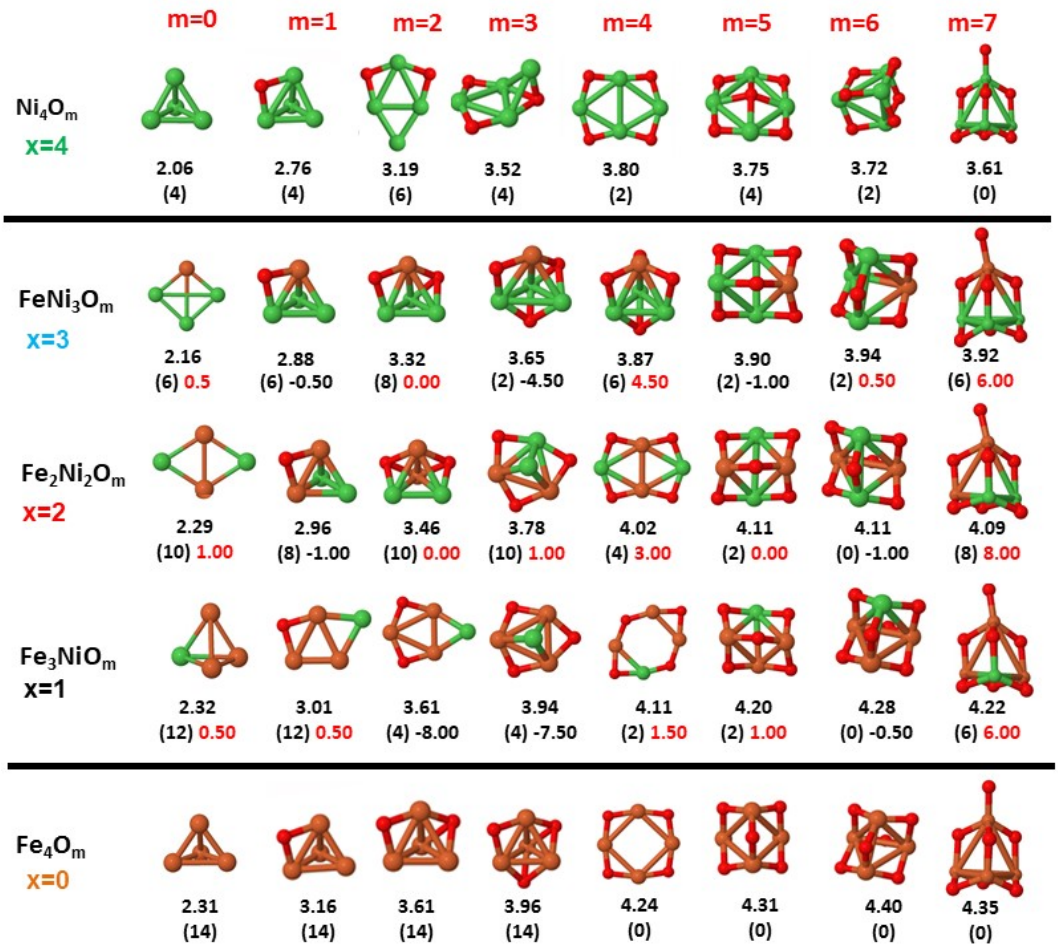

Figura 5.4: Putative global minimum structures of pure and mixed oxide clusters tetrameres. Numbers below structures are the binding energy per atom (in eV), numbers in parenthesis are the magnetic moment (in μ_B), and the third number (in the case that appear) is the excess magnetic moment (in μ_B) defined in Eq. 5.1.

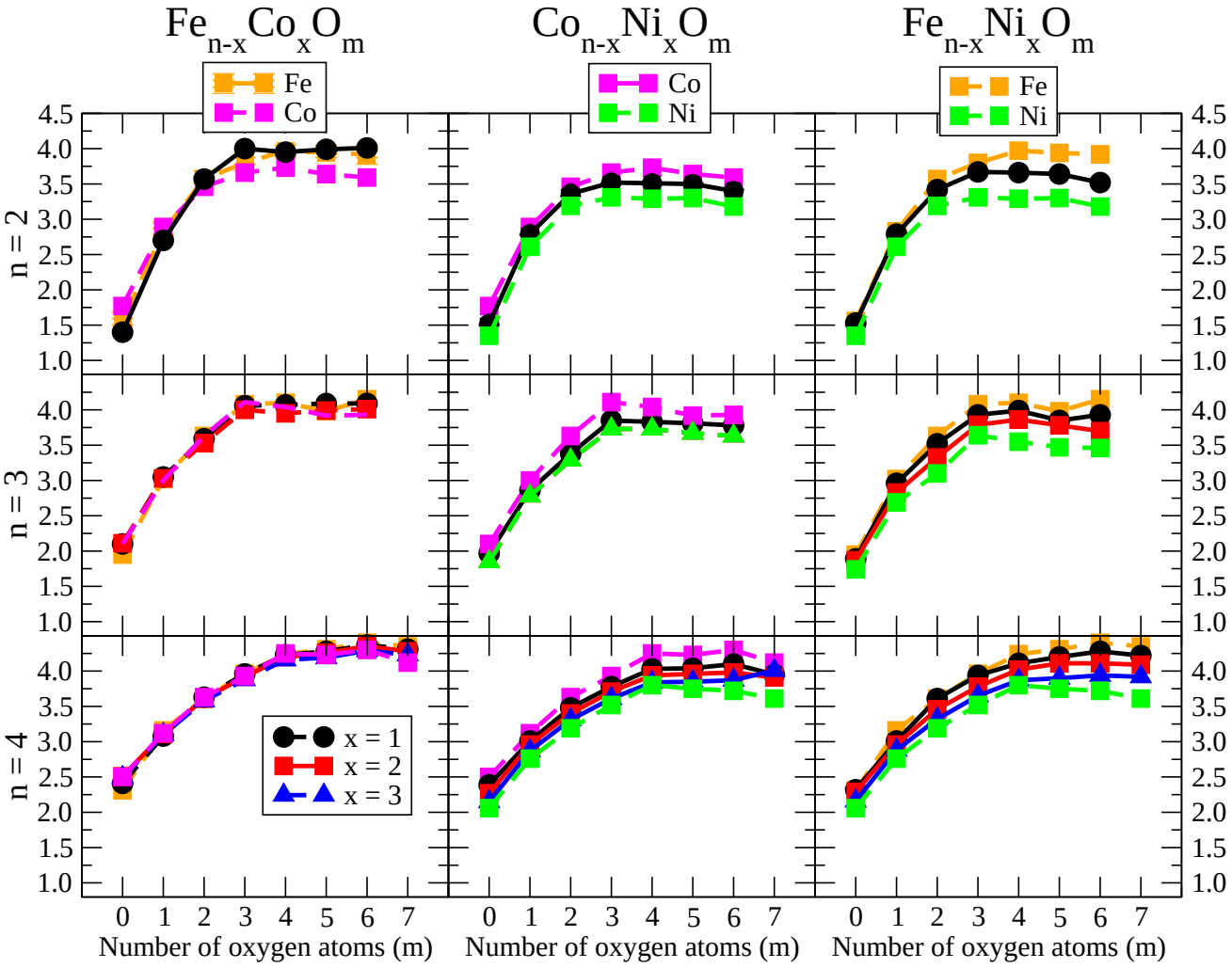

Figura 5.5: Binding energy of $A_{n-x}B_xO_m$ clusters (A, B = Fe, Co, Ni; $0 \leq x \leq n$; $m = 1 - 7$)

its emergence at different oxygen concentration for the different TM compositions is connected with the relative strength of the respective metal-oxygen bonds.

vi) The metal-oxygen binding lowers as going from Fe to Co and Ni. The metal-metal binding also lowers as going from Fe to Co and Ni (Co and Ni being very similar in this respect). Therefore, general structural trends are also consistent with the binding energy per atom plotted in Fig. 5.5 for the oxides. For TM oxide dimers, and in connection with the discussion of the oxygen saturation, we note a shift to lower m in the maximum of binding energy as going from Fe to Co and Ni which means that adsorption of more oxygen atoms does not increase the binding despite the partial ionic contribution because this competes with the metal-metal binding which weakens at the same time. The weakening of the metal-metal binding is manifested in the less compact metal skeleton (lower average metal-metal inter-atomic distance) that results as m increases. Moreover, the results for the binding energies indicate that the higher the concentration of Fe in the TM oxide clusters the higher their absolute stability which may be important for practical purposes. On the other hand, the higher the Ni content, the lower the exothermic character of oxidation or, in other words, less prone to oxidation will be the nanoparticle, which may also be important for practical purposes.

vii)The relative differences of electronegativities between the TM atoms, although small, support also this trend. Electronegativity lowers as going from Fe to Ni so that the tendency towards electron donation to O should be stronger in Fe.

Up to which extent those facts have consequences on the magnetic properties of these systems is discussed in the next subsection.

Although several general structural and energetic trends have been found and rationalized in terms of simple arguments, quantum confinement effects and non scalability of physical and chemical properties inherent to this range of sizes makes that certain anomalies or unexpected structures that depart from

the rule are found. This confirms the need of performing explicit calculations for each individual system at the nanoscale. For instance, Ni_2O_3 has a bent linear structure with exclusively metal-oxygen bonds, similar to that found in In_2O_3 (chapter 7); Co_2O_6 with exclusively metal-oxygen bonds, Ni_2O_6 with three oxygen molecules. Fe_3O_4 and Ni_3O_4, hollow (no top); Co_3O_4 hollow-bridge. $FeNiO_4$ does not have, either, a $Fe-Ni$ bond.

5.2 Magnetic properties

Small clusters of late 3d TM atoms are super paramagnetic with very low magnetic anisotropy energy. However, the parallel magnetic couplings and relatively high spin polarization due to electron localization make them having high total spin magnetic moments. Nanoparticles with high total moments and low magnetic anisotropy are relevant, for instance, for applications in which rotation of the nanoparticles should not affect the orientation of the moment when an external field is applied. This behavior is adequate for designing magnetic markers in nanomedicine, where particle agglomeration is also to be avoided. TM oxide clusters are among the most relevant magnetic nanoparticles in this context and, therefore, besides the absolute stability, already discussed in the previous subsection, it is important to achieve: (i) high total magnetic moments, and (ii) robustness of the total magnetic moment (mainly contributed by the TM atoms) against oxidation. The discussion of the present subsection is oriented towards the determination of those binary TM oxide clusters with particularly high total moments among the investigated ones $A_{n-x}B_xO_m$, the determination of those compositions that lead to more robust magnetic moments against oxidation, and finally the seek of general trends that could be valid for larger sizes.

The total magnetic moment of $A_{n-x}B_xO_m$ ($A, B = Fe, Co, Ni$; $0 \leq x \leq n$) as a function of the oxygen concentration m is shown in Figs. 5.6, 5.7 and 5.8 for n=2, 3 and 4, respectively, in the upper panels.

As a simple measure of the benefit of mixing TM atoms, from the magnetic

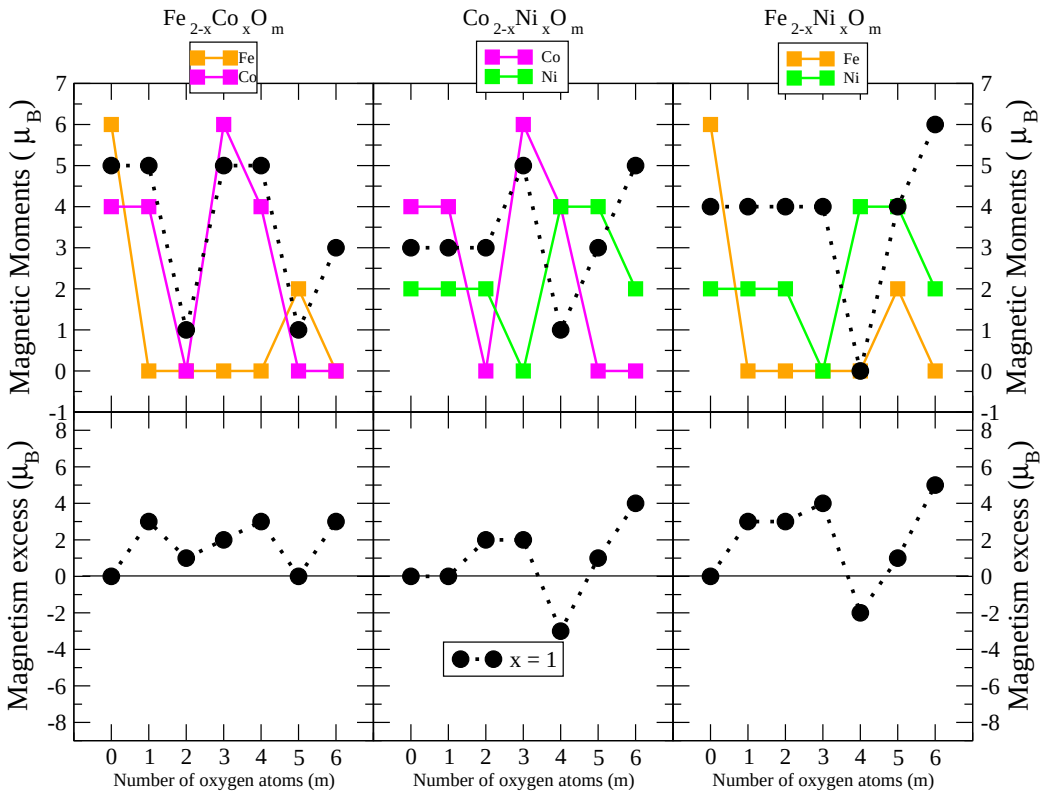

Figura 5.6: Magnetic moment (upper panels) and magnetism excess (lower panels) of pure and mixed oxide clusters dimers.

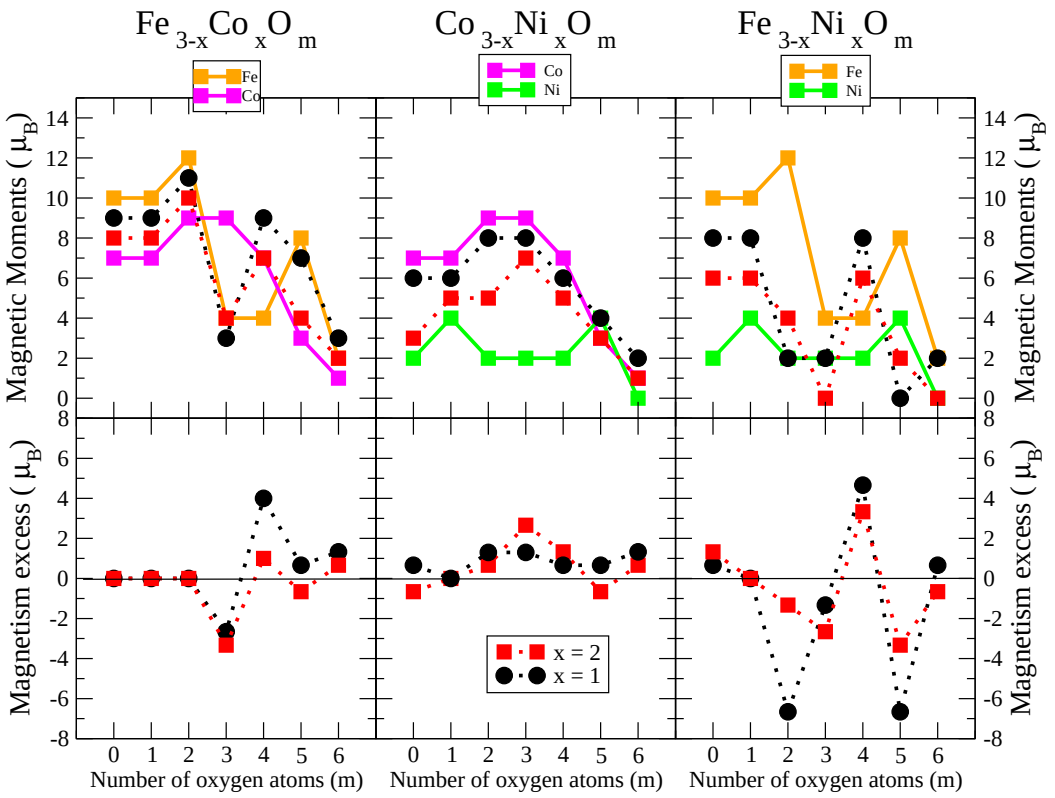

Figura 5.7: Magnetic moment (upper panels) and magnetism excess (lower panels) of pure and mixed oxide clusters trimmers.

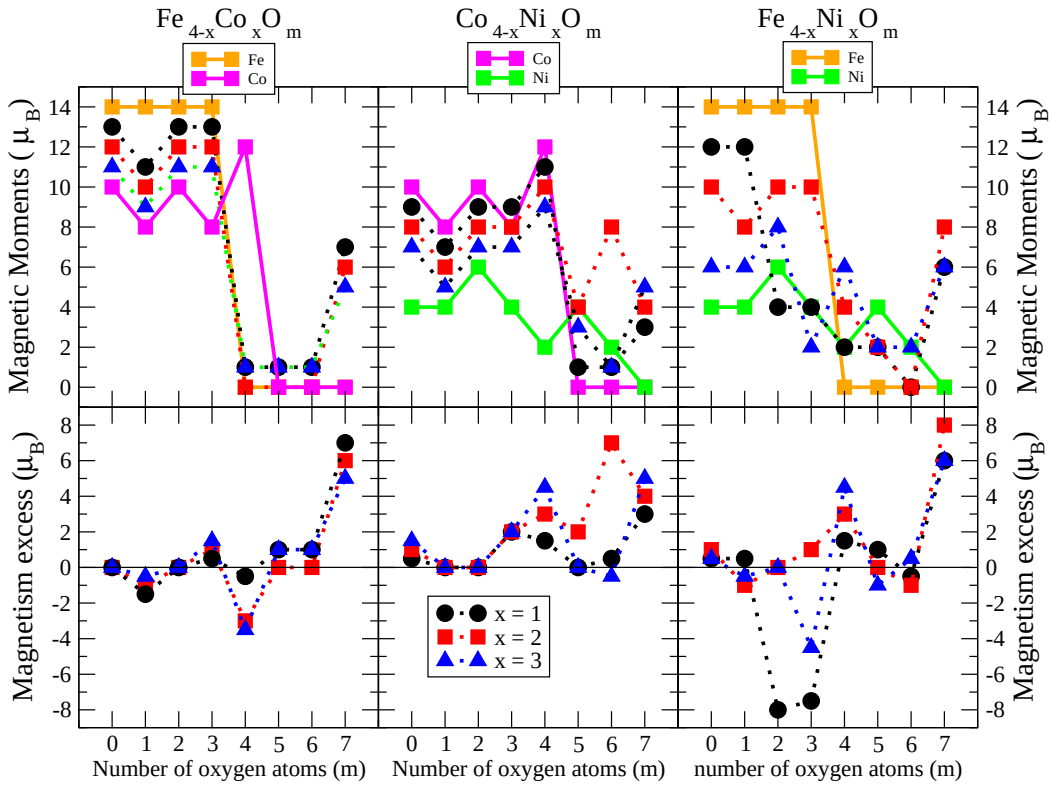

Figura 5.8: Magnetic moment (upper panels) and magnetism excess (lower panels) of pure and mixed oxide clusters tetrameres.

point of view, in our systems, we define the excess magnetic moment μ_{exc}:

$$\mu_{exc}(A_{n-x}B_xO_m) = \mu(A_{n-x}B_xO_m) - \frac{n-x}{n}\mu(A_nO_m) - \frac{x}{n}\mu(B_nO_m) \qquad (5.2)$$

where $\mu(S)$ is the total magnetic moment of the system S. Thus, $\mu(A_nO_m)$ and $\mu(B_nO_m)$ are the total moments of the oxide clusters of TM elements A and B in their respective global minimum structures at the oxygen concentration m. The excess magnetic moment is zero for TM oxide clusters of a single TM element by definition. Positive excess magnetic moments indicate that formation of the corresponding oxide nanoalloy is magnetically favorable as compared to an ideal mixture. The ideal mixture would follow a simple Vegard law, according to which the total moment of the oxide nanoalloys follows a linear behavior connecting the magnetic moments of the pure oxide clusters, A_nO_m and B_nO_m, obeying the quantization of the total spin. We note that similar magnitudes are often used in the analysis of energetic or compactness of nanoalloys (excess energy and excess radius, respectively) but that the excess magnetic moment was not defined so far, up to our knowledge.

In the lower panels of Figs. 5.6, 5.7, and 5.8, we plot the excess magnetic moment of the binary TM oxide clusters, as a function of the oxigen concentration m.

Among the late 3d elements Fe has the most d-holes in its active valence states. This means that is has the largest local magnetic moments among the late TM elements but, at the same time, antiparallel couplings are easier to be promoted in Fe systems than in Co and Ni ones (notice that Fe is closer to Cr in the periodic table than Co and Ni). Electron transfer to O makes Fe to electronically approach Mn (which already exhibits antiparallel couplings in certain atomic arrangements) and weakens the $Fe - Fe$ interaction and the parallel magnetic couplings reminiscent from the Fe bulk ferromagnetism. This is the mechanism through which oxidation quenches the moment of the Fe dimer (Fig. 5.1) for nearly all oxidation rates m, and strongly reduces that of the trimer (Fig. 5.2) and tetramer (Figs. 5.3 and 5.4) except for the lowest m in both cases. The enhancement of μ in Fe_3O_5 is an unexpected magnetic

trend related with the particular structural arrangement and the strengthen of the $Fe - O$ interaction to the point that the magnetic coupling between Fe and O in that particular geometry forces the oxygen mediated $Fe - Fe$ magnetic coupling to be parallel. This has been discussed in detail in chapter 4. Therefore, a general trend is that the Fe cluster must reach a critical size and metal-metal coordination to retain the parallel couplings under oxidation, at least at low oxygen rates. Another general trend is that the magnetic moment of iron oxide clusters is not robust against oxidation, the magnetic moment is totally quenched when the oxygen atoms are equal to the number of iron atoms.

As compared to iron clusters, those of cobalt approach magnetic saturation due to the less d-holes in the active band states which render them more ferromagnetic-like although with less spin-polarization than their Fe counterparts. Their magnetic moment is preserved up to at higher oxidation rates than in the case of iron. For example, Co_3O_m and Co_4O_m retains a remarkable high magnetic moment until $m = 4$ (in iron it is up to $m = 3$).

The $Fe-Co$ mixing combining the stronger tendency of Co towards parallel couplings with the larger spin polarization of Fe is particularly beneficial in the case of dimers where, for $m = 1, 2, 4$ and 6, $FeCoO_m$ has larger total moment than Co_2O_m (108) (in Fe oxides the moment was eve quenched). This is reflected in the excess magnetic moment which is positive in dimers and with maxima in most of those values of m. Mixing is favourable for dimers considering that the moment in iron oxide clusters is quenched (For Co it is also quenched for $m = 5$ and 6, but the mixtures have a noticeable magnetic moment, in both cases, being equal to 3 for $m = 6$) and so the mix produces a magnetic particle with moment close to or higher than that of the cobalt oxide dimers.

For larger sizes in the $FeCo$ clusters ($n = 3$ and $n = 4$) this trend is maintained for all m values, except for the rings $n = m = 3$ and $n = m = 4$, where the geometrical factor has an important role, as we will analyze below. For the $m = 3$ series, pure Fe oxide groups have a larger magnetic moment than

those of Co except for three and four oxygen atoms. When Fe and Co atoms are mixed (See Fig. 5.7), except for Fe_2CoO_4 and Fe_2CoO_6 no other mixture have larger magnetic moment that the pure Fe and Co clusters. Despite this, the excess magnetic moment is greater than or equal to zero for almost all alloys (except for Fe_2CoO_3, $FeCo_2O_3$ and $FeCo_2O_5$), this is an indication that the mixing is favorable from the magnetic point of view. Actually for $n = 3$ with low oxidation states, where the Fe has higher magnetic moments than those of Co, the fact of mixing is favorable, in the sense that substituting some Co atoms for Fe, it is possible to increase the moments of Co oxides; this also happens in high oxidation states, $m = 5$ and 6 where the magnetic moment of the Fe oxides is still greater than those of Co; in $m = 4$ where the magnetic moment of the Co oxide is greater than that of the Fe oxide, the $Fe - Co$ mixing is beneficial, with magnetic moments equal to or greater than both magnetic moments of the Co and Fe oxides, particularly the composition Fe_2Co, with a high index of magnetism of excess of 4.

Ni clusters exhibit magnetic saturation with strong parallel couplings. Since Ni has even less d-holes than Co in the active valence states, the spin polarization is lower than in Co which gives rise to smaller local magnetic moments in general. Ni oxide clusters also retain the magnetic moment under oxidation, with three exception Ni_2O_3, Ni_3O_6 and Ni_4O_7, being Ni_2O_3 one of the structural anomalies already mentioned in the previous subsection. In fact, this cluster adopts a bent linear structure with exclusively metal-oxygen bonds which imposes indirect Ni-Ni magnetic couplings mediated by O.

Mixing Fe and Ni has a somewhat similar effect as mixing Fe and Co. In dimers it is beneficial for most oxidation rates, leading to a rather constant moment of $4\mu_B$ for $m < 5$ (except for $m = 4$ with $0\mu_B$ and $6\mu_B$ for $m = 6$), values that at least double the moment of the corresponding Ni_2O_m and explain the high positive value of the excess magnetic moment. Besides, the magnetic moment of $FeNiO_2$ and $FeNiO_6$ is $3\mu_B$ larger than their $FeCo$ counterparts which means that here Ni promotes parallel couplings but not Co. $FeNiO_4$, however, is in a single state associated to the anomalous structure (already

mentioned in the previous subsection) in which no direct $Fe-Ni$ bond exist and thus the indirect $Fe-Ni$ magnetic coupling is mediated by O. In trimers, $Fe-Ni$ alloying only increases the moment at the oxygen concentration $m=4$ and otherwise the pure Fe or Ni oxide clusters perform better. The excess magnetic moment reflects this fact with negative values for most oxidation rates and a marked positive value at $m=4$ for both Fe-Ni alloy compositions, but higher in the case of Fe_2Ni for the same reason as in $Fe-Co$ nanoalloys: the maximum the Fe content with parallel magnetic couplings in the system, the maximum the total moment. In tetramere, alloying is only beneficial for $m=4$ and particularly for $m=7$ where a single Ni impurity is enough to promote the parallel couplings and enhance the total moment of the pure oxides by more than twice. Once the parallel couplings are restored, the moment drops as the relative concentration of Fe reduces, that is as going from Fe_3NiO_7 to $Fe_2Ni_2O_7$ and to $FeNi_3O_7$ due to the lower spin-polarization in Ni than in Fe and the corresponding lower contribution to the total moment. We note that $m=7$ is an oxygen rate at which the structures of the pure and binary TM tetramer oxides are similar, but that this is not essential for the above magnetic trend to be fulfilled. For instance, the same can be observed in Fe-Ni trimer nanoalloys for $m=4$ despite the fact that nanoalloys have a structural arrangement different from that of the pure TM oxides. The excess magnetic moment of tetramer oxides also reflects the benefit of alloying particularly for those oxygen rates.

In Co-Ni oxide nanoalloys, for dimers and form the point of view of maximizing the total magnetic moment, $Co-Ni$ oxide clusters with $m=2$ and 7 are the best performing one. The magnetic moments of Ni oxides clusters increase, by substituting some of its atoms for Co, being the excess magnetism indices equal to 2, 1 and 4 for $m=2$, 3, $m=5$ and $m=7$. The only case where the index of excess magnetism is negative is $m=4$, although we emphasize that there is a degenerate state (with magnetic moment equal to 5 and excess index equal to 1, at 0.01 eV). For larger sizes, $n=3$ and $n=4$ this trend is maintained for all m values. For $n=4$, the nanoalloy with equal number of

Co and Ni stands out with magnetism excess greater than 2 for $m = 3$ to 7.

5.3 conclusions and perspectives

Mixed transition metal oxide nanoparticles were studied for small sizes (dimers, trimers and tetramers). We have found many promising results from the point of view of the magnetic properties. The nanoalloys formed by Co and Ni (dimers, trimers and tetrameres) preserve the magnetic moment of the unoxidized clusters and increases for some oxidation rates. For dimers, the three nanoalloys (FeCo, CoNi and FeNi) have a magnetic moment of excess bigger than zero, for almost all oxidation rates (except $m = 4$ in $CoNi$ and $FeNi$) In the case of trimmers the best alloys are those that involve Co and Ni, especially Co_2Ni, for which the magnetism of excess is always equal to or bigger than that of its pure counterparts. While the best nanoalloys are formed by Fe and Ni, where for almost all oxidation rates the magnetic moment is less than for the pure clusters Fe_3O_m and Ni_3O_m. Finally, for the tetramers, all the nanoalloys of Co and Ni have a magnetic moment of excess bigger than or equal to that of the pure clusters for almost all oxidation rates (except for $CoNi_3O_6$). The three alloys (Co_3Ni, Co_2Ni_2 and $CoNi_3$) are magnetically favorable. The alloys of Fe and Co follow the same behavior as the pure iron oxides clusters, with a high magnetic moment for a low oxidation rate and low magnetic moment when the system is saturated with oxygen. In this chapter we have found that the alloys of Fe and Ni, are good from the magnetic point of view when they are oxidized. This opens the way to the study of larger clusters of this alloy. Finding larger systems that are able to preserve the magnetic moment against oxidation, would have great applications in different areas such as nanomedicine.

Chapter 6

Titanium oxide nanowires and clusters.

Ese niño ajeno al paso de las horas y que
está poniendo en marcha su reloj no es
consciente de que incuba el mal de aurora
ese mal del animal que ya soy yo.
Luis Eduardo Aute.

We studied the structural, energetics, and electronic properties of free-standing $(TiO_2)_N$ nano-wires with different cross sections (Section 6.1). The DFT SIESTA code is used with the PBE form of the GGA to the exchange and correlation to relax the structures following standard protocols. The $(TiO_2)_N$ nano-wire considered are of two different forms: i) built by linear superposition of regular blocks with different cross sections of Ti atoms (2, 3 and 4) based on the ground state cluster reported in the literature for (TiO_2), ii) built by the superposition of any of the two following low-energy clusters reported in the literature: by Zheng-Wang (110) or by Aguilera-Granja (111), or by Salazar-Villanueva (112) and their respective coworkers. Our results prove that in general prolate-like nanowires are stable in a variety of forms. This property allows us to define families according to their characteristics building blocks which define their cross sections. All of these linearly grown objects are energetically stable and they could be essentially grown to any length. However, the electronic properties vary enormously among the different families and within

the families the length of the particle serves as a modulating parameter to control their properties. In this way a variety of systems going from insulators to conductors with some intermediate semiconductor characters could be found. Their polarities also present changing properties which can be controlled by the geometrical parameters. All in all these systems appear as systems that could be tuned to a desired electronic behavior by choosing the appropriate building block, direction of growth and length of the chain.

Also, we report the structural, energetics, and electronic properties of free-standing binary clusters $(TiO_2)_{10}$ with substitutional metallic and non-metallic impurities (Section 6.2). The selected $(TiO_2)_{10}$ cluster has tetrahedral symmetry and is the putative low energy structure for this size. The substitutional impurity can be located at a vertex (4 sites) or at an edge (6 sites). The former has a binding energy only 0.03 eV/atom less than the latter, so they can be considered as almost degenerate. A total of 28 impurities are considered in the present report. We study the edge substitutional place since this environment is very similar to the corresponding one in the bulk, which makes these system a model for the bulk-like structures. Another advantage of the cluster considered here is that its energy gap is as large as the one presented in the bulk phases (anatase an rutile). This system allows us to mimic the bulk behavior without the use of intrasite Coulomb corrections (U) usually applied to the $3d$ orbital electrons of Ti atoms U_d and $2p$ orbital electrons of the O atoms U_p; they are generally applied as parameters to fit the real energy gap observed in bulk (TiO_2) systems. We show results for the formation energies, energy gaps and magnetism suggesting a way to control the band gap by means of the use of the appropriate impurity used in the substitution.

6.1 Titanium dioxide nanowires

The main goal of these calculations is to minimize the binding energy E_{b}, which is defined as the total energy per atom in the following way:

$$E_{\mathrm{b}}[(\mathrm{TiO_2})_N] \;=\; \frac{E_{\mathrm{Total}}[(\mathrm{TiO_2})_N] - NE_{\mathrm{atom}}(\mathrm{Ti}) - 2NE_{\mathrm{atom}}(\mathrm{O})}{3N}\ . \quad (6.1)$$

where $E_{Total}[(TiO_2)_N]$ is the total energy of the system, $E_{atom}(Ti)$ and $E_{atom}(o)$ are the corresponding individual atomic energies for Ti and O respectively, and $3N$ is the total number of atoms within the cluster.

Once the binding energy stabilizes according to previously defined protocol the structure is accepted as stable.It can be noticed that the binding energy decreases (it becomes more negative) as the length of the particle increases which is one indicator for stability. Of course this is a local energy minimum and other indicators should also be considered to reach a true minimum. For the purposes of this work it is enough to bear in mind that the proposed one directional growth is feasible.

6.1.1 Building blocks

The wire-like structures will be progressively grown from seeds or building blocks preserving the cross section with periodic translational symmetry along a predetermined direction. Fig. 6.1 presents four of such building blocks. Diagram (a) presents a single $(TiO_2)_2$ building block designated as D-2 which will be used to build the thinnest wires with the only condition that the number of O atoms with a single bond has been minimized (since free oxygen atoms mean less stable structures (111)); Diagram (b): Two views of a structure of $(TiO_2)_{10}$ according to Zheng et al. (110) designated as K-10 from now on. Diagram (c): Two views of the structure of $(TiO_2)_{10}$ according to previous work by Aguilera-Granja and coworkers, (111) designated a A-10 from now on. Diagram (d): presents two views of the structure of $(TiO_2)_{14}$ (designated as SP-14 from now on), which is obtained by truncating the SP-19 (112) structure mentioned above (5 Ti atoms on one end are eliminated so a single square pyramid with 14 Ti atoms is left, thus allowing for more structural combinations in the growing process).

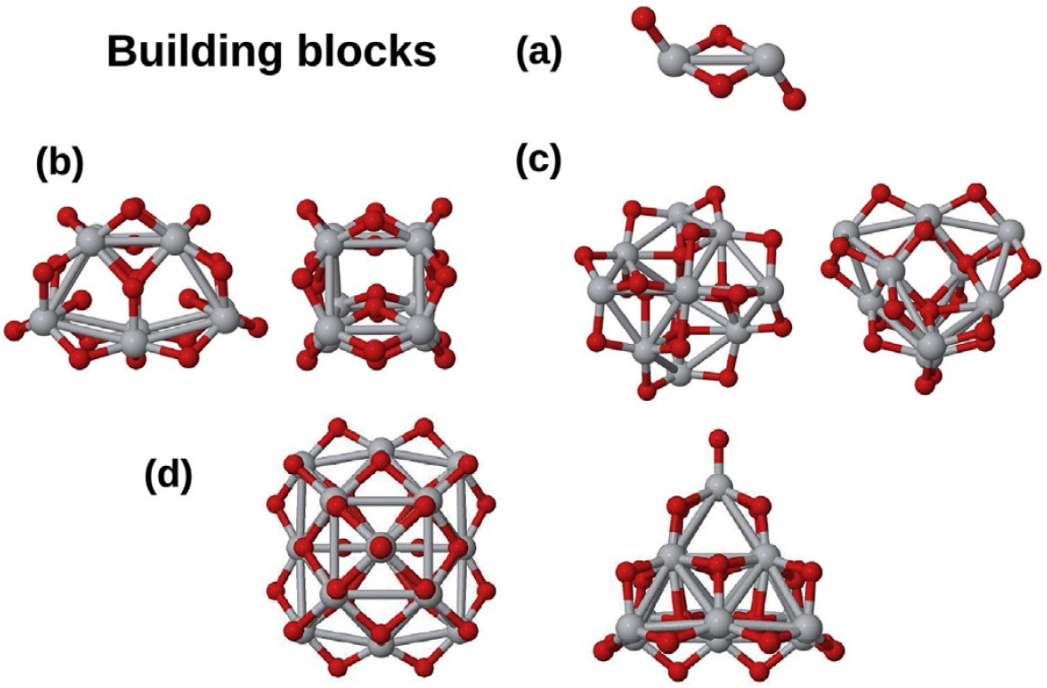

Figura 6.1: Building blocks used for growing elongated structures: (a) basic unit D-2 with a single pair of Ti atoms; (b) K-10 structure (10 Ti atoms) ; (c) A-10 structure (10 Ti atoms), SP-14 (14 Ti atoms).

Following previous definitions particles with N Ti atoms using D-2, K-10, A-10 and SP-14 seeds will be designated as D-N, K-N, A-N, SP-N respectively. A large number of elongated structures were tried using these building blocks but we will report only those prolate clusters with minimum number of single bonded O atoms and the lowest binding energy for each size.

6.1.2 Geometry of K-N structures

Fig. 6.2 presents the structures built along the direction perpendicular to the pentagon formed by the Ti atoms in K-10 (Fig. 6.1(b)), which is the most natural linear growing direction. Clusters are presented at intervals of 5 in the number of Ti atoms. It is also possible to grow prolate structures along

a different direction, however such structures present severe reconstructions; moreover it is necessary that the incoming portions of the growing structure alternate orientation to cancel curvature. From now on we refer only to the chains based on K-10 following the growing direction illustrated in Fig. 6.2.

The average interatomic distances and the average coordination numbers are presented in Table I. As it can be seen the coordination number for O atoms in these structures is 2 approximately with just very few single bonded O atoms, which is an indication for stable structures. Two cut off criteria are used in this Table to define nearest neighbors which has implications in the coordination number: 3.2 Å and 3.6 Å. Structures stop at $N = 40$ due to calculation limitations and not due to stability of the rods; this point will be discussed below.

6.1.3 Geometry of A-N structures

Fig. 6.3 presents the structures built along one of the two equivalent growing directions based on A10 (Fig. 6.1(c)). The lowest energy structures of this series are shown here.

As it can be seen the coordination number for O atoms in most of these structures is 2 (which is corroborated in the lower part of Tables I). However the rod for $N = 26$ leaves 4 single bonded O atoms at the ends. We will come back to this point in the discussions below. Structures stop at $N = 40$ due to calculation limitations and not due to stability of the wires.

In general both A-N and K-N geometries present a bimodal distribution of nearest-neighbor distances. This fact is already present in the volumetric phases (for rutile and anatase) where a sharper bimodal distribution maximizing at two distances First Nearest Neighbours (FNN) and First Nearest Next Neighbours (FNNN) can be observed with approximate values of 3.0 Å and 4.5 Å respectively, corresponding to first and second neighbors of Ti-Ti pairs in the bulk. (111, 113)

The fact that both A-N and K-N allow a growing procedure at small steps is the main reason to develop Table I for these structures only. Moreover, they

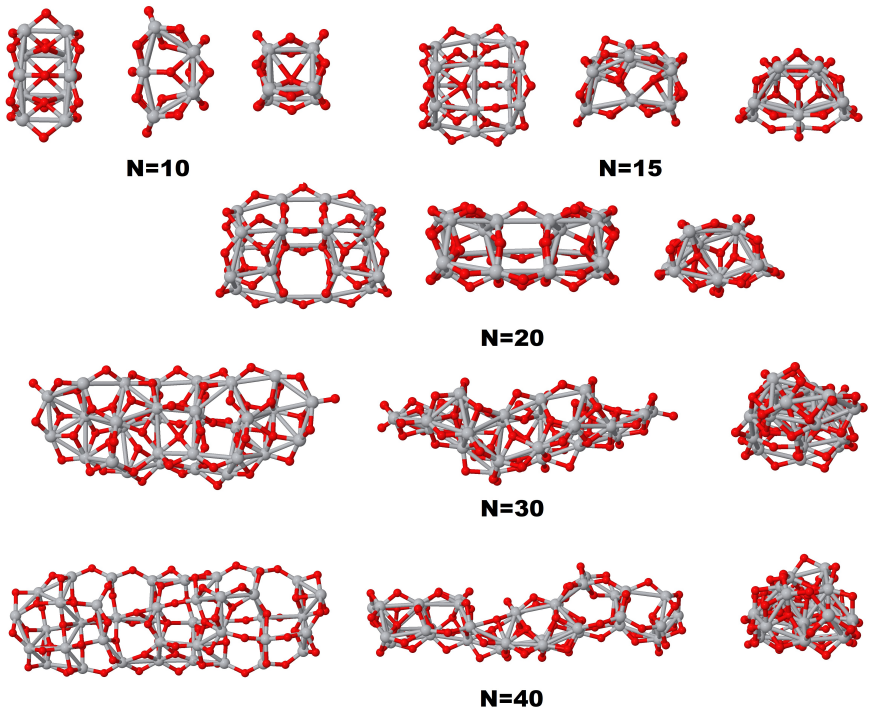

Figura 6.2: View along the 3 orthogonal axes for the generated K-N rod-like structures using building block K-10 (Fig. 6.1(b)) as a seed along one possible direction as discussed in the text. N is the total number of Ti atoms in the particle.

both reach $N = 40$ exactly.

6.1.4 Geometry of the thin structures

Fig. 6.4 shows 3 families of thin wires constructed by means of the building block illustrated in Fig. 6.1 (a). (Top) Four structures with cross section formed by 2 Ti atoms designated D-N from now on (D-8, D-12, D-16 and D-22 are shown); (Center) Five structures with cross section formed by 3 Ti atoms in a triangle designated by T-N from now on (T-9, T-12, T-18, T-24, and T-30 are shown); (Bottom) Four structures with cross section formed by 4 Ti atoms in a rhombus (almost a square) designated by Q-N from now on (Q-16, Q-24,

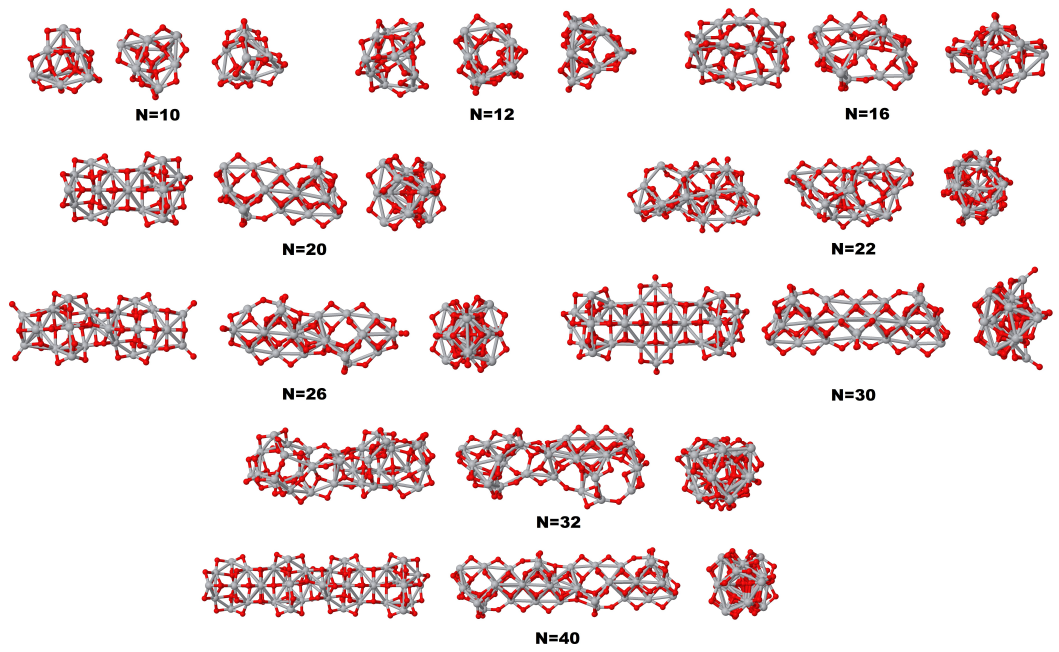

Figura 6.3: View along the 3 orthogonal axes for the generated A-N rod-like structure using the building block A-10 structure as a seed. Only the low-energy configurations of the A-N series are shown. N represents the total number of Ti atoms.

Tabla 6.1: Geometrical properties of the $(TiO_2)_N$ wires. The first column identifies the family and length of the rod; second and third columns give the nearest-neighbor interatomic distances in Å; the fourth column gives the Ti-Ti coordination numbers (second one in parentheses) according to the two distance cut off criteria given in the text; the last column gives the coordination number for Ti-O proximity. The K-N family is presented on the top of the Table while the A-N family is presented in the bottom part of the Table.

Size N	Ti-Ti Dist.	Ti-O Dist.	Ti-Ti Coord.	Ti-O Coord.
K-10	2.924	1.914	2.80(3.00)	2.20
K-15	2.910	1.895	1.87(3.33)	2.03
K-20	2.984	1.937	2.10(3.50)	2.17
K-30	2.972	1.959	3.20(3.93)	2.07
K-40	2.971	1.926	2.53(3.87)	2.09
A-10	2.967	1.957	3.60(3.60)	2.20
A-12	2.948	1.929	3.67(3.75)	2.09
A-16	2.952	1.919	3.87(4.16)	2.09
A-20	2.998	1.949	3.65(3.68)	2.25
A-22	2.997	1.940	3.23(3.23)	2.14
A-26	2.957	1.972	2.96(4.23)	2.31
A-30	2.948	1.971	3.93(4.53)	2.27
A-32	2.958	1.943	3.78(4.27)	2.28
A-40	2.951	1.960	3.50(3.95)	2.39

Q-32, Q-40 are shown).

As it can be seen single bonded O atoms lay at the ends of these structures only, which is an indication for low binding energies. All of these series could be indefinitely continued without apparent stability problems. We stopped at the previous largest structures due to calculations limitations only.

The average interatomic distances and the average coordination numbers for the thin structures formed by 2, 3 and 4 Ti atoms in the transversal section (D, T and Q, respectively) are presented in Table II. We are using here the same two cut-off criteria as in previous Table I. We observe here a behavior similar to that of K-N and A-K structures in Table I regarding to the Ti-Ti and Ti-O interatomic distances. The differences are observed in the coordination number (number of neighbours) as expected due to the reduced cross section of this family.

6.1.5 Geometry of SP-N structures

Fig. 6.5 presents the structures built based on the structure of the SP-14 (square pyramid with 14 Ti atoms) building block presented in (Fig. 6.1 (d)). Since this seed is bulkier than all the others the rod-like structure is harder to realize. To overcome this point still preserving the symmetry of the building block we connect successive blocks in different ways but always using the 4-fold symmetry axis of the pyramid as the growing direction.

So the members of this family are: the seed itself SP-14, with 9 Ti atoms in the square basis one at each vertex, one in the middle of each side and one at the center of the square basis, then 4 atoms at the vertices of a square at middle height and finally just one atom at the top; SP-18 formed by two pyramids pointing in opposite directions and sharing the basis without the atom at their centers (this is a "hollow" structure); SP-19, which is the same as previous one with the atom at the center of the common basis; SP-26 two truncated pyramids with their basis in opposite directions without the atom at the top; SP-27 same as before but with the common atom at the top; SP-32 which is formed from SP-27 just adding the single middle square and the atom on top (5 Ti atoms) to complete the pyramyd on any of the two basis; SP-37 just does the same on the other extreme thus leaving a symmetric prolate structure.

6.1.6 Binding energy of all structures

In spite at times the rod shape is not perfectly achieved the idea is that the overall growing direction prevails when adding new TiO_2 molecules and relaxing the energy until a local minimum is found. Each one of the previously defined growing mechanisms (K-N, A-N, SP-N, D-N, T-N and Q-N) will be called a family or series from now on, and each member of a family has a unique N number of TiO_2 "molecules". The binding energies for all previously described structures are reported in Fig. 6.6.

Several comments related to this figure follow next. Even for the same N value several stable structures are possible which is along the line of a

Tabla 6.2: Geometrical properties of the thin wires with sections formed by 2 (D family), 3 (T family) and 4 Ti (Q family) atoms. The first column identifies the family and length of the rod; second and third columns give the nearest-neighbor interatomic distances in Å; the fourth column give the Ti-Ti coordination numbers according to the two distance cut off criteria given in the text (second one criteria is in parentheses); the last column gives the coordination number for $Ti - O$ proximity.

Size N	Ti-Ti Dist.	Ti-O Dist.	Ti-Ti Coord.	Ti-O Coord.
D-8	2.88	1.89	2.75(3.50)	2.12
D-12	2.94	1.89	3.17(3.67)	2.17
D-16	2.96	1.90	3.37(3.75)	2.31
D-22	2.98	1.95	3.54(3.82)	2.36
T-9	2.98	1.86	0.67(3.11)	1.89
T-12	2.97	1.86	0.50(3.33)	1.92
T-18	3.02	1.86	0.78(3.44)	1.97
T-24	2.93	1.86	0.50(3.50)	2.00
T-30	2.93	1.86	0.40(3.60)	2.00
Q-16	2.87	1.83	0.75(2.83)	2.06
Q-24	3.01	1.94	2.71(3.83)	2.33
Q-32	3.15	1.94	3.31(4.19)	2.47
Q-40	3.03	1.94	3.83(4.10)	2.52

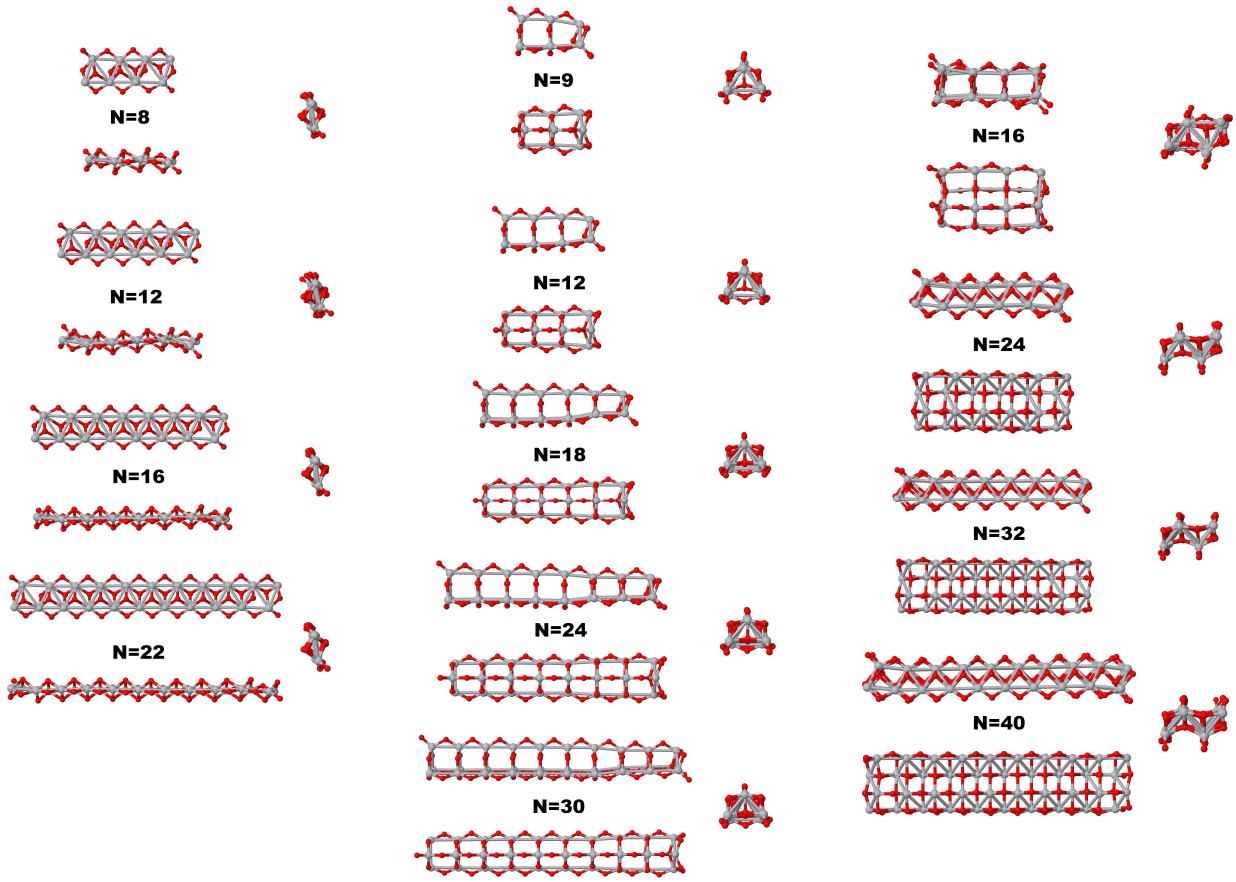

Figura 6.4: Views along the 3 orthogonal axes for the generated K-N rod-like structures using building blocks: D-N with a pair of Ti atoms (left side), T-N with a triangle of Ti atoms (medium side) and Q-N with a rhombus of Ti atoms (right side)

.

previous discussion recalling that even in the bulk several (at least three) phases are possible. These prolate structures remain stable (decrease their binding energy) as N grows. Both K-10, A-10 and SP-14 building blocks lead to stable structures growing along previously defined directions. Some of the structures growing from the tetrahedral base (A-10) and those built from the pyramidal seed (SP-14) have slightly lower binding energies than other particles with approximately the same stoichiometry. However, even these binding energies are over the extrapolated line joining the optimized tetrahedral base (A-10) and the bulk binding energy ($N \to \infty$). This feature is more clearly appreciated when the comparison is done with a fully tetrahedral structure with $N = 20$ (shown by the asterisk in Fig. 6.6, which appears as independent of the chain structures) whose binding energy is lower than any prolate structure reported in this figure. This cluster is the ground state structure for the N=20 system ($(TiO_2)_{20}$) (113). This means that all of the stable particles in the chain represent possible structures based on local energy minima, which nevertheless are quite stable allowing for further directional growing minimizing the binding energy even more. Differences among different families are only of the order of few % (less than 4%), which means that the binding energies of the rod-like clusters of TiO_2 are comparable among themselves.

The main electronic properties of the structures reported here are presented in Fig. 6.7: (Top) gives the size dependence of HOMO-LUMO energy gaps over 1 eV; (Bottom) presents the electric dipole per atom for the chains, when it is relevant. The variety of values obtained for the HOMO-LUMO gaps suggests different electronic behaviors. Some of them showing insulator-like behavior (IX(a) and (b)) for gaps of a few eV and others approaching a metallic character (IX (c)) for gaps of just a few meV.

Let us first discuss the energy gaps in Fig. 6.7 (Top). Chains D-N are in the insulator rank with practically constant gap over 2 eV. Most of the wires A-N and K-N present a well established insulator behavior, with the exceptions of A-26 and K-30 which tend towards a hard semi-conductor character; actually these cases are shown as local minima in terms of energy-gap size dependence.

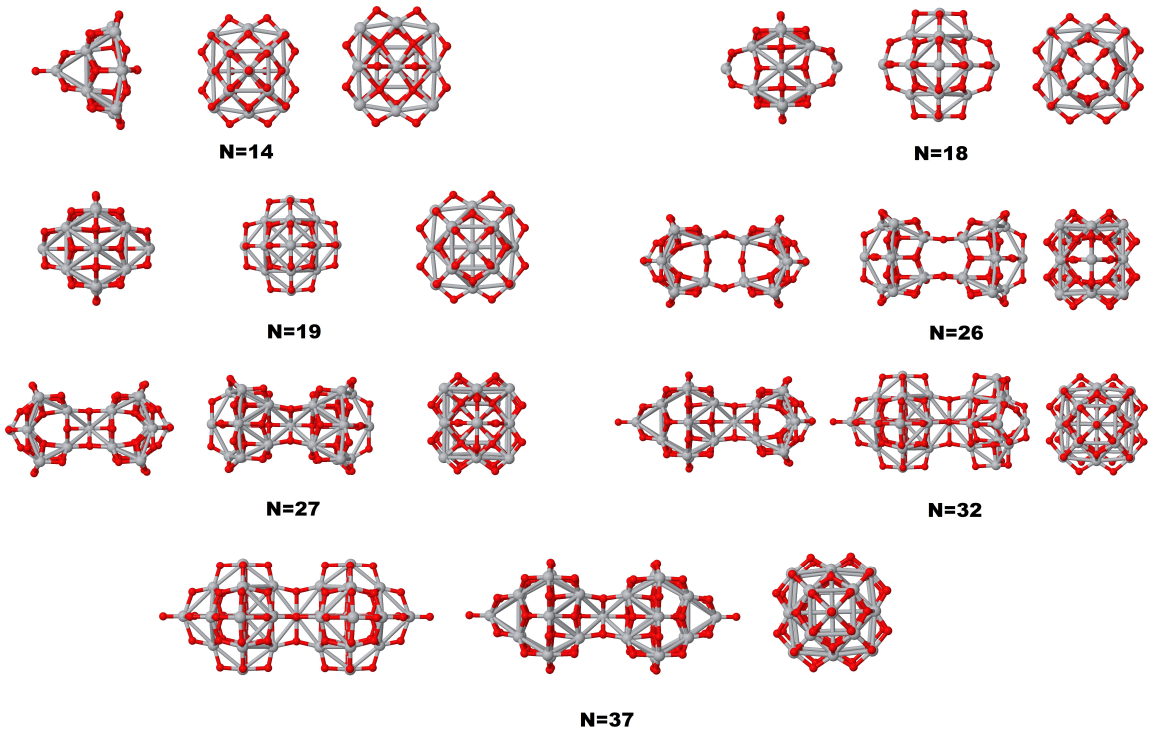

Figura 6.5: Views along the 3 orthogonal axes for the generated K-N rod-like structures using the building block SP-10 with cross sections based using on the SP-N seed. N is the total number of Ti atoms.

The family SP-N presents a mixed behavior with a semiconductor character for N=14, 18 and 19, then could behave as insulators for N=26 and 27, to jump to a low-gap semiconductor for N=32 and 37.

All the series Q-N presents well defined semiconductor-like character with an almost size-independent gap around 1.4 ev (between Si and InP in bulk systems) for the whole range of sizes. On the other hand the T-N series (not shown in the figure) presents a weak semi-conductor character with a relative small gaps in the case of small N values mainly due to finite size effects and due to the Ti dangling bonds that introduce electronic state into the gap. However in the limit when N goes to infinit a hard insulator behavior is observed for this nanowires.

The oscillations in the dipole moment presented in Fig. 6.7 (Bottom) are very impressive. High values are obtained for the short particles with triangular cross sections, while the dipole moment vanished completely for A-10 and A-30. Weak behavior is present in elements of different chains like A-26, T-30 and K-40, which have electric dipole per atom with very similar low value. However, it is not possible to obtain a general tendency for the electric dipole of these small nanorods, except T-N where two regions are clearly observed: high dipolar values for sizes smaller than N=24 and a jump to a small value for next larger size. The SP-N family shows no dipolar character with the only exception of the seed N=14 which has the highest dipolar moment of the whole series.

Previous results are interesting in the sense that the conducting character and the polarizability of these systems could be tailored both by the seed (cross section) and length of the wire. Thus, for instance, if a semiconductor with a high polarizability is needed this could be the case of K-30 with a band gap of about 1.6 eV (in between GaAs and CdSe) and an average dipole moment of about 0.5. A complete variety of systems could be available if the growing mechanisms is properly tuned. An additional problem is the deposition of the nanowires on a substratum, and how the electronic properties of the free standing systems are affected when supported. Therefore our present work is

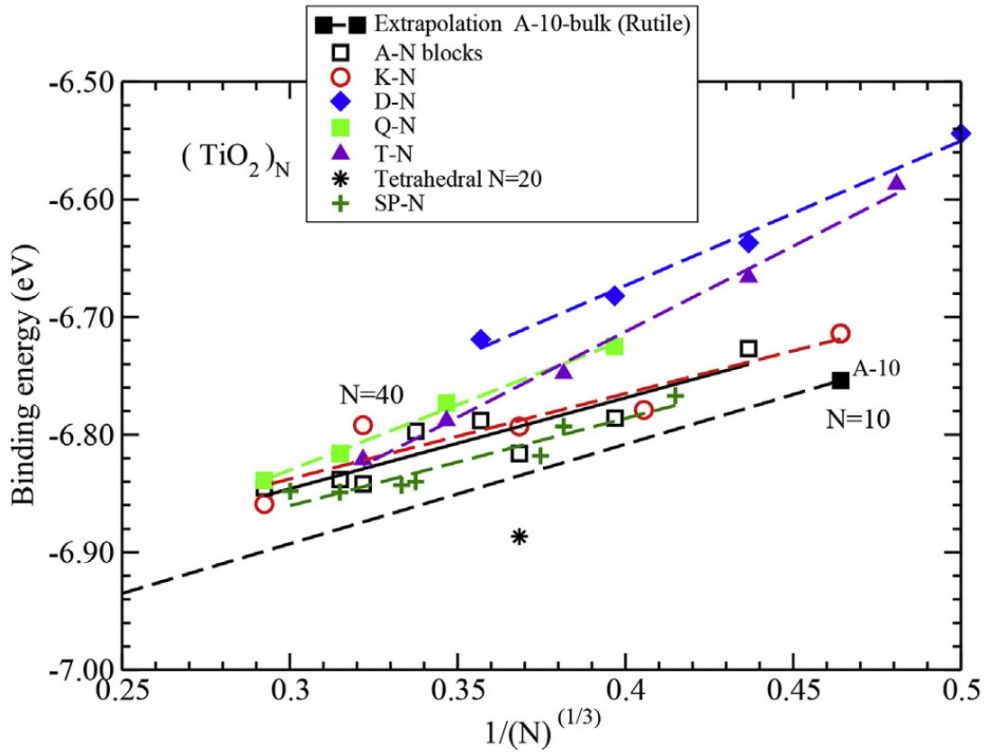

Figura 6.6: Binding energy as a function of $1/N^3$, where N is the number of Ti-atoms in the cluster. All families considered in this paper appear in this plot. The lines are a guide to the eyes only. Notice that D-N, T-N and Q-N results fit fairly reasonably linear dependencies. The asterisk represents the binding energy of the tetrahedral particle with $N = 20$ Ti atoms.

a first step in this direction as a variety of possibilities could be focused onto particular goals.

6.1.7 Vertical energies and density of states

The vertical ionization potential (VIP) and the vertical electron affinity (VEA) are defined as

$$\text{VIP} = E_{(\text{TiO}_2)_N^+} - E_{(\text{TiO}_2)_N} , \tag{6.2}$$

$$\text{VEA} = E_{(\text{TiO}_2)_N} - E_{(\text{TiO}_2)_N^-} , \tag{6.3}$$

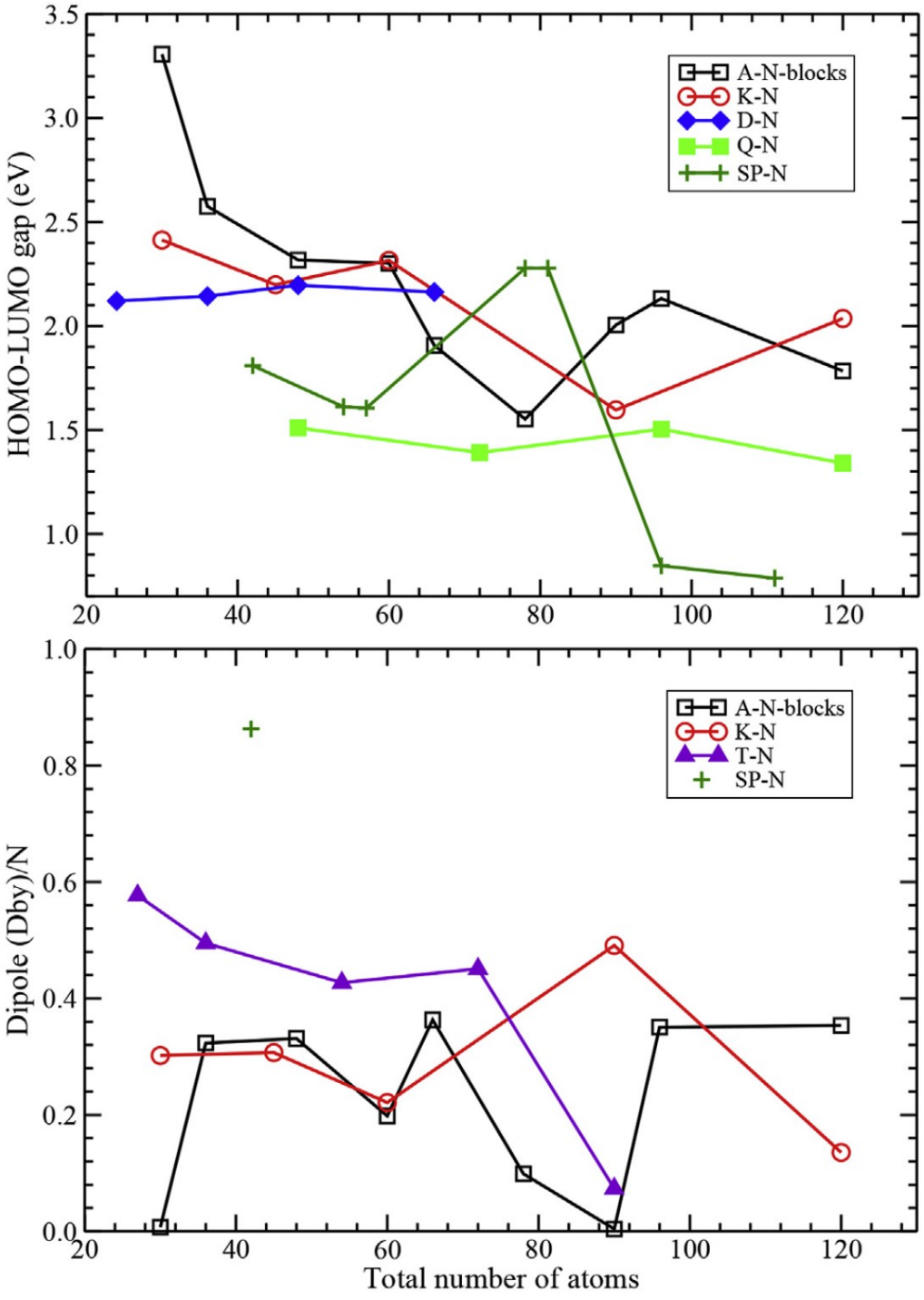

Figura 6.7: In the top panel the gap (HOMO-LUMO) in eV and the electric dipole in the low panel for the different series of the nano-wires considered here. The T-N family does not show gap except for the smallest one that has a 0.34 eV gap (non shown in the figure). For the electric dipole results the D-N and the Q-N series have practically negligible values.

where $E_{(TiO_2)_N^+}$ and $E_{(TiO_2)_N^-}$ are the total energies for the respective anionic and cationic systems with the same structure as the optimized neutral one, while $E_{(TiO_2)_N}$ is the total energy of the neutral system coming from the optimization.

In Fig. 6.8 we present the VIP and the VEA for the nanowires based on the A-10 and the K-10 building blocks as functions of the total number of atoms (3N) in the clusters. The lines are an aid to the eye to illustrate the size dependence of these functions for each family. The general behavior is as it could be expected: an almost monotonic decrease (increase) is observed for VIP (VEA) with some smooth oscillations slowly converging to some value. The results reported here for VIP and VEA are in agreement with previous calculated theoretical values reported for clusters (111).

We can also fix the number of elements and move through different families to observe the changes in the electronic properties. This is done in Fig. 6.9 for N=12, looking at the total density of states for A-12 (a), D-12 (b) and T-12 (c) that are plotted with respect to a common energy axis. The energy gap decreases from top to bottom, which approximately resembles the cases of an insulator (a), a semiconductor (b) and a metal (c). Fig. 6.9(Top) showed that the electronic character of the particle can be tuned by the length of the wire; Fig. 6.9 now shows that the cross section can also be used as a design control for these particles thus providing a bast parameter space to reach the desired properties. It is important to notice that the main contribution to the HOMO (p-orbitals) comes from the O atoms in the case of the insulator-like nanowires. On the other hand, it is the d-orbitals of the Ti atoms the main contribution to the LUMO. In the case of the metallic-like systems the d-orbitals from the Ti atoms are dominant at the neighborhood of the Fermi level. This behavior is also observed for the electronic occupation of the HOMO and LUMO states in the case of the insulator and metallic-like characters for large sized nanowires in our calculations.

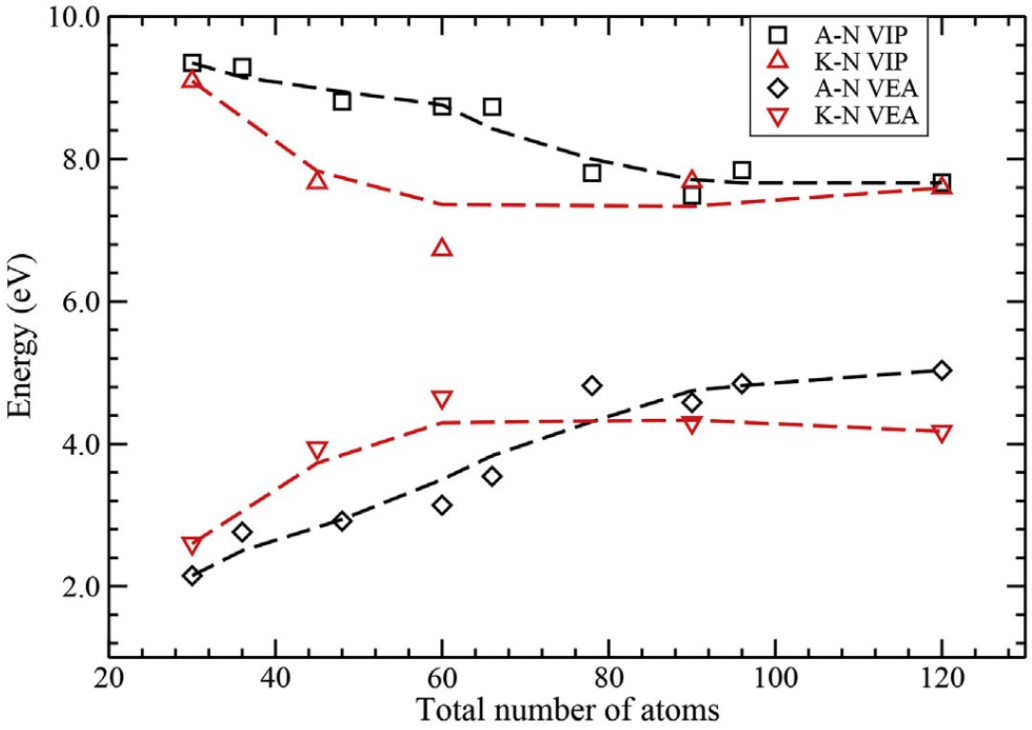

Figura 6.8: Vertical Ionization Potential (VIP) and Vertical Electron Affinity (VEA) for the nanowires base on A-10 and K-10 building blocks as functions of the total number of atoms (3N).

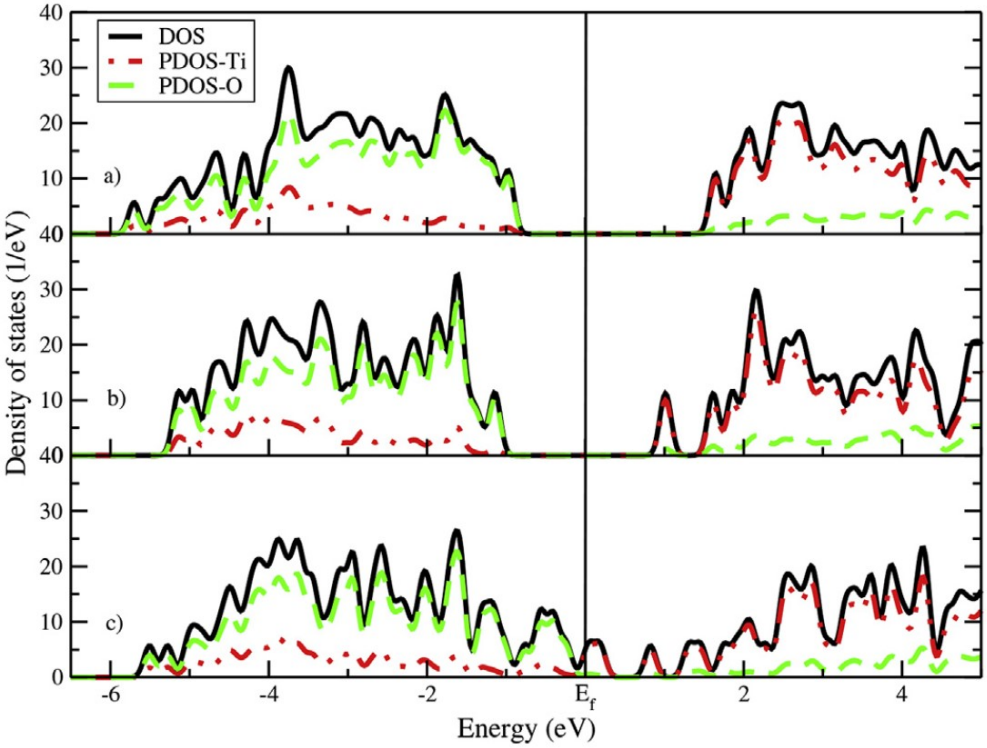

Figura 6.9: Total Density of states (continuous line) and for components Ti (dot line) and O (dash line) for (a) A-12, (b) D-12 and (c) T-12. The nano-wires (a) and (b) are insulators, where as nanowire (c) shows clearly metallic-like behavior.

6.2 $(TiO_2)_{10}$ clusters with impurities

We study the structural, energetics, and electronic properties of free-standing binary clusters $(TiO_2)_{10}$ with substitutional metallic and non-metallic impurities. The selected $(TiO_2)_{10}$ cluster has tetrahedral symmetry and is the putative low energy structure for this size. The substitutional impurity can be located at a vertex (4 sites) or at an edge (6 sites). The former has a binding energy only 0.03 eV/atom less than the latter, so they can be considered as almost degenerate. A total of 28 impurities are considered in the present report. We study the edge substitutional place since this environment is very similar to the corresponding one in the bulk, which makes these system a model for the bulk-like structures. Another advantage of the cluster considered here is that its energy gap is as large as the one presented in the bulk phases (anatase an rutile). This system allows us to mimic the bulk behavior without the use of intracity Coulomb corrections (U) usually applied to the $3d$ orbital electrons of Ti atoms U_d and $2p$ orbital electrons of the O atoms U_p; they are generally applied as parameters to fit the real energy gap observed in bulk (TiO_2) systems. We show results for the formation energies, energy gaps and magnetism suggesting a way to control the band gap by means of the use of the appropriate impurity used in the substitution.

6.2.1 Atomic configurations

Most of the present work is based on a particular $(TiO_2)_{10}$ cluster, which presents tetrahedral symmetry and has proven to be the most stable geometrical structure for a TiO_2 cluster so far, it is worth noticing this cluster presents an energy gap comparable to the bulk gap (3.31 eV) (111). There are two possible sites as candidates for admitting a substitutional impurity: at the vertices and at the edges of the $(TiO_2)_{10}$ tetrahedron. Both sites offer low energy conditions in comparison with any interstitial inclusion of impurities. In general, the most favorable site for a substitutional impurity is the vertex. However, for most of the impurities the energy differences with respect to the

edge site is less than 0.03 eV/atom, which makes these two configurations as almost degenerate even at zero temperature which is the case in the present study. Coordination number at a vertex are very seldom in the bulk, while conditions at an edge site are more similar to what substitutional impurities will find on the surface of materials. Since in this work we want to stay close to systems that mimic the bulk behavior we will mainly focus on impurities occupying the edge sites. In such cases the local coordinations of Ti-atoms is related to the six-fold coordinated sites in both rutile and anatase phases, where six oxygens occupy positions as first nearest neighbors. In addition the $(TiO_2)_{10}$ cluster presents 4 vertex positions and 6 edge positions as shown in Fig. 6.10 a) and b); so in equal energy conditions it is an edge position the most likely one, which we can extend to the nearly degenerate case to some extent.

Besides considering the Ti edge position as substitutional site for all impurities, we also considered the natural substitution of O by non-metallic atoms. Namely, we considered elements with $2sp$ and $3sp$ configurations substituting an O atom located at an edge close to the previously considered position for the substituted Ti atom (the selected O atom to be replaced is shown in Fig. 6.10(b) with the (SI) label) . Results are presented in the Table C.1 of the Appendix C and will be discussed inthere.

Another advantage of using this finite cluster as a model for bulk behavior is that it reproduces the main characteristics of the density of states of the bulk concerning the type of energy levels and even the energy gap (111). This last point is very important since a finite size bulk calculation (atomic base plus periodic boundary conditions) aiming to produce the appropriate energy gap would need approximations that would imply hybrid functionals or adjustments in the intra-sites interaction U by means of extra terms GGA+U or LDA+U, as already mentioned above but here we discuss it more broadly (114, 115, 116, 117, 118), These corrections to the Coulomb contribution (U) are applied to the $3d$ orbital electrons of Ti atoms U_d and $2p$ orbital electrons of the O atoms U_p as adjustable parameters to fit the energy gap close to the values observed

in bulk (TiO_2) systems. Empirical rules for using parameters U_d and U_p can be seen in Parks' work (114), where it is shown how the gap can be adjusted as much as desired. This fit has two disadvantages: on one hand it introduces energy terms difficult to interpret in reality, while on the other hand it implies costly computer calculations. We propose to avoid all of this by using a cluster which from the very start possesses a band gap and density of states similar to the bulk system without the introduction of fitting parameters.

6.2.2 Results

In Fig. 6.10(a) and (b) we present two different views of the geometrical structure of the $(TiO_2)_{10}$ cluster considered here: light gray balls represent Ti atoms, small red balls are Oxygen atoms and a green ball represents an impurity on one of the 6 edge positions. Fig. 6.10(c) highlights the environment of the substitutional impurity in the $(TiO_2)_{10}$ cluster. For comparison, Fig. 6.10(d) shows the environment of the substitutional impurity for the rutile phase.

The optimized geometrical structure after relaxation shows small deformations that depend on the impurity. In general, for the case of the *sp* elements the local symmetry is broken and the impurity is displaced towards one of the Ti atoms (depending on the valence of the impurity). These new positions tend to open the two faces of the tetrahedron not connected to the impurity in a way that resembles the wings of a flying butterfly; this effect is more pronounced for the light elements. Exceptions are Al and Si whose presence leaves the pure cluster structure basically unaltered. In the cases of impurities involving the $3d$ and $4d$ TM the tetrahedral geometric structure is only slightly altered and only small deformations modulated by the atomic radius sizes are presented; this effect is also observed for the middle and late $5d$.

The density of states (DOS) of the $(TiO_2)_{10}$ pure system (putative Ground State (GS) structure) is presented in Fig. 6.11. The occupied electronic levels are marked by horizontal lines under the curve while the energies of the empty states are left unmarked. The system presents a clear insulator behavior with a band gap of 3.31 eV, which has already identified as very close to the energy

gaps for the anatase and rutile bulk phases. The gap was calculated by means of the HOMO and LUMO states. As the different dopants are considered the values of the HOMO and LUMO energies change accordingly, however it is important to use the DOS given in Fig. 6.11 for the pure system as a reference when discussing the electronic properties of the doped structures.

The binding energy $E_{\rm b}$ of the altered system Ti_9XO_{20} (X is a specific impurity for each system), defined as the total energy per atom, is obtained in the following way:

$$E_{\rm b}[({\rm Ti_9XO_{20}})] = \frac{E_{\rm Total}[({\rm Ti_9XO_{20}})] - 9E_{\rm atom}({\rm Ti}) - E_{\rm atom}({\rm X}) - 20E_{\rm atom}({\rm O})}{30} \,. \quad (6.4)$$

Once the binding energy converges according to the protocol described in previous Section the structure is accepted as stable. The binding energy (in eV/atom) is illustrated in Fig. 6.12 using the atomic number of the impurity as the abscissa.

It is interesting to notice that the variation of binding energy values for this set of 29 systems are contained in a range of about half eV per atom only and all of them lay near or under -7.0 $eV/atom$. Actually the most stable structure remains the pure system for $Z = 22$. In general the binding energy stability decreases almost in a monotonic way as a function of the atomic number within each series; exceptions are observed for Si, Cr and Mn and some inflections for the $4d$ and $5d$ series.

If we use the pure system as a reference we can say that the variations in the binding energy are always positive and in the range of 0.08 and 0.5 eV/atom. The smallest differences appear at the beginning of the series increasing from there with the atomic number.

The formation energy is defined as:

$$E_{\rm Formation}[({\rm Ti_9XO_{20}})] = E_{\rm Total}[({\rm Ti_9XO_{20}})] - E_{\rm Unrelaxed}[({\rm Ti_9O_{20}})] - E_{\rm atom}({\rm X}). \quad (6.5)$$

Results for this function are presented as open circles in Fig. 6.13 using the atomic number as the abscissa. For comparison the previously discussed

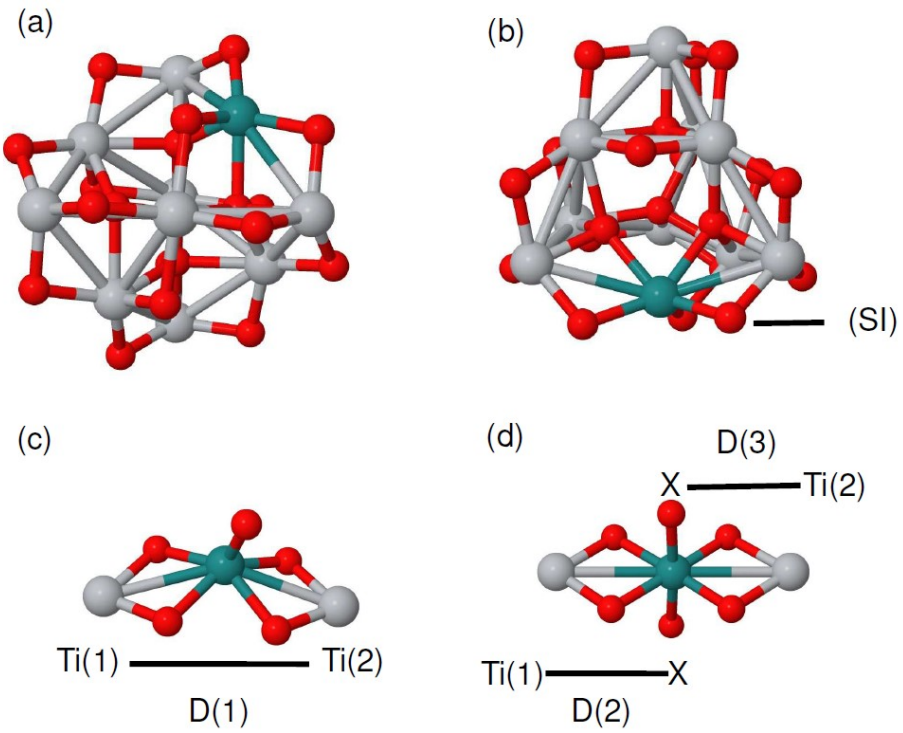

Figura 6.10: In (a) and (b) two views of the cluster $(TiO_2)_{10}$ used in most of the present calculation. Oxygen atoms are represented by small (red) balls, Ti atoms are represented by clear large balls; the edge site to be occupied by the impurity is marked in darker color. The local environment surrounding the impurity in the cluster is shown in (c). The equivalent environment for the bulk rutile phase is shown in (d). Distances $D(1)$, $D(2)$ and $D(3)$ are used in Eq. (3).

binding energy results are superposed here as small filled circles; the different scale for these two different energies is apparent. The ordering in the series is similar to the one observed for the binding energy per atom with Si, Cr and Mn altering the monotonic dependence with the atomic number. Inflections points are again present for the $4d$ and $5d$ series.

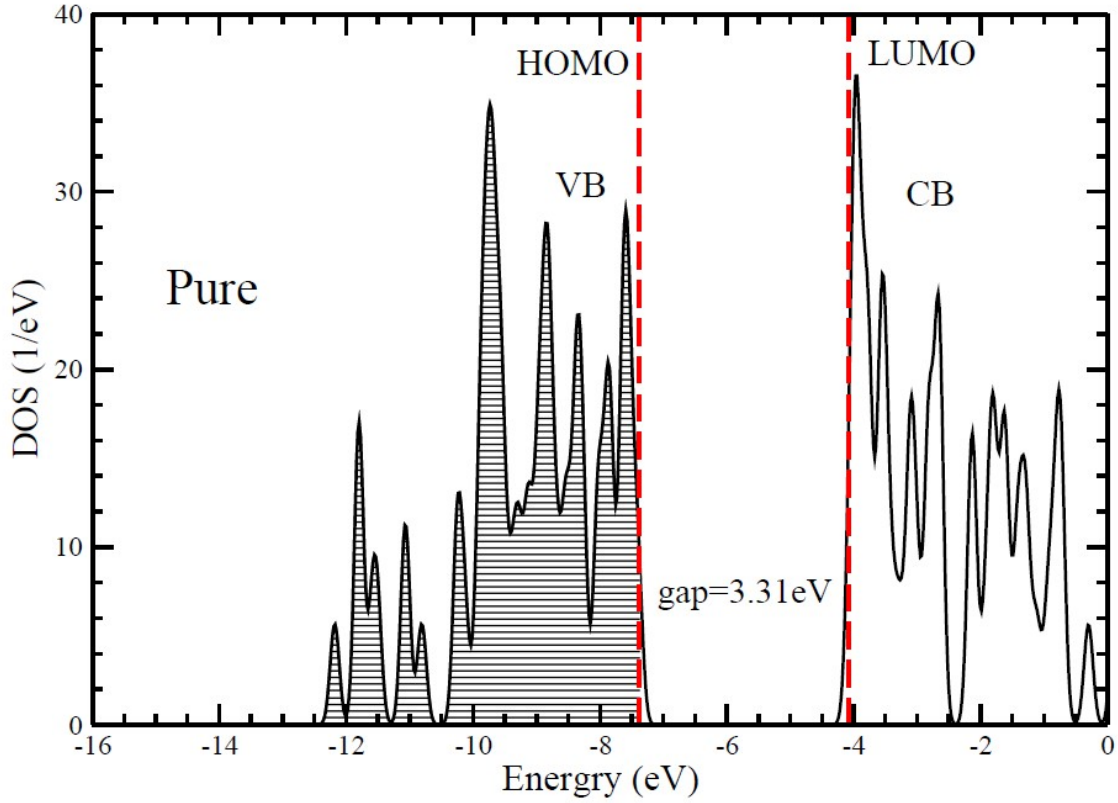

Figura 6.11: Ground state DOS for the cluster $(TiO_2)_{10}$ to be used as a reference for the DOS in the presence of impurities. The dashed vertical lines mark the gap of the system considering the eigenvalues of the problem. Horizontal lines indicate the occupied states. VB (CB) stands for Valence (Conducting) Band.

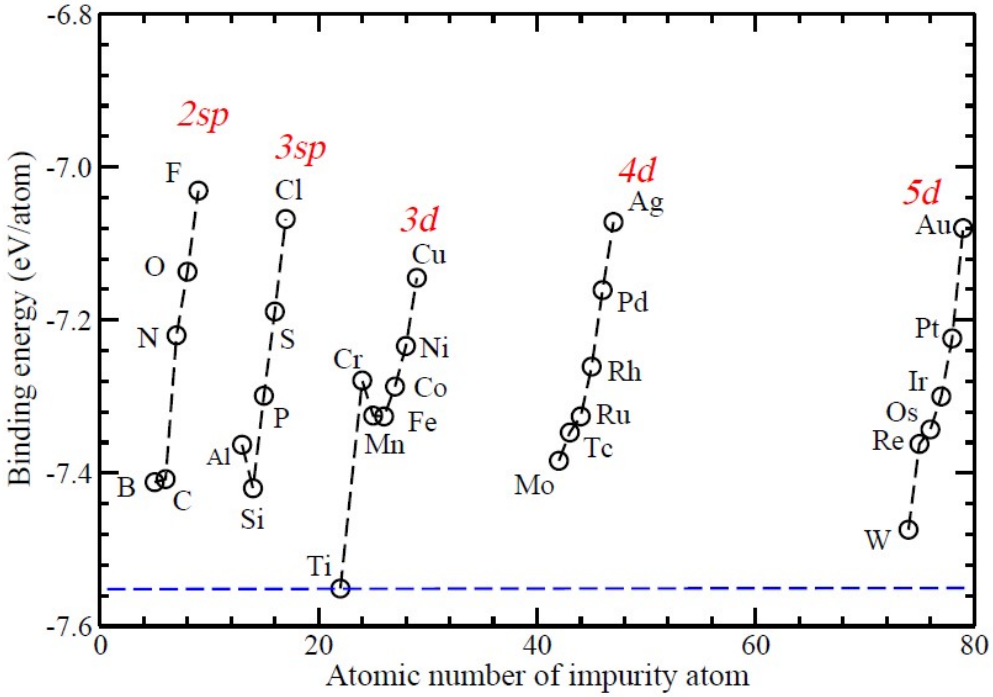

Figura 6.12: Binding energy for the Ti_9XO_{20} system doped with the different impurities. The horizontal dashed line corresponds to the undoped system (Ti as a fake impurity) to be used as a reference.

Results for the geometrical properties of the clusters Ti_9XO_{20} are presented in Table 6.3, separated by series according to the electronic labeling. In first column we list the impurities (and its atomic number in parenthesis). The second column gives the number of oxygen neighbors to the X-impurity in the structure. Twin columns three and four give the two different Ti-X distances on the same edge (the impurity is usually displaced from the central position). Column five gives the average Ti-X distance obtained from the values in previous columns. Column six renders the value for the deformations parameter D as defined by Eq. 6.6 in terms of the distances shown in the Fig. 6.10:

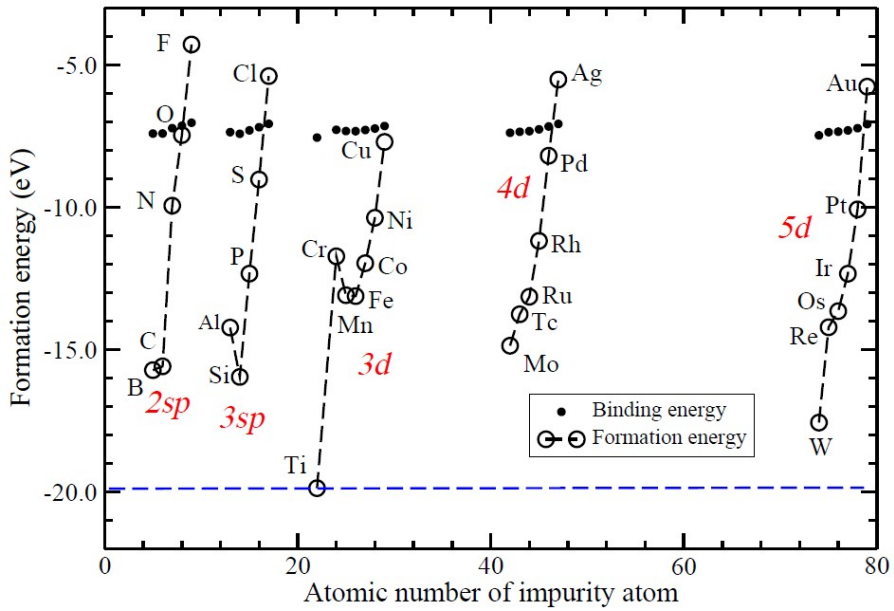

Figura 6.13: Formation energy (open circles) for the Ti_9XO_{20} system with the different impurities. Additionally, previously reported binding energies are also included here by means of small filled circles. The horizontal dashed line corresponds the pure case.

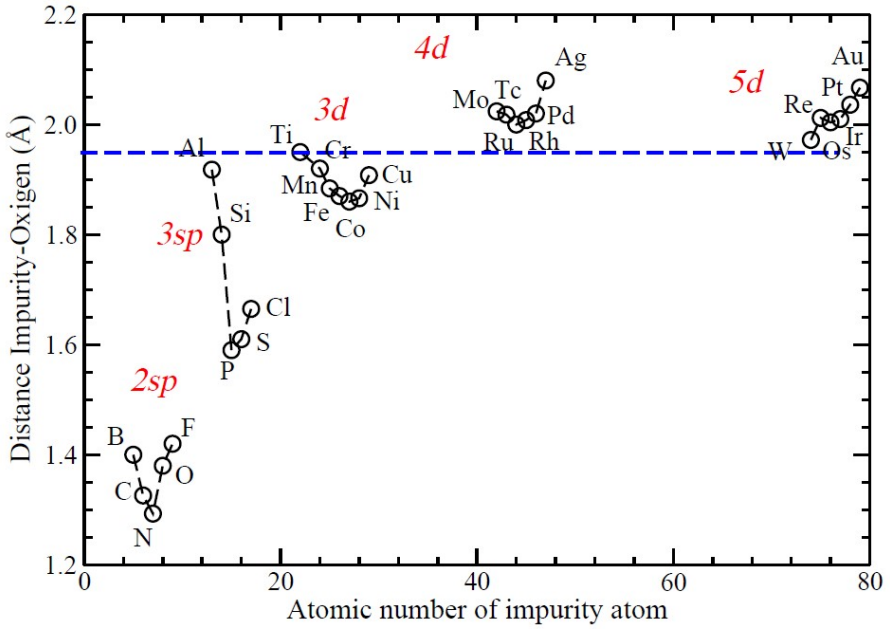

Figura 6.14: Interatomic distance X-O for the Ti_9XO_{20} systems for the different impurities. The horizontal dashed line corresponds to the $Ti-O$ distance to be used as a reference.

$$D = \frac{D(1)}{D(2)+D(3)} , \tag{6.6}$$

where $D(1)$ is the direct distance between the two Ti atoms on the edge where the impurity is placed, while $D(2)$ and $D(3)$ are the distances between the X-imputity and the Ti atoms on that edge. For example in the case of F(W) the direct distance $D(1)$ is 6.382 (5.548) Å, $D(2)$ and $D(3)$ are 3.820 (2.980) and 6.090 (3.010) Å, respectively, then the deformation parameter is $D = 0.644$ (0.952) which corresponds to the largest (lowest) deformation for the system included in Table 6.3.

In Fig. 6.14 we present the interatomic X-O average distances, which present a grouping according to the electronic properties of the series but the dependence with the atomic number is non monotonic. The group $2sp$ presents the shortest X-O distances, with X=N as the true minimum. The $3sp$ series presents a larger distribution of distances with X=P at the minimum. The

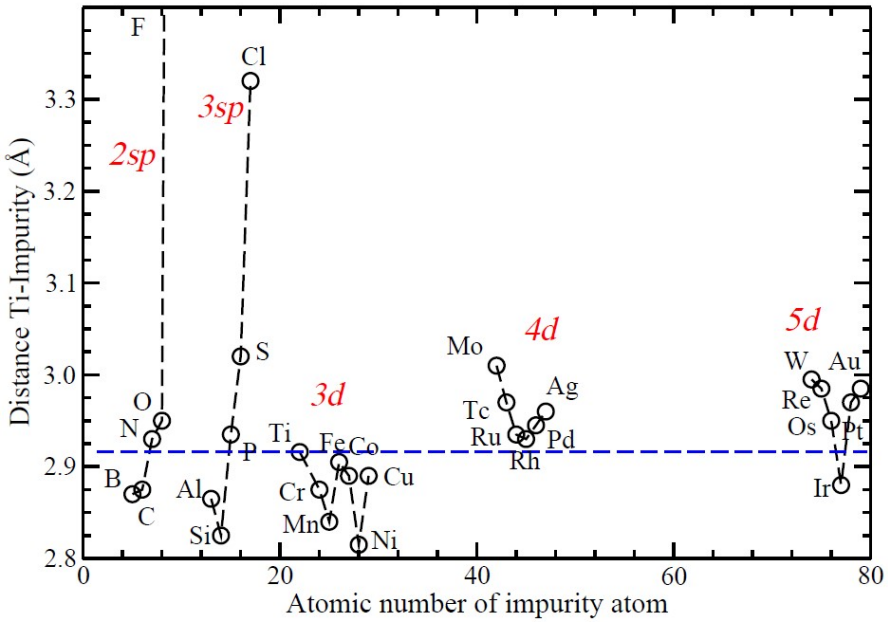

Figura 6.15: Interatomic distance $Ti - X$ for the Ti_9XO_{20} systems for the different impurities. The horizontal dashed line corresponds to the $Ti - Ti$ distance in the pure system to be used as a reference. The value for F is out of scale (almost 5 $\AA$).

Tabla 6.3: Geometrical properties of the system. In column one is the type of impurity and its atomic number (Z) in parenthesis, in colum two the number of oxigen neighbours, in column three the two different Ti-O distances on the edge where the impurity was placed, in colum four the average distance using the twin colums, and finally in column six the deformation parameter as defined in Eq.(3).

Impurity X (Z)	Num. Oxygens Neighbors of X	Distances($\AA$) Ti-X(1) and Ti-X(2)	Ave. Distance ($\AA$) Ti-X	Deformation Parameter
$2sp$				
B (5)	3	2.810, 2.930	2.870	0.871
C (6)	3	2.820, 2.930	2.875	0.871
N (7)	3	2.960, 2.900	2.930	0.870
O (8)	2	2.960, 2.940	2.950	0.846
F (9)	1	3.820, 6.090	4.955	0.644
$3sp$				
Al (13)	5	2.850, 2.880	2.865	0.969
Si (14)	5	2.790, 2.860	2.825	0.961
P (15)	3	2.730, 3.140	2.935	0.932
S (16)	2	3.120, 2.920	3.020	0.940
Cl (17)	2	3.430, 3.210	3.320	0.830
$3d$				
Ti (22)	**5**	**2.870, 2.960**	**2.916**	**0.957**
Cr (24)	5	2.830, 2.920	2.875	0.965
Mn (25)	5	2.800, 2.880	2.840	0.972
Fe (26)	4	2.910, 2.900	2.905	0.940
Co (27)	4	2.900, 2.880	2.890	0.941
Ni (28)	5	2.780, 2.850	2.815	0.982
Cu (29)	4	2.920, 2.860	2.890	0.931
$4d$				
Mo (42)	5	2.980, 3.040	3.010	0.950
Tc (43)	5	2.930, 3.010	2.970	0.966
Ru (44)	5	2.890, 2.980	2.935	0.966
Rh (45)	5	2.900, 2.960	2.930	0.973
Pd (46)	5	2.910, 2.980	2.945	0.985
Ag (47)	4	2.930, 2.990	2.960	0.983
$5d$				
W (74)	5	2.980, 3.010	2.995	0.952
Re (75)	5	2.940, 3.030	2.985	0.961
Os (76)	5	2.910, 2.990	2.950	0.964
Ir (77)	5	2.740, 3.020	2.880	0.976
Pt (78)	5	2.930, 3.010	2.970	0.983
Au (79)	4	2.950, 3.020	2.985	0.983

$3d$ family presents a cloud of distances just underneath the average distance for the undoped system, which is marked by a horizontal dashed line. Both $4d$ and $5d$ families present clouds with values just over the distance for the undoped system. Worth noticing, the X-O average distances for Al and Si are comparable to the $3d$ cloud, which is in agreement with the oxygen coordination number as presented in column two of Table 6.3. The nobel metals tend to present large X-O distances, which is clearly appreciated for the cases of Au and Ag presenting the largest distances in Fig. 6.14. In the $3d$ series the Cu-O distance is large but not large enough and it is the third of the family just under the distance for Cr-O.

The dependence of the average Ti-X distance on the impurity is shown in Fig. 6.15. In the case of the $2sp$ series this distance increases monotonically with the atomic number; when going from B to O it varies from 2.85 to 2.95 $\mathring{A}$, reaching an average value of almost $5\mathring{A}$ for the case of F. The series of $3sp$ presents a Ti-X average distance increasing with the atomic number with the only exception of Si. In the case of the $3d$ series the distances fall in a cloud with values just under the value for the undoped cluster that is indicated by a horizontal dashed line. Both $4d$ and $5d$ series present clouds with values just over the undoped system with a small deviation for the case of Ir.

The deformation parameter presented in column six of Table 6.3 deserves a special discussion. The case of F is by far the one that deforms the most the original structure due to its large electronegativity. From this argument it is not surprising that the next impurities deforming the original system are Cl, O, P and S all of them accompanying F in the upper right corner of the periodic table. On the contrary, the impurities that almost pass unnoticed in deforming the original cluster are Cr, Mo y W which are isoelectronic among them and occupy the fourth column of the transition metal elements. Other d systems deviate only slightly from the reference value 0.957 corresponding to Ti in Table 6.3. Due to the similar environment it can be expected that the general trends presented by our results of valid for small clusters (Table 6.3) are also valid for bulk when the deformation parameter is close to the reference

value (undoped case).

The magnetic moments for all the clusters are presented in Fig. 6.16 with open circles, the local magnetic moments for the corresponding impurity are presented by means of small filled circle. In general, the impurity is coupled to the TiO_2 matrix in a ferromagnetic way, with the exceptions of O for the *sp*-elements and Cr for the TM, both showing antiferromagnetic coupling. Doping with *sp*-elements produce clusters with successive even-odd magnetic behavior according to the atomic number of the impurity, that is non magnetic for even and magnetic moment of $1\mu_B$ for the impurities with odd number of electrons. The main magnetization for these systems comes from the oxygen atoms as can be seen on the left-hand side of Fig. 6.16. The magnetization of the TM-impurities have a less monotonous dependence as illustrated in the same figure; here the main source for the magnetic contributions comes from the TM-impurity, which also explains the amplitude reached by the magnetic moment of the system for some impurities. Chromium is anomalous in the $3d$ series presented in Fig. 6.16, since it presents antiferromagnetic coupling to the matrix. Notice that the total magnetic moment of the system tend to be the same for TM impurities belonging to the same column of the Periodic Table, with with the exceptions of Fe and Co (hard magnetic impurities). The corresponding iso-electronic impurities for Fe (Ru, Os) and Co (Rh, Ir) show different values for the total magnetic moments. There are few reports in the literature on the magnetic properties of impurities in TiO_2, however our results agree with those reported for Mo, Os in volume (119, 120) and Pt in the case of clusters (121).

The cluster $(TiO_2)_{10}$ is almost a non-polar material, that is, its electric dipole moment is practically zero (0.021 Dbys). However, the inclusion of a different element in the matrix produces a redistribution of charge, which can lead to an electric dipole in the system. In Fig. 6.17 we present the charge transferred from the impurity to the matrix. The dashed line in this figure represents the value for the case of the undoped cluster. All those impurities close to this horizontal line lead to an electric polarity equivalent to non-polar

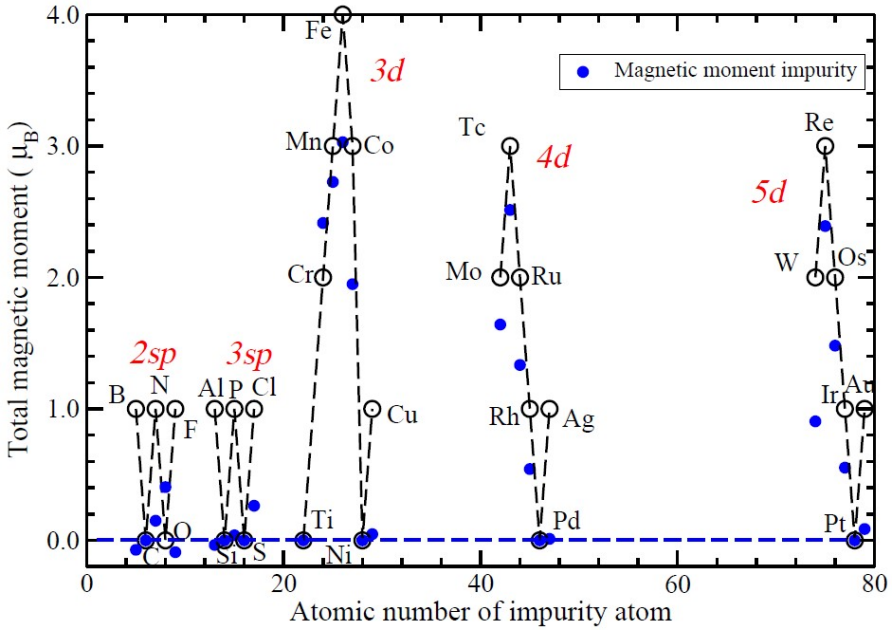

Figura 6.16: Total magnetic moment for the cluster Ti_9XO_{20} indicating the impurities by open symbols. In the cases of Fe, Co and Ni additional calculations with fix-spin value were carried out to be sure that the magnetic solution is the right one. Small filled symbols show the local magnetic moment of the impurities.

systems. The elements that are more distant from this reference line in each series (F, S, Cu, Ag and Au) produce the systems with the largest electric dipoles as can be seen also in Fig. 6.18. In this same figure, it is illustrated how the electric dipole grows monotonically with the atomic number for the $2sp$ series. However, for the other series a zig-zag behavior prevails leaving at the middle of the series the impurities leading to the lower electric dipole of the respective set (P, Mn, Ru and Os).

The most important magnitude to be monitored along the impurity variations is the energy gap of each doped cluster. The reference value is the undoped cluster whose gap is 3.31 eV (very similar to the bulk values in rutile and anatase). Fig. 6.19 shows the energy gaps for doped systems according

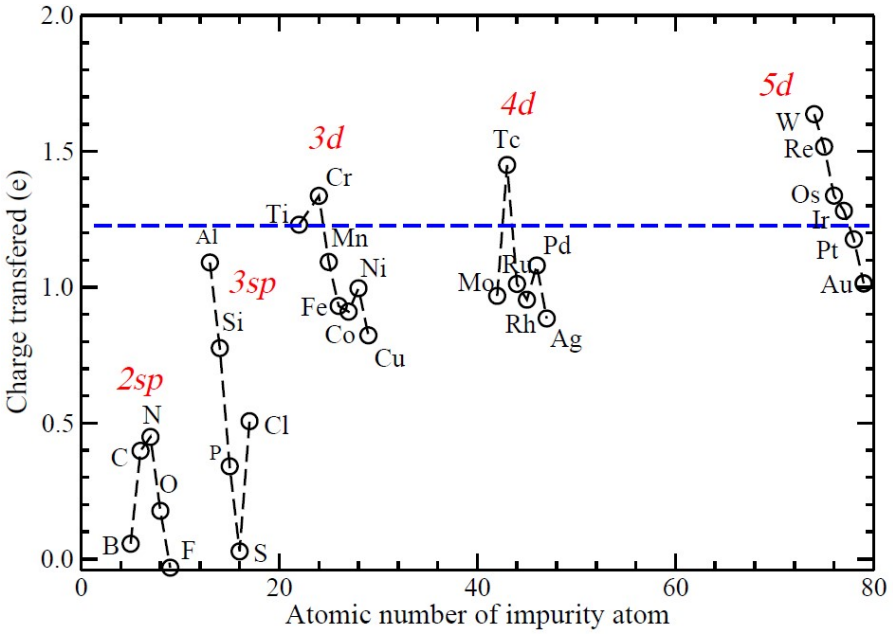

Figura 6.17: Charge transferred from the impurity to the matrix in the cluster Ti_9XO_{20}. The positive value indicates that the matrix lost electrons. Notice that F is the only one gaining electrons although in a marginal way. The horizontal dashed line corresponds to the pure system.

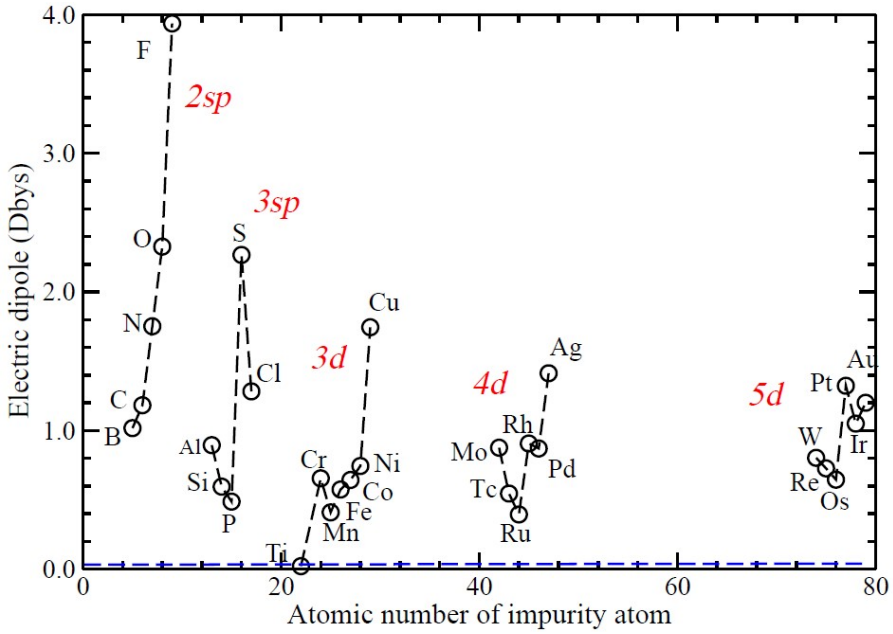

Figura 6.18: Total electric dipole as a function of the different impurities for the Ti_9XO_{20} system. The horizontal dashed line corresponds to the pure system.

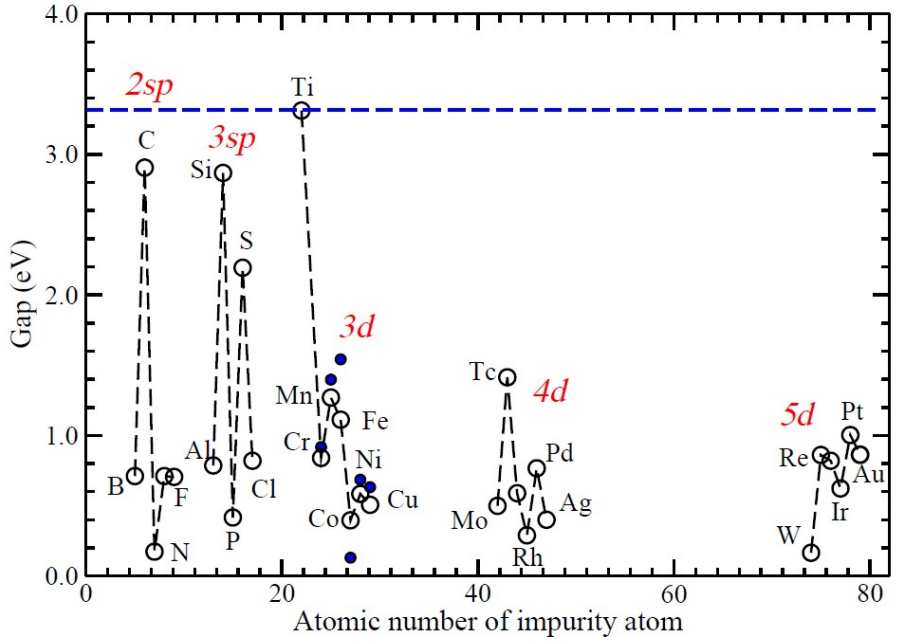

Figura 6.19: Gap as a function of the different impurities for the Ti_9XO_{20} system; the corresponding eigenvalues were used directly in this calculation. Notice the heart rate shape for the results of the *nd*-TM series. The gaps calculated for the system $Ti_{19}XO_{40}$ are given by small filled symbols; this twice as large tetrahedral cluster has similarly energy gap as the Ti_9XO_{20} system. The horizontal line corresponds to the pure system.

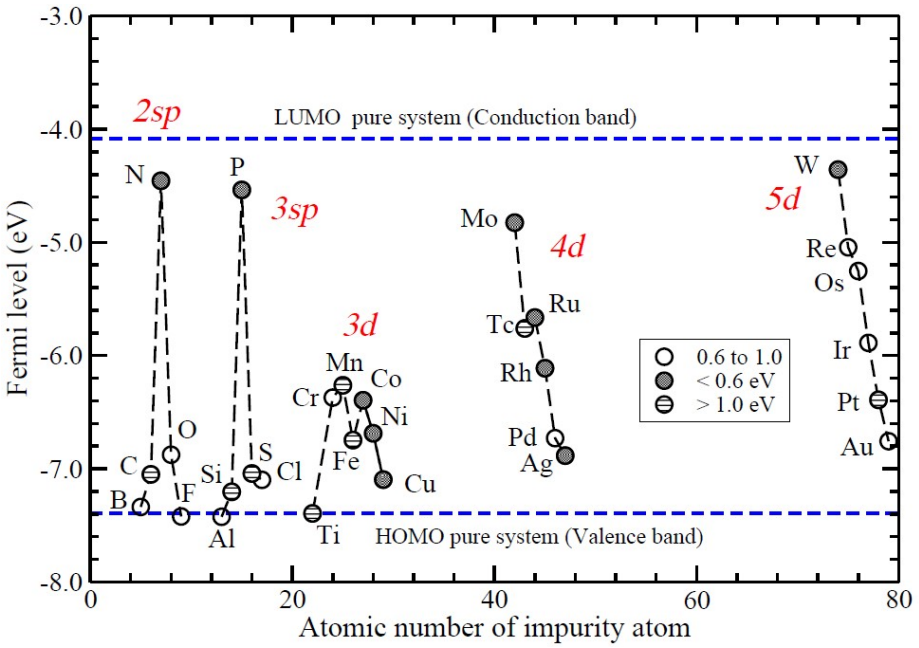

Figura 6.20: Fermi level position as a function of the different impurities for the Ti_9XO_{20} system. Horizontal dashed lines correspond to the HOMO and the LUMO for the pure case as a reference. Open circles correspond to gaps in the range 0.6 to 1.0 eV, grey circles correspond to gaps lower than 0.6 eV, and dashed symbols correspond to gaps larger than 1.0 eV.

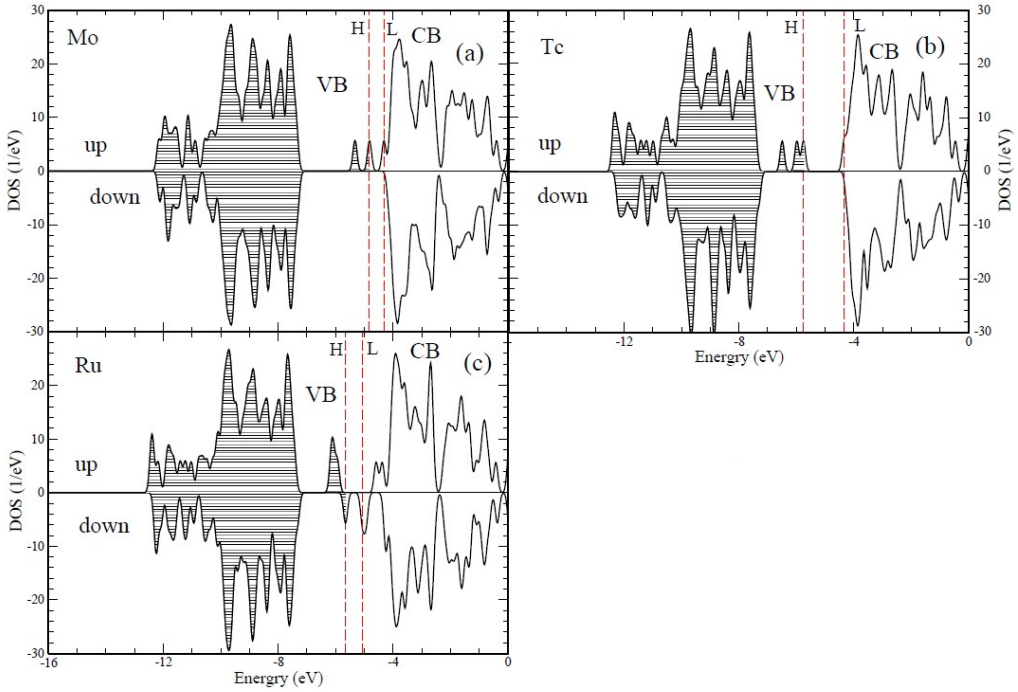

Figura 6.21: Spin-up and spin-down DOS for Mo (a), Tc (b) and Ru (c) impurities in the Ti_9XO_{20} system (initial part of the $4d$ series). The non-monotonous dependence of the impurity levels can be readily appreciated. Vertical lines correspond to the HOMO (H) and LUMO (L) levels. Horizontal lines mark the occupied electronic states.

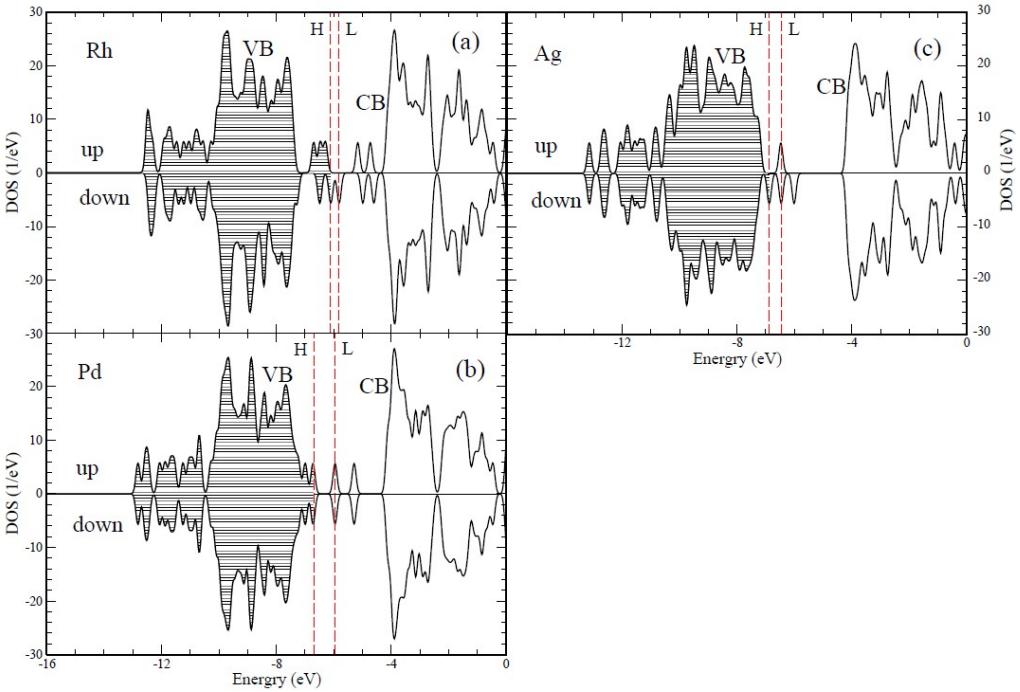

Figura 6.22: Spin-up and spin-down DOS for Rh (a), Pd (b) and Ag (c), impurities in the Ti_9XO_{20} system (last part of the $4d$ series). The non-monotonous dependence of the impurity levels is clearly shown. Vertical dash lines correspond to the HOMO (H) and LUMO (L) levels. Horizontal lines mark the occupied electronic states. Notice the symmetric DOS for the Pd impurity due to its non-magnetic behavior.

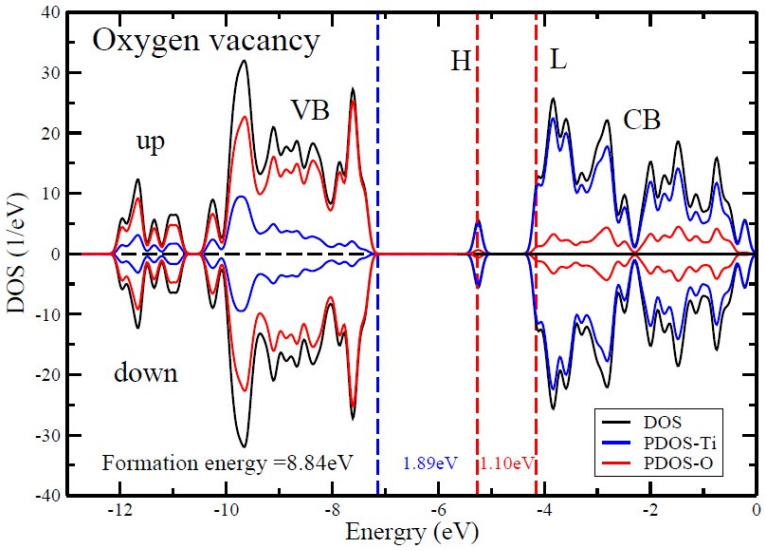

Figura 6.23: DOS for the differents species in the cluster $(TiO_2)_{10}$ with an oxygen vacancy. The results mimic the bulk behavior in a reasonable way.

the atomic number of the impurity. The horizontal dashed line is a reference for the undoped material where Ti is a fake impurity to complete the series.

The first general result is that the gap is extremely sensitive to the type of impurity placed at the edge position. Thus, substituting atoms from the $2sp$ group narrows the gap to a few tenths of eV with the exceptions of C and N: the former keeps the system as an insulator introducing states under the VB, while the latter turns the system into a semi-metal or narrow gap semiconductor with states near the bottom of CB. For the $3sp$ series, Si and S have a behavior similar to C only closing the gap a bit more while P follows the tendency of N in the previous series. The cases of Al and Cl is similar to the cases of B and F atoms.

TM impurities offer a variety of possible gaps ranging from 1.41 eV in the case of Tc to 0.17 for W. So upon choosing the right TM substituting element the energy gap can be tuned between a normal semiconductor to a narrow gap semiconductor with a gradual distribution of possible energy gaps. We are aware that this is a simplified way of classifying the transport properties of these systems since de DOS near the Fermi level also plays an important role here. However, it is offered with the idea of showing a variety of possibilities that could be discussed originating from this useful cluster approach. Moreover, the choice of the right impurity for a given purpose can be combined with other desired properties of the system beyond the transport ones.

It is important to mention that we also calculated the energy gap by means of hybrid functionals (B3LYP) (122). Results are very similar to those obtained using the plain SIESTA code with PBE (123), and presented in Fig. 10 (as well as the comparison in Fig. C.1). The main difference is just a uniform displacement of the values of about 1.96 eV corresponding to the inclusion of a 20 percent Fock interaction (122). However, our model does not require here the inclusion of this type of corrections since due to natural or accidental reasons the band gap of the pure cluster is comparable to the one of the bulk. Then, we can expect that the impurity states will not be absorbed either by the VB or by the CB. All of these results and other electronic properties are

comparatively presented in the Appendix D by Figures C.1, C.2 and C.1Fe3.

A very important condition is the position of the Fermi level E_F for the case of each dopant. These results are presented as circles in Fig. 11, which indirectly tells us the position of the energy levels of the impurity without looking into each density of states. In addition we have also included here as dashed lines the HOMO and LUMO values of the pure system to be used as references. However, it is important to bear in mind that the presence of the impurity may slightly alter these values. The energy gap ranges are given by the color of the circle as indicated by the inset of Fig. 6.20.

We now discuss the different series as presented in Fig. 6.20. For the $2sp$ ($3sp$) group E_F is closer to the HOMO as compared to the pure system with the exception of N (P) which is closer to LUMO; the impurity levels are closer to the VB and/or CB. Occasionally, some impurity present deep levels like in the case of C (Si). The gap ranges from intermediate to large with the exception of the gap of N (P) which is small.

In the case of the $3d$ group (from Cr to Cu) E_F is found in a small region near HOMO progressing towards VB in a non monotonic way; the impurity levels lay in between VB and CB originating both small and large gaps. Cr is particularly interesting since its level lay just in the middle producing and intermediate gap.

E_F descents almost monotonically with the atomic number for the $4d$ ($5d$) series, presenting a "shoulder" for the case of Ru (Os very slightly). In the case of the $4d$ series The impurity levels are in between CB and VB slightly closer to the latter, giving rise to small gaps since E_F is surrounded by impurity levels. Exceptions to this behavior are Tc and Pd: the former produces a large gap since E_F is over the impurity levels; the latter produces an intermediate gap due to the spread of the impurity levels which is larger to any other element of the series. In the case of the series $5d$ the impurity levels are in between the bands descending monotonically from near CB to near VB as the atomic number increases showing a great dispersion. Since the E_F is surrounded by impurity levels intermediate gaps are produced, with the exceptions of the

small gap of W (E_F is over its impurity levels and near CB) and the large gap of Pt (its impurity levels split laying either close to VB or CB).

The spin polarized DOS of Ti_9XO_{20} for the elements of the series $4d$ are presented in Figs. 6.21 and 6.22. The position of the HOMO and LUMO were obtained from the corresponding eigenvalues. For the representation of the DOS we have used a broadening of 0.1 eV, which is the reason for the tails above (HOMO) and below (LUMO). The dashed lines (under the DOS graphic) indicates the occupied states. The VB is at the left of the HOMO (H), while the CB is at the right of the LUMO (L). Starting with Mo (top) the impurity states are in the vicinity of the CB, going to Tc (middle) the states of the impurity go towards the proximity of VB, them, continuing to Ru at the end (botton) the impurity levels are found again towards the center of the band gap. The analysis continues in Fig. 6.22 with Rh (top) where the impurity levels are scattered throughout the gap. As we continue to Pd (middle) and Ag (bottom) we find the impurity levels closer to VB.

Previous results and discussions show in general that a variety of positions for the impurity levels within the gap are found; this is particularly true for the $2sp$, $3sp$ and $3d$ series. Moreover, such positions do not follow any monotonous order with respect to the atomic number as the one presented by the Fermi level in the cases of the $4d$ and the $5d$ series as illustrated clearly in Fig. 6.20. So no a priori behavior can be ventured in general previous to the calculations.

6.2.3 Size effects and comparison

It has been pointed out by Umebayashi (124) that in the case of $3d$ transition metals doped in (TiO_2) rutile, the localized levels shifts to lower energies as the atomic number of the dopant increases. In spite this work does not consider magnetism in the calculation these general results serve as a general reference for related contributions like ours. Actually, this observation is in agreement with our model but only in the paramagnetic case (non polarized calculations) as it can be seen from the position of the Fermi level. Thus, for Cr, Mn, Fe, Co and Ni our results for the E_F are -4.97 eV (gap aprox 0.59eV), -5.22 eV (mini-

gap aprox 0.22eV), -5.75 eV (mini gap 0.12eV), -6.23 eV (gap 0.87 eV) and -6.39 eV (gap 0.59 eV) respectively. As it can be appreciated the E_F tends to lower energies as the atomic number of the impurity increases.

As it can be noticed the impurity concentration is 10 % for the case of our $(TiO_2)_{10}$ cluster without the possibility of reaching lower concentrations. To overcome the difficulty of the high impurity concentration we consider (for this purpose only) the larger cluster $(TiO_2)_{20}$ which has also tetrahedral structure and an energy gap (3.22 eV) very close to the one of $(TiO_2)_{10}$ cluster and also close to the gap of the bulk in pure system. This tetrahedral structure is the putative ground state for $(TiO_2)_{20}$ as demonstrated by F. Illas and coworkers (113). For an edge impurity in the twice as large cluster (5 % concentration) in the case of the paramagnetic regime we get the following Fermi levels: -5.57 (gap= 0.58eV), -5.81 (gap= 0.29eV), -6.27 (mini gap=0.15 eV), -6.89 (gap=0.88 eV) and -7.05 (gap=0.68 eV) for Cr, Mn, Fe, Co and Ni impurities respectively. As it can be seen these results (valid for the paramagnetic case) are only slightly different from those of the smaller cluster and higher concentration (quoted in the previous paragraph). These combined results favor the idea of approaching the bulk behavior with clusters that mimic the main features of the bulk.

Nevertheless, when the spin polarization is considered the dependence of the energy levels with the atomic number is far from lineal as commented in the previous two paragraphs for the paramagnetic case. This is evident from the results presented in Fig. 6.19 which show that this is evan more so for the impurities with strong magnetic character such as the $3d$-TM. As a way to rule out a determinant size dependence we did the same calculations (spin polarized) for the larger cluster, namely $(TiO_2)_{20}$ finding results similar to those of the small cluster used in most of this paper. As an example we list next the comparative results for the $3d$ series ordered as Cr, Mn, Fe, Co, Ni and Cu. In the case of $(TiO_2)_{10}$ we get the following ordered E_F values (and corresponding gaps) -5.96 eV (gap 0.84 eV), -5.62 (gap 1.27 eV), -6.19 (gap 1.11 eV), -6.20 (gap 0.40 eV), -6.40 (gap 0.58) , and -6.84 (gap 0.51 eV) respectively

(open circles in Fig. 6.19). The equivalent results for $(TiO_2)_{20}$ are -6.47 eV (gap 0.92 eV), -6.42 (gap 1.40 eV), -6.64 (gap 1.54 eV), -6.63 (gap 0.13 eV), -7.05 (gap 0.69), and -7.29 (gap 0.63 eV) respectively (small close circles in Fig. 6.19). The values for the energy gap follow the same tendency for both clusters; The Fermi level values are a bit more negative in the larger cluster (15 % at the most) but without changing the behavior observed in the smaller one. These results are important to indicate that the calculations performed with TM impurities in $(TiO_2)_{10}$ have the basic ingredients to mimic the general properties of the bulk (TiO_2) with impurities.

Worth notice that our results for the band gap follow the same behavior as those reported by Y. Wang and coworkers (125) using PBE (123) within the GGA approximation. What the cited work reports are the HOMO-LUMO values with respect to the impurity levels (which is unusual since most of other works use VB and CB of the doped system as reference levels). In any case Wang's results for the HOMO-LUMO (using the VB and the CB as references) are 0.92 eV for Cr, 1.68 eV for Mn, 0.69 eV for Fe, 0.51 eV for Co, 0.23 eV for Ni, and 0.63 eV for Cu, while ours are 0.84 eV, 1.27 eV, 1.11 eV, 0.40 eV, 0.58 eV, and 0.51 eV, following the same sequence. The differences in the values can be due to the fact that Wang's calculations are intended for the anatase phase, and in their calculations the bulk band gap is underestimated (they obtain 2.21 eV instead of 3.2 eV which is the actual value). As presented above, our calculations are more adequate to represent (actually mimic) the rutile phase and strictly corresponds to finite size (cluster with impurities). It is important to underline again that previous results are clearly different from those obtained in the paramagnetic approximation (126), thus showing the importance of performing spin-polarized calculations.

We now discuss the results obtained when an O site of the $(TiO_2)_{10}$ cluster is left empty. We have chosen any of the 4 internal O atoms near the edge Ti atom to study the O vacancy effects. The immediate effect is the surge of a new electronic state with energy 1.16 eV underneath the CB. The corresponding formation energy of this particular $(Ti_{10}O_{19})$ system is 8.86 eV. The

corresponding DOS is presented in Fig. 6.23. On the other hand, experiments have found this electronic state in the rutile phase located in the range [0.7,1.0] eV under the CB which is not far from our calculations (122, 127, 128).

Despite our systems are far to describe all features of a bulk system it is interesting to notice that the tetrahedral local symmetry present in both $(TiO_2)_{10}$ and $(TiO_2)_{20}$ leads to some results similar to those found experimentally for the bulk. Thus in the case of the latter the energy gap is 3.22 eV and the vacancy level is to be found 0.67 eV under the CB, values very close to the experimental ones discussed above or at least the tendency is preserved.

6.3 conclusions and perspectives

TiO_2 can be grown along determined directions in several different structural with patterns leading to elongated stable structures (prolate-like shape). This facility to accommodate atoms in several possible geometries is consistent with the three phases exhibited in the bulk TiO_2 structures. As the systems get smaller the long range crystalline ordering is lost which adds more possibilities thus allowing for different stable particles at the molecular or subnanoscopic level.

Five different families were considered in the present study. One of these families (A-N) presents the tendency to lowest binding energy and the thinnest family (D-N) has the highest binding energy; differences are only in the range of 0.2 eV/atom decreasing rapidly with N, the number of Ti atoms. Moreover, the difference between A-N and K-N families tends to be in the order of few meV/atom.

There is no apparent size limitation and the binding energies minimize as the chains get longer and longer. So these systems could be grown to any desired length without apparent structural limitations.

The electronic properties are diverse among the families. D-N chains present a clear insulating character. Families A-N, and K-N exhibit an oscillating behavior but most structures are insulators. Family Q-N is mostly a semicon-

ductor. The T-N family presents semi-metallic to metallic character. However this general classification must be revised for the actual size of the wire as the energy gap oscillates strongly with the length of the chain for each family.

The polarity of the particles also changes from family to family oscillating strongly with the size of the particle. The T-N family tends to decrease the dipole component with size. The K-N family exhibits strong variations presenting a maximum for N=30, same size at which the family A-N present zero polarizability. The family A-N also has zero dipole moment for N=10, while oscillating for other sizes. So it is not easy to draw general tendencies with size in the case of polarizability.

The challenge is also along the experimental line. We have shown here that there are several cross sections that can support the growth of tiny wire-like TiO_2 chains. Eventually some experimental groups could attempt to achieve this task which could be rewarding due to the variety of properties that could be varied.

We are aware that an additional theoretical problem arises from previous results: the stability of previous structures after deposition on possible substrates. The actual use of these particles require to hold them in space, which requires a surface on which they can be permanently deposited. However, the proximity of other electronic orbitals can modify the properties of the systems which were considered free standing in vacuum in the calculations above. However, that would be a different problem which would require to consider different possible substrates for the families above and others that could be further considered. in our calculation will be the deposition of the nanowires on a substrate, and that electronic properties maybe slightly modify respect to the free standing systems here considered.

The simulated results for edge substitutional impurities in $(TiO_2)_{10}$ in all cases and in $(TiO_2)_{20}$ for some selected cases allow us to give general tendencies of the role of such impurities in TiO_2 in the bulk and in the rutile phase in particular. This is so because these two clusters retain most of the electronic properties of the bulk which makes them good candidates to test the system

at a smaller scale. In particular, the energy gap of the clusters is very close to the corresponding one in rutile (see Fig. 6.11).

The binding energy of the doped $(TiO_2)_{10}$ cluster in general increases as the atomic number of the impurity (See Fig. 6.12), becoming less stable than the undoped system particularly at the end of the series, the smallest deviation in energy is presented by W, and largest ones by F, Cl, Ag and Au. The formation energy follows a similar behavior but in a much wider region of energy values (See Fig. 6.13). The shortest interatomic distances between the impurity and the oxygen atoms are observed for the non-metallic impurities; $TM - O$ distances are slightly different from those of the pure system. The impurities deform the local environment presenting the greatest deformations in the case of non-metallic impurities particularly by F, Cl and S (See Figs. 6.14 and 6.15).

The magnetic moment of the Ti_9XO_{20} clusters is mainly given by impurity (X). Generally, the interaction TM-matrix is ferromagnetic with the only exception presented by Cr where the interaction is antiferromagnetic. The non-metallic impurities do not present a significant magnetization; an alternating even/odd behavior in the total magnetization is presented here (See Fig. 6.16). The charge transfer and the electric dipole show a complex dependence with the atomic number of the impurity; the largest values of both properties are observed for the non-metallic impurities in general (See Fig 6.17 and 6.18). Substitutions impurity doping provides a broad range of possible energy gaps with gradual intermediate possibilities; it is then possible to tune to a desired energy gap by choosing the appropriate impurity (See Fig. 6.19). Naturally, the impurity presence also modifies the Fermi level in a complex way particularly in the non-metallic and the $3d$ impurities; in the cases of $4d$ and $5d$ impurities an almost linear dependence with the atomic number is observed (See Fig. 6.20).

The modification of the impurity concentration reached by the considera-

tion of the larger tetrahedral cluster $(TiO_2)_{20}$ did not modify the main conclusions obtained from the smaller cluster (See Fig. 6.19). The main reasons for this being the fact that the geometric structure in both clusters is tetrahedral and that the DOS are very similar with almost identical gaps. The density of states seems to be one of the most sensitive properties affected by doping in the TiO_2 systems and no clear tendency with the atomic number in the impurity states introduced in the gap of the DOS for the TM was found (See Figs. 6.21 and 6.22).

Additionally we presented results for the DOS in the case of an Oxygen edge vacancy in the case of the original cluster $(TiO_2)_{10}$ (see Fig 6.23). A new electronic state was found under the CB at an energy comparable to the one experimentally reported (122). A similar result was also obtained for an inner edge vacancy in the case of the cluster $(TiO_2)_{20}$. The description of vacancies using this approach is at least plausible.

Although previous results do not necessarily represent the true values for the corresponding properties in the bulk, they give general tendencies of the range of variations these values could have. In addition, they also provide a guide as to which impurity could be tried in a real TiO_2 system to achieve a desired property.

Chapter 7

Small indium oxide clusters.

Si al discutir sientes que tu voz se enciende, ten en cuenta que en igual medida tu razon se apaga.
Luis Eduardo Aute.

Although indium is not a transition metal element, we have decided to study indium oxide clusters in the context of react experimental measurements of fragmentation. In this section, we complement the studies reported in previous chapters by conducting DFT calculations, for indium oxide clusters for which photodissociation experiments exist. We performed a systematic study of the atomic and electronic structures, as well as related properties of $In_nO_m^{0/\pm}$ clusters with n= 1-6 and m = 1-8. We calculated the fragmentation channels of the charged clusters, with particular focus on the cationic ones for which we compared with the experimental results of Knight *et al.* (129).

7.1 Geometrical configurations and electronic properties

In this section we report the geometrical, electronic and stability properties, as well as fragmentation paths of the $In_nO_m^{0/\pm}$ (n = 1-6 and m =1-8) clusters (Fig. 6.1-6.9), with particular emphasis on the cationic ones for which experiments exist.

Tabla 7.1: Results for the adiabatic ionization potential, (IP, in eV), average In-O inter-atomic distance, (R_{In-O}, in Å), and spin magnetic moment (μ, in μ_B) of the smaller indium oxide clusters, compared with previous theoretical results available in the literature.

	$\underline{IP}$			$\underline{R_{In-O}}$		$\underline{\mu}$		
Isomer	Ref.(130)	Ref.(131)	Ours	Ref.(130)	Ours	Ref.(130)	Ref(131)	ours
InO	9.01	8.92	8.89	2.06	2.16	1	1	1
In_2O	8.71	7.61	7.46	1.93	2.07	0	—	0
InO_2	7.62	—	9.94	1.85	1.95	1	—	1
In_2O_2	8.16	—	7.80	1.87	2.13	0	—	0

In Fig. 6.2, 6.4-6.9 are shown the structures of the global minimum and several low lying energy configurations of $[In_nO_m]^{(0/\pm)}$ clusters with $n = 2-6$ and $m = 1-8$. To each one of them is assigned the "n.m-Label" signature, being "Label" a roman number to distinguish the different isomers with n Indium and m Oxygen atoms. The signature "n.m-I" always corresponds to the global minimum of the cationic cluster. Below that signature are given three numbers corresponding to the total energy differences (in eV) with respect to the respective global minima states of the neutral, cationic, and anionic cluster of the same size and composition. To clarify the notation, let us explain two examples. The 2.1-I structural family is shared by the three charge states of In_2O, the respective geometries only slightly differing due to relaxation effects. On the other hand, the geometries of $In_2O_2^+$ and $In_2O_2^-$ both belong to the 2.2-I structural family, being this structure an isomer of the neutral In_2O_2 cluster at 0.10 eV above its global minimum which has a geometry of type 2.2-II, and so on and so forth. We want to stress that full relaxation is performed for each different charge state, and that our choice of presenting the results referring to structural families is based on the fact that structural relaxations associated to charge states led, in general, to slight differences in the geometries, not perceivable in a drawing.

In the left panel of Fig. 6.10 is plotted the binding energy per atom of the

global minima states of these neutral and charged clusters as a function of the number of oxygen atoms, and in the right panel of the same figure is plotted the second energy difference of energy with respect to the number of oxygen atoms.

In order to analyze the geometrical and electronic properties of the global minima states of these clusters, we determined the In-In and In-O average coordination (Fig. 6.11) and distances (Fig. 6.12) as a function of the number of oxygen atoms. In Fig. 6.13 is shown the total magnetic moment, and finally, in Fig. 6.14 are shown the IPs and EAs of the neutral clusters. Notice that the difference IP-EA is the fundamental gap (132) of the cluster.

Before entering into the details of each In_nO_m group of clusters with fixed n, we discuss the general structural and electronic trends. The binding energy per atom (Fig. 6.10) increases with the number of oxygen atoms up to $m = n$, beyond which it remains nearly constant. This means that we can gain energy by adding oxygen atoms until we saturate the cluster, which happens roughly for the stoichiometric neutral In_nO_n or the $In_nO_{n+1}^+$ cationic clusters. The second energy difference (right panels of Fig. 3.10) exhibits peaks for $In_3O_4^{0/+}$, $In_4O_4^-$, In_4O_5, $In_5O_4^{0/-}$, $In_5O_6^{0/-}$, $In_6O_3^+$, $In_6O_4^0$, and $In_6O_6^{0/-}$. This means that those clusters are particularly stable with respect to the addition or substraction of an oxygen atom. Particularly interesting is the peak at In_6O_6, the planar geometry which can be viewed as a triangle (6.6-III in Fig. 6.9) formed by three In_2O_2 units (see structure 2.2-II in Fig. 6.2. However, the positively and negatively charged clusters, $In_6O_6^{\pm}$ (6.6-I in Fig. 6.9), have both the same three-dimensional geometry, which is specially stable against the addition or substraction of an oxygen atom only for the anion $In_6O_6^-$, according to the second energy difference.

The nearly flat behavior of the binding energies per atom when the oxygen content increases is also found for the adiabatic ionization potentials and adiabatic electron affinities (see Fig. 6.14). Note that the difference between the binding energy per atom of the neutral and cationic clusters, $\Delta(n, m)$, is equal to the difference between the ionization potential of the neutral cluster

and that of the In atom, divided by the total number of atoms $n+m$, that is $\Delta(n,m) = [\mathrm{IP}(\mathrm{In}_n\mathrm{O}_m)$ - IP(In)$]/(n+m)$. We see in Fig. 6.10 that $\Delta(n,m) > 0$, except for In_3O, In_5O and In_5O_2. As $\Delta(n,m)$ is small and nearly constant for all clusters with $n \geq 3$, we see that the adiabatic ionization potentials of Fig. 6.14 show a nearly regular increase when the oxygen content increases. A notable exception occurs for In_6O_6, which gives a peak consistent with the extra stability already noted in the trend of the second energy difference. The fundamental gap of the neutral clusters, defined as the difference between the adiabatic ionization potential and the adiabatic electron affinity (134), shows enhanced values for In_4O_2, In_6O_4, and In_6O_6, also in accordance with the special stability manifested in the peaks of the second energy difference (see Fig. 6.10).

The In-In average distance (Fig. 6.12) strongly varies for the small clusters, ranging between 2.8 Å and 3.9 Å, while for the larger clusters, it stabilizes around 3.3 Å. An exception is the $In_2O_4^-$ anion, due to its special geometry (see Fig. 6.2). In the low oxidation regime, we obtain two-dimensional structures with the oxygen and indium atoms intermixed, that is with more interconnected In-O units. However, as the number of oxygen atoms increases, the cluster structures become more compact, as illustrated in Fig. 6.12. The average In-In coordination decreases up to $m = n-1$, and increases for $m \geq n$ pointing to a transition from structures with weak bonds between indium atoms to more compact structures having an indium subcluster capped with oxygen atoms. An interesting remark is that the structures of In_nO clusters for n=2-6 are those of the corresponding global minima states of In_n with the oxygen inside (the only exception is In_5O).

7.1.1 $In_2O_m^{0/\pm}, m = 1-6.$

The structures of the global minima states for this series are linear for m =1 and 2 (for In_2O_2 the global minimum is the isomer 2.2-II, which is a two-dimensional structure), and for $m > 2$ are two-dimensional with at least two oxygen atoms binding molecularly. This behavior is only observed in this series.

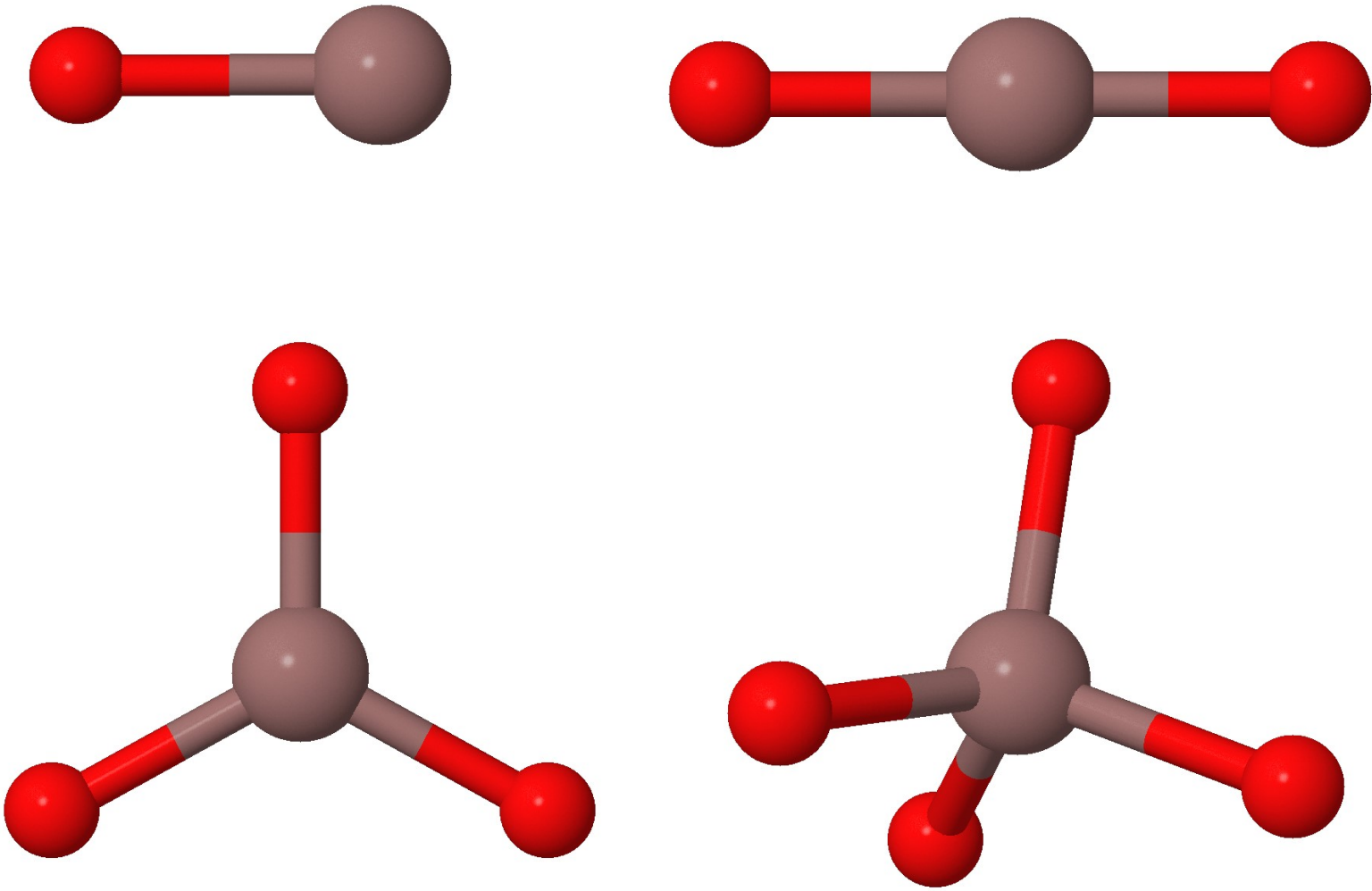

Figura 7.1: Low-energy isomers of $[InO_m]^+$ with m = 1-4.

We can identify the 2.2-II motif in most of these clusters, both in the global minimum and in the isomers. The average In-In distance (Fig. 6.12) increases with the number of oxygen atoms up to a certain number of oxygens (m=3 for $In_2O_m^{\pm}$ and $m = 4$ for In_2O_m) and decreases beyond that. (The calculated distance between the indium atoms in the dimer In_2 is 3.10 Å). Thus, by increasing the number of oxygen atoms, the In-In bonds become stronger. The discussion of the geometries 2.3-I and 2.3-II was given in section 3. The average InO distance oscillates between 2.06 and 2.21 Å. For In_2 we obtain 5.39 and 0.92 eV for the I_P and EA, respectively. The I_P slightly overestimate the experimental value obtained by DeMaria *et al.* (133) (5.08 ± 0.3 eV) by 6%, but the E_A substantially differs from the experimental value obtained by Gausa *et al.* (134) (1.27 ± 0.1 eV) by 38%. The binding energy per atom (Fig. 6.10) of all clusters (except In_2O^-) enter in a narrow energy window of 0.15 eV. The second energy difference (Fig. 6.10) of the neutral clusters does not show stability peaks, in contrast with that of the charged clusters.

7.1.2 $In_3O_m^{0/\pm}, m = 1 - 6.$

For the global minimum of In_3 we obtained an isosceles triangle with a magnetic moment of $3\mu_B$, and an average In-In distance of 3.23Å. The experimental value (134) of the E_A of In_3 is 1.50 ± 0.25 eV, notably higher than our result of 1.00 eV. We obtain for $(In_3O_m)^{0/\pm}$ clusters, as for $In_2O_m^{0/\pm}$, low dimensional structures when $m \leq 3$ (the global minima states are two-dimensional). For $m \geq 4$ the structures become three-dimensional. The geometry of 2.2-II is a motif that can be identified in many clusters of this series. Oxygen rich clusters have a triangular sub-cluster of indium atoms, which is equilateral for $m = 4$ and isosceles for $m = 5$ and $m = 6$. The average $In - In$ inter-atomic distance (left panels of Fig. 6.12) decreases as increasing the number of oxygen atoms. The average In-In coordination (Fig. 6.11) decreases for $m = 2$ and then increases for $m = 3$ and $m = 4$, beyond which it remains constant. Note that this is precisely the size at which the transitions between two and three-dimensional structures takes place and, even more, this cluster has the highest

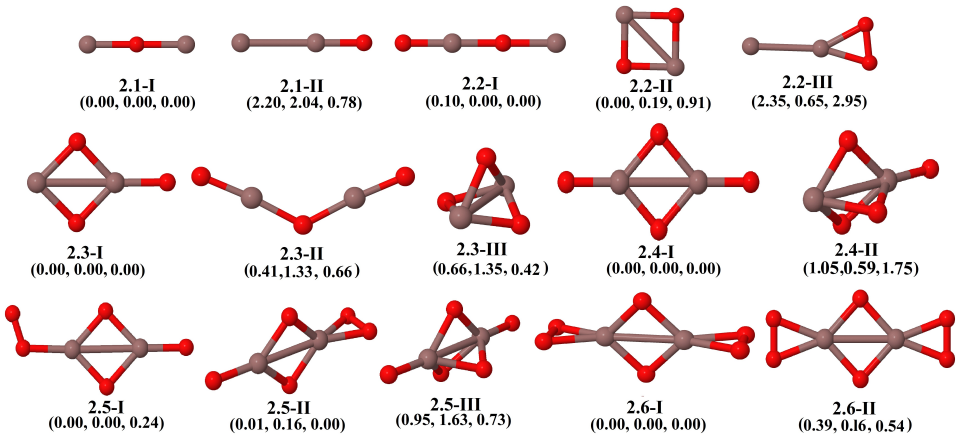

Figura 7.2: Low-energy isomers of $[In_2O_m]^+$ with m = 1-4, named by the "n.m-Label" signature. "Label" is a roman number to distinguish all the different isomers which contain n Indium and m Oxygen atoms. The signature " "n.m-I" corresponds always to the ground state of the cationic cluster. Below that signature are given three numbers corresponding to the total energy (in eV) with respect to the ground state of the neutral, cationic, and anionic cluster, respectively.

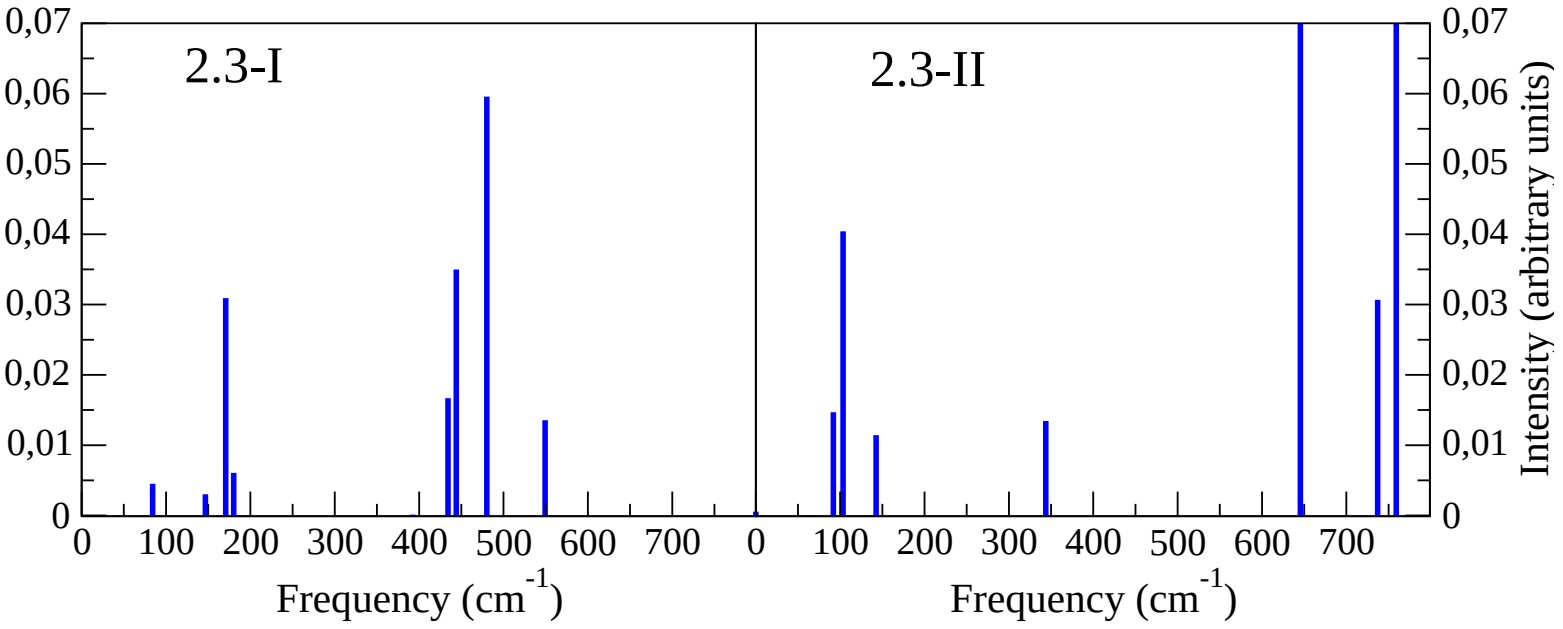

Figura 7.3: Vibrational spectra of $In_2O_3^+$ with the structure 2.3-I (left) and 2.3-II (right) shown in Fig. 6.2.

peak of stability in the second energy difference (Fig. 6.10) regardless of the charge state. This indicates again that the In-In interactions become stronger as the number of atoms of oxygen increases.

For the cationic $In_3O_2^+$ cluster we obtain the kite-like 3.2.I structure, with an indium atom bonded on top of an oxygen atom, while the global minimum of the neutral cluster is a linear chain (3.2-II) with interconnected indium and oxygen atoms (this is the largest one-dimensional global minimum structure found in this work). In_3O_4 and In_3O_5 both have an indium subcluster capped with the oxygen atoms. Finally, In_3O_6 is the only structure in which an ozonil group bridging two In atoms can be identified.

In the left panels of Fig. 6.5 are represented the total density of states (DOS), as well as the In and O projected DOS, of In_3O_2 (kite-like 3.2.II structure) and $In_3O_2^+$ (linear 3.2.I structure). We observe that the DOS of the neutral cluster corresponds to a nearly-zero-gap system. The bands around the HOMO and LUMO levels have different spin character, a characteristic required to design spin-valves devices. The high hybridization of In and O components along the valence-conduction energy range is analyzed further in the right panels of Fig. 6.5, where the orbital projected DOS is shown. We see that the main component of the HOMO is the $5p$ orbital of In, with a non negligible contribution of $2p$ of O. In contrast, the band at $\sim$ 1 eV is dominated by the $2p$ orbital with a minor contribution of $5p$. After ionization of In_3O_2 a drastic change occurs, both in the atomic configuration, which changes from planar (two dimensional) to linear (one dimensional), and in the electronic structure, which exhibits a strong redistribution with an opening of a large HOMO-LUMO gap. The higher symmetry of $In_3O_2^+$ is manifested in the higher degree of degeneration of its energy spectrum as compared with that of the neutral In_3O_2, as it can be observed comparing the respective DOS. Thus, the loss of an electron leads to pushing the remaining occupied states well above the Fermi level, opening the occupied-unoccupied gap, and forcing a symmetry adapted change of geometry. Notice that $In_3O_2^+$ is a very stable closed-shell *sp*-cluster with 16 valence electrons and a gap $\leq$ 3 eV which quali-

fies it as a wide gand gap system with potential optoelectronic applications at extreme conditions.

A similar, but less pronounced change in the DOS is shown in the left panels of Fig. 6.6 for the transition, after ionization, from a neutral nearly-zero-gap In_3O_6 into an semi-conducting $In_3O_6^+$ cluster. In this case there is no change of geometry and the opening of the gap is smaller than that discussed above (lower electronic redistribution). Nevertheless, the $In_3O_6^+$ cation is a closed shell cluster, with 32 valence electrons and a gap $\sim$ 0.8 eV. Interestingly, the bunch of states around the HOMO and LUMO levels of the neutral cluster have equal contributions from the In and O valence orbital. Thus, comparing with the DOS of In_3O_2, we infer that when the ratio of Oxygen to Indium atoms increases, the contribution of Oxygen $2p$ electrons to the bunch of levels around the HOMO increases, as expected. Finally, in the right panels of Fig. 6.6, is analyzed the contribution of the different oxygen atoms of the ozonil group in the neutral In_3O_6 and charged $In_3O_6^+$ global minimum structure (3.6.I), relative to the total Oxygen contribution in the DOS. We observe that the central O atom of the ozonil group does not contribute the DOS around the HOMO of the neutral species. Thus, the central ozonil oxygen atom is not involved in the ionization process. On the other hand, an optimized structure for In_3O_6 formed by three O-O peroxy units bridging the three sides of an In_3 triangle is less stable by far ($\sim$ 1.3 eV for the neutral and $\sim$ 1.0 eV for the charged species) than our global minimum structure (3.6-I of Fig. 6.3).

7.1.3 $In_4O_m^{0/\pm}, m = 1 - 7.$

The structure of the global minimum of In_4 is a square of 3.0 Åper side, with magnetic moment of $2\mu_B$. The first isomer is a tetrahedron with sides of 3.26 /Åand total magnetic moment of $4\mu_B$. The E_A for the global minimum is 1.56 eV, in agreement with the experimental value (1.70$\pm$0.25 (134)). In the $In_4O_m^{0/\pm}$ series with $m < 5$, including the first isomers, we have two-dimensional structures (except 4.3-III and 4.4-IV), and they contain the 2.2-II motif.

As in the previous series, one can see (left panels of Fig.6 .12) that the

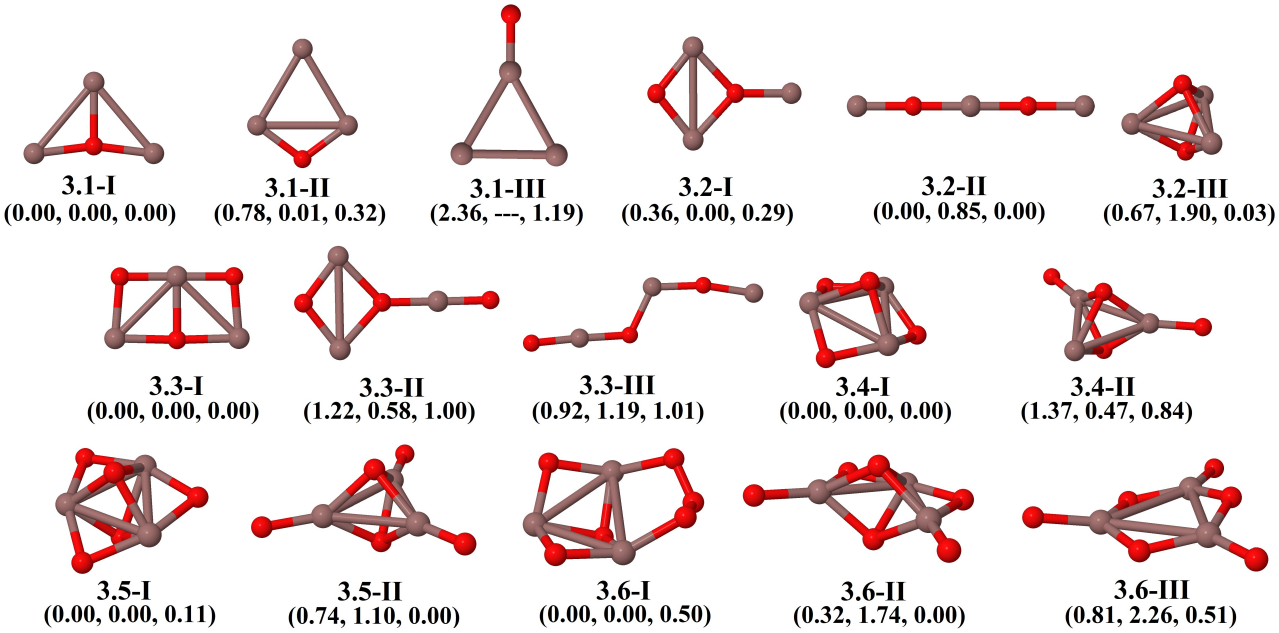

Figura 7.4: Low-energy isomers of $In_3O_m^+$ with m = 1-6. The notation is as in Fig. 6.2.

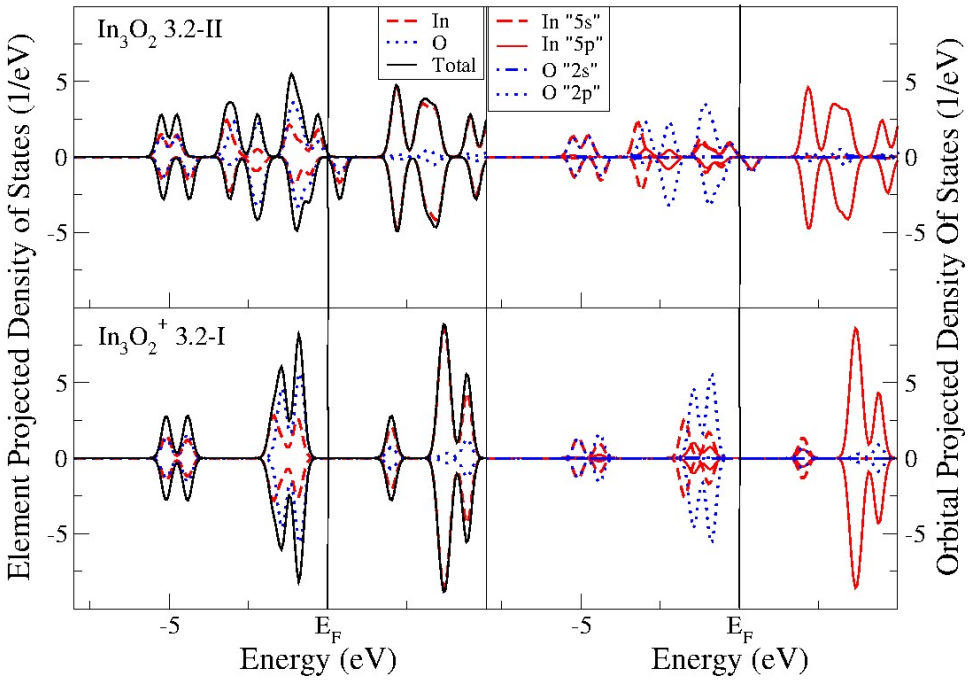

Figura 7.5: Left: The black continuos lines represent the total density of states (DOS) of neutral In_3O_2 (3.2.II, upper panel) and cationic $In_3O_2^+$ (3.2.I, bottom panel) clusters. The red dashed and blue dotted curves represent the contribution to DOS of Indium and Oxygen component atoms, respectively. Right: The partial contributions to the total DOS of In_3O_2 and $In_3O_2^+$ due to $2s$ and $2p$ electrons of Oxygen (blue dashed and blue dots, respectively) and to $5s$ and $5p$ electrons of Indium (red dashed and red dots, respectively). The Fermi level has been placed at zero energy.

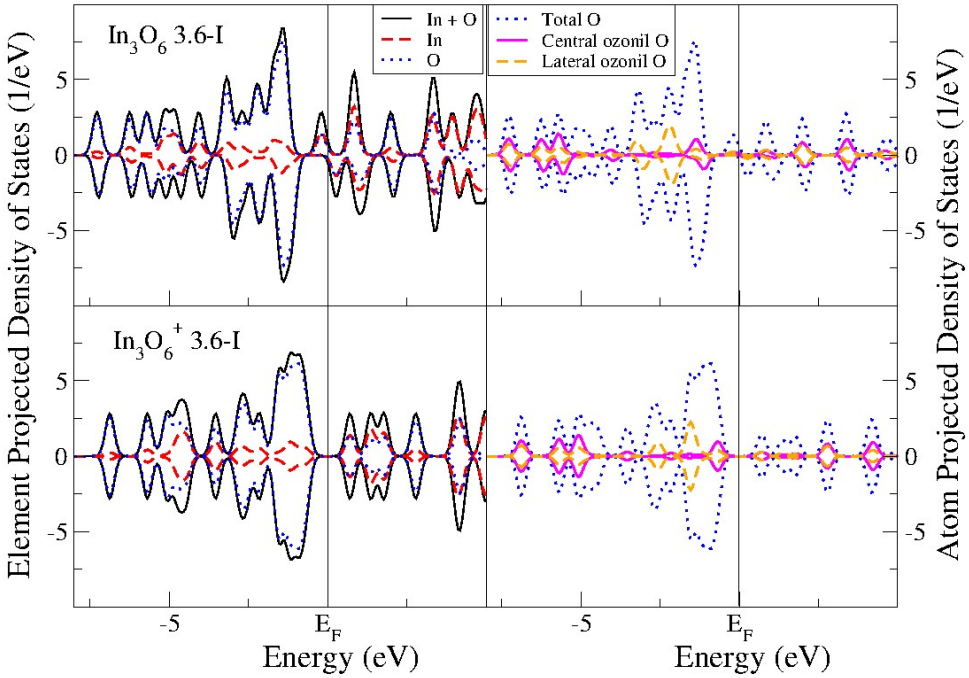

Figura 7.6: Left: total DOS (black continuos line) and the partial contributions of In (red dashed line) and O atoms (blue dotted line) of neutral In_3O_6 (upper panel) and cationic $In_3O_6^+$ (bottom panel). Both, neutral and cationic species have the ground state structure 3.6.I shown in Fig. 6.4. Right: partial contribution of oxygen atoms (blue dotted curves) to total DOS of In_3O_6 (upper panel) and $In_3O_6^+$ (bottom panel). The contributions from the central oxygen atom and the two lateral oxygen atoms of the ozonil group in 3.6.I structure, are represented by red-continuous and cyan-dashes lines, respectively. The Fermi level has been placed at zero energy.

average $In-In$ distance decreases as increasing the number of oxygen atoms. The average In-In coordination (Fig. 6.11) decreases up to $m = 3$ and then increases up to $m = 6$. Precisely, for the cationic species, at $m = 6$ the average In-In coordination is maximum, the average In-In distance is minimal, and we have a stability peak in the second energy difference (Fig. 6.10 right panels). The binding energy per atom increases with the number of oxygen atoms up to $m = 4$, reaching a saturation and remaining almost constant for higher oxidation states regardless the charge state and the number of oxygen atoms.

The global minimum of In_4O is a square of 3.24 Åper side, with a central oxygen atom. The experimental value for the I_P of this cluster is 5.74±0.1 eV (131), in good agreement with our calculation (5.68 eV). For In_4O_2 the structure is a ring of the 2.2-II type with additional indium atoms on top on each oxygen atom. That structure is the most stable of this series (for neutral and cationic states); note that it fits the highest peak in the second energy difference. As we will see later, the charged $In_4O_2^+$ cluster is predicted to fragment more favorably into In_2O^+ and In_2O, in full agreement with the experimental results reported by Knight *et al.* (129). The global minimum of In_4O_3 is built out from ring 2.2-II. The structure of $In_4O_4^{0,\pm}$ clusters strongly depends on the charge state. For the clusters $In_4O_m^{0,\pm}$ with $m = 5, 6$ and 7, we have a square indium sub-cluster with four oxygen atoms shared between bridge and hollow sites.

7.1.4 $In_5O_m^{0/\pm}, m = 1 - 8.$

The global minimum for In_5 is a trapezoidal-like planar structure, with an E_A of 1.85 eV, in very good agreement with the experimental value of 1.90±0.25 (134). For this structure the I_P is 5.80 eV, and has an average $In-In$ distance of 3.03 Å. In the $(In_5O_m)^{0/\pm}$ series we have only two two-dimensional structures, namely for isomer 5.1.II (in the anionic state) and for isomer 5.4-II. The global minimum of all structures with $m < 6$, that is, when the In-O bonds predominate, contains the 2.2-II motif (the only exception is 5.1-I). Instead, for oxygen rich clusters ($m \geq 6$), we obtain an indium sub-cluster with InO bonds

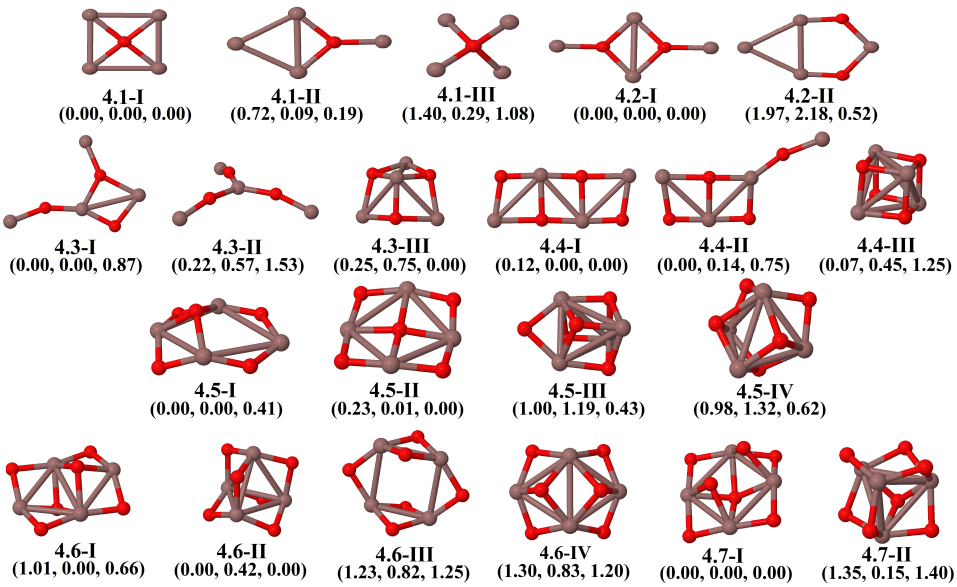

Figura 7.7: Low-energy isomers of $[In_4O_m]^+$ with m = 1-7. The notation is as in Fig. 6.2.

at the surface. The average $In-In$ distance decreases up to $m=3$, beyond which it increases up to $m=6$, where the second energy difference present a stability peak. $(In_5O_6)^{0/\pm}$ are the first clusters with a structure based on an In sub-cluster. In_5O has different structure for the anionic state than for the neutral and cationic ones. The I_P of the neutral cluster is 5.25 eV (131), in reasonable agreement with the experimental value 5.61±0.1 eV. The global minimum structure of In_5O_2 has a 2.2-II sub-cluster with three indium atoms bonded to it. This structure, which is also the most stable one for the cationic state, corresponds the highest peak in the second energy difference (Fig. 6.10). The 5.3-I structure is formed by two rings of 2.2-II type sharing an InO dimer. The 5.4-I structure is still nearly two-dimensional, formed by an In atom in the apex of a square of In atoms with the oxygen atoms bonded at the edges of that square. Their planar 5.4-II isomeric structure lie only at 0.05 eV, 0.12 eV, and 0.09 eV above the respective neutral, cationic and anionic lowest energy isomers. Structure 5.5-I has a tetrahedron-like indium sub-cluster with the O atoms bonded at hollow sites and one InO unit on top position over one In atoms. Cluster 5.6-I is cubic as 5.5-I, but with a In_2O substructure bonded on one face. The In_5O_7 structure has a quasi-planar In sub-cluster (like in the global minimum of In_5), with five O atoms bonded on bridge sites, and two on hollow sites. The $In-In$ average distance is 3.28 Å, so that the formation of the oxide has the effect of increasing the distances between the indium atoms (3.03 Åfor pure In_5). Finally, the In_5O_8 structure is the same as that of In_5O with six additional oxygen atoms in bridge positions, and the whole structure contains 2.2-II motifs.

7.1.5 $In_6O_m^{0/\pm}, m=1-8.$

The global minimum of In_6 is a triangular prism, with an E_A of 1.86 eV, in good agreement with the experimental value of Gausa *et al.* (134) (1.75±0.15). For this series, the average $In-In$ distance remains constant (about 3.3 Å), while the average $In-O$ distance decreases up to $m=5$, then for $m=6$ increases for the neutral and anionic states, and decreases again for the cationic

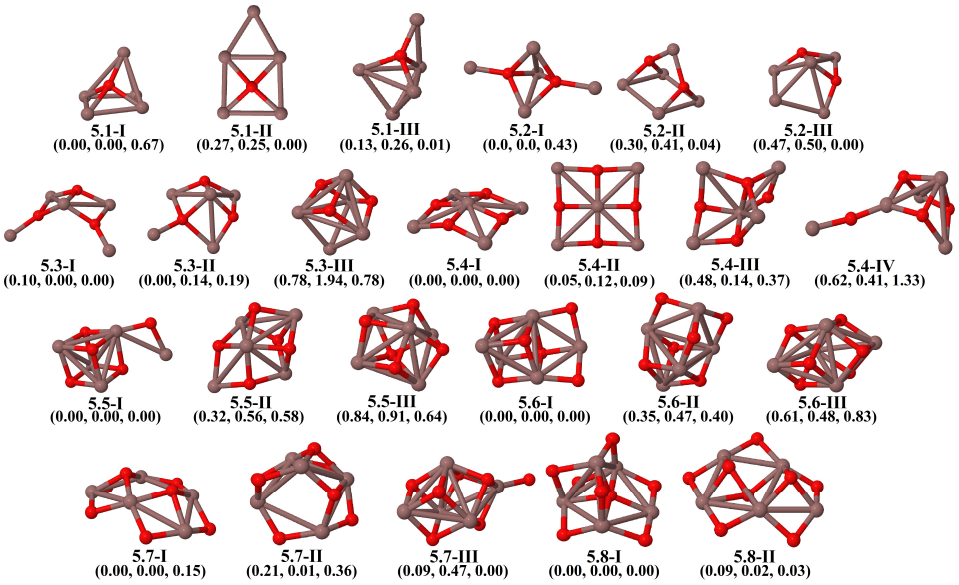

Figura 7.8: Low-energy isomers of $[In_5O_m]^+$ with m = 1-8. The notation is as in Fig. 6.2.

one, remaining constant (about 2.2 Å) for $m = 7$ and $m = 8$. As in all previous series, the 2.2-II motif is present in almost all the $(In_6O_m)^{0/\pm}$ structures, with predominance of In-O bonds. The only global minimum structure which contains a core formed by an indium sub-cluster is 6.8-I, with a octahedron-like shape and the eight oxygen atoms bonded on hollow sites. This structure has the largest average In-In and $In - O$ coordinations. The global minimum of In_6O is a triangular prism with the oxygen atom in the center. For the neutral cluster we obtain an I_P of 6.03 eV in good agreement with the experimental value of Janssens *et al.* (131) (>5.95±0.1). For In_6O_2 the structure depends on the charge state. For the neutral and anionic states the structure is octahedral-like with each of the oxygen atoms bonded to four indium atoms. The cationic state structure is now open, but each oxygen atom is still bonded to four indium atoms. In_6O_3 contains a In_3 triangular sub-cluster with InO units bonded to it. This cluster has the largest $In - In$ average inter-atomic distance within this series. The In_6O_4 structure is formed by three 2.2-II rings sharing two InO units. For the neutral state, this cluster has the highest stability peak in the second energy difference (Fig. 6.10). The global minimum structure of In_6O_5 is composed of the 6.4-I motif with an InO unit bonded to it. For the neutral state, this cluster has the lowest second energy difference (Fig. 6.10), so it can loose or gain an additional oxygen atom with a lower energy penalty than for other stoichiometries. The ground state structure of In_6O_6 is open, with alternating indium and oxygen atoms. This cluster has the highest stability peak in the second energy difference for the neutral and anionic states, while for the cationic state it has the lowest non negative value. For In_6O_7 the structure is more compact, and for the neutral and anionic states it is the lowest minimum of the second energy difference.

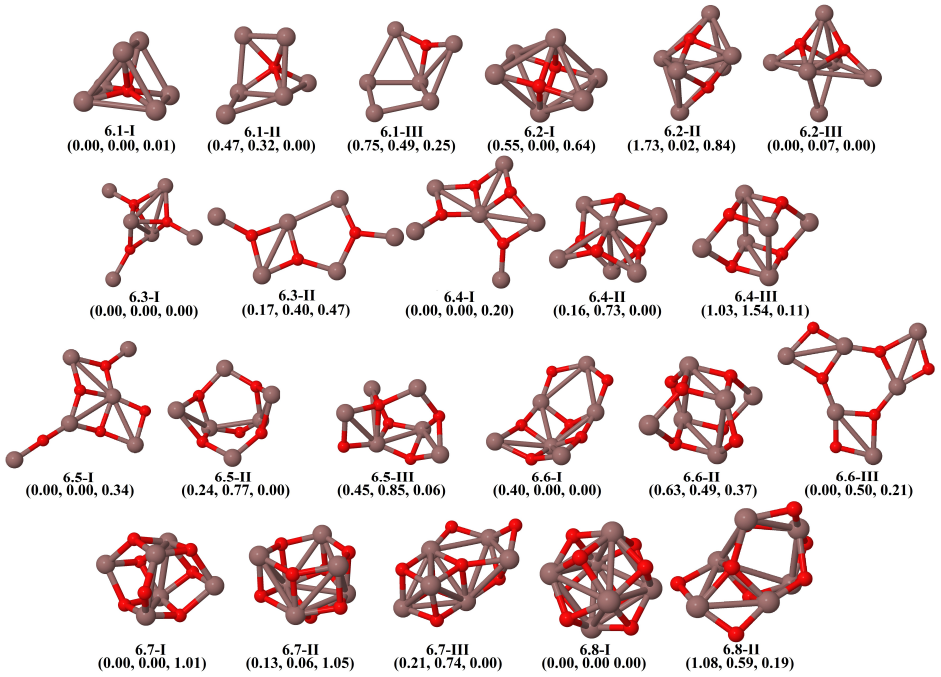

Figura 7.9: Low-energy isomers of $[In_6O_m]^+$ with m = 1-8. The notation is as in Fig. 6.2.

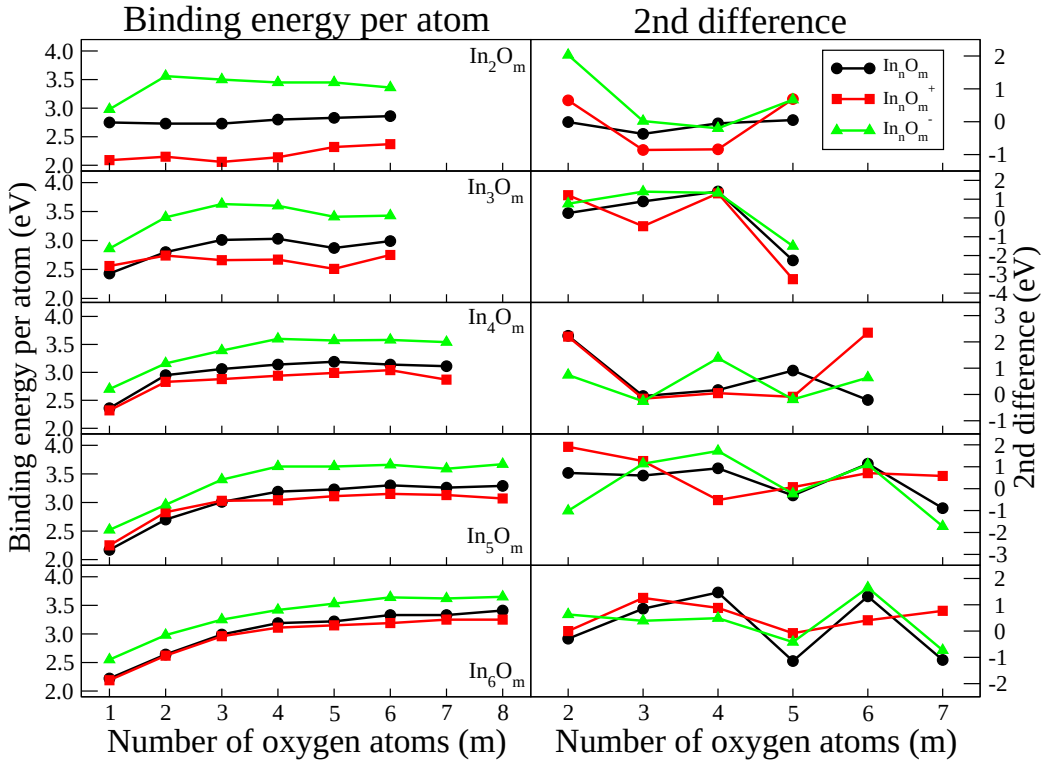

Figura 7.10: Binding energy per atom (left panels) and second difference of energy (right panels) of $[In_nO_m]^{(0/\pm)}$ with $n = 1-6$ and $m = 1-8$ clusters as a function of the number of oxygen atoms (m).

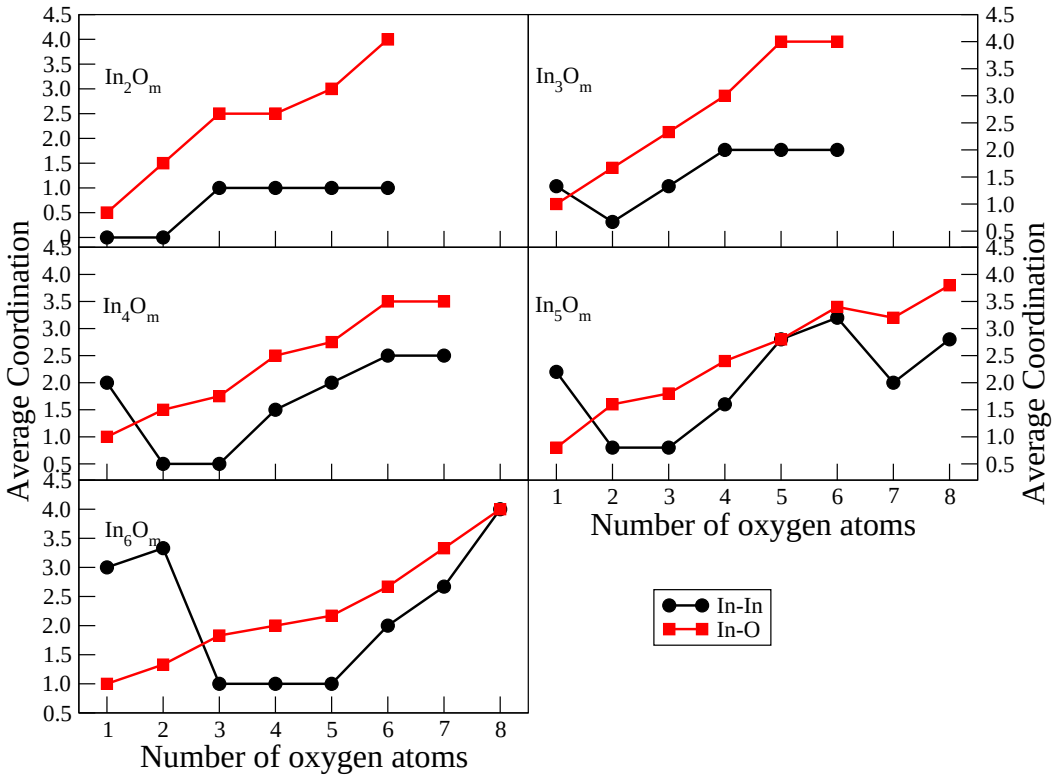

Figura 7.11: Average coordination of In_nO_m with n = 1-6 and m = 1-8.

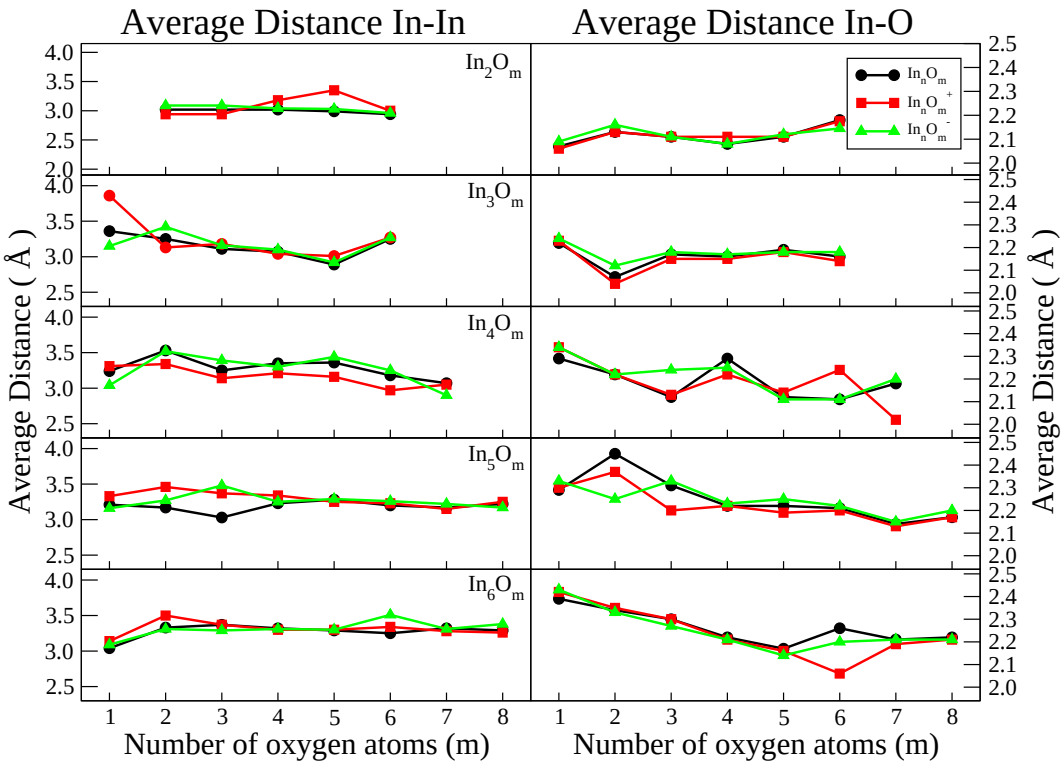

Figura 7.12: Average $In-In$ (left panels) and $In-O$ (right panels) distance of $[In_nO_m]^{(0/\pm)}$ with $n = 1-6$ and $m = 1-8$ clusters as a function of the number of oxygen atoms (m)

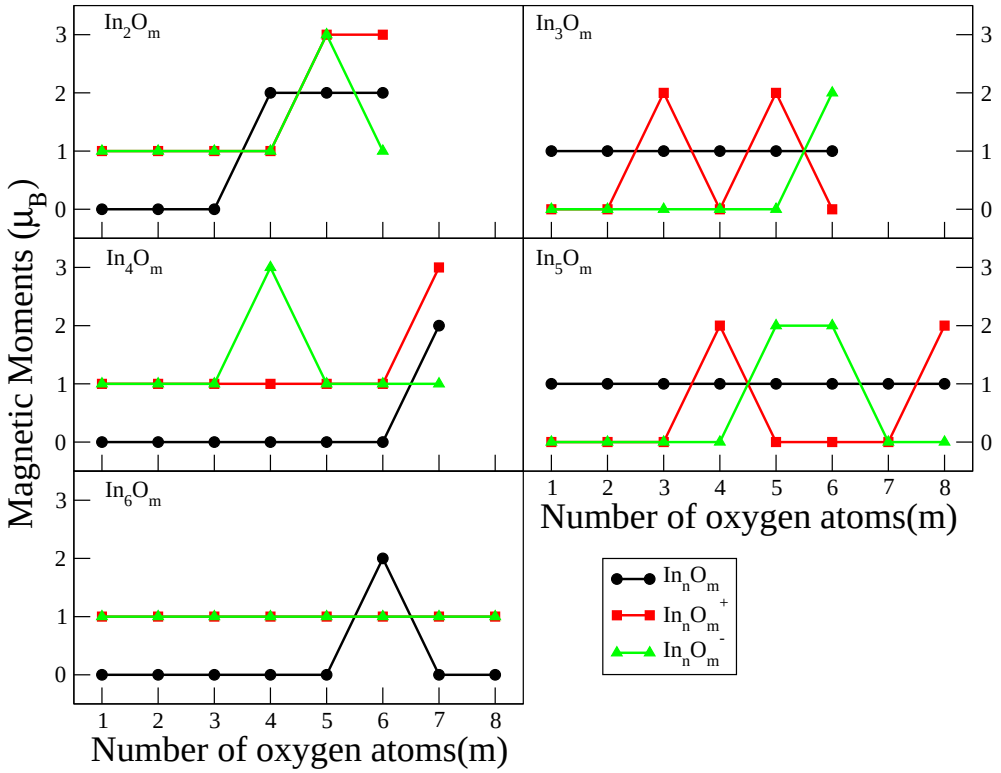

Figura 7.13: Magnetic moment of $In_nO_m^{0/\pm}$ with $n = 1 - 6$ and $m = 1 - 8$.

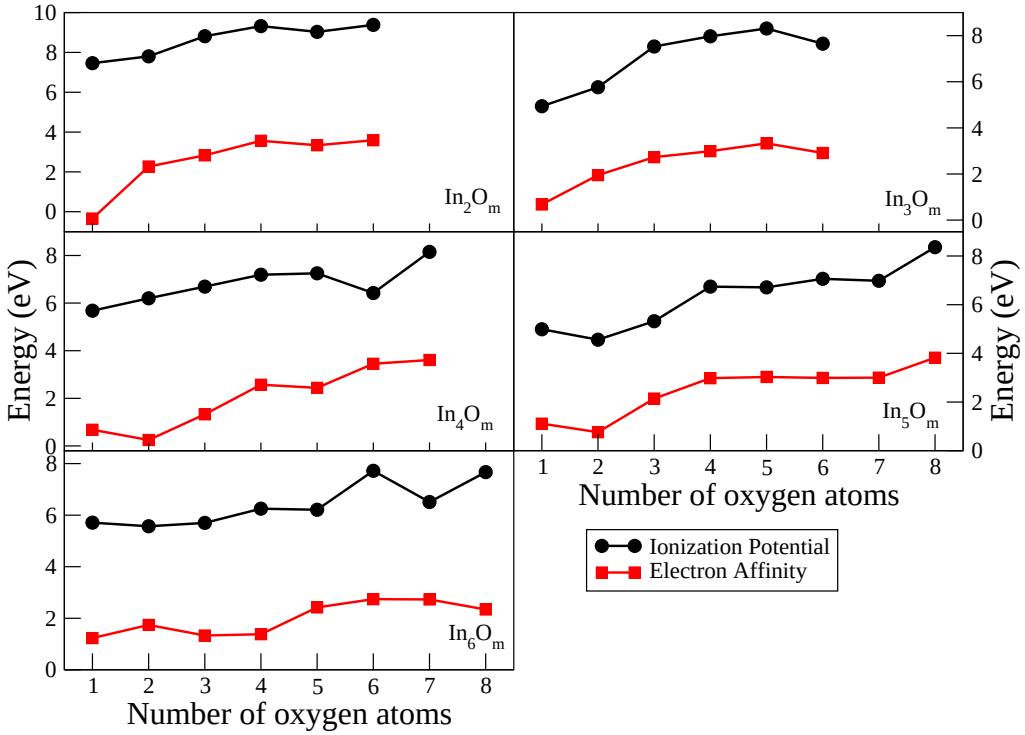

Figura 7.14: Ionization potential (I_P) and electron affinity (E_A) of $[In_nO_m]^+$ with n = 1-6 and m = 1-8. The difference IP-EA is the fundamental gap of the cluster.

7.2 Fragmentation channels of cationic and anionic clusters.

We focus of the fragmentation patterns of cationic clusters, for which experimental data exist (129), although we also provide a table, at the end, with our prediction for the anionic clusters, that could be tested in future experiments. In order to study the fragmentation channels of charged clusters, we calculated the fragmentation energies defined as follows:

$$E_f(n,m) = [E(x,y)^{\pm}] + [E(n-x,m-y)] - [E(n,m)^{\pm}] \ ,$$

where the first two terms are the energies of product-clusters one of which results charged, and the last term is the energy of the parent charged cluster. This process is endothermic so that the smaller $E_f(n,m)$ in absolute value, the more favorable the fragmentation will be along the corresponding channel. Note that our definition is based on total energies of initial and final states and no energy barriers are considered which could be important in certain cases (if structural rearrangement of the parent-cluster occurs prior to fragmentation, for instance). We have considered a large number of possible fragmentation channels, although we only report the most favorable ones. For the cationic cluster these are the following:

(i) $In_{n-1}O_m + In^+$,

(ii) $In_{n-1}O_m^+ + In$,

(iii) $In_{n-1}O_{m-1}^+ + InO$,

(iv) $In_{n-1}O_{m-2}^+ + InO_2$,

(v) $In_nO_{m-1}^+ + O$,

and

(vi) $In_{n-2}O_{m-1} + In_2O^+$.

We focus our discussion on those channels, except when specifically indicated. The values of the fragmentation energies are collected in Table 2 for cationic clusters. In order to check the accuracy of our results, we performed calculations with VASP for the fragmentation of cluster In_3O^+. We obtain similar results with both approaches. The values for the energies required to

perform the fragmentations, given in parentheses below (first values for SIESTA and second values for VASP) are of the same order with both codes.

$In_3O^+ \rightarrow In_2O^+ + In$, (0.99/1.04 eV)

$In_3O^+ \rightarrow In^+ + In_2O$, (1.99/1.63 eV)

$In_3O^+ \rightarrow In_3{}^+ + O$, (4.88/4.93 eV)

and

$In_3O^+ \rightarrow In_2{}^+ + InO$, (7.34/7.95 eV)

As a general trend, the biggest product-cluster is the one that retains the positive charge in the fragmentation, except when the products are $In^+ + In_{n-1}O_m$ and $In_2O^+ + In_{n-2}O_{m-1}$. This is in full agreement with the experimental results of Knight *et al.* (129). Experimentally, four prominent channels are found, corresponding to the loss of In^+, In_2O^+, In_3O^+ or $In_3O_2{}^+$ respectively.

We find, also in agreement with the experimental results of Knight *et al.* (129), that for poor-oxygen clusters ($m = n$, $m = n - 1$, $m = n - 2$ and $m = n - 3$), the most favorable fragmentation channel corresponds to the loss of In^+, except for:

$In_5O_2{}^+ \rightarrow In_3O^+ + In_2O$,

$In_4O_2{}^+ \rightarrow In_2O^+ + In_2O$,

and

$In_5O_3{}^+ \rightarrow In_3O_2{}^+ + In_2O$.

For rich-oxygen clusters ($m = n + 1$) the most favorable fragmentation occurs also by loosing In^+, with the only exceptions of $In_4O_5{}^+$ (which fragments in $In_4O_4^+ + O$), and $In_5O_6{}^+$ (which fragments in $In_2O^+ + In_3O_4$).

It is interesting to analyze not only the most favorable fragmentation channels, but also other possible ones. In the photodissociation experiment (129), the fragmentation of $In_3O_2{}^+$ can be produced through three possible channels:

$In_3O_2{}^+ \rightarrow In^+ + In_2O_2$,

$In_3O_2{}^+ \rightarrow In_2O^+ + InO$,

and

$In_3O_2{}^+ \rightarrow In_3O^+ + O$.

The first channel, leading to In^+, is the most favorable one, while the other two are observed in the experiment with similar relative abundance of products in the corresponding mass spectrum. Moreover, the cluster $In_3O_2{}^+$ does not fragment in channels different from those three ones, an indication of the low probability of them to occur. The fragmentation energies resulting from our calculations for $In_3O_2{}^+$ are consistent with the experimental results (Table II). The lowest fragmentation energy (2.68 eV in absolute value) is obtained for the channel leading to In^+, and the energies to fragment the parent cluster in the two other ways differ by only 0.2 eV. Besides, other fragmentation channels require, at least, energies higher than 4.5 eV, that is nearly 2 eV higher than in the most favorable channel. Other examples are discussed in what follows.

For the cluster $In_4O_3{}^+$, four fragmentation channels are experimentally found as the most favorable ones:

$In_4O_3{}^+ \rightarrow In^+ + In_3O_3$,

$In_4O_3{}^+ \rightarrow In_2O^+ + In_2O_2$,

$In_4O_3{}^+ \rightarrow In_3O^+ + InO_2$,

and

$In_4O_3{}^+ \rightarrow In_3O_2{}^+ + InO$,

which are also the most favorable channels according to our calculations, all them with fragmentation energies lower than 3 eV. As regards other less favorable channels, the experiments reveal the following two:

$In_4O_3{}^+ \rightarrow In_2O_2{}^+ + In_2O$,

and

$In_4O_3{}^+ \rightarrow In_2{}^+ + In_2O_3$,

which enter in a fragmentation energy window of 3 to 3.5 eV in our calculations. No other fragmentation of $In_4O_3{}^+$ is experimentally observed. We obtain that other fragmentations (not observed in the experiment) require energies larger than 3.5 eV which appears as a threshold energy for fragmentation of this parent cluster.

Let us analyze now the parent-cluster $In_5O_4{}^+$. Our calculations lead to four favorable channels,

$In_5O_4{}^+ \rightarrow In^+ + In_4O_4$,

$In_5O_4{}^+ \rightarrow In_2O^+ + In_3O_3$,

$In_5O_4{}^+ \rightarrow In_3O_2{}^+ + In_2O_2$,

and

$In_5O_4{}^+ \rightarrow In_3O^+ + In_2O_3$,

in full agreement with the results of Knight *et al.* (129). The more (less) prominent of these experimental peaks corresponds to the fragmentation into In^+ (In_3O^+), in agreement with the lowest (highest) predicted fragmentation energy.

Apart from those channels, the experiment reveals other potential channel:

$In_5O_4{}^+ \rightarrow In_4O_3{}^+ + \mathrm{InO}$,

that correspond to our next favorable fragmentation path with a fragmentation energy of 3.42 eV. No other channels are reported experimentally. As regards the rest of channels for $In_5O_4{}^+$, not experimentally observed, we find high fragmentation energies. For instance, the loss of a neutral In atom requires an energy cost of nearly 4 eV, and higher energies for other channels. We can estimate the threshold energy for fragmentation of $\mathrm{In_5O_4{}^+}$ to be at least 4 eV.

In general, most of the fragmentations that require energies larger than 4.0 eV in our work do not appear in the experiment of Knight (129); the only exception is the fragmentation of $In_4O_4{}^+$ in $In_3O^+ + InO_3$. Although our overall agreement with the photodissociation experiments (129) is good, we note, that there are certain fragmentations that require energies lower than 4.0 eV (according to our calculations) but that do not appear in the experiment. This could be indicative of the presence of a significative energy barrier, or simply of the fact that our global minimum is not the structure present in the experiment. The overall good agreement between our calculations and the fragmentation experiments provides further support to our predicted global minimum structures for small indium oxide clusters.

For the sake of completeness, we have also determined the fragmentation energies of anionic $In_nO_m^-$ clusters, collected in Table 3. Although there are no experimental results available, we hope that these results will motivate

Tabla 7.2: Calculated fragmentation energies (in eV) for several channels for the cationic clusters. In bold are the most prevalent experimental channels as measured by Knight *et al.* (129), and underlined is the stronger experimental signal (when available from ref. (129)) among those channels.

Parent	Fragments							
Clusters	In^+	In_2O^+	In_3O^+	$In_3O_2^+$	In	O	InO	In_2O
In_3O^+	**1.99**	**0.99**	—	—	—	7.34	4.88	—
$In_3O_2^+$	**2.68**	**3.67**	**3.47**	—	5.13	—	—	4.51
$In_3O_3^+$	**2.35**	**2.78**	—	2.26	5.69	—	3.60	5.27
$In_3O_4^+$	1.86	3.58	2.27	—	4.96	3.60	4.61	6.50
$In_4O_2^+$	**2.60**	**2.47**	**2.95**	3.26	—	5.39	—	—
$In_4O_3^+$	**2.12**	**2.88**	**3.00**	**2.66**	4.19	3.19	—	3.32
$In_4O_4^+$	**2.27**	**3.57**	**4.37**	**2.80**	4.78	3.29	3.69	4.67
$In_4O_5^+$	3.98	3.96	6.51	4.34	6.83	3.45	4.44	5.80
$In_5O_2^+$	**2.10**	**3.83**	**1.31**	**4.59**	2.84	3.33	4.44	—
$In_5O_3^+$	**2.83**	**3.60**	**2.95**	**2.25**	4.06	4.41	3.46	—
$In_5O_4^+$	**2.13**	**3.08**	**3.51**	**2.63**	3.92	3.15	3.42	3.15
$In_5O_5^+$	**2.36**	**3.61**	**3.99**	**3.66**	4.15	3.67	3.81	4.11
$In_5O_6^+$	2.30	1.98	4.63	4.12	4.69	3.61	3.96	6.32
$In_6O_4^+$	2.46	3.43	2.79	2.99	3.70	4.42	3.06	2.66
$In_6O_5^+$	2.30	3.11	3.18	2.85	3.56	3.54	3.45	2.90
$In_6O_6^+$	1.97	3.28	5.06	3.33	3.57	3.62	3.39	3.07
$In_6O_7^+$	3.17	3.65	5.08	5.61	4.70	4.02	3.81	4.03

experimental groups to carry out the measurements.

Tabla 7.3: Calculated fragmentation energies (in eV) of $In_nO_m^-$ for several channels. In bold are the most favourable fragmentation channels predicted in our calculations for the anionic clusters.

Parent	Fragments							
Clusters	In^-	In_2O^-	In_3O^-	$In_3O_2^-$	In	O	InO	In_2O
In_3O^-	**2.41**	**2.49**	—	—	—	6.16	4.20	—
$In_3O_2^-$	5.30	4.26	5.57	—	**2.77**	—	—	**1.80**
$In_3O_2^-$	7.41	5.92	5.29	4.81	4.32	—	**3.78**	**2.80**
$In_3O_3^-$	7.76	7.41	—	**3.13**	3.94	**3.40**	3.93	3.93
$In_3O_4^-$	6.73	8.18	—	—	3.13	**2.08**	**2.23**	3.60
$In_4O_2^-$	4.22	**1.80**	3.78	**2.00**	—	5.49	—	—
$In_4O_3^-$	4.94	3.87	5.38	2.96	**1.95**	4.75	—	**1.26**
$In_4O_4^-$	6.90	6.28	8.57	4.92	3.65	5.11	**3.26**	**3.11**
$In_4O_5^-$	8.48	6.54	10.58	6.32	4.89	3.31	**3.17**	**2.64**
$In_5O_2^-$	2.22	**2.02**	**1.01**	2.20	1.70	5.54	3.40	—
$In_5O_3^-$	5.10	4.29	4.89	**2.00**	**3.51**	6.56	4.47	—
$In_5O_4^-$	6.78	5.68	7.61	4.74	**3.82**	5.42	5.14	**2.61**
$In_5O_5^-$	6.90	6.22	8.25	5.74	4.19	**3.69**	3.72	**2.90**
$In_5O_6^-$	8.16	8.41	9.06	6.60	4.45	**3.92**	**4.33**	4.74
$In_6O_2^-$	4.18	3.11	**2.70**	3.79	3.16	6.04	4.91	**2.09**
$In_6O_3^-$	4.41	2.60	3.82	2.54	**2.01**	5.41	4.78	**2.01**
$In_6O_4^-$	4.85	3.94	4.80	3.27	**1.61**	5.02	3.24	**2.28**
$In_6O_5^-$	5.74	4.73	6.19	3.77	2.45	4.53	**2.35**	**1.70**
$In_6O_6^-$	6.73	6.12	9.40	5.57	3.48	4.95	**3.61**	**3.34**
$In_6O_7^-$	7.21	6.75	8.70	7.13	3.96	3.30	**2.99**	**2.96**

7.3 conclusions and perspectives

Neutral and charged $In_nO_m^{0/\pm}$ clusters, with n=1-6 and m=1-8, have been theoretically investigated in the framework of the DFT-GGA theory. Low-dimensional structures are found for $n < 5$ with low oxygen content while more compact three-dimensional structures, with an In subcluster, are more stable in the oxygen-rich phase and also for $n \geq 5$. The binding energy per atom increases with the number of oxygen atoms up to the equiatomic composition at which the energy gain upon oxidation saturates and further O atoms start to be attached at low coordinated positions or even in molecular form in some cases close to the maximum oxidation rate.

Based on total energy differences between the obtained global minimum configurations, we explored the possible fragmentation channels of the charged

clusters. In the cationic clusters, the biggest product-cluster, with few exceptions, is the one that retains the charge in the fragmentation. Most clusters ($m = n$, $m = n-1$, $m = n-2$ and $m = n-3$), preferentially fragment loosing In^+. Our ranking for fragmentation channels, comprising not only the most favorable one but also others, correlates in general with the relative intensities of corresponding fragments experimentally observed. We identify energy thresholds for those channels to occur, the highest being 4.0 eV; most of the fragmentation channels that require energies larger than 4.0 eV in our work do not appear in the experiment. The few experimentally observed channels that we fail to reproduce are probably those for which a significative energy barrier should be taken into account, or simply other global minimum configurations different from those proposed in this work are involved in the process. Overall, the calculated trends are in agreement with photodissociation experiments, a fact that provides further support to our predicted global minimum structures for these small indium oxide clusters.

We hope that the structural and electronic properties of the small $In-O$ clusters reported in this work can help in future nanotechnology research based on indium-oxide.

Chapter 8

Conclusions

Las historias no acaban por que alguien escriba la palabra "fin".
No siempre hay un asesino, algunas veces toca morir, lo que
viene se va, como suele pasar el viento, el tiempo.
Luis Eduardo Aute

8.1 Versión en español

En este trabajo hemos realizado una serie de cálculos computacionales, con la finalidad de estudiar propiedades estructurales, electrónicas, magnéticas, catalíticas y de fragmentación de diferentes sistemas de óxidos de metales de transición. Los cálculos fueron realizados con con los códigos SIESTA y VASP, códigos basados en la teoría funcional de la densidad. El código SIESTA utiliza pseudo potenciales y bases de estados localizados (combinación de orbitales atóómicos), lo que permite hacer cálculos precisos con un coste computacional moderado, mientras que el código VASP utiliza un conjunto de base de ondas planas en lugar de orbitales pseudoatómicos numéricos, y las interacciones del núcleo se tratan mediante el enfoque de proyector onda aumentada (PAW) en lugar de pseudopotenciales.

Los estudios realizados en esta tesis se dividen en dos partes. Por un lado, el estudio de propiedades fundamentales de pequeños cúmulos de óxidos de

metales de transición, como primer paso para el entendimiento del comportamiento de diversos cúmulos metales de transición. Dentro de este grupo, se encuentran el estudio de cúmulos de óxidos de níquel, hierro, cobalto e indio. Por otro lado, están las aplicaciones, como la absorción de monóxido de carbono en óxidos de níquel, o la mezcla de hierro, níquel y cobalto con la finalidad de aumentar el momento magnético de los cúmulos oxidados.

Uno de los principales temas de investigación de esta tesis, fue el estudio de los cumulos óxidos de níquel ($Ni_nO_m^{\pm/0}$). Como primer paso, estudiamos diversas propiedades de los cúmulos puros de níquel oxidados como función de la tasa de oxidación. Encontramos estructuras en forma de anillo para cúmulos con el mismo número de átomos de níquel y oxigeno, en el que el momento magnético es apagado por la interacción del oxigeno. El estudio de la estabilidad de estos cúmulos, demostró que las estructuras con n=m y n=m+1, son más estables que en las que el número de oxigeno es superior al níquel. Además, el estudio del magnetismo, demostró que el momento magnético no es apagado en general para grandes tasas de oxidación, sino que en algunos casos se conserva e incluso es mayor que el de los cúmulos de níquel puros. Realizamos también, los primeros pasos para el estudio de absorción de monóxido de carbono en cúmulos de óxidos de níquel. Como parte de las aplicaciones de los óxidos de níquel, estudiamos las aleaciones níquel-plata (Ag_xNi_y con $x + y = 13$ and 55), con la finalidad de preservar el momento magnético del níquel ante la oxidación. Para esto, proporcionamos un recubrimiento de plata al cumulo Ni_{13}. Al oxidar el cumulo $Ag_{42}Ni_{13}$, encontramos que el momento magnético total del cumulo es conservado, más aun, el momento magnético del cumulo que se encuentra casi en su totalidad concentrado en el core (átomos de níquel), se acumula aun mas en el core conforme la tasa de oxidación aumenta.

Para los cúmulos de óxidos de hierro, al igual que para los óxidos de cúmulos de níquel, como primer paso, estudiamos diversas propiedades fundamentales como función de la tasa de oxidación. Para estos cúmulos, obtenemos una gran variedad de estructuras. Para una baja tasa de oxidación, las estructuras de estos óxidos, son la de los cúmulos puros de hierro capeados con átomos

de oxigeno. Cúmulos planos en forma de anillo para Fe_3O_3 y Fe_4O_4. Para grandes tasas de oxidación las estructuras se construyen con unidades FeO. Y finalmente, cuando el numero de oxígenos es grande, aparece la absorción de oxigeno molecular. Hemos encontrado un resurgimiento del comportamiento magnético nunca antes reportado para los clusters de óxido de hierro. Se sabe que el momento magnético de los clusters de hierro se apaga cuando se oxidan, debido a los acoplamientos antiferromagnéticos. Para las series Fe_4O_m y Fe_5O_m, encontramos que para grandes tasas de oxidación, los acoplamientos antiferromagnéticos desaparecen y el momento magnético del sistema aumenta, debido a bajos momentos magnéticos locales del hierro, pero con acoplamientos paralelos.

Una de las aplicaciones de esta tesis fue la mezcla de hierro, cobalto y níquel, con el fin de preservar el momento magnético de los cumulos mezclados. Estudiamos para tamaños pequeños, todas las posibles aleaciones de estos tres elementos. La energía de enlace por átomo indica que la construcción de estas nanoaleaciones es energéticamente posible. Encontramos que para los dimeros, el hecho de mezclar estos elementos conserva mejor el momento magnético ante la oxidación que el de sus homólogos puros. Para los trimeros y tetrameros, las mejores aleaciones desde el punto de vista de la conservación del momento magnético, son aquellas que están hechas con hierro y níquel.

Finalmente, y aunque no es un metal de transición, estudiamos los cumulos $In_nO_m^{0/\pm}$, con n=1-6 y m=1-8. Encontramos estructuras de baja dimensión por $n < 5$ con baja tasa de oxígeno. La energía de enlace por átomo aumenta con el número de átomos de oxígeno hasta la composición equiatómica en la cual la ganancia de energía con la oxidación se satura y otros O átomos comienzan a unirse en posiciones de coordinación bajas o incluso en forma molecular en algunos casos cerca del tasa máxima de oxidación. Con el fin de confirmar la fiabilidad de nuestros cálculos, exploramos los posibles canales de fragmentación de los clusters ionizados, comparando con mediciones experimentales de fotofragmentación. El cumulo mas grande, con pocas excepciones, es el que conserva la carga en la fragmentación. La mayoría de los clusters,

se fragmentan preferentemente en In^+. Nuestro ranking de canales de fragmentación, que comprende no solo el más favorable sino también otros, se correlaciona en general con las intensidades relativas de los fragmentos correspondientes observados experimentalmente. Identificamos los umbrales de energía para que esos canales ocurran, el más alto es 4.0 eV. La mayoría de los canales de fragmentación que requieren energías mayores a 4.0 eV en nuestros calculos no aparecen en el experimento.

8.2 English version

In this work we have made a series of computational calculations, with the purpose of studying structural, electronic, magnetic, catalytic and fragmentation properties of different transition metal oxide systems. The calculations were made with the codes SIESTA and VASP, codes based on the density functional theory. The SIESTA code uses pseudo potentials and bases of localized states (combination of atomic orbitals), which allows precise calculations with a moderate computational cost, while the VASP code uses a plane-waves basis set instead of numerical pseudoatomic orbitals, and core interactions are treated by the projector-augmented wave (PAW) approach instead of pseudopotentials.

The studies carried out in this thesis are divided into two parts. On the one hand, the study of the fundamental properties of small oxide clusters of transition metals, as a first step for the understanding of the behavior of various transition metal clusters. Within this group, the study of oxide clusters of nickel, iron, cobalt and indium is found. On the other hand, there are the applications, such as the absorption of carbon monoxide in nickel oxides, or the mixture of iron, nickel and cobalt in order to increase the magnetic moment of the oxidized clusters

One of the main research topics of this thesis was the study of nickel oxides clusters ($Ni_nO_m^{\pm/0}$). As a first step, we studied several properties of pure oxidized nickel clusters as a function of the oxidation rate. We find ring-shaped structures for clusters with the same number of nickel and oxygen atoms, in

which the magnetic moment is quenched by the interaction with oxygen. The study of the stability of these clusters, showed that structures with $n = m$ and $n = m+1$, are more stable than those in which the number of oxygen is greater than nickel. In addition, the study of magnetism, showed that the magnetic moment is not quenched in general for high rates of oxidation, but in some cases it is preserved and even higher than that of the pure nickel clusters. We also carried out the first steps to study the absorption of carbon monoxide in nickel oxide clusters. As part of the applications of nickel oxides, we studied nickel-silver alloys (Ag_xNi_y with $x + y = 13$ and 55), with the aim of preserving the magnetic moment of nickel against oxidation. For this, we provide a silver coating to the cluster Ni_{13}. When oxidizing the $Ag_{42}Ni_{13}$ cluster, we find that the total magnetic moment of the cluster is conserved. Moreover, the magnetic moment of the cluster that is almost entirely concentrated in the core (nickel atoms), accumulates even more in the core according to the oxidation rate increases

For the iron oxide clusters, as for the nickel oxide clusters, as a first step, we studied several fundamental properties as a function of the oxidation rate. For these clusters, we obtain a great variety of structures. For a low rate of oxidation, the structures of these oxides, are those of the pure iron clusters caped with oxygen atoms. flat ring-like clusters for Fe_3O_3 and Fe_4O_4. For large oxidation rates the structures are constructed with FeO units. Finally, when the number of oxygen is large, the absorption of molecular oxygen appears. We have found a resurgence magnetic behavior never before reported for iron oxide clusters. It is known that the magnetic moment of the iron clusters is quenched when they are oxidized, due to antiferromagnetic couplings. For the Fe_4O_m and Fe_5O_m series, we found that for large oxidation rates, the antiferromagnetic couplings disappear and the magnetic moment of the system increases, due to low local magnetic moments of the iron, but with parallel couplings.

One of the applications of this thesis was the mixture of iron, cobalt and nickel, with the purpose of preserve the magnetic moment of the mixed clusters. We studied for small sizes, all possible alloys of these three elements. The

binding energy per atom indicates that the construction of these nanoalloys are energetically possible. We find that for the dimers, the fact of mixing these elements, conserves better the magnetic moment against the oxidation than that of its pure counterparts. For the trimers and tetramers, the best alloys from the point of view of conservation of the magnetic moment, are those that are made with iron and nickel

Finally, and even though it's not a transition metal we studied the $In_nO_m^{0/\pm}$ clusters, with n=1-6 and m=1-8. Low-dimensional structures are found for $n < 5$ with low oxygen rate. The binding energy per atom increases with the number of oxygen atoms up to the equiatomic composition at which the energy gain upon oxidation saturates and further O atoms start to be attached at low coordinated positions or even in molecular form in some cases close to the maximum oxidation rate. In order to confirm the reliability of our calculations, we explored the possible fragmentation channels of the charged clusters, comparing with experimental measurements of photofragmentation. The biggest product-cluster, with few exceptions, is the one that retains the charge in the fragmentation. Most clusters, preferentially fragment loosing In^+. Our ranking for fragmentation channels, comprising not only the most favorable one but also others, correlates in general with the relative intensities of corresponding fragments experimentally observed. We identify energy thresholds for those channels to occur, the highest being 4.0 eV; most of the fragmentation channels that require energies larger than 4.0 eV in ours calculations does not appear in the experiment.

Appendix

Appendix A

Appendix of chapter 3

A.1 Small nickel oxide clusters.

Tabla A.1: Several properties of low-energy isomers of neutral Ni_3O_m clusters with m = 1-6: Sym = molecular symmetry; $E_b(n,m)$ = binding energy per atom in eV; I_p = ionization potential in eV; E_a = electron affinity in eV; μ = magnetic moment in Bohr magnetons (μ_B); D(Ni-Ni)= average distance between first neighbour nickel atoms in Å; D(Ni-O) = average distance between first neighbour nickel-oxygen atoms in Å

Signature			neutral				
$n.m$-isomer	Sym	$E_b(n,m)$	I_p	E_a	μ	D(Ni-Ni)	D(Ni-O)
3.1-I	C_{3v}	2.69	6.56	0.72	4	2.38	1.94
3.1.II	C_s	2.66	7.01	1.10	4	2.34	1.84
3.1.III	C_{2v}	2.49	7.46	1.59	4	2.29	1.70
3.2-I	C_s	3.16	7.54	2.13	4	2.46	1.82
3.2-II	C_s	3.11	7.15	1.47	4	2.43	1.92
3.2-III	C_{2v}	3.01	6.99	1.20	2	2.50	1.97
3.3-I	D_{3h}	3.64	8.50	2.47	2	2.44	1.80
3.3-II	C_s	3.33	7.98	2.56	4	2.55	1.85
3.3-III	$C_{\infty v}$	3.27	7.57	2.59	2	-	1.74
3.4-I	C_{3v}	3.56	8.90	2.94	2	2.54	1.89
3.4-II	C_s	3.52	8.66	2.95	4	2.52	1.81
3.4-III	C_1	3.30	8.32	4.47	2	2.60	1.89
3.5-I	D_{3h}	3.42	8.98	3.23	4	2.53	1.94
3.5-II	C_1	3.36	9.45	4.17	6	2.67	1.88
3.6-I	C_s	3.44	9.69	4.49	4	3.23	1.76
3.6-II	C_s	3.43	8.74	3.49	4	2.83	1.87

Tabla A.2: Several properties of low-energy isomers of $[Ni_3O_m]^{\pm}$ cationic and anionic clusters with m = 1-6: Sym = molecular symmetry; $E_b(n,m)$ = binding energy per atom in eV; μ = magnetic moment in Bohr magnetons (μ_B); D(Ni-Ni)= average distance between first neighbour nickel atoms in Å; D(Ni-O) = average distance between first neighbour nickel-oxygen atoms in Å

Signature				cation/anion	
$n.m$-isomer	Sym	$E_b(n,m)$	μ	D(Ni-Ni)	D(Ni-O)
3.1-I	C_{3v}/C_1	2.98/2.84	3	2.44/2.42	1.89/1.92
3.1.II	C_{3v}/C_s	2.83/2.90	3	2.57/2.32	1.78/1.88
3.1.III	C_s/C_{2v}	2.55/2.85	5/3	2.34/2.28	1.74/1.72
3.2-I	C_{2v}/C_s	3.20/3.56	5	2.89/2.46	1.81/1.85
3.2-II	C_s	3.22/3.38	5	2.62/2.42	1.91/1.95
3.2-III	D_{3h}/C_{2v}	3.24/3.31	5	2.58/2.57	1.96/1.99
3.3-I	D_{3h}	3.51/4.03	1/3	3.12/2.51	1.79/1.82
3.3-II	C_s	3.28/3.73	1/5	2.73/2.17	1.85/1.89
3.3-III	$C_{\infty v}$	3.29/3.68	3/5	- / -	1.75/1.76
3.4-I	C_s/C_{3v}	3.35/3.95	5	2.79/2.51	1.89/1.94
3.4-II	C_s	3.38/3.92	5	2.70/2.51	1.81/1.83
3.4-III	C_1/ -	3.22/ -	5/-	2.74/ -	1.90/ -
3.5-I	D_{3h}	3.27/3.81	5/3	2.60/2.48	1.92/1.96
3.5-II	C_1/C_s	3.14/3.86	7	2.72/2.62	1.88/1.90
3.6-I	C_s/C_1	3.22/3.93	7/5	3.35/3.29	1.77/1.77
3.6-II	C_s	3.32/3.80	5/3	2.92/2.74	1.87/1.87

Tabla A.3: Several properties of low-energy isomers of neutral Ni_4O_m clusters with m = 1-7: Sym = molecular symmetry; $E_b(n,m)$ = binding energy per atom in eV; I_p = ionization potential in eV; E_a = electron affinity in eV; μ = magnetic moment in Bohr magnetons (μ_B); D(Ni-Ni)= average distance between first neighbour nickel atoms in Å; D(Ni-O) = average distance between first neighbour nickel-oxygen atoms in Å

Signature			neutral				
$n.m$-isomer	Sym	$E_b(n,m)$	I_p	E_a	μ	D(Ni-Ni)	D(Ni-O)
4.1-I	C_{2v}	2.76	6.55	1.06	4	2.41	1.83
4.1-II	C_{3v}	2.73	6.30	0.90	4	2.38	1.97
4.1-III	C_{2v}	2.62	6.89	1.72	6	2.34	1.82
4.2-I	C_{2v}	3.19	7.55	2.33	6	2.48	1.82
4.2-II	C_s	3.18	7.12	1.72	6	2.50	1.90
4.2-III	C_s	3.17	7.36	2.44	4	2.49	1.81
4.3-I	C_s	3.52	7.52	2.41	4	2.48	1.85
4.3-II	C_s	3.47	7.13	2.52	0	2.50	1.83
4.3-III	C_{3v}	3.42	6.81	1.85	2	2.60	1.94
4.4-I	C_{2v}	3.80	8.09	3.53	2	2.68	1.79
4.4-II	C_{3v}	3.75	8.00	2.54	8	2.71	1.87
4.4-III	T_d	3.74	7.73	1.61	0	2.71	1.98
4.5-I	C_{2v}	3.75	8.44	3.09	4	2.81	1.89
4.5-II	C_{2v}	3.69	7.89	3.30	2	2.76	1.81
4.5-III	C_{2v}	3.66	7.64	3.56	4	2.55	1.82
4.6-I	C_2	3.72	8.72	3.61	2	2.92	1.83
4.6-II	C_s	3.66	8.89	3.62	6	2.66	1.91
4.6-III	D_{4h}	3.62	8.11	3.77	6	2.48	1.96
4.7-I							
4.7-II	C_{3v}	3.59	9.09	4.17	4	2.63	1.89
4.7-III	C_{2v}	3.57	9.49	4.16	6	2.61	1.92

Tabla A.4: Several properties of low-energy isomers of $[Ni_4O_m]^{\pm}$ cationic and anionic clusters with m = 1-7: Sym = molecular symmetry; $E_b(n,m)$ = binding energy per atom in eV; μ = magnetic moment in Bohr magnetons (μ_B); D(Ni-Ni)= average distance between first neighbour nickel atoms in Å; D(Ni-O) = average distance between first neighbour nickel-oxygen atoms in Å

Signature				cation/anion	
$n.m$-isomer	Sym	$E_b(n,m)$	μ	D(Ni-Ni)	D(Ni-O)
4.1-I	C_{2v}/C_2	2.99/2.95	5	2.47/2.36	1.82/1.85
4.1-II	C_s	3.01/2.88	5/3	2.52/2.39	1.91/1.97
4.1-III	C_{2v}	2.78/2.94	5	2.36/2.38	1.81/1.82
4.2-I	C_{2v}/C_s	3.22/3.56	7/5	2.69/2.39	1.82/1.85
4.2-II	C_s	3.28/3.45	5	2.58/2.48	1.86/1.90
4.2-III	C_s/ -	3.23/ -	7/-	2.64/ -	1.83/ -
4.3-I	C_s	3.55/3.85	7/5	2.75/2.46	1.85/1.87
4.3-II	C_s/C_{3v}	3.55/3.81	7/5	2.74/2.46	1.90/1.85
4.3-III	C_{3v}	3.55/3.67	7/5	2.77/2.58	1.95/1.98
4.4-I	C_1/D_{4h}	3.67/4.15	5/7	3.23/2.46	1.78/1.82
4.4-II	C_{3v}/C_s	3.61/3.97	9/7	2.76/2.56	1.86/1.90
4.4-III	T_d	3.66/3.85	1/7	2.78/2.69	1.96/2.00
4.5-I	C_{4v}/C_s	3.67/4.08	3/7	2.84/2.81	1.89/1.87
4.5-II	C_{2v}	3.67/4.05	1/3	3.08/2.68	1.78/1.84
4.5-III	C_{2v}/C_s	3.67/4.04	5	3.08/2.64	1.79/1.84
4.6-I	C_{3v}/T_d	3.65/4.07	3/11	3.11/2.75	1.84/1.87
4.6-II	C_s	3.54/4.01	7/5	2.71/2.64	1.90/1.92
4.6-III	C_{2h}/D_{4h}	3.58/3.98	5	2.79/2.45	1.91/1.99
4.7-I		/	/	/	/
4.7-II	C_{3v}	3.46/3.96	9/3	2.81/2.55	1.89/1.89
4.7-III	C_{2v}/C_s	3.41/3.94	7/5	2.70/2.55	1.92/1.92

Tabla A.5: Several properties of low-energy isomers of neutral Ni_5O_m clusters with m = 1-8: Sym = molecular symmetry; $E_b(n,m)$ = binding energy per atom in eV; I_p = ionization potential in eV; E_a = electron affinity in eV; μ = magnetic moment in Bohr magnetons (μ_B); D(Ni-Ni)= average distance between first neighbour nickel atoms in Å; D(Ni-O) = average distance between first neighbour nickel-oxygen atoms in Å

Signature			neutral				
$n.m$-isomer	Sym	$E_b(n,m)$	I_p	E_a	μ	D(Ni-Ni)	D(Ni-O)
5.1-I	C_s	2.81	6.53	1.53	4	2.41	1.81
5.1-II	C_{2v}	2.72	5.79	1.48	6	2.44	1.86
5.1-III	C_{4v}	2.68	6.06	0.95	4	2.42	1.98
5.2-I	C_s	3.20	6.68	1.98	4	2.55	1.93
5.2-II	C_s	3.19	6.77	2.01	6	2.52	1.89
5.2-III	C_{2v}	3.18	6.90	1.85	6	2.50	1.82
5.3-I	C_s	3.49	6.40	2.46	6	2.50	1.89
5.3-II	C_s	3.48	6.99	1.82	4	2.57	1.92
5.3-III	C_s	3.46	7.10	2.41	6	2.62	1.85
5.4-I	C_{2v}	3.75	7.79	2.87	8	2.56	1.87
5.4-II	C_1	3.68	7.35	2.55	8	2.65	1.92
5.4-III	C_s	3.61	7.99	2.83	4	2.59	1.81
5.5-I	C_{2v}	3.80	7.85	3.56	2	3.08	1.75
5.5-II	C_{2v}	3.74	7.52	2.57	2	2.81	1.95
5.5-III	C_1	3.73	7.61	2.54	2	2.80	1.93
5.5-IV	C_{2v}	3.72	7.44	2.89	2	2.61	1.81
5.6-I	C_{2v}	3.86	8.33	3.54	8	2.79	1.79
5.6-II	C_{3v}	3.80	8.03	3.15	8	2.78	1.91
5.6-III	D_{3h}	3.78	7.85	2.67	6	2.66	1.97
5.7-I	C_s	3.83	8.55	3.52	0	2.13	1.85
5.7-II	C_s	3.82	8.54	3.55	4	2.83	1.86
5.7-III	C_{2v}	3.80	7.40	3.79	6	2.98	1.80
5.8-I	C_s	3.77	8.81	4.06	6	2.98	1.81
5.8-II	C_1	3.73	8.63	3.87	8	2.90	1.91
5.8-III	C_2	3.67	8.93	4.02	6	2.72	1.94

Tabla A.6: Several properties of low-energy isomers of $[Ni_5O_m]^{\pm}$ cationic and anionic clusters with m = 1-8: Sym = molecular symmetry; $E_b(n,m)$ = binding energy per atom in eV; μ = magnetic moment in Bohr magnetons (μ_B); D(Ni-Ni)= average distance between first neighbour nickel atoms in Å; D(Ni-O) = average distance between first neighbour nickel-oxygen atoms in Å

Signature				cation/anion	
$n.m$-isomer	Sym	$E_b(n,m)$	μ	D(Ni-Ni)	D(Ni-O)
5.1-I	C_s	3.01/3.04	5	2.45/2.41	1.81/1.85
5.1-II	C_s/C_{2v}	3.05/2.95	5	2.51/2.44	1.89/1.88
5.1-III	C_{4v}	2.96/2.83	5/3	2.44/2.43	1.99/1.98
5.2-I	C_s/ -	3.35/ -	7/-	2.63/ -	1.93/ -
5.2-II	C_s	3.33/3.46	7/5	2.65/2.44	1.87/1.92
5.2-III	C_{2v}	3.30/3.43	5	2.51/2.49	1.80/1.83
5.3-I	C_s	3.53/3.78	7	2.61/2.51	1.87/1.91
5.3-II	C_s	3.57/3.69	7	2.71/2.58	1.92/1.95
5.3-III	C_s	3.53/3.74	5	2.69/2.53	1.83/1.87
5.4-I	C_s/C_{2v}	3.74/4.05	9/7	2.69/2.53	1.86/1.88
5.4-II	C_s	3.72/3.95	9/7	2.81/2.56	1.91/1.95
5.4-III	C_s	3.58/3.91	5/3	2.65/2.30	1.81/1.84
5.5-I	C_s/D_{5h}	3.78/4.14	1	3.17/2.88	1.75/1.77
5.5-II	C_{2v}	3.77/3.99	3/9	2.84/2.71	1.93/1.96
5.5-III	C_1/C_s	3.76/3.99	5/9	2.90/2.71	1.92/1.96
5.5-IV	C_1	3.75/3.99	11/7	2.90/2.63	1.94/1.92
5.6-I	D_{3h}	3.81/4.09	5/7	2.86/2.80	1.86/1.81
5.6-II	C_s	3.78/4.08	7	2.93/2.77	1.90/1.92
5.6-III	D_{3h}	3.77/4.01	7/5	2.73/2.66	1.96/1.98
5.7-I	C_s	3.76/4.10	3	2.73/2.61	1.85/1.87
5.7-II	C_1/C_s	3.75/4.10	5	2.86/2.76	1.86/1.88
5.7-III	C_2/C_{2v}	3.83/4.11	5	3.00/2.92	1.80/1.85
5.8-I	C_s	3.69/4.07	7/5	3.06/2.88	1.82/1.84
5.8-II	C_1	3.66/4.01	9/7	2.83/2.86	1.91/1.91
5.8-III	C_2/C_s	3.58/3.97	9/9	2.79/2.75	1.94/1.96

Tabla A.7: Several properties of low-energy isomers of neutral Ni_6O_m clusters with m = 1-9: Sym = molecular symmetry; $E_b(n,m)$ = binding energy per atom in eV; I_p = ionization potential in eV; E_a = electron affinity in eV; μ = magnetic moment in Bohr magnetons (μ_B); D(Ni-Ni)= average distance between first neighbour nickel atoms in Å; D(Ni-O) = average distance between first neighbour nickel-oxygen atoms in Å

Signature			neutral				
$n.m$-isomer	Sym	$E_b(n,m)$	I_p	E_a	μ	D(Ni-Ni)	D(Ni-O)
6.1-I	C_s	2.88	6.33	1.39	6	2.45	1.95
6.1-II	C_{3v}	2.87	6.33	1.68	6	2.46	1.92
6.1-III	C_{2v}	2.86	6.60	1.85	6	2.43	1.84
6.2-I	C_{2v}	3.25	6.78	1.83	8	2.51	1.92
6.2-II	C_{2v}	3.21	6.98	2.03	6	2.52	1.92
6.2-III	D_{3d}	3.18	6.64	1.72	4	2.48	1.90
6.3-I	C_{3v}	3.56	7.15	3.15	8	2.52	1.92
6.3-II	C_s	3.44	6.83	2.05	6	2.53	1.93
6.3-III	C_{2v}	3.44	7.36	2.34	8	2.54	1.83
6.4-I	T_d	3.80	7.45	2.37	8	2.56	1.92
6.4-II	C_1	3.64	7.11	3.95	4	2.38	1.89
6.4-III	D_{2h}	3.63	7.07	2.35	6	2.62	1.92
6.5-I	C_1	3.80	7.40	3.90	10	2.83	1.88
6.5-II	C_1	3.78	7.24	2.74	10	1.73	1.92
6.5-III	C_{3v}	3.81	7.61	2.59	4	2.59	1.92
6.6-I	D_{3h}	3.87	7.21	2.89	2	2.58	1.93
6.6-II	C_s	3.86	7.19	2.92	2	2.79	1.92
6.6-III	C_1	3.82	7.80	3.90	2	3.09	1.75
6.7-I	C_{3v}	3.92	7.99	3.52	4	2.59	1.94
6.7-II	C_s	3.90	8.26	3.31	4	2.61	1.93
6.7-III	C_s	3.83	8.38	3.60	10	2.77	1.88
6.8-I	O_h	3.98	8.84	3.91	4	2.59	1.94
6.8-II	D_{4h}	3.82	8.76	4.25	6	2.64	1.83
6.9-I	C_{4v}	3.88	9.01	4.35	8	2.68	1.95

Tabla A.8: Several properties of low-energy isomers of $[Ni_6O_m]^{\pm}$ cationic and anionic clusters with m = 1-9: Sym = molecular symmetry; $E_b(n,m)$ = binding energy per atom in eV; μ = magnetic moment in Bohr magnetons (μ_B); D(Ni-Ni)= average distance between first neighbour nickel atoms in Å; D(Ni-O) = average distance between first neighbour nickel-oxygen atoms in Å

Signature				cation/anion	
$n.m$-isomer	Sym	$E_b(n,m)$	μ	D(Ni-Ni)	D(Ni-O)
6.1-I	C_s	3.07/3.05	7/5	2.52/2.45	1.92/1.97
6.1-II	C_{2v}/C_{3v}	3.07/3.10	7	2.65/2.43	1.91/1.94
6.1-III	C_{2v}	3.02/3.06	7	2.45/2.42	1.82/1.86
6.2-I	C_{2v}	3.36/3.46	7	2.51/2.49	1.90/1.93
6.2-II	C_{2v}	3.30/3.45	5/7	2.47/2.45	1.83/1.84
6.2-III	C_2/C_1	3.32/3.38	7/5	2.51/2.45	1.89/1.92
6.3-I	C_s/C_{3v}	3.62/3.78	9/7	2.69/2.51	1.90/1.92
6.3-II	C	3.54/3.65	7	2.67/2.52	1.91/1.95
6.3-III	C_{2v}	3.48/3.69	7	2.56/2.52	1.80/1.83
6.4-I	T_d	3.83/4.02	5/7	2.59/2.54	1.89/1.92
6.4-II	C_1/ -	3.70/ -	9/-	2.71/ -	1.89/ -
6.4-III	D_{4h}/D_{2h}	3.70/3.86	7/5	2.71/2.55	1.89/1.93
6.5-I	C_1/D_{3h}	3.83/4.14	11/9	2.53/2.51	1.88/1.87
6.5-II	C_1	3.82/4.02	11/9	2.81/2.65	1.92/1.94
6.5-III	C_{3v}/C_1	3.82/4.03	5/7	2.68/2.58	1.92/2.01
6.6-I	C_s/C_{3v}	3.91/4.10	1/7	3.03/2.72	1.94/1.95
6.6-II	C_1/D_{2h}	3.91/4.10	3/11	2.77/2.60	1.91/2.01
6.6-III	D_{6h}/C_1	3.81/4.07	1/11	3.33/2.92	1.75/1.79
6.7-I	C_{3v}	3.90/4.18	7/3	2.67/2.58	1.94/1.94
6.7-II	C_s	3.86/4.15	5	2.67/2.67	1.92/1.94
6.7-III	C_s/C_1	3.78/4.10	11/9	2.83/2.74	1.87/1.89
6.8-I	O_h	3.90/4.25	5/3	2.62/2.58	1.94/1.95
6.8-II	D_{4h}	3.74/4.11	7/9	2.75/2.75	1.83/1.84
6.9-I	C_{4v}	3.79/4.16	9/7	2.76/2.66	1.95/1.95

Tabla A.9: Several properties of low-energy isomers of neutral Ni_7O_m clusters with m = 1-10: Sym = molecular symmetry; $E_b(n,m)$ = binding energy per atom in eV; I_p = ionization potential in eV; E_a = electron affinity in eV; μ = magnetic moment in Bohr magnetons (μ_B); D(Ni-Ni)= average distance between first neighbour nickel atoms in Å; D(Ni-O) = average distance between first neighbour nickel-oxygen atoms in Å

Signature			neutral				
$n.m$-isomer	Sym	$E_b(n,m)$	I_p	E_a	μ	D(Ni-Ni)	D(Ni-O)
7.1-I	C_s	2.96	6.31	1.66	8	2.47	1.92
7.1-II	C_s	2.93	6.12	1.81	8	2.48	1.92
7.1-III	C_s	2.91	6.11	1.68	8	2.45	1.94
7.2-I	C_s	3.29	6.77	1.99	8	2.49	1.92
7.2-II	C_2	3.25	6.56	1.98	8	2.45	1.93
7.2-III	C_s	3.21	6.56	1.84	6	2.48	1.91
7.3-I	C_{3v}	3.58	7.95	2.13	8	2.50	1.92
7.3-II	C_{3v}	3.57	6.77	1.88	8	2.52	1.92
7.3-III	C_1	3.41	6.61	3.00	8	2.56	1.94
7.4-I	C_s	3.71	7.13	2.44	8	2.54	1.91
7.4-II	C_s	3.71	7.21	2.61	8	2.54	1.89
7.4-III	C_{3v}	3.58	6.53	2.53	4	2.53	1.93
7.5-I	C_s	3.87	7.52	3.06	10	2.54	1.90
7.5-II	C_{2v}	3.74	7.30	3.84	10	2.66	1.93
7.5-III	C_s	3.72	6.86	2.60	8	2.66	1.80
7.6-I	C_{3v}	3.89	7.43	3.40	12	2.65	1.88
7.6-II	C_{3v}	3.86	7.23	2.99	12	2.66	1.94
7.6-III	C_1	3.86	7.50	3.44	10	2.54	1.90
7.7-I	C_{3v}	3.93	7.55	2.99	2	2.82	1.88
7.7-II	C_s	3.89	7.60	3.00	6	2.72	1.94
7.7-III	C_{3v}	3.86	7.84	3.34	4	2.53	1.95
7.8-I	C_s	3.96	7.81	3.32	6	2.82	1.84
7.8-II	C_s	3.95	7.94	3.24	4	2.83	1.88
7.8-III	C_s	3.94	7.98	3.53	2	2.85	1.88
7.9-I	C_s	3.98	8.24	3.65	4	2.88	1.90
7.9-II	C_{3v}	3.96	8.26	3.63	4	2.85	1.90
7.10-I	C_{3v}	4.01	8.43	3.87	6	2.91	1.91

Tabla A.10: Several properties of low-energy isomers of $[Ni_7O_m]^{\pm}$ cationic and anionic clusters with m = 1-10: Sym = molecular symmetry; $E_b(n,m)$ = binding energy per atom in eV; μ = magnetic moment in Bohr magnetons (μ_B); D(Ni-Ni)= average distance between first neighbour nickel atoms in Å; D(Ni-O) = average distance between first neighbour nickel-oxygen atoms in Å

Signature				cation/anion	
$n.m$-isomer	Sym	$E_b(n,m)$	μ	D(Ni-Ni)	D(Ni-O)
7.1-I	C_s	3.14/3.15	7	2.50/2.44	1.90/1.93
7.1-II	C_s/C_1	3.13/3.14	7	2.49/2.47	1.91/1.95
7.1-III	C_1/C_s	3.11/3.10	7	2.58/2.45	1.90/1.93
7.2-I	C_1/C_s	3.40/3.50	9/7	2.52/2.47	1.91/1.92
7.2-II	C_2	3.38/3.45	7	2.51/2.48	1.91/1.95
7.2-III	C_s	3.34/3.40	7/5	2.52/2.47	1.90/1.93
7.3-I	C_s/C_{3v}	3.65/3.78	9/7	2.59/2.49	1.90/1.93
7.3-II	C_s/C_{3v}	3.57/3.65	9/7	2.66/2.52	1.90/1.93
7.3-III	C_1	3.52/3.70	9/7	2.62/2.69	1.93/1.94
7.4-I	C_s	3.76/3.92	9/7	2.61/2.53	1.90/1.93
7.4-II	C_1/C_s	3.75/3.93	9/7	2.67/2.55	1.88/1.90
7.4-III	C_{3v}	3.69/3.80	11/9	2.79/2.54	1.94/1.97
7.5-I	C_s/C_{2v}	3.89/4.12	11/9	2.62/2.53	1.88/1.91
7.5-II	C_s/C_{2v}	3.77/4.05	11/9	2.74/2.68	1.92/1.97
7.5-III	C_s	3.79/3.93	9/7	2.73/2.66	1.92/1.94
7.6-I	C_{3v}/C_s	3.91/4.14	5/11	2.79/2.63	1.84/1.89
7.6-II	C_1/C_{3v}	3.90/4.08	13/11	2.85/2.60	1.94/1.97
7.6-III	C_s/C_1	3.87/4.11	11/9	2.79/2.86	1.89/1.92
7.7-I	C_{3v}	3.94/4.14	1/5	2.84/2.78	1.88/1.92
7.7-II	C_s	3.91/4.10	11/7	2.79/2.68	1.93/1.95
7.7-III	C_{3v}	3.85/4.09	11/3	2.57/2.52	1.92/1.95
7.8-I	C_s	3.95/4.17	7/5	2.85/2.58	1.93/1.93
7.8-II	C_1/C_s	3.94/4.16	5/9	2.89/2.82	1.88/1.91
7.8-III	C_1/C_s	3.93/4.17	3	3.05/2.80	1.87/1.89
7.9-I	C_s	3.95/4.20	3/5	2.92/2.82	1.89/1.91
7.9-II	C_{3v}	3.93/4.18	11/5	2.95/2.82	1.91/1.91
7.10-I	C_{3v}	3.97/4.23	5	2.91/2.88	1.90/1.92

Tabla A.11: Several properties of low-energy isomers of neutral Ni_8O_m clusters with m = 1-10: Sym = molecular symmetry; $E_b(n,m)$ = binding energy per atom in eV; I_p = ionization potential in eV; E_a = electron affinity in eV; μ = magnetic moment in Bohr magnetons (μ_B); D(Ni-Ni)= average distance between first neighbour nickel atoms in Å; D(Ni-O) = average distance between first neighbour nickel-oxygen atoms in Å

Signature			neutral				
$n.m$-isomer	Sym	$E_b(n,m)$	I_p	E_a	μ	D(Ni-Ni)	D(Ni-O)
8.1-I	C_s	3.03	6.32	1.76	8	2.45	1.92
8.1-II	C_1	3.00	6.30	1.70	8	2.51	1.93
8.1-III	C_s	2.99	6.35	1.88	8	2.53	1.90
8.2-I	C_{2v}	3.35	6.69	1.94	8	2.46	1.92
8.2-II	C_s	3.27	6.56	1.91	8	2.56	1.91
8.2-III	C_s	3.24	6.81	2.38	10	2.54	1.82
8.3-I	C_1	3.50	6.57	2.23	8	2.54	1.91
8.3-II	C_s	3.48	6.83	2.38	8	2.56	1.89
8.3-III	C_s	3.47	6.66	2.28	10	2.50	1.90
8.4-I	C_{2v}	3.67	7.15	2.62	10	2.53	1.91
8.4-II	S_2	3.64	6.88	2.32	8	2.58	1.90
8.4-III	C_1	3.64	7.06	2.69	10	2.51	1.90
8.5-I	C_{2v}	3.84	7.33	2.61	10	2.53	1.94
8.5-II	C_1	3.73	5.98	2.86	10	2.62	1.90
8.5-III	C_{2v}	3.70	7.09	2.78	12	2.60	2.09
8.6-I	C_1	3.88	8.18	3.11	4	2.65	1.91
8.6-II	C_{4v}	3.87	9.41	2.83	12	2.56	1.98
8.6-III	C_{2v}	3.72	7.39	2.92	4	2.52	1.94
8.7-I	C_1	3.94	7.33	3.26	10	2.70	1.91
8.7-II	C_s	3.92	7.27	2.96	12	2.77	1.93
8.7-III	C_1	3.92	7.46	2.93	8	2.80	1.94
8.8-I	C_1	3.97	7.40	3.20	4	2.71	1.83
8.8-II	C_s	3.96	7.30	3.40	8	2.75	1.92
8.9-I	C_1	4.00	7.82	3.35	8	2.93	1.93
8.9-II	C_1	3.97	7.06	3.72	8	2.78	1.92
8.9-III	C_1	3.97	7.39	3.66	12	2.78	1.94
8.10-I	C_1	4.02	7.92	3.99	2	2.80	1.85
8.10-II	C_1	4.00	8.07	3.93	4	2.60	1.91

Tabla A.12: Several properties of low-energy isomers of $[Ni_8O_m]^{\pm}$ cationic and anionic clusters with m = 1-10: Sym = molecular symmetry; $E_b(n,m)$ = binding energy per atom in eV; μ = magnetic moment in Bohr magnetons (μ_B); D(Ni-Ni)= average distance between first neighbour nickel atoms in Å; D(Ni-O) = average distance between first neighbour nickel-oxygen atoms in Å

Signature				cation/anion	
$n.m$-isomer	Sym	$E_b(n,m)$	μ	D(Ni-Ni)	D(Ni-O)
8.1-I	C_s	3.18/3.21	9/7	2.48/2.46	1.91/1.93
8.1-II	C_1	3.15/3.17	9/7	2.54/2.51	1.92/1.94
8.1-III	C_s	3.15/3.19	9	2.52/2.53	1.90/1.94
8.2-I	C_{2v}	3.45/3.53	9/7	2.52/2.46	1.91/1.92
8.2-II	C_s	3.39/3.45	9/7	2.59/2.55	1.91/1.92
8.2-III	C_s	3.33/3.46	9	2.57/2.51	1.82/1.84
8.3-I	C_s/C_1	3.60/3.69	9/7	2.45/2.39	1.91/1.93
8.3-II	C_s	3.56/3.69	9/7	2.56/2.52	1.88/1.89
8.3-III	C_s	3.56/3.66	11/9	2.55/2.55	1.90/1.92
8.4-I	C_1/C_{2v}	3.72/3.88	11/9	2.61/2.51	1.90/1.92
8.4-II	C_1/s_4	3.70/3.82	9/7	2.63/2.57	1.89/1.91
8.4-III	C_s/C_1	3.69/3.85	11/9	2.62/2.60	1.89/1.91
8.5-I	C_{2v}	3.87/4.03	11/9	2.55/2.50	1.93/1.96
8.5-II	C_1	3.87/3.94	11/9	2.65/2.63	1.88/1.92
8.5-III	C_{2v}	3.75/3.91	13/11	2.63/2.64	1.96/1.98
8.6-I	C_{2v}/C_1	3.85/4.10	7	2.68/2.80	1.90/1.89
8.6-II	C_{4v}	3.90/4.06	11	2.65/2.55	1.96/1.97
8.6-III	C_{2v}	3.75/3.92	5/3	2.57/2.51	1.93/1.95
8.7-I	C_1	3.96/4.14	9	2.80/2.69	1.91/1.92
8.7-II	C_1/C_s	3.95/4.10	9/11	2.74/2.67	1.92/1.95
8.7-III	C_1	3.93/4.10	11/9	2.87/2.74	1.90/1.97
8.8-I	C_1	3.99/4.16	7	2.75/2.73	1.91/1.93
8.8-II	C_s/C_{4v}	3.98/4.15	5/7	2.76/2.78	1.92/1.93
8.9-I	C_1	3.99/4.20	9/7	2.75/2.89	1.93/1.94
8.9-II	C_1	4.00/4.18	7	2.80/2.66	1.86/1.93
8.9-III	C_s/C_1	3.98/4.18	11/7	2.81/2.77	1.87/1.87
8.10-I	C_2	4.01/4.24	9/7	2.81/2.78	1.91/1.92
8.10-II	C_1	3.98/4.21	9/7	2.65/2.54	1.93/1.93

Tabla A.13: Several properties of low-energy isomers of $[Ni_8O_m]^{\pm}$ cationic and anionic clusters with m = 1-10: Sym = molecular symmetry; $E_b(n,m)$ = binding energy per atom in eV; μ = magnetic moment in Bohr magnetons (μ_B); D(Ni-Ni)= average distance between first neighbour nickel atoms in Å; D(Ni-O) = average distance between first neighbour nickel-oxygen atoms in Å

Signature			neutral						
$n.m$-isomer	E_t	E_b/atom	$\triangle E$	I_p	E_a	$I_p - E_a$	D(Ni-Ni)	D(Ni-O)	μ
6.0-I	20.61	2.62	0.00	6.77	1.86	4.91	2.35	—	8
6.0-II	20.21	2.55	0.40	6.30	1.81	4.49	2.15	—	6
6.0-III	20.17	2.54	0.45	6.36	1.85	4.51	2.30	—	6
6.0-IV	20.08	2.53	0.54	6.65	1.96	4.68	2.26	—	8
6.1-I	27.63	3.02	0.00	6.54	1.83	4.71	2.37	1.89	6
6.1-II	27.60	3.02	0.03	6.72	2.11	4.61	2.35	1.77	8
6.1-III	27.55	3.01	0.08	6.46	2.05	4.41	2.36	1.88	8
6.1-IV	26.42	2.85	1.21	6.16	1.82	4.34	2.31	1.95	6
6.2-I	35.44	3.43	0.00	6.95	2.21	4.74	2.39	1.82	6
6.2-II	35.32	3.42	0.12	6.77	2.14	4.63	2.41	1.86	8
6.2-III	35.19	3.40	0.25	7.08	2.26	4.82	2.49	1.77	6
6.2-IV	35.13	3.39	0.31	6.64	2.21	4.43	2.39	1.84	4
6.3-I	43.54	3.78	0.00	7.36	2.37	4.99	2.44	1.87	8
6.3-II	42.60	3.67	0.94	7.03	2.23	4.80	2.43	1.87	6
6.3-III	42.30	3.64	1.25	7.09	2.50	4.59	2.48	1.78	8
6.3-IV	42.09	3.62	1.45	6.87	2.38	4.49	2.41	1.86	6
6.4-I	51.66	4.06	0.00	6.92	2.59	4.33	2.40	1.88	8
6.4-II	50.17	3.91	1.49	7.31	2.70	4.62	2.52	1.83	6
6.4-III	50.16	3.91	1.51	7.24	2.41	4.83	2.52	1.85	4
6.4-IV	50.14	3.91	1.52	7.21	2.43	4.78	2.49	1.86	6
6.5-I	58.60	4.18	0.00	8.56	3.37	5.18	2.47	1.79	10
6.5-II	57.71	4.10	0.89	7.79	2.69	5.10	2.48	1.86	2
6.5-III	57.61	4.09	0.99	7.71	3.05	4.66	2.49	1.83	8
6.5-IV	57.21	4.05	1.39	7.68	3.50	4.18	2.51	1.89	10
6.6-I	64.11	4.16	0.00	8.04	3.11	4.92	2.48	1.88	2
6.6-II	63.95	4.15	0.16	8.04	3.09	4.96	2.49	1.87	2
6.6-III	63.72	4.13	0.39	8.30	3.22	5.08	2.52	1.87	8
6.6-IV	63.52	4.11	0.59	7.45	3.70	3.74	2.58	1.88	6
6.7-I	70.61	4.22	0.00	8.42	3.45	4.97	2.49	1.89	4
6.7-II	70.04	4.18	0.57	8.28	4.02	4.26	2.58	1.87	4
6.7-III	70.01	4.18	0.60	7.82	3.44	4.37	2.52	1.88	6
6.7-IV	69.41	4.13	1.20	8.57	3.54	5.03	2.62	1.82	8
6.8-I	77.26	4.29	0.00	8.73	3.90	4.83	2.49	1.89	4
6.8-II	74.53	4.09	2.73	8.77	4.19	4.58	2.56	1.78	6
6.8-III	74.28	4.08	2.98	7.69	3.55	4.14	2.52	1.87	2
6.8-IV	74.13	4.06	3.13	8.18	3.59	4.60	2.49	1.91	4
6.9-I	81.34	4.17	0.00	8.87	4.40	4.47	2.58	1.90	8
6.9-II	80.83	4.14	0.51	8.60	5.07	3.53	2.50	1.90	4
6.9-III	80.19	4.10	1.14	8.37	3.72	4.65	2.79	1.83	4
6.9-IV	79.90	4.08	1.44	8.62	3.96	4.66	2.74	1.84	6

Tabla A.14: Several properties of low-energy isomers of $[Ni_8O_m]^{\pm}$ cationic and anionic clusters with m = 1-10: Sym = molecular symmetry; $E_b(n,m)$ = binding energy per atom in eV; μ = magnetic moment in Bohr magnetons (μ_B); D(Ni-Ni)= average distance between first neighbour nickel atoms in Å; D(Ni-O) = average distance between first neighbour nickel-oxygen atoms in Å

Signature		cation/anion	
$n.m$-isomer	E_t	$\triangle E$	μ
6.0-I	13.85/22.47	0.07/0.00	7
6.0-II	13.91/22.02	0.00/0.45	5/7
6.0-III	13.81/22.02	0.11/0.45	5/7
6.0-IV	13.43/22.04	0.48/0.43	5/7
6.1-I	21.09/29.46	0.01/0.25	7/5
6.1-II	20.88/29.71	0.20/0.00	5/7
6.1-III	21.09/29.60	0.00/0.11	5/7
6.1-IV	20.26/28.24	0.83/1.47	5
6.2-I	28.49/37.66	0.06/0.00	7/5
6.2-II	28.55/37.46	0.00/0.20	7
6.2-III	28.11/37.45	0.43/0.21	7
6.2-IV	28.49/37.34	0.06/0.32	5/1
6.3-I	36.18/45.91	0.00/0.00	9/7
6.3-II	35.57/44.83	0.61/1.08	7/5
6.3-III	35.20/44.79	0.97/1.12	7
6.3-IV	35.22/44.47	0.96/1.45	5
6.4-I	44.74/54.25	0.00/0.00	1/7
6.4-II	42.86/52.87	1.89/1.39	7/5
6.4-III	42.92/52.57	1.83/1.68	7/5
6.4-IV	42.94/52.57	1.81/1.68	5
6.5-I	50.04/61.98	0.00/0.00	9
6.5-II	49.92/60.40	0.12/1.57	5/3
6.5-III	49.91/60.66	0.14/1.32	9/7
6.5-IV	49.53/60.71	0.52/1.27	11/9
6.6-I	56.07/67.23	0.00/0.00	3
6.6-II	55.91/67.04	0.17/0.19	5/3
6.6-III	55.42/66.94	0.65/0.29	13/9
6.6-IV	56.08/67.23	0.00/0.00	5/3
6.7-I	62.19/74.06	0.00/0.00	5/3
6.7-II	61.76/74.06	0.44/0.00	5/3
6.7-III	62.19/73.45	0.00/0.61	5/5
6.7-IV	60.84/72.95	1.35/1.10	9
6.8-I	68.53/81.16	0.00/0.00	5/3
6.8-II	65.75/78.71	2.78/2.45	7/9
6.8-III	66.59/77.83	1.94/3.33	5/3
6.8-IV	65.95/77.71	2.58/3.45	3/3
6.9-I	72.47/85.74	0.00/0.16	5/7
6.9-II	72.23/85.90	0.24/0.00	5/3
6.9-III	71.82/83.91	0.64/1.98	9/3
6.9-IV	71.28/83.86	1.18/2.04	7/5

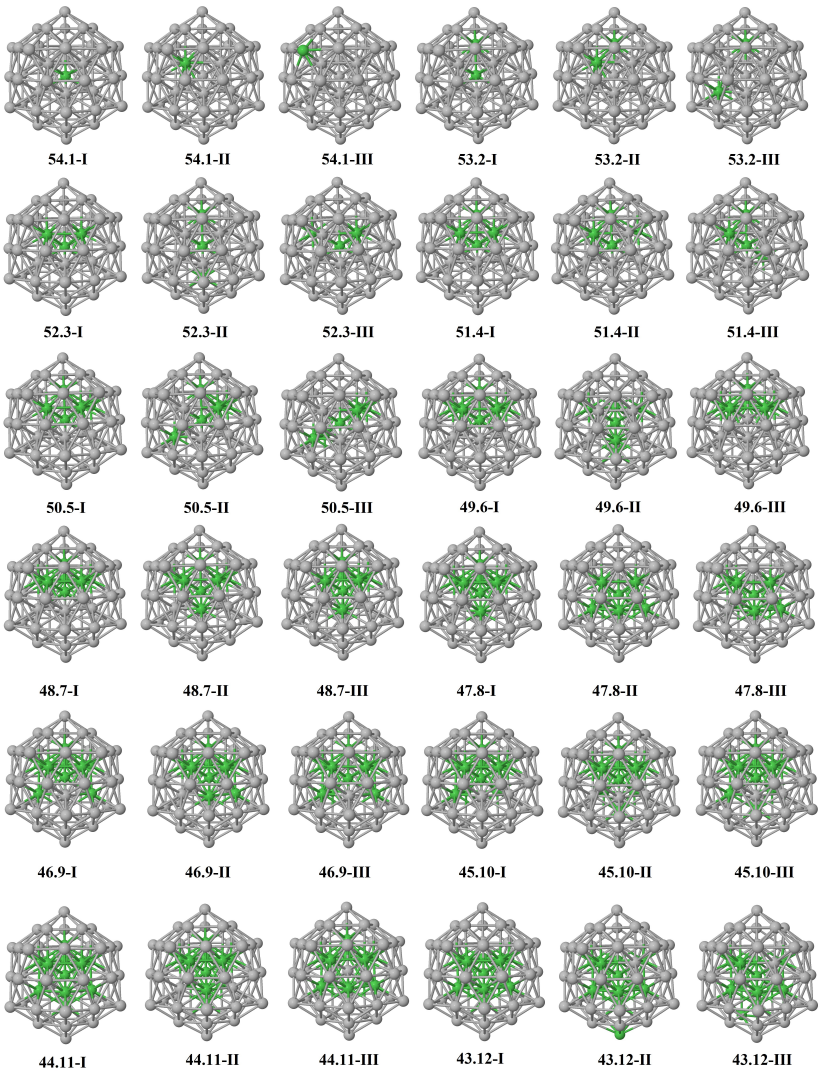

Figura A.1: Putative ground state and first two low-energy homotops from $Ag_{54}Ni$ to $Ag_{43}Ni_{12}$ clusters.

A.2 Oxidation of nickel-silver nanoalloys.

Tabla A.15: Several properties of the ground state and low-energy homotops of neutral Ag_xNi_y nanoalloys with $x + y = 55$: E_b = binding energy per atom (in eV); $\triangle$ = Energy difference (in eV) with respect to the ground estate; I_p = adiabatic ionization potential (in eV); E_a = adiabatic electron affinity (in eV); μ = total spin magnetic moment (in μ_B).

x.y-isomer	Eb	ΔE	I_p	E_a	I_p-E_a	I_p+E_a	μ (neutral)	μ (cationic)	μ (anionic)
55.0-I	2.40	0.00	4.08	1.51	2.57	5.59	3	4	2
54.1-I	2.43	0.00	4.21	1.53	2.68	5.74	4	3	3
54.1-II	2.42	0.58	4.13	1.46	2.67	5.60	4	3	3
54.1-III	2.42	0.67	4.18	1.52	2.66	5.71	4	3	3
53.2-I	2.45	0.00	4.17	1.59	2.58	5.76	3	2	4
53.2-II	2.44	0.51	4.10	1.52	2.58	5.62	3	2	4
53.2-III	2.44	0.57	4.09	1.51	2.58	5.60	3	2	4
52.3-I	2.47	0.00	4.12	1.54	2.58	5.66	2	1	3
52.3-II	2.47	0.02	4.12	1.53	2.59	5.65	2	1	3
52.3-III	2.47	0.06	4.11	1.53	2.58	5.65	2	1	3
51.4-I	2.50	0.00	4.06	1.48	2.57	5.54	1	0	2
51.4-II	2.49	0.06	4.06	1.48	2.58	5.53	1	0	2
51.4-III	2.49	0.06	4.06	1.48	2.58	5.54	1	0	2
50.5-I	2.52	0.00	4.11	1.42	2.70	5.53	0	1	1
50.5-II	2.52	0.05	4.11	1.41	2.69	5.52	0	1	1
50.5-III	2.52	0.06	4.14	1.42	2.72	5.55	0	1	1
49.6-I	2.54	0.00	4.05	1.43	2.62	5.47	1	2	4
49.6-II	2.54	0.12	4.14	0.43	3.71	4.57	1	2	0
49.6-III	2.53	0.50	4.27	1.61	2.66	5.88	1	2	0
48.7-I	2.57	0.00	4.15	1.32	2.83	5.48	2	3	3
48.7-II	2.57	0.08	4.17	1.38	2.79	5.56	2	3	3
48.7-III	2.57	0.10	4.14	1.32	2.82	5.45	2	3	3
47.8-I	2.59	0.00	4.19	1.45	2.74	5.64	3	4	2
47.8-II	2.59	0.12	4.17	1.48	2.69	5.66	3	4	2
47.8-III	2.59	0.13	4.31	1.48	2.83	5.79	3	4	2
46.9-I	2.61	0.00	4.22	1.49	2.74	5.71	4	5	3
46.9-II	2.61	0.02	4.18	1.53	2.66	5.71	4	5	3
46.9-III	2.61	0.03	4.22	1.30	2.92	5.52	4	5	3
45.10-I	2.63	0.00	4.21	1.52	2.69	5.73	5	6	4
45.10-II	2.63	0.02	4.20	-1.08	5.28	3.12	5	6	4
45.10-III	2.63	0.08	5.03	-1.15	6.19	3.88	5	6	4
44.11-I	2.66	0.00	4.23	1.50	2.73	5.73	6	7	5
44.11-II	2.66	0.07	4.24	1.54	2.69	5.78	6	7	5
44.11-III	2.64	1.19	4.29	1.57	2.72	5.85	6	7	5
43.12-I	2.68	0.00	4.29	1.55	2.74	5.84	7	8	6
43.12-II	2.68	0.29	4.31	1.57	2.73	5.88	7	8	6
43.12-III	2.68	0.29	4.31	1.59	2.72	5.90	7	8	6

Tabla A.16: Same caption as in Table A.15.

x.y-isomer	Eb	ΔE	I_p	E_a	I_p-E_a	I_p+E_a	μ (neutral)	μ (cationic)	μ (anionic)
42.13-I	2.71	0.00	4.35	1.54	2.81	5.89	8	9	7
42.13-II	2.70	0.44	4.36	1.60	2.76	5.95	8	9	7
42.13-III	2.69	1.01	5.53	-2.24	7.77	3.29	8	9	7
41.14-I	2.72	0.00	4.39	1.69	2.70	6.09	9	10	8
41.14-II	2.72	0.02	4.38	1.64	2.75	6.02	9	10	8
41.14-III	2.72	0.39	4.41	1.75	2.66	6.16	9	10	8
40.15-I	2.75	0.00	4.41	1.72	2.70	6.13	10	11	9
40.15-II	2.75	0.05	4.43	1.78	2.65	6.21	10	11	9
40.15-III	2.74	0.08	4.41	1.68	2.73	6.09	10	11	9
39.16-I	2.77	0.00	4.44	1.68	2.76	6.12	11	12	10
39.16-II	2.77	0.12	4.45	1.78	2.67	6.23	11	12	10
39.16-III	2.77	0.17	4.43	1.72	2.70	6.15	11	12	10
38.17-I	2.79	0.00	4.44	1.70	2.73	6.14	12	13	11
38.17-II	2.79	0.01	4.46	1.73	2.73	6.19	12	13	11
38.17-III	2.79	0.07	4.46	1.71	2.75	6.17	12	13	11
37.18-I	2.81	0.00	4.50	1.69	2.81	6.19	13	14	12
37.18-II	2.81	0.02	4.49	1.80	2.69	6.30	13	14	12
37.18-III	2.81	0.04	4.46	1.73	2.73	6.19	13	14	12
36.19-I	2.83	0.00	4.49	1.71	2.77	6.20	14	15	13
36.19-II	2.83	0.04	4.47	1.77	2.70	6.24	14	15	13
36.19-III	2.83	0.04	4.44	1.76	2.68	6.20	14	15	13
35.20-I	2.86	0.00	4.56	1.81	2.75	6.38	15	16	14
35.20-II	2.86	0.04	4.48	1.79	2.69	6.28	15	16	14
35.20-III	2.85	0.15	4.56	1.82	2.73	6.38	15	16	14
34.21-I	2.88	0.00	4.55	1.84	2.71	6.40	16	17	15
34.21-II	2.88	0.10	4.56	1.87	2.69	6.43	16	17	15
34.21-III	2.88	0.11	4.62	1.93	2.69	6.55	16	17	15
33.22-I	2.91	0.00	4.65	1.92	2.73	6.57	17	18	16
33.22-II	2.90	0.05	4.60	1.89	2.71	6.49	17	18	16
33.22-III	2.90	0.18	4.56	1.86	2.70	6.43	17	18	16
32.23-I	2.93	0.00	4.67	1.94	2.73	6.61	18	19	17
32.23-II	2.93	0.11	4.63	1.91	2.71	6.54	18	19	17
32.23-III	2.92	0.64	4.59	1.91	2.69	6.50	18	19	17
31.24-I	2.95	0.00	4.72	2.02	2.70	6.74	19	20	18
31.24-II	2.95	0.03	4.70	1.98	2.72	6.68	19	20	18
31.24-III	2.95	0.28	4.66	1.93	2.73	6.59	19	20	18

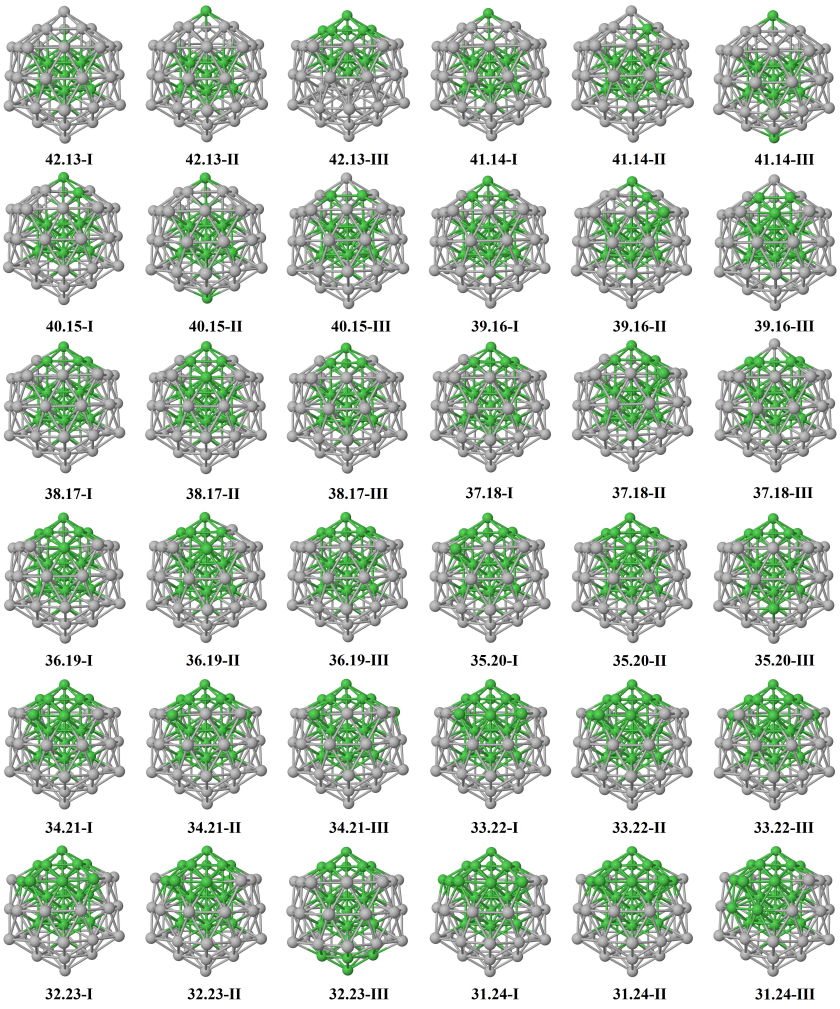

Figura A.2: Putative ground state and first two low-energy homotops from $Ag_{42}Ni_{13}$ to $Ag_{31}Ni_{24}$ clusters.

Tabla A.17: Same caption as in Table A.15.

x.y-isomer	Eb	ΔE	I_p	E_a	I_p-E_a	I_p+E_a	μ (neutral)	μ (cationic)	μ (anionic)
30.25-I	2.98	0.00	4.76	2.03	2.73	6.79	20	21	19
30.25-II	2.98	0.07	4.77	2.04	2.73	6.80	20	21	19
30.25-III	2.96	0.93	4.71	1.97	2.74	6.68	20	21	19
29.26-I	3.00	0.00	4.80	2.08	2.71	6.88	21	22	20
29.26-II	3.00	0.02	4.79	2.05	2.74	6.85	21	22	20
29.26-III	2.99	0.45	4.78	2.02	2.75	6.80	21	22	20
28.27-I	3.03	0.00	4.83	2.13	2.70	6.96	22	23	21
28.27-II	3.02	0.05	4.87	2.16	2.71	7.03	22	23	21
28.27-III	3.02	0.06	4.86	1.46	3.40	6.32	22	23	21
27.28-I	3.05	0.00	4.89	2.20	2.69	7.08	23	24	22
27.28-II	3.05	0.04	4.88	2.17	2.71	7.05	23	24	22
27.28-III	3.05	0.15	4.89	2.19	2.70	7.08	23	24	22
26.29-I	3.07	0.00	4.91	2.23	2.69	7.14	24	25	23
26.29-II	3.07	0.16	4.92	2.22	2.71	7.14	24	25	23
26.29-III	3.07	0.24	4.93	2.23	2.70	7.15	24	25	23
25.30-I	3.10	0.00	4.96	2.25	2.71	7.21	25	26	24
25.30-II	3.09	0.09	5.14	2.28	2.86	7.42	25	26	24
25.30-III	3.09	0.10	4.99	2.26	2.73	7.25	25	26	24
24.31-I	3.12	0.00	5.00	2.28	2.73	7.28	26	27	25
24.31-II	3.12	0.04	5.00	2.28	2.72	7.27	26	27	25
24.31-III	3.12	0.07	5.02	2.28	2.73	7.30	26	27	25
23.32-I	3.14	0.00	5.05	2.33	2.72	7.37	27	28	26
23.32-II	3.14	0.10	5.04	2.31	2.73	7.35	27	28	26
23.32-III	3.14	0.19	5.05	2.32	2.72	7.37	27	28	26
22.33-I	3.17	0.00	5.08	2.36	2.72	7.43	28	29	27
22.33-II	3.17	0.05	5.08	2.35	2.72	7.43	28	29	27
22.33-III	3.16	0.07	5.08	2.36	2.72	7.45	28	29	27
21.34-I	3.19	0.00	5.12	2.38	2.74	7.51	29	30	28
21.34-II	3.18	0.59	5.14	2.40	2.74	7.54	29	30	28
21.34-III	3.17	0.85	5.10	2.37	2.73	7.46	29	30	28
20.35-I	3.21	0.00	5.14	2.44	2.71	7.58	30	31	29
20.35-II	3.21	0.12	5.03	2.42	2.61	7.45	30	31	29
20.35-III	3.21	0.15	5.01	2.42	2.59	7.43	30	31	29
19.36-I	3.23	0.00	5.12	2.47	2.65	7.58	31	22	30
19.36-II	3.23	0.01	5.11	2.48	2.63	7.58	31	22	30
19.36-III	3.23	0.17	5.04	3.04	2.00	8.07	31	22	30

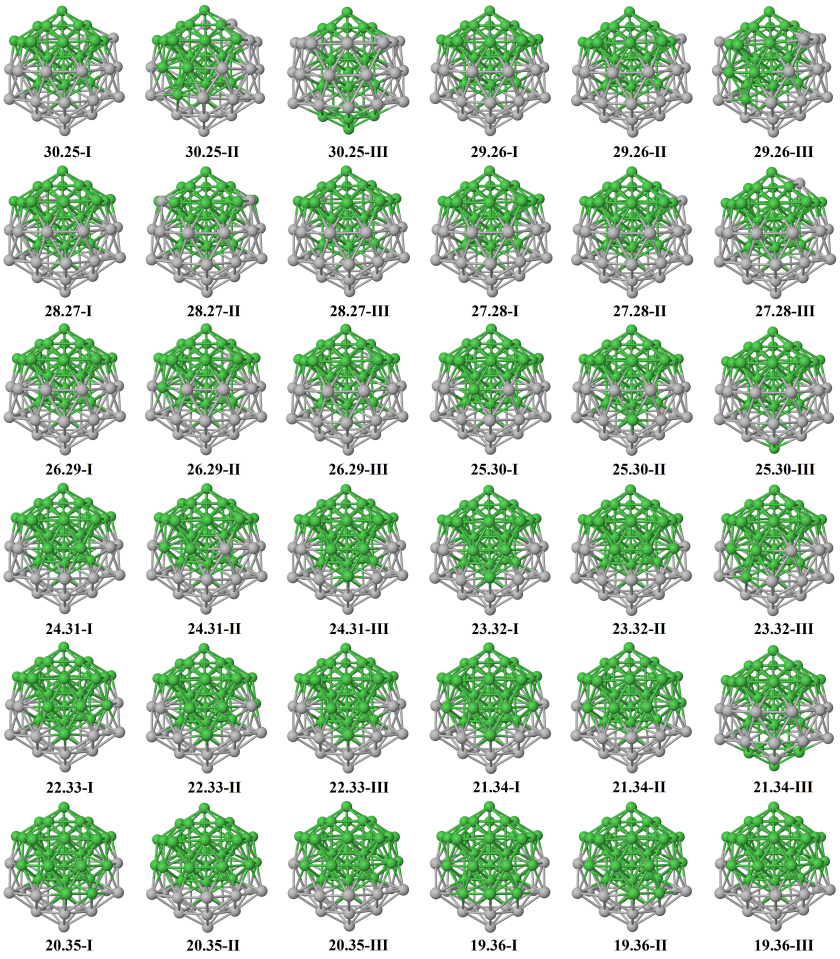

Figura A.3: Putative ground state and first two low-energy homotops from $Ag_{30}Ni_{25}$ to $Ag_{19}Ni_{36}$ clusters.

Tabla A.18: Same caption as in Table A.15.

x.y-isomer	Eb	ΔE	I_p	E_a	I_p-E_a	I_p+E_a	μ (neutral)	μ (cationic)	μ (anionic)
18.37-I	3.26	0.00	5.10	2.48	2.62	7.59	32	23	31
18.37-II	3.25	0.05	5.06	2.42	2.65	7.48	22	23	31
18.37-III	3.25	0.07	5.07	2.42	2.65	7.48	22	23	31
17.38-I	3.28	0.00	5.16	2.43	2.73	7.59	23	24	22
17.38-II	3.28	0.05	5.10	2.38	2.73	7.48	23	24	24
17.38-III	3.28	0.17	5.11	2.39	2.72	7.50	23	24	24
16.39-I	3.30	0.00	5.14	2.41	2.74	7.55	24	25	23
16.39-II	3.30	0.02	5.17	2.47	2.71	7.64	24	25	23
16.39-III	3.30	0.16	5.16	2.44	2.72	7.60	24	25	23
15.40-I	3.33	0.00	5.20	2.47	2.73	7.67	25	26	24
15.40-II	3.32	0.09	5.19	2.46	2.73	7.65	25	26	24
15.40-III	3.32	0.22	5.21	2.47	2.74	7.68	25	26	24
14.41-I	3.35	0.00	5.26	2.53	2.73	7.79	26	27	25
14.41-II	3.35	0.03	5.26	2.53	2.73	7.79	26	27	27
14.41-III	3.35	0.05	5.24	2.51	2.73	7.75	26	27	25
13.42-I	3.37	0.00	5.30	2.57	2.74	7.87	27	28	26
13.42-II	3.37	0.08	5.31	2.58	2.73	7.89	27	28	26
13.42-III	3.37	0.15	5.28	2.56	2.72	7.85	27	28	26
12.43-I	3.40	0.00	5.39	2.67	2.72	8.06	28	29	27
12.43-II	3.40	0.05	5.34	2.61	2.73	7.95	28	29	27
12.43-III	3.40	0.19	5.33	2.59	2.73	7.92	28	29	27
11.44-I	3.42	0.00	5.41	2.66	2.74	8.07	29	30	28
11.44-II	3.42	0.01	5.46	2.72	2.74	8.18	29	30	30
11.44-III	3.42	0.14	5.37	2.63	2.74	8.01	29	30	28
10.45-I	3.45	0.00	5.50	2.75	2.74	8.25	30	31	29
10.45-II	3.44	0.17	5.45	2.71	2.73	8.16	30	31	29
10.45-III	3.44	0.17	5.45	2.71	2.73	8.16	30	31	29
9.46-I	3.47	0.00	5.54	2.80	2.74	8.34	31	32	30
9.46-II	3.47	0.01	5.53	2.80	2.74	8.33	31	32	30
9.46-III	3.47	0.09	5.51	2.77	2.74	8.27	31	32	30
8.47-I	3.50	0.00	5.57	2.83	2.73	8.40	32	33	31
8.47-II	3.50	0.00	5.59	2.82	2.77	8.41	32	33	31
8.47-III	3.49	0.08	5.57	2.08	3.49	7.65	32	33	31
7.48-I	3.52	0.00	5.61	2.87	2.73	8.48	33	34	32
7.48-II	3.52	0.07	5.57	2.84	2.72	8.41	33	34	32
7.48-III	3.52	0.14	5.59	2.85	2.73	8.44	33	34	32

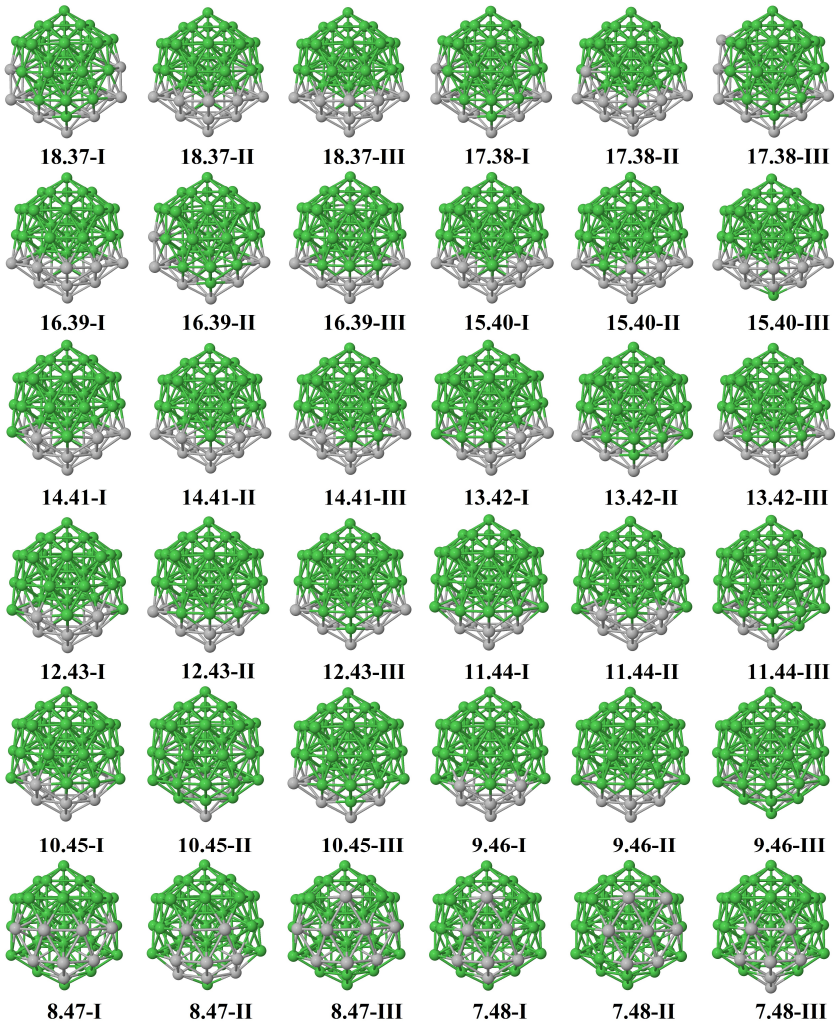

Figura A.4: Putative ground state and first two low-energy homotops from $Ag_{18}Ni_{37}$ to Ag_7Ni_{48} clusters.

Tabla A.19: Same caption as in Table A.15.

x.y-isomer	Eb	ΔE	I_p	E_a	I_p-E_a	I_p+E_a	μ (neutral)	μ (cationic)	μ (anionic)
6.49-I	3.54	0.00	5.66	2.91	2.74	8.57	34	35	33
6.49-II	3.54	0.04	5.64	2.91	2.73	8.55	34	35	33
6.49-III	3.54	0.13	5.67	2.75	2.92	8.43	34	35	33
5.50-I	3.57	0.00	5.69	2.95	2.73	8.64	35	36	34
5.50-II	3.56	0.03	5.69	2.95	2.73	8.64	35	36	34
5.50-III	3.56	0.03	5.71	2.99	2.72	8.70	35	36	34
4.51-I	3.59	0.00	5.75	3.03	2.72	8.78	36	37	35
4.51-II	3.59	0.01	5.72	3.00	2.73	8.72	36	37	35
4.51-III	3.59	0.02	5.72	3.05	2.67	8.77	36	37	35
3.52-I	3.61	0.00	5.78	3.06	2.73	8.84	37	38	36
3.52-II	3.61	0.02	5.78	3.06	2.72	8.84	37	38	36
3.52-III	3.61	0.08	5.76	3.03	2.72	8.79	37	38	36
2.53-I	3.64	0.00	5.82	3.09	2.72	8.91	38	39	37
2.53-II	3.64	0.03	5.81	3.09	2.72	8.90	38	39	37
2.53-III	3.64	0.07	5.81	3.09	2.72	8.90	38	39	37
1.54-I	3.66	0.00	5.84	3.13	2.71	8.98	39	40	38
1.54-II	3.66	0.09	5.83	3.12	2.71	8.95	39	40	38
1.54-III	3.64	1.26	5.86	3.15	2.71	9.01	39	40	38
0.55-I	3.69	0.00	5.90	3.19	2.71	9.09	40	41	39

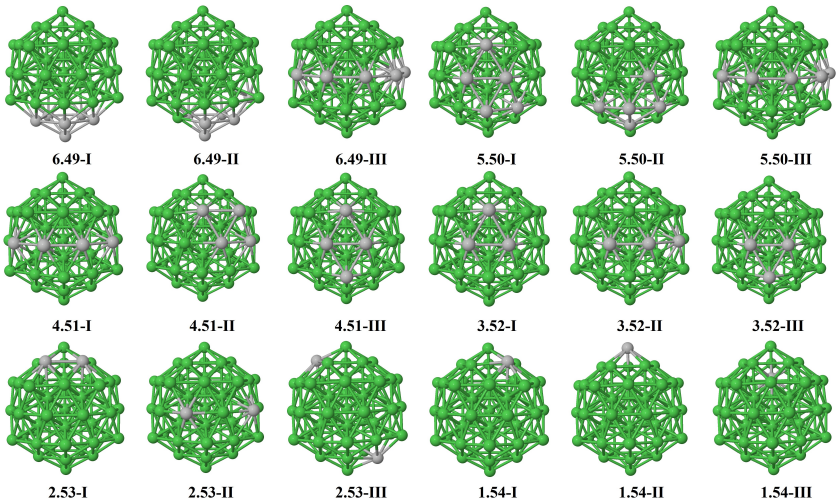

Figura A.5: Putative ground state and first two low-energy homotops from Ag_6Ni_{49} to $AgNi_{54}$ clusters.

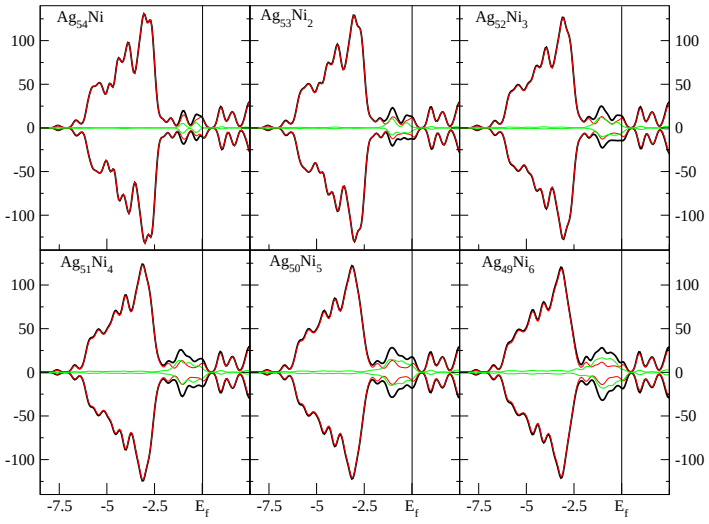

Figura A.6: Total DOS (black line), partial contribution of silver (red line) and nickel atoms (green line) of $Ag_{54}Ni$ to $Ag_{49}Ni_6$ clusters.

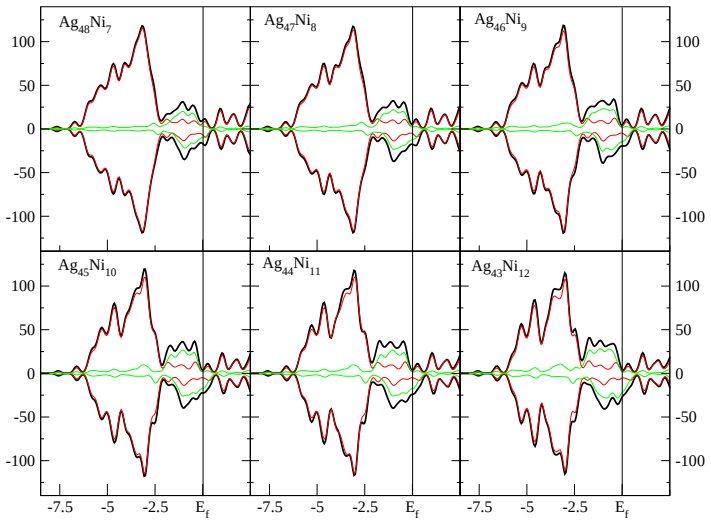

Figura A.7: Total DOS (black line), partial contribution of silver (red line) and nickel atoms (green line) of $Ag_{48}Ni_7$ to $Ag_{43}Ni_{12}$ clusters.

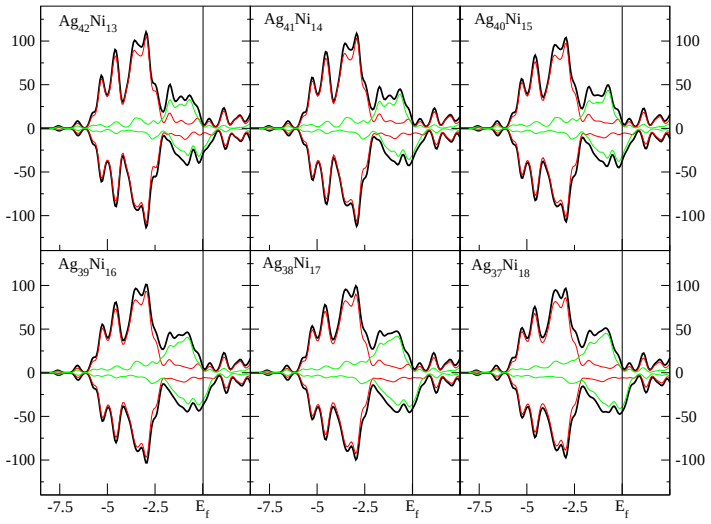

Figura A.8: Total DOS (black line), partial contribution of silver (red line) and nickel atoms (green line) of $Ag_{42}Ni_{13}$ to $Ag_{37}Ni_{18}$ clusters.

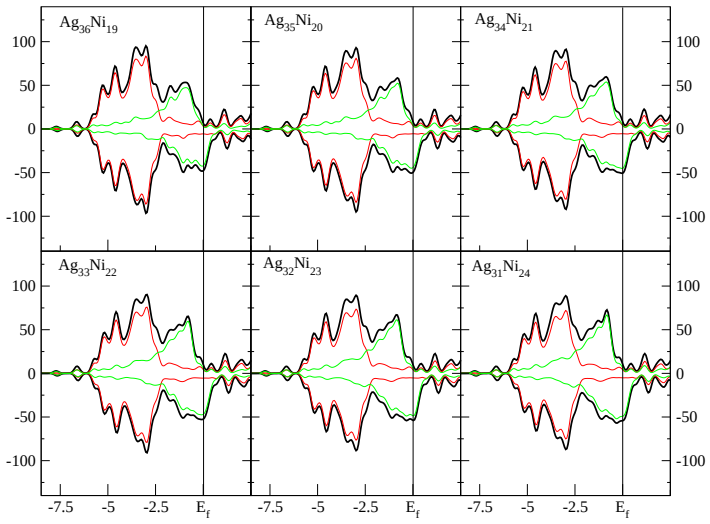

Figura A.9: Total DOS (black line), partial contribution of silver (red line) and nickel atoms (green line) of $Ag_{36}Ni_{19}$ to $Ag_{31}Ni_{24}$ clusters.

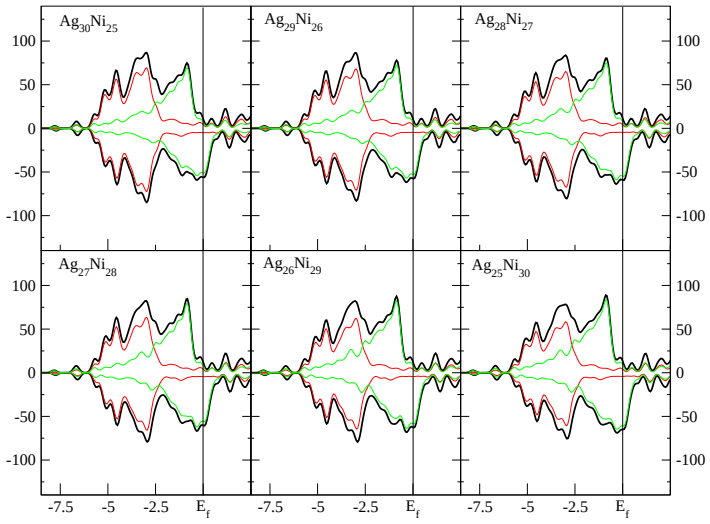

Figura A.10: Total DOS (black line), partial contribution of silver (red line) and nickel atoms (green line) of $Ag_{30}Ni_{25}$ to $Ag_{25}Ni_{30}$ clusters.

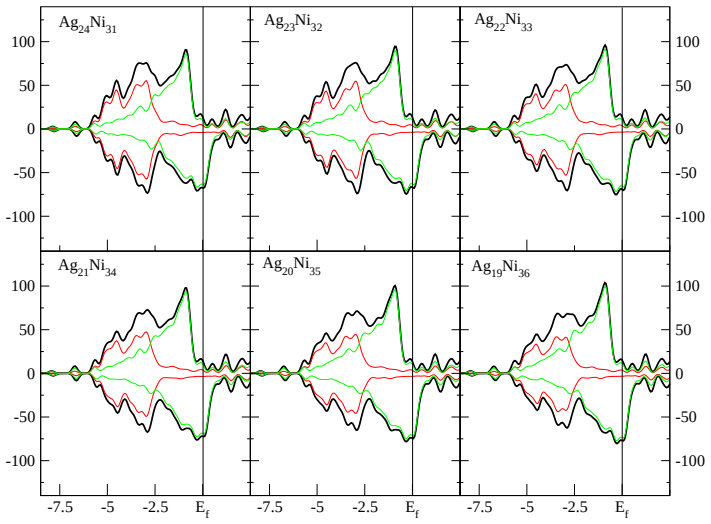

Figura A.11: Total DOS (black line), partial contribution of silver (red line) and nickel atoms (green line) of $Ag_{24}Ni_{31}$ to $Ag_{19}Ni_{36}$ clusters.

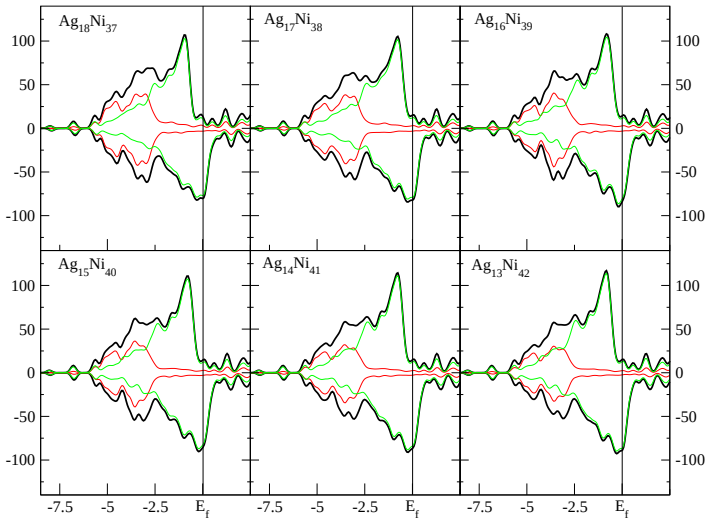

Figura A.12: Total DOS (black line), partial contribution of silver (red line) and nickel atoms (green line) of $Ag_{18}Ni_{37}$ to $Ag_{13}Ni_{42}$ clusters.

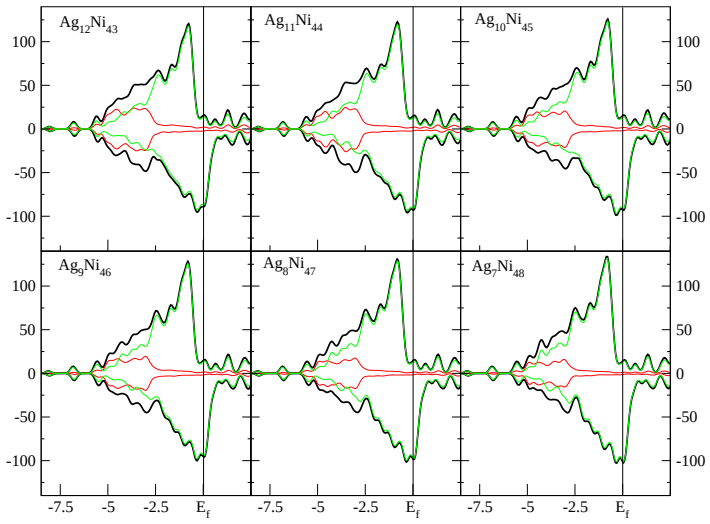

Figura A.13: Total DOS (black line), partial contribution of silver (red line) and nickel atoms (green line) of $Ag_{12}Ni_{43}$ to Ag_7Ni_{48} clusters.

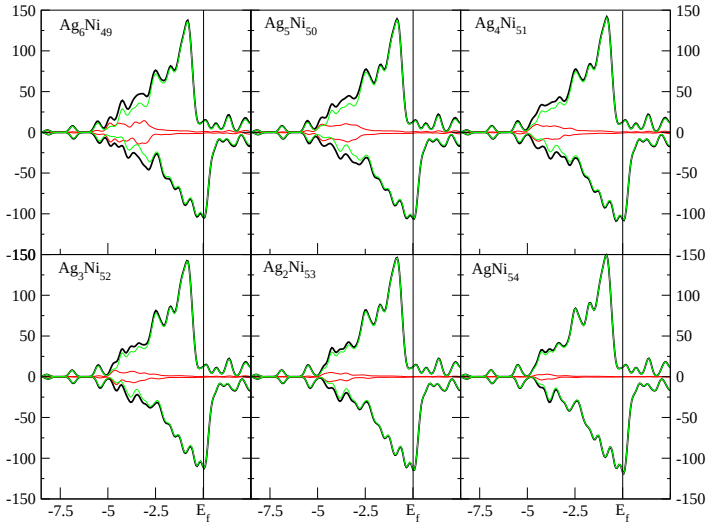

Figura A.14: Total DOS (black line), partial contribution of silver (red line) and nickel atoms (green line) of Ag_6Ni_{49} to $AgNi_{54}$ clusters.

Appendix B

Appendix of chapter 4

B.1 Small iron oxide clusters.

Tabla B.1: Several properties of low-energy isomers of neutral Fe_3O_m clusters with m = 1-9: $E_b(n,m)$ = binding energy per atom in eV; I_p = ionization potential in eV; E_a = electron affinity in eV; μ = magnetic moment in Bohr magnetons (μ_B); D(Fe-Fe)= average distance between first neighbour nickel atoms in Å; D(Fe-O) = average distance between first neighbour nickel-oxygen atoms in Å.

Signature			neutral				
$n.m$-isomer	$E_b(n,m)$	I_p	E_a	μ	D(Fe-Fe)	D(Fe-O)	I_p-E_a
3.1-I	3.02	6.94	1.19	10	2.33	1.84	5.75
3.1-II	2.84	6.55	1.22	10	2.34	1.99	5.34
3.1-III	2.68	6.16	1.29	10	2.12	1.92	4.87
3.2-I	3.63	7.29	1.78	12	2.48	1.86	5.51
3.2-II	3.44	7.04		10	2.39	1.96	7.04
3.2-III	3.42	6.67	1.20	12	2.41	2.02	5.47
3.3-I	4.08	7.72	2.21	4	2.62	1.83	5.51
3.3-II	3.72	8.07	2.36	12	2.51	1.91	5.72
3.3-III	3.61	6.98	2.49	6	—	1.78	4.49
3.4-I	4.10	8.05	2.45	4	2.63	1.92	5.60
3.4-II	4.10	8.18	2.83	10	2.52	1.79	5.35
3.4-III	4.08	8.09	2.78	2	2.52	1.79	5.31
3.5-I	4.10	8.83	3.43	4	2.88	1.77	5.41
3.5-II	3.99	8.64	3.00	4	2.56	1.92	5.64
3.5-III	3.92	9.61	3.86	4	2.62	1.85	5.74
3.6-I	4.14	9.63	4.09	2	3.27	1.75	5.55
3.6-II	4.08	9.14	3.74	4	2.68	1.75	5.40
3.6-III	3.87	8.22	2.94	4	2.82	1.84	5.28
3.7-I	4.11	9.53	4.27	4	2.81	1.81	5.26
3.7-II	4.00	9.19	4.13	4	—	1.78	5.06
3.7-III	3.97	9.62	4.25	0	2.71	1.89	5.36
3.8-I	3.97	10.26	4.67	6	2.71	1.86	5.59
3.8-II	3.93	9.25	4.04	2	—	1.81	5.21
3.8-III	3.79	9.05	3.60	0	2.69	1.92	5.45
3.9-I	3.86	10.00	4.87	2	2.66	1.88	5.13
3.9-I	3.84	9.30	4.16	4	—	1.84	5.14
3.9-II	3.67	8.73	4.16	4	—	1.81	4.57

Tabla B.2: Several properties of low-energy isomers of $[Fe_3O_m]^{\pm}$ cationic and anionic clusters with m = 1-9: $E_b(n,m)$ = binding energy per atom in eV; μ = magnetic moment in Bohr magnetons (μ_B); D(Fe-Fe)= average distance between first neighbour nickel atoms in Å; D(Fe-O) = average distance between first neighbour nickel-oxygen atoms in Å.

Signature				cation/anion
$n.m$-isomer	$E_b(n,m)$	μ	D(Fe-Fe)	D(Fe-O)
3.1-I	3.29 3.28	11	2.45/2.35	1.85/1.88
3.1-II	3.21 3.11	9/11	2.38/2.39	1.98/2.01
3.1-III	3.14 2.97	11	2.23/2.16	1.92/1.94
3.2-I	3.78 3.96	3/11	2.73/2.41	1.80/1.87
3.2-II	3.64 3.97	11	2.50/2.39	1.95/1.96
3.2-III	3.69 3.63	11	2.41/2.40	2.01/2.03
3.3-I	4.13 4.43	3/11	2.54/2.43	1.81/1.87
3.3-II	3.72 4.09	11	2.60/2.44	1.87/1.92
3.3-III	3.79 4.01	5	—	1.78/1.79
3.4-I	4.10 4.43	5	2.82/2.53	1.91/1.94
3.4-II	4.08 4.48	3/9	2.73/2.29	1.79/1.83
3.4-III	4.08 4.46	3/11	2.73/2.29	1.79/1.83
3.5-I	4.00 4.51	3	2.97/2.80	1.76/1.79
3.5-II	3.91 4.35	5	2.68/2.47	1.94/1.97
3.5-III	3.73 4.39	5	2.65/2.62	1.84/1.88
3.6-I	3.96 4.58	5/1	3.21/3.33	1.77/1.77
3.6-II	3.96 4.48	5/3	—/2.53	1.74/1.77
3.6-III	3.84 4.18	5/3	3.15/2.69	1.82/1.86
3.7-I	3.96 4.53	3	2.73/—	1.79/1.82
3.7-II	3.88 4.40	5	—	1.77/1.77
3.7-III	3.81 4.38	1	2.69/2.66	1.88/1.90
3.8-I	3.77 4.39	5/3	2.72/2.64	1.85/1.75
3.8-II	3.81 4.28	3	—	1.81/1.82
3.8-III	3.70 4.11	1/3	2.71/2.66	1.91/1.94
3.9-I	3.70 4.26	3	2.68/2.64	1.88/1.89
3.9-I	3.74 4.18	5/3	—	1.89/1.86
3.9-II	3.61 4.00	7/3	—	1.80/1.80

Tabla B.3: Several properties of low-energy isomers of neutral Fe_4O_m clusters with m = 1-14: $E_b(n,m)$ = binding energy per atom in eV; I_p = ionization potential in eV; E_a = electron affinity in eV; μ = magnetic moment in Bohr magnetons (μ_B); D(Fe-Fe)= average distance between first neighbour nickel atoms in Å; D(Fe-O) = average distance between first neighbour nickel-oxygen atoms in Å.

Signature			neutral				
$n.m$-isomer	$E_b(n,m)$	I_p	E_a	μ	D(Fe-Fe)	D(Fe-O)	I_p-E_a
4.1-I	3.16	6.88	—	14	2.44	1.86	—
4.1-II	3.01	6.07	1.70	12	2.39	1.96	4.37
4.1-III	2.91	6.60	1.55	14	2.41	1.83	5.05
4.2-I	3.61	7.01	1.47	14	2.46	1.93	5.54
4.2-II	3.57	7.03	1.70	14	2.47	1.86	5.33
4.2-III	3.55	7.14	1.91	14	2.47	1.84	5.22
4.3-I	3.96	7.23	—	14	2.47	1.96	—
4.3-II	3.94	7.11	2.14	14	2.54	1.90	4.97
4.3-III	3.86	7.95	2.03	16	2.57	1.87	5.92
4.4-I	4.24	7.36	2.40	0	2.85	1.80	4.95
4.4-II	4.19	7.74	2.35	16	2.60	1.86	5.39
4.4-III	4.16	7.60	0.89	2	2.61	2.00	6.71
4.5-I	4.31	7.39	2.73	0	2.78	1.83	4.66
4.5-II	4.30	7.96	2.53	0	2.55	1.93	5.42
4.5-III	4.30	8.00	2.81	0	2.75	1.92	5.19
4.6-I	4.40	8.02	3.30	0	2.75	1.82	4.72
4.6-II	4.26	8.24	3.26	0	2.64	1.92	4.98
4.6-III	4.24	8.32	2.94	0	2.66	1.91	5.38
4.7-I	4.35	8.43	3.44	0	2.86	1.80	4.99
4.7-II	4.26	8.74	3.60	0	2.67	1.87	5.14
4.7-III	4.24	8.57	3.77	14	2.55	1.90	4.80
4.8-I	4.29	9.19	3.82	0	2.96	1.79	5.37
4.8-II	4.23	8.98	3.94	12	2.51	1.86	5.04
4.8-III	4.18	9.02	4.01	0	2.73	1.85	5.02
4.9-I	4.27	9.12	4.46	8	—	1.77	4.66
4.9-II	4.16	9.48	4.48	12	2.61	1.84	5.00
4.9-III	4.09	9.04	-9.04	14	2.55	1.88	18.09
4.10-I	4.24	9.67	4.90	8	—	1.75	4.77
4.10-II	4.14	8.87	4.53	10	—	1.78	4.34
4.10-III	4.13	9.09	4.31	0	—	1.77	4.79
4.11-I	4.14	9.53	4.78	10	—	1.79	4.74
4.12-I	4.03	9.38	5.00	12	—	1.82	4.39
4.13-I	3.94	9.39	5.23	0	—	1.83	4.16
4.14-I	3.90	9.48	4.54	0	—	1.88	4.94

Tabla B.4: Several properties of low-energy isomers of $[Fe_4O_m]^{\pm}$ cationic and anionic clusters with m = 1-14: $E_b(n,m)$ = binding energy per atom in eV; μ = magnetic moment in Bohr magnetons (μ_B); D(Fe-Fe)= average distance between first neighbour nickel atoms in Å; D(Fe-O) = average distance between first neighbour nickel-oxygen atoms in Å.

Signature				cation/anion
$n.m$-isomer	$E_b(n,m)$	μ	D(Fe-Fe)	D(Fe-O)
4.1-I	3.39/—	13/—	2.44/—	1.84/—
4.1-II	3.40/3.32	13/15	2.46/2.43	1.96/1.88
4.1-III	3.20/3.19	15	2.35/2.29	1.83/1.84
4.2-I	3.77/3.83	15	2.48/2.46	1.93/1.96
4.2-II	3.74/3.83	15	2.56/2.48	1.86/1.87
4.2-III	3.70/3.85	15/13	2.54/2.41	1.84/1.86
4.3-I	4.07/—	15/—	2.63/—	1.94/—
4.3-II	4.07/4.23	15	2.59/2.51	1.89/1.93
4.3-III	3.87/4.13	15	2.67/2.61	1.86/1.84
4.4-I	4.32/4.52	1	2.86/—	1.79/1.80
4.4-II	4.23/4.47	1/15	2.79/2.52	1.87/1.93
4.4-III	4.22/4.26	7/15	2.50/—	2.04/1.99
4.5-I	4.38/4.60	1	2.73/2.70	1.81/1.85
4.5-II	4.31/4.57	1	2.58/2.42	1.92/1.90
4.5-III	4.30/4.59	1	2.82/2.69	1.92/1.93
4.6-I	4.40/4.72	1	2.59/—	1.82/1.87
4.6-II	4.24/4.57	1	2.76/2.61	1.87/1.91
4.6-III	4.21/4.52	1	2.76/2.62	1.90/1.92
4.7-I	4.32/4.65	1	2.78/2.60	1.79/1.82
4.7-II	4.19/4.57	1	2.72/2.63	1.86/1.89
4.7-III	4.19/4.57	1	2.71/2.64	1.86/1.88
4.8-I	4.20/4.60	11	2.58/—	1.79/1.80
4.8-II	4.15/4.54	13/1	2.58/2.64	1.85/1.87
4.8-III	4.10/4.50	1	2.73/2.69	1.84/1.88
4.9-I	4.18/4.60	9	—	1.76/1.77
4.9-II	4.04/4.49	11/13	2.67/2.6	1.83/1.86
4.9-III	4.01/3.38	15/13	2.58/2.47	1.90/1.89
4.10-I	4.13/4.58	7/9	—	1.74/1.76
4.10-II	4.08/4.46	1/9	—	1.80/1.81
4.10-III	4.05/4.42	1	—	1.76/1.78
4.11-I	4.04/4.45	9	—	1.78/1.79
4.12-I	3.95/4.34	11	—	1.81/1.82
4.13-I	3.86/4.24	1	—	1.83/1.83
4.14-I	3.81/4.14	3/1	—	1.86/1.85

Tabla B.5: Several properties of low-energy isomers of neutral Fe_5O_m clusters with m = 1-15: $E_b(n,m)$ = binding energy per atom in eV; I_p = ionization potential in eV; E_a = electron affinity in eV; μ = magnetic moment in Bohr magnetons (μ_B); D(Fe-Fe)= average distance between first neighbour nickel atoms in Å; D(Fe-O) = average distance between first neighbour nickel-oxygen atoms in Å.

Signature			neutral				
$n.m$-isomer	$E_b(n,m)$	I_p	E_a	μ	D(Fe-Fe)	D(Fe-O)	I_p-E_a
5.1-I	3.14	6.57	1.78	16	2.44	1.85	4.79
5.1-II	3.11	6.28	1.57	16	2.47	1.96	4.71
5.1-III	3.08	—	1.56	16	2.45	1.87	—
5.2-I	3.58	6.89	1.96	16	2.47	1.83	4.93
5.2-II	3.57	6.61	1.76	16	2.47	1.92	4.85
5.2-III	3.56	6.54	1.70	18	2.55	1.97	4.84
5.3-I	3.94	7.03	1.88	16	2.54	1.92	5.15
5.3-II	3.90	6.93	-0.89	18	2.56	1.88	7.82
5.3-III	3.89	7.04	2.20	18	2.52	1.89	4.85
5.4-I	4.21	6.25	2.44	18	2.56	1.92	3.82
5.4-II	4.03	7.77	2.84	16	2.54	1.84	4.93
5.4-III	4.03	6.93	2.17	20	2.62	1.98	4.76
5.5-I	4.28	6.87	2.79	4	2.70	1.86	4.08
5.5-II	4.28	7.56	2.98	4	2.65	1.77	4.58
5.5-III	4.26	7.37	2.37	4	2.64	1.94	4.99
5.6-I	4.47	9.16	2.33	2	2.59	1.81	6.83
5.6-II	4.38	7.79	2.99	4	2.68	1.82	4.81
5.6-III	4.36	7.63	2.86	4	2.58	1.89	4.77
5.7-I	4.45	8.05	3.25	4	2.74	1.89	4.79
5.7-II	4.43	7.87	3.34	2	2.74	1.82	4.53
5.7-III	4.35	7.93	3.48	4	2.73	1.90	4.45
5.8-I	4.43	8.16	3.64	2	2.80	1.82	4.51
5.8-II	4.31	7.60	4.00	4	2.69	1.93	3.60
5.8-III	4.30	8.08	3.51	4	2.71	1.80	4.57
5.9-I	4.38	8.75	3.73	2	2.83	1.82	5.01
5.9-II	4.38	9.25	3.66	2	2.92	1.81	5.59
5.10-I	4.33	8.91	4.54	14	2.76	1.82	4.36
5.10-II	4.31	8.77	4.13	2	2.90	1.90	4.64
5.10-III	4.25	8.57	3.99	2	2.81	1.84	4.58
5.11-I	4.32	9.54	4.30	16	2.74	1.82	5.23
5.11-II	4.28	8.84	4.63	14	—	1.82	4.20
5.11-III	4.27	8.84	4.27	2	—	1.78	4.57
5.12-I	4.27	9.18	5.03	12	—	1.77	4.15
5.12-II	4.26	10.28	3.96	14	2.89	1.85	6.32
5.12-III	4.22	8.89	5.45	12	2.84	1.81	3.44
5.13-I	4.22	9.37	5.23	10	—	1.77	4.14
5.13-II	4.19	9.79	5.12	12	—	1.79	4.67
5.13-III	4.15	9.50	5.06	2	—	1.80	4.44
5.14-I	4.14	9.42	5.11	12	—	1.80	4.31
5.14-II	4.12	9.88	5.62	2	—	1.79	4.26
5.14-III	4.10	9.27	5.46	0	—	1.75	3.81
5.15-I	4.07	9.70	5.31	10	—	1.72	4.40
5.15-II	4.06	9.75	5.25	10	—	1.81	4.50
5.15-III	4.05	8.92	5.28	12	—	1.82	3.64

Tabla B.6: Several properties of low-energy isomers of $[Fe_5O_m]^{\pm}$ cationic and anionic clusters with m = 1-15: $E_b(n,m)$ = binding energy per atom in eV; μ = magnetic moment in Bohr magnetons (μ_B); D(Fe-Fe)= average distance between first neighbour nickel atoms in Å; D(Fe-O) = average distance between first neighbour nickel-oxygen atoms in Å.

Signature				cation/anion
$n.m$-isomer	$E_b(n,m)$	μ	D(Fe-Fe)	D(Fe-O)
5.1-I	3.38/3.41	15/17	2.50/2.42	1.84/1.85
5.1-II	3.40/3.35	17	2.52/2.47	1.96/2.00
5.1-III	3.32/—	17/—	2.45/—	1.90/—
5.2-I	3.75/3.84	17	2.54/2.47	1.82/1.85
5.2-II	3.77/3.80	17	2.54/2.50	1.91/1.94
5.2-III	3.78/3.79	17	2.54/2.51	1.96/1.97
5.3-I	4.06/4.15	19/17	2.60/2.50	1.92/1.93
5.3-II	4.04/3.78	19/17	2.60/2.49	1.88/1.87
5.3-III	4.01/4.14	17	2.56/2.52	1.88/1.91
5.4-I	4.41/4.47	19/17	2.60/2.50	1.90/1.92
5.4-II	4.06/4.33	15/17	2.56/2.52	1.82/1.86
5.4-III	4.15/4.26	19	2.59/2.57	1.96/1.99
5.5-I	4.40/4.55	3	2.58/2.65	1.88/1.84
5.5-II	4.32/4.56	5/3	2.69/2.53	1.81/1.79
5.5-III	4.32/4.48	5/19	2.74/2.62	1.92/1.95
5.6-I	4.36/4.67	3/15	2.83/2.70	1.88/1.91
5.6-II	4.40/4.64	3/5	2.65/2.58	1.82/1.89
5.6-III	4.40/4.61	3/5	2.65/2.67	1.88/1.92
5.7-I	4.45/4.71	5/3	2.71/2.59	1.87/1.89
5.7-II	4.44/4.69	1/3	2.67/—	1.82/—
5.7-III	4.36/4.63	5/3	2.85/2.63	1.89/1.91
5.8-I	4.42/4.70	3	3.01/2.79	1.81/1.82
5.8-II	4.35/4.58	3/5	2.66/2.65	1.89/1.94
5.8-III	4.30/4.56	5	2.76/2.64	1.88/1.81
5.9-I	4.33/4.63	3	2.94/2.78	1.81/1.84
5.9-II	4.29/4.63	3	2.87/2.84	1.90/1.92
5.10-I	4.27/4.63	3/13	2.71/2.58	1.81/1.83
5.10-II	4.26/4.58	3	2.98/2.75	1.90
5.10-III	4.21/4.51	3/1	2.85/2.73	1.84/1.85
5.11-I	4.22/4.58	15/13	2.79/2.59	1.72/1.82
5.11-II	4.23/4.56	1/3	—	1.77/1.79
5.11-III	4.22/4.53	1/13	—	1.70/1.94
5.12-I	4.20/4.56	11	—	1.77/1.78
5.12-II	4.13/4.49	13/3	2.73/2.63	1.80/1.81
5.12-III	4.17/4.53	13	—/2.79	1.81/1.82
5.13-I	4.14/4.50	4/11	—	1.73/1.77
5.13-II	4.10/4.47	12/13	—	1.79/1.81
5.13-III	4.06/4.42	11	—	1.79/1.81
5.14-I	4.07/4.40	11/13	—	1.80
5.14-II	4.03/4.41	9/13	—	1.86/1.79
5.14-III	4.03/4.38	1/13	—/2.83	1.79/1.91
5.15-I	3.98/4.32	11	—	1.80/1.81
5.15-II	3.97/4.32	9/1	—	1.81/1.90
5.15-III	4.01/4.31	1/1	—	1.82/1.83

Tabla B.7: Several properties of low-energy isomers of neutral Fe_6O_m clusters with m = 1-15: $E_b(n,m)$ = binding energy per atom in eV; I_p = ionization potential in eV; E_a = electron affinity in eV; μ = magnetic moment in Bohr magnetons (μ_B); D(Fe-Fe)= average distance between first neighbour nickel atoms in Å; D(Fe-O) = average distance between first neighbour nickel-oxygen atoms in Å.

Signature			neutral				
$n.m$-isomer	$E_b(n,m)$	I_p	E_a	μ	D(Fe-Fe)	D(Fe-O)	I_p-E_a
6.1-I	3.25	6.33	1.54	20	2.5	1.96	4.80
6.1-II	3.21	6.52	1.74	20	2.48	1.86	4.79
6.1-III	3.20	—	1.57	20	2.48	1.98	—
6.2-I	3.64	6.41	1.41	20	2.53	1.94	5.01
6.2-II	3.59	—	1.74	20	2.52	1.91	—
6.2-III	3.59	6.12	1.70	20	2.58	1.95	4.42
6.3-I	3.96	6.44	1.57	20	2.56	1.94	4.87
6.3-II	3.87	7.23	2.30	20	2.53	1.84	4.93
6.3-III	3.86	6.40	1.81	20	2.57	1.96	4.59
6.4-I	4.22	6.65	1.88	20	2.57	1.94	4.77
6.4-II	4.22	6.61	2.19	20	2.55	1.97	4.42
6.4-III	4.11	7.06	2.62	0	2.5	1.89	4.44
6.5-I	4.34	7.60	2.70	22	2.66	1.96	4.90
6.5-II	4.31	6.46	2.08	2	2.59	1.92	4.37
6.5-III	4.30	6.80	2.14	22	2.66	1.85	4.67
6.6-I	4.41	6.92	3.08	0	2.59	1.98	3.84
6.6-II	4.41	7.63	2.93	0	2.56	1.83	4.69
6.6-III	4.40	6.94	2.66	0	2.67	1.96	4.28
6.7-I	4.43	6.99	2.68	0	2.65	1.96	4.31
6.7-II	4.42	7.11	2.77	20	2.52	1.97	4.34
6.7-III	4.38	7.66	2.91	24	2.73	1.98	4.75
6.8-I	4.47	7.55	3.10	8	2.69	1.97	4.45
6.8-II	4.44	12.57	3.15	0	2.70	1.90	9.42
6.8-III	4.34	8.04	3.85	0	2.78	1.82	4.19
6.9-I	4.54	7.39	3.87	0	—	1.81	3.52
6.9-II	4.45	7.50	3.27	2	2.65	1.91	4.23
6.9-III	4.42	7.81	3.57	16	2.67	1.93	4.24
6.10-I	4.51	7.95	3.68	0	2.75	1.791	4.27
6.10-II	4.46	8.33	3.94	2	2.7	1.87	4.39
6.10-III	4.45	8.08	3.75	0	2.84	1.82	4.33
6.11-I	4.46	8.11	3.92	0	—	1.79	4.19
6.11-II	4.46	7.96	3.81	0	—	1.78	4.16
6.11-III	4.41	8.95	3.78	18	2.74	1.84	5.17
6.12-I	4.42	8.17	4.37	0	—	1.77	3.80
6.12-II	4.32	8.59	4.32	0	2.78	1.87	4.27
6.12-III	4.31	9.19	4.92	24	2.84	1.86	4.27
6.13-I	4.39	8.73	4.48	0	—	1.78	4.25
6.13-II	4.38	8.71	4.75	2	2.87	1.8	3.95
6.13-III	4.38	8.56	4.39	0	—	1.76	4.17
6.14-I	4.34	8.79	5.01	2	—	1.75	3.78
6.14-II	4.25	9.12	4.58	0	2.85	1.88	4.54
6.14-III	4.15	9.19	5.34	0	2.75	1.81	3.85
6.15-I	4.30	9.03	5.02	8	—	1.73	4.01
6.15-II	4.26	9.13	4.91	0	—	1.77	4.23
6.15-III	4.26	8.94	5.16	2	—	1.77	3.79
6.15-I	4.23	9.16	5.08	0	—	1.75	4.08
6.15-II	4.22	9.03	5.29	0	—	1.76	3.74

Tabla B.8: Several properties of low-energy isomers of $[Fe_6O_m]^{\pm}$ cationic and anionic clusters with m = 1-15: $E_b(n,m)$ = binding energy per atom in eV; μ = magnetic moment in Bohr magnetons (μ_B); D(Fe-Fe)= average distance between first neighbour nickel atoms in Å; D(Fe-O) = average distance between first neighbour nickel-oxygen atoms in Å.

Signature				cation/anion
$n.m$-isomer	$E_b(n,m)$	μ	D(Fe-Fe)	D(Fe-O)
6.1-I	3.49/3.45	21	2.5/2.51	1.96/1.97
6.1-II	3.4/3.44	21	2.52/2.47	1.85/1.88
6.1-III	—/3.40	—/19	—/2.46	—/1.99
6.2-I	3.84/3.80	21/19	2.56/2.51	1.94/1.95
6.2-II	—/3.79	—/19	—/2.50	—/1.92
6.2-III	3.82/3.78	19/21	2.57/2.55	1.92/1.97
6.3-I	4.14/4.12	21/19	2.61/2.52	1.94/1.98
6.3-II	3.96/4.11	21/19	2.58/2.50	1.84/1.85
6.3-III	4.04	21	2.63/2.57	1.95/1.98
6.4-I	4.36/4.39	21	2.64/2.54	1.93/1.96
6.4-II	4.36/4.42	21/19	2.64/2.52	1.94/1.98
6.4-III	4.21/4.36	21	2.61/2.56	1.91/1.92
6.5-I	4.38/4.58	23/21	2.69/2.6	1.94/1.99
6.5-II	4.45/4.49	1/21	2.69/2.55	1.94/1.93
6.5-III	4.41/4.48	23/21	2.73/2.61	1.95/1.97
6.6-I	4.51/4.66	1	2.66/2.68	1.97
6.6-II	4.44/4.64	1	2.61/2.51	1.83/1.86
6.6-III	4.49/4.61	1	2.71/2.62	1.94/1.97
6.7-I	4.51/4.63	1	2.65/2.64	1.83/1.97
6.7-II	4.49/4.62	21/19	2.59/2.48	1.95/1.98
6.7-III	4.41/4.60	23	2.78/2.71	1.95/1.98
6.8-I	4.50/4.68	3/15	2.64/2.53	1.94/1.95
6.8-II	4.11/4.65	1	2.67/2.70	1.89/1.92
6.8-III	4.34/4.61	1	2.69/2.76	1.81/1.84
6.9-I	4.59/4.79	1	—/2.74	1.80/1.82
6.9-II	4.48/4.66	1/3	2.66/2.62	1.89/1.93
6.9-III	4.43/4.65	7/1	2.75/2.70	1.94/1.96
6.10-I	4.52/4.74	1	2.69/2.70	1.79/1.80
6.10-II	4.44/4.70	1	2.76/2.67	1.86/1.87
6.10-III	4.45/4.68	1	—/2.82	1.82/1.83
6.11-I	4.46/4.69	1	—/2.86	1.77/1.79
6.11-II	4.46/4.67	1	—	1.77/1.79
6.11-III	4.36/4.63	19/3	2.77/2.8	1.83/1.84
6.12-I	4.41/4.65	1	—/2.84	1.78/1.81
6.12-II	4.29/4.56	1	2.79/2.71	1.85/1.89
6.12-III	4.25/4.58	25/23	—/2.81	1.86
6.13-I	4.59/4.87	1	—/2.81	1.77/1.78
6.13-II	4.35/4.63	3/1	2.86/2.79	1.77/1.80
6.13-III	4.35/4.61	1	—	1.76
6.14-I	4.53/4.82	1	2.86/—	1.74/1.78
6.14-II	4.20/4.47	1	2.83/2.84	1.83/1.88
6.14-III	4.09/4.41	21	—/2.81	1.83/1.84
6.15-I	4.47/4.76	1/9	—	1.73/1.74
6.15-II	4.21/4.49	1	—	1.76/1.77
6.15-III	4.22/4.50	3/1	—	1.76/1.79
6.15-I	4.38/4.67	7/1	—	1.75/1.76
6.15-II	4.18/4.46	9/1	—	1.76

Tabla B.9: Several properties of low-energy isomers of neutral Fe_7O_m clusters with m = 1-15: $E_b(n,m)$ = binding energy per atom in eV; I_p = ionization potential in eV; E_a = electron affinity in eV; μ = magnetic moment in Bohr magnetons (μ_B); D(Fe-Fe)= average distance between first neighbour nickel atoms in Å; D(Ni-O) = average distance between first neighbour nickel-oxygen atoms in Å.

Signature			neutral				
$n.m$-isomer	$E_b(n,m)$	I_p	E_a	μ	D(Fe-Fe)	D(Fe-O)	I_p-E_a
7.1-I	3.33	6.27	1.55	22	2.46	1.97	4.71
7.1-II	3.29	6.09	1.59	22	2.48	1.97	4.51
7.1-III	3.28	6.20	1.75	24	2.67	1.96	4.45
7.2-I	3.64	6.19	1.63	22	2.52	1.96	4.56
7.2-II	3.62	6.60	1.98	22	2.53	1.91	4.62
7.2-III	3.62	6.17	1.69	22	2.51	1.95	4.48
7.3-I	3.92	6.38	1.71	22	2.55	1.94	4.67
7.3-II	3.86	6.22	1.90	22	2.55	1.94	4.32
7.3-III	3.84	6.25	2.30	22	2.51	1.92	3.96
7.4-I	4.12	6.87	2.27	24	2.59	1.92	4.60
7.4-II	4.11	6.67	2.19	24	2.61	1.95	4.48
7.4-III	4.10	6.70	2.37	24	2.60	1.92	4.34
7.5-I	4.32	6.95	2.51	24	2.61	1.93	4.44
7.5-II	4.27	8.06	3.10	24	2.64	1.83	4.97
7.5-III	4.25	6.65	2.58	24	2.59	1.95	4.07
7.6-I	4.39	6.85	2.25	2	2.61	1.93	4.60
7.6-II	4.38	6.73	2.37	26	2.68	1.86	4.36
7.6-III	4.37	7.18	2.98	26	2.68	1.91	4.20
7.7-I	4.54	7.35	2.91	2	2.72	1.91	4.44
7.7-II	4.48	7.09	2.68	18	2.66	1.92	4.41
7.7-III	4.47	6.99	2.80	2	2.58	1.90	4.19
7.8-I	4.54	7.13	3.00	2	2.65	1.85	4.13
7.8-II	4.53	7.42	3.11	4	2.66	1.74	4.31
7.8-III	4.49	7.48	3.07	4	2.67	1.92	4.42
7.9-I	4.53	7.44	3.31	2	2.73	1.91	4.13
7.9-II	4.52	7.43	3.13	6	2.70	1.92	4.31
7.9-III	4.47	7.14	3.44	18	2.61	1.92	3.70
7.10-I	4.58	6.92	3.82	0	2.79	1.82	3.10
7.10.II	4.56	6.66	4.19	4	2.71	1.90	2.47
7.10-III	4.50	7.57	3.65	4	2.69	1.91	3.92
7.11-I	4.56	8.09	3.82	4	2.73	1.85	4.27
7.11-II	4.56	8.28	3.33	0	2.71	1.91	4.95
7.11-III	4.51	6.74	4.65	4	2.73	1.94	2.09
7.12-I	4.53	8.20	4.02	4	2.83	1.91	4.18
7.12-II	4.52	8.58	4.09	4	2.74	1.85	4.49
7.12-III	4.52	8.36	3.77	2	2.80	1.83	4.59
7.13-I	4.54	8.27	4.20	4	2.82	1.78	4.08
7.13-II	4.49	8.47	4.15	2	2.86	1.90	4.32
7.13-III	4.47	8.66	5.03	4	2.84	1.87	3.63
7.13-IV	4.46	8.22	4.42	4	2.84	1.88	3.80
7.14-I	4.52	8.54	4.33	2	2.83	1.82	4.21
7.14-II	4.46	8.35	4.43	4	—	1.77	3.92
7.14-III	4.45	8.66	4.46	4	2.72	1.8	4.21
7.15-I	4.44	8.75	4.70	6	—	1.77	4.05
7.15-II	4.41	8.15	4.60	4	—	1.78	3.55
7.15-III	4.35	8.55	5.04	6	2.92	1.80	3.50
7.15-IV	4.26	8.66	5.60	4	2.83	1.80	3.07

Tabla B.10: Several properties of low-energy isomers of $[Fe_7O_m]^{\pm}$ cationic and anionic clusters with m = 1-15: $E_b(n,m)$ = binding energy per atom in eV; μ = magnetic moment in Bohr magnetons (μ_B); D(Fe-Fe)= average distance between first neighbour nickel atoms in Å; D(Fe-O) = average distance between first neighbour nickel-oxygen atoms in Å.

Signature				cation/anion
$n.m$-isomer	$E_b(n,m)$	μ	D(Fe-Fe)	D(Fe-O)
7.1-III	3.51/3.48	23	2.52/2.50	1.95/1.96
7.2-I	3.84/3.80	23	2.55/2.53	1.95/1.97
7.2-II	3.78/3.82	23	2.56/2.54	1.90/1.93
7.2-III	3.82/3.79	23/21	2.55/2.49	1.95/1.98
7.3-I	4.08/4.07	23/21	2.57/2.53	1.93/1.95
7.3-II	4.04/4.03	23	2.58/2.56	1.94/1.96
7.3-III	4.02/4.05	23	2.57/2.53	1.92/1.93
7.4-I	4.22/4.31	25	2.63/2.56	1.92/1.94
7.4-II	4.24/4.30	25/23	2.62/2.56	1.94/1.95
7.4-III	4.22/4.31	23	2.61/2.57	1.91/1.93
7.5-I	4.41/4.52	25/23	2.66/2.57	1.92/1.94
7.5-II	4.27/4.52	23	2.67/2.61	1.82/1.84
7.5-III	4.36/4.45	25/23	2.64/2.59	1.96/1.97
7.6-I	4.48/4.55	3	2.68/2.60	1.92/1.96
7.6-II	4.48/4.55	3/25	2.70/2.64	1.96/1.99
7.6-III	4.44/4.59	3/25	2.69/2.64	1.88/1.92
7.7-I	4.59/4.74	1/3	2.76/2.71	1.90/1.92
7.7-II	4.54/4.66	3/5	2.54/2.52	1.90/1.93
7.7-III	4.55/4.66	3	2.58/2.58	1.89/1.91
7.8-I	4.60/4.73	3	2.72/2.93	1.93/1.94
7.8-II	4.57/4.73	3	2.68/2.62	1.72/1.75
7.8-III	4.53/4.68	3/5	2.70/2.67	1.91/1.94
7.9-I	4.57/4.73	1	2.76/2.68	1.90/1.92
7.9-II	4.56/4.71	5/7	2.69/2.65	1.91/1.94
7.9-III	4.53/4.68	5/19	2.68/2.65	1.93/1.94
7.10-I	4.65/4.80	5/3	—/2.75	1.83/1.82
7.10.II	4.64/4.79	1	2.78/2.74	1.92/1.94
7.10-III	4.53/4.71	5	2.72/2.75	1.90/1.82
7.11-I	4.56/4.77	5/3	2.79/2.74	1.84/1.78
7.11-II	4.54/4.73	3/19	2.73/2.66	1.90/1.91
7.11-III	4.58/4.76	3/1	2.96/2.87	1.90/1.92
7.12-I	4.52/4.73	3	2.88/2.80	1.86/1.95
7.12-II	4.49/4.73	1/3	2.72/2.80	1.83/1.84
7.12-III	4.51/4.71	1/3	2.74/2.68	1.83/1.84
7.13-I	4.53/4.75	3	2.82/2.78	1.83/1.84
7.13-II	4.47/4.69	3/3	2.75/2.84	1.87/1.90
7.13-III	4.43/4.71	5/5	2.85/2.85	1.89
7.13-IV	4.45/4.68	1/3	2.86/2.84	1.78/1.80
7.14-I	4.49/4.72	3/1	2.87/2.80	1.82/1.83
7.14-II	4.44/4.66	5/3	—	1.80/1.82
7.14-III	4.42/4.65	5/3	2.80/2.85	1.81/1.83
7.15-I	4.41/4.65	7/5	—	1.7/1.81
7.15-II	4.41/4.61	5	—/2.80	1.77/1.79
7.15-III	4.32/4.57	5/13	2.94/2.76	1.80/1.81
7.15-IV	4.23/4.51	3/25	2.85/2.85	1.80/1.86

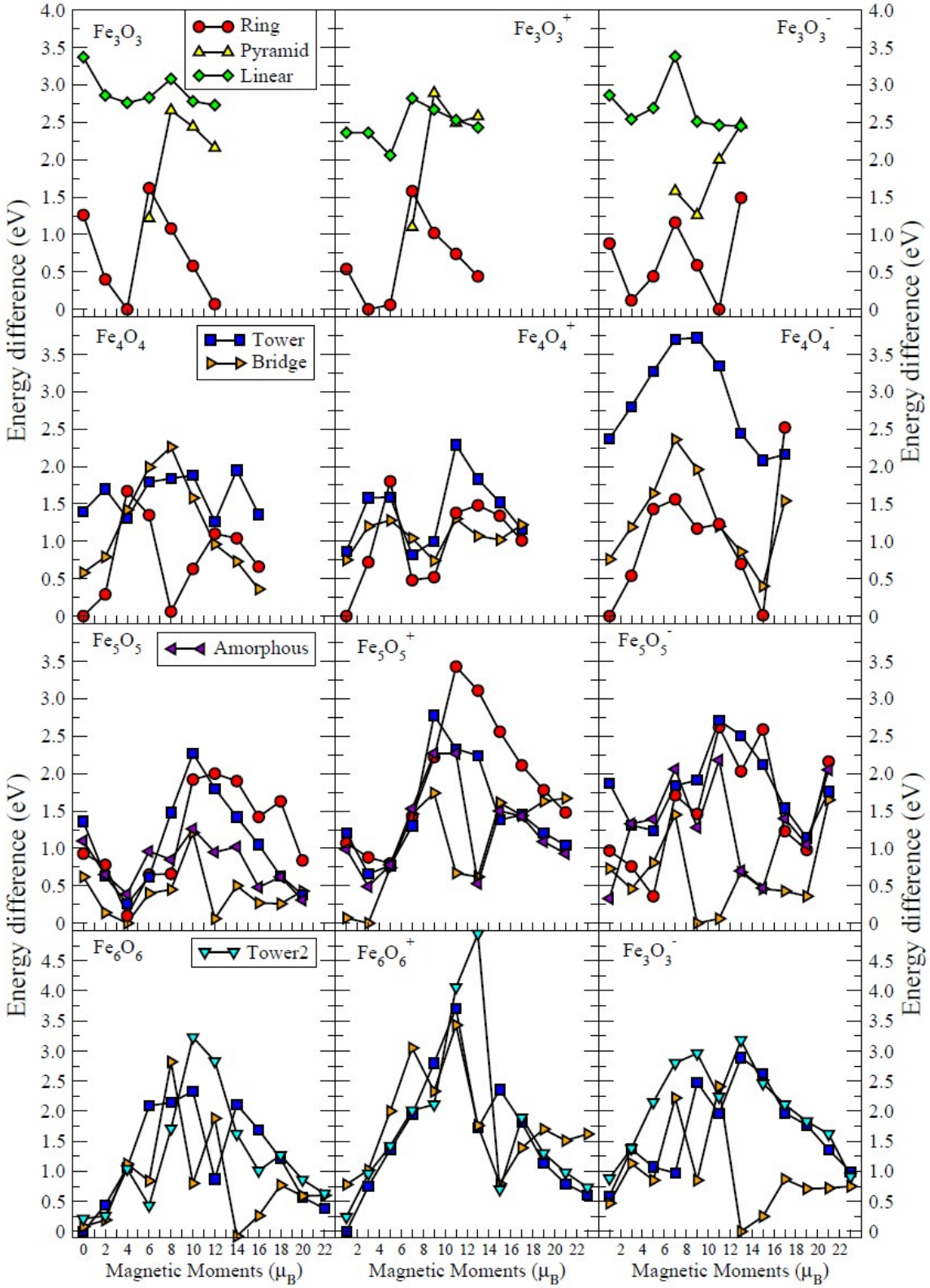

Figura B.1: Energy difference (with respect to our putative ground state) as a function of the spin state of several structural arrangements of the stoichiometric clusters $Fe_nO_n^{0/\pm}$.

Appendix C

Appendix of chapter 6

C.1 Substitutional impurities of the $2sp$ and $3sp$ series at a surface oxygen edge site.

($2sp$ or $3sp$) impurities are placed at the external Oxygen edge atom labeled (SI) in Fig. 6.10(b). The binding energies of these systems are calculated by means of a similarity expression as given by Eq. 6.4 in the main text. The general tendency of the binding energy in this case is opposite to the case of the same impurities substituting for Ti in the same system: the binding energy now grows with the atomic number except at the end of the series. The magnetic moment present values other than 0 and 1, reaching values of 2 μ_B for the cases of C and S. The Fermi levels decrease with the atomic number except for the heavier elements. The energy gap alternates consecutive values for the $2sp$ series but it is more complicated for the case of the $3sp$ series. The electric dipole show even-odd dependence with the atomic number for the $2sp$ series while a more complex dependence is observed for the $3sp$ series. The charge transfer is now from the matrix to the impurity with the only exception of Si where a marginal transfer in the opposite direction is found. The average distance Ti-impurity goes from 1.890Åto 2.310 Åin the case of $2sp$ impurities, while for the $3sp$ impurities these distances are larger reaching an apex for the

Tabla C.1: Selected structural and electronic important properties for $2sp$ or $3sp$ substitutional impurities placed at an edge Oxygen site. The following parameters are reported from left to right: binding energy, total magnetic moment of the cluster (and impurity magnetic moment) Fermi energy, energy gap, charge transferred from the matrix to the impurity, average interatomic distances between Ti and impurity, and finally the Ti-Ti distance on the edge the impurity sits near its center (the reference value of this parameter for the pure cluster is 2.960 Å.). The reference value where O plays the role of a fake impurity is presented emphasized.

Impurity	E_{Bin} eV/atom	Mag. Mom. μ_B	E_F eV	Gap eV	Dipole Debyes	Q(t) e	Ti-Imp. Å	Ti-Ti Å
$2sp$								
5 B	-7.338	1.0 (0.56)	-4.952	0.589	0.473	0.350	2.310	3.420
6 C	-7.391	2.0 (1.51)	-5.599	1.163	0.256	0.056	2.085	3.220
7 N	-7.409	1.0 (0.90)	-6.299	0.966	0.429	0.351	1.980	3.020
8 **O**	**-7.550**	**0.0 (0.0)**	**-6.243**	**3.310**	**0.021**	**0.559**	**1.890**	**2.960**
9 F	-7.446	1.0 (0.0)	-4.284	0.165	0.878	0.519	2.075	3.160
$3sp$								
13 Al	-7.298	1.0 (0.54)	-4.446	0.438	2.089	0.082	2.885	3.300
14 Si	-7.332	2.0 (1.30)	-4.978	0.372	0.866	-0.021	2.590	3.434
15 P	-7.355	1.0 (0.90)	-5.589	1.052	1.157	0.178	2.475	3.240
16 S	-7.429	0.0 (0.0)	-5.406	2.112	1.682	0.450	2.375	3.180
17 Cl	-7.340	1.0 (0.0)	-4.423	0.374	0.181	0.253	2.490	3.200

case of Al. The deformation of the Ti-Ti edge over which the impurity lands is always larger than the reference level corresponding to the presence of an Oxygen atom as fake impurity (shown emphasized in Table T1).

C.2 Comparison of some electronic properties using PBE and B3LYP.

Comparison of the electronic gap and electric dipole for some selected impurities are presented in Figs. D.1 and D.2. As the general tendencies are the

same whether PBE or B3LYP are used in these representative elements it does not seem necessary to report these results for all the impurities.

C.3 Spin sweep for selected items.

With respect to the magnetic properties of $(TiO_2)_{10}$ with one impurity. We did calculations for some selected impurity atoms (Fe, Co, Ni, Mo, Tc) for all the possible spin values or multiplicities (spin-sweep) using the hybrid functional B3LYP and the results for the lowest energy values (ground state magnetic solutions) agree with those calculated by means of SIESTA-PBE under the *"true spin"* scheme reported in the main text of this work.

To illustrate the coupling of a Transition Metal impurity state with those of the TiO2 (pristine, see Fig. 6.11) we calculated the electronic DOS for the case of a Fe impurity by means of SIESTA. These results are shown in Fig. S3. The total magnetic moment of the system is 4.0 μ_B and the Fe contribution is $\approx 3.0\mu_B$.

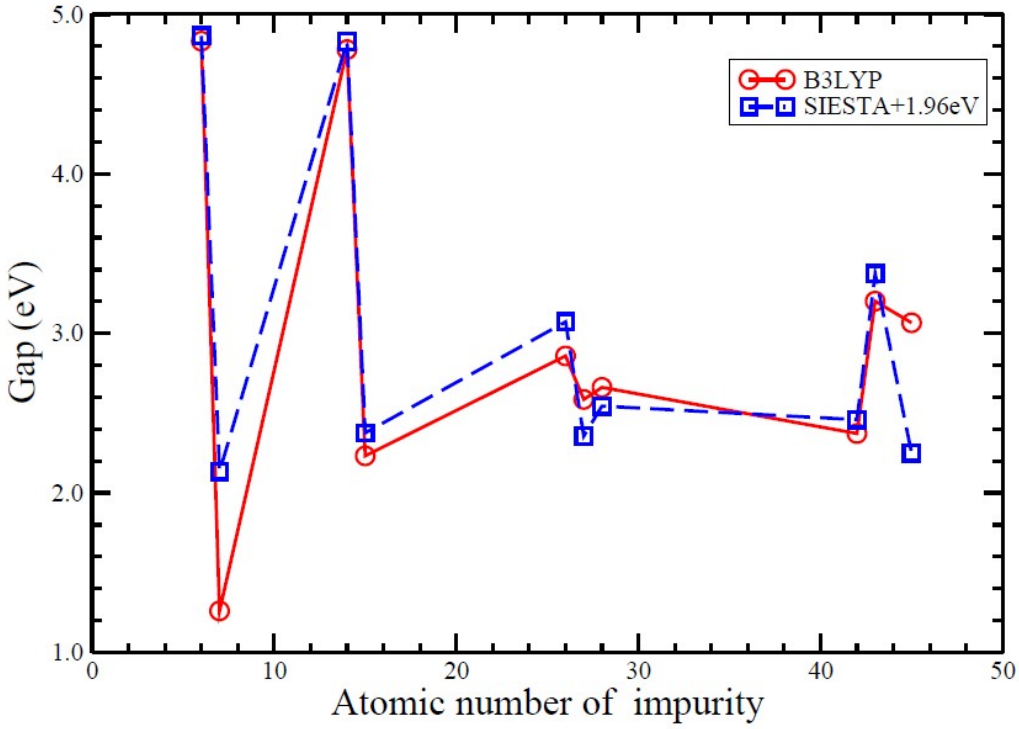

Figura C.1: Comparison of the energy gaps calculated using PBE and B3LYP. The tendency is the same independent of the numerical technique used except for a displacement of 1.96 eV due to the Fock contribution for the case of B3LYP. Since the general tendency is the same nearly independent of the atomic number of the impurity only results for some selected impurities are shown.

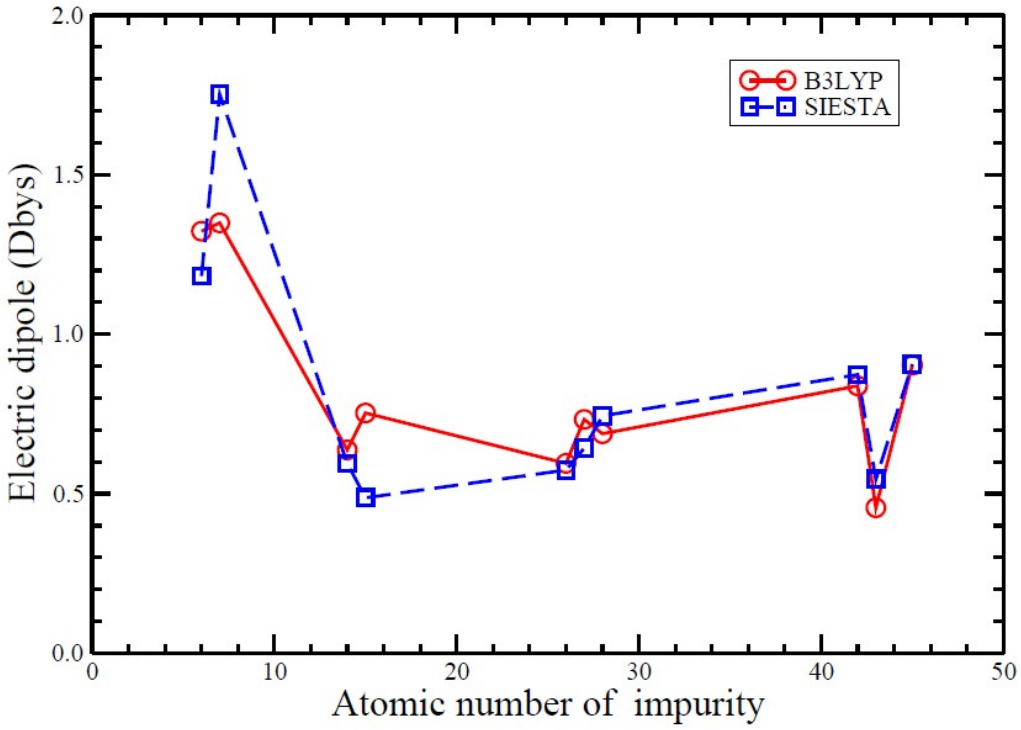

Figura C.2: Comparison of the electric dipole calculated using PBE and B3LYP for some selected impurities. Similarly to previous case the general tendencies are the same

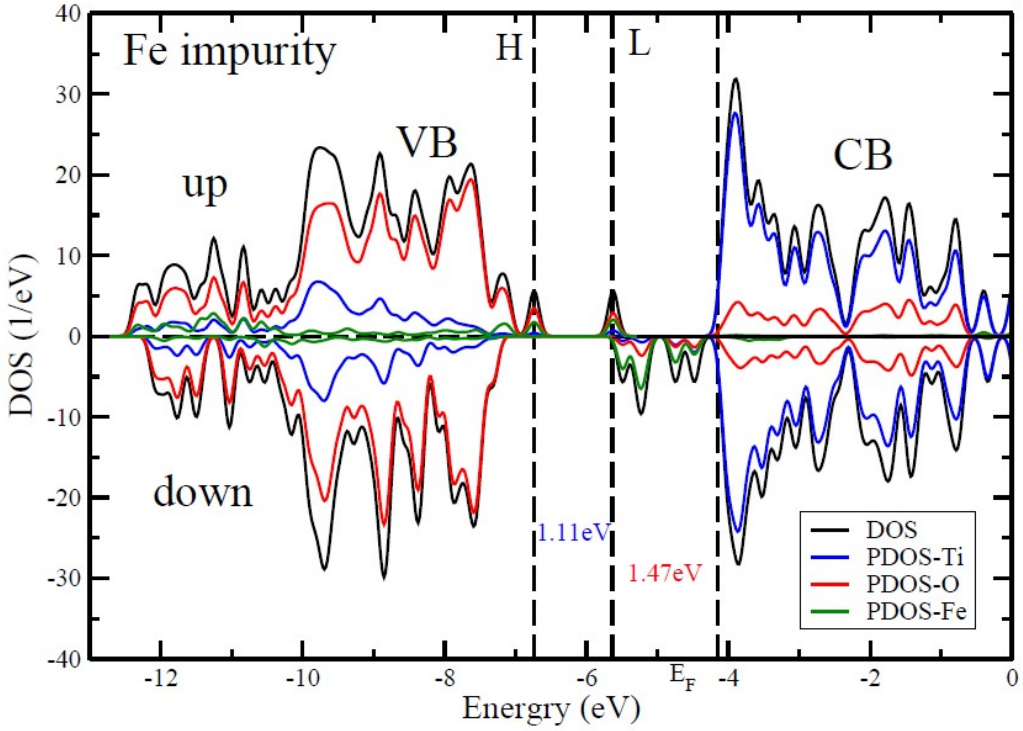

Figura C.3: Contribution of the different species to the DOS for Fe (picked as an example) as an edge substitutional impurity for the system $(TiO_2)_{10}$.

Appendix D

List of publications

- R. H. Aguilera-del-Toro, F. Aguilera-Granja, L. C. Balbas and A. Vega; Structure, fragmentation patterns, and magnetic properties of small nickel oxide clusters; Physical Chemistry Chemical Physics, 2017, 19, 3366.
- R. H. Aguilera-del-Toro, F. Aguilera-Granja, L. C. Balbas, A. Vega; Structure, fragmentation patterns, and electronic properties of small indium oxide clusters; Theoretical Chemistry Accounts, 2018, 137, 54.
- R. H. Aguilera-del-Toro, F. Aguilera-Granja, E.E. Vogelc; Structural and electronic properties of $(TiO_2)_N$ nanowires: A density functional theory investigation, Journal of Physics and Chemistry of Solids, 2018, 119, 175-182.
- R. H. Aguilera-del-Toro, P.G. Alvarado-Leyva, A. Vega; Uncovering the magnetic properties of the $Ag_xNi_y(x + y = 55)$ nanoalloys in the whole composition range; Journal of Magnetism and Magnetic Materials, 2019, 474, 551-562.
- R. H. Aguilera-del-Toro, F. Aguilera-Granja, E.E. Vogel; Structural and electronic properties of $(TiO_2)_{10}$ clusters with impurities: A density functional theory investigation; (SUBMITTED-2019).

Bibliography

[1] L. I. Lungu, M. Radulescu, G. D. Mogosanu and A. M. Grumezescu, pH sensitive core-shell magnetic nanoparticles for targeted drug delivery in cancer therapy, *Rom. J. Morphol. Embryol.*, 2016, **57**, 23-32.

[2] S. Jadhav, S. Gaikwad, M. Nimse and A. Rajbhoj, Copper Oxide Nanoparticles: Synthesis, Characterization and Their Antibacterial Activity, *J. Cluster Sci.*, 2011, **22**, 121-129.

[3] Y. Qiang, J. Antony, A. Sharma, J. Nutting, D. Sikes and D. Meyer, Iron/iron oxide core-shell nanoclusters for biomedical applications, *J. Nanopart. Res.*, 2006, **8**, 489-496.

[4] S. Nie, Y. Xing, G. J. Kim and J. W. Simons, Nanotechnology applications in cancer, *Annu. Rev. Biomed. Eng.*, 2007, **9**, 257-288.

[5] A. S. Gupta, Nanotechnology applications in diagnosis and treatment of metastasis, *Nanomedicine*, 2014, **9**, 1517.

[6] A. Azam, A. S. Ahmed, M. Oves, M. S. Khan, S. S. Habib and A. Memic, Impact of nanotechnology in cancer: emphasis on nanochemoprevention, *Int. J. Nanomedicine*, 2012, **7**, 591-605.

[7] S. Laurent, D. Forge, M. Port, A. Roch, C. Robic, L. V. Elst and R. N. Muller, Magnetic Iron Oxide Nanoparticles: Synthesis, Stabilization,

Vectorization, Physicochemical Characterizations, and Biological Applications, *Chem. Rev*, 2008, **108**, 2064-2110.

[8] N. Jones, B. Ray, K. T. Ranjit and A. C. Manna, Antibacterial activity of ZnO nanoparticle suspensions on a broad spectrum of microorganisms, *FEMS Microbiol. Lett.*, 2008, **279**, 71-76.

[9] Q. A. Pankhurst, J. Connolly,S. K. Jones and J. Dobson, Applications of magnetic nanoparticles in biomedicine, *J. Phys. D: Appl. Phys.*, 2003, **36**, 167-181.

[10] H. Wang, Li-Feng Cui, Y. Yang, H. S. Casalongue, J. T. Robinson, Y. Liang, Yi Cui and Hongjie Da, Mn_3O_4-Graphene Hybrid as a High-Capacity Anode Material for Lithium Ion Batteries, *J. AM. CHEM. SOC.*, 2010, **132**, 13978-13980.

[11] B. Koo, H. Xiong, M. D. Slater, V. B. Prakapenka, M. Balasubramanian, P. Podsiadlo,C. S. Johnson, T. Rajh and E. V. Shevchenko, Hollow Iron Oxide Nanoparticles for Application in Lithium Ion Batteries, *Nano Lett.*, 2012, **12** 2429-2435.

[12] Z.-S. Wu, W. Ren, L. Wen, L. Gao, J. Zhao, Z. Chen, G. Zhou, F. Li and H.-M., Graphene Anchored with Co_3O_4 Nanoparticles as Anode of Lithium Ion Batteries with Enhanced Reversible Capacity and Cyclic Performance, *Cheng, ACS Nano*, 2010, **4** 3187-3194.

[13] P. K. Stoimenov, R. L. Klinger, G. L. Marchin, and K. J. Klabunde, Metal Oxide Nanoparticles as Bactericidal Agents, *Langmuir*, 2002, **18**, 6679-6686.

[14] N. Tran, A. Mir, D. Mallik, A. Sinha, S. Nayar and T. J Webster, Bactericidal effect of iron oxide nanoparticles on Staphylococcus aureus, *Int. J. Nanomedicine*, 2010, **5**, 277-283.

[15] I. Sondi and B. Salopek-Sondi, Silver nanoparticles as antimicrobial agent: a case study on E. coli as a model for Gram-negative bacteria, *J. Colloid Interface Sci.*, 2004, **275** 177-182.

[16] S. Zhang, X. Zhao, H. Niu, Y. Shi, Y. Cai and G. Jiang, Superparamagnetic Fe_3O_4 nanoparticles as catalysts for the catalytic oxidation of phenolic and aniline compounds, *J. Hazard Mater*, 2009, **167** 560-566.

[17] F. Jiao and H. Frei, Nanostructured Cobalt Oxide Clusters in Mesoporous Silica as Efficient Oxygen-Evolving Catalysts, *Angew. Chem.*, 2009, **121**, 1873-1876.

[18] A. S. Teja and Pei-Yoong Koh, Prog. Cryst. Growth. Ch. **55** 22 (2010).

[19] C. L. Carnes and K. J. Klabunde, The catalytic methanol synthesis over nanoparticle metal oxide catalysts, *J. Mol. Catal. A: Che*, 2003, **194**, 227-236.

[20] N. Lopez and J. K. Norskov, Catalytic CO Oxidation by a Gold Nanoparticle: A Density Functional Study, *J. Am. Chem. Soc*, 2002, **124** 11262-11263.

[21] G. E. Johnson, N. M. Reilly, A.W. Castleman Jr, Effect of charge state and stoichiometry on the structure and reactivity of nickel oxide clusters with CO, *J. Mass Spectrom.*, 2009, **208**, 93-100.

[22] F. Piccinno, F. Gottschalk, S. Seeger and B. Nowack, Industrial production quantities and uses of ten engineered nanomaterials in Europe and the world, *J. Nanopart. Res*, 2012, **14**, 1109-1120.

[23] A.A. Keller, S. Mc.Ferran, A. Lazareva and S. Suh, Global life cycle releases of engineered nanomaterials, *J. Nanopart. Res*, 2013, **15**, 1692-1709.

[24] K.P. Kühn, I.F. Cahbemy, K. Massholder *el al.*, Disinfection of surfaces by photocatalytic oxidation with titanium dioxide and UVA light, *Chemosphere*, 2003, **53**, 71-77.

[25] G. Rajakumar, A.A. Rahuman, S.M. Roopan *el al.*, Fungus-mediated biosynthesis and characterization of Ti_2O nanoparticles and their activity against pathogenic bacteria, *Spectrochim Acta A*, 2012, **91**, 23-29.

[26] M.A. Vargas-Reus, K. Memarzadeh, J. Huang, G.G. Ren and R.P. Allaker, Antimicrobial activity of nanoparticulate metal oxides against peri-implantitis pathogens, *Int. J. Antimicrob. Agents*, 2012, **40**, 135-139.

[27] S. Martel, Magnetic nanoparticles in medical nanorobotics, *J. Nanopart. Res.*, 2015, **17**, 7590.

[28] R.H. Kodama, Magnetic nanoparticles, *J. Mag. Mag. Mat.*, 1999, **200**, 359-372.

[29] A.H. Lu, E.L. Salabas and F. Schueth, Magnetic nanoparticles: synthesis, protection, functionalization, and application, *Angew. Chem. Int. Ed.*, 2007, **46**, 1222-1244.

[30] C.J. Jia, M. Schwickardi, C. Weidenthaler, W. Schmidt, S. Korhonen, B.M. Wecichuysen and F. Schueth, $Co_3O_4 - SiO_2$ Nanocomposite: A Very Active Catalyst for CO Oxidation with Unusual Catalytic Behavior, *J. Am. Chem. Soc.*, 2011, **133**, 11279-11288.

[31] K. Takahashi, Iron oxide cluster induced barrier-free conversion of nitric oxide to ammonia, *Chem. Commun.*, 2015, **51**, 4062-4064.

[32] N.F. Atta, A.H. Ibrahim, and A. Galal, Nickel oxide nanoparticles/ionic liquid crystal modified carbon composite electrode for determination of neurotransmitters and paracetamol, *New J. Chem.*, 2016, **40**, 662-673.

[33] P. Poizot, S. Laruelle, S. Grugeon, L. Dupont and J.M. Tarascon, Nano-sized transition-metal oxides as negative-electrode materials for lithium-ion batteries, *Nature*, 2000, **407**, 496-499.

[34] G. Eranna, B.C. Joshi, D.P. Runthala and R.P. Gupta, Oxide Materials for Development of Integrated Gas Sensors-A Comprehensive Review, *Crit. Rev. Solid State*, 2004, **29**, 111-188.

[35] I. Kobal, M. Senegacnik and H. Kobal, ^{13}C and ^{14}C kinetic isotope effects in the catalytic oxidation of CO over NiO catalyst, *J. Catal.*, 1977, **49**, 1-7.

[36] G.A. El-Shobaky, A.M. Ghozza, Effect of ZnO doping on surface and catalytic properties of NiO and Co_3O_4 solids, *Mater. Lett.*, 2004, **58**, 699-705.

[37] W. Yao, C. Huang, J. Ye, Hydrogen Production and Characterization of $MLaSrNb_2NiO_9$ $(M = Na, Cs, H)$ Based Photocatalysts, *Chem. Mater.* 1977, **22**, 1107-1113.

[38] X. Shu, J. He and D. Chen, Visible-Light-Induced Photocatalyst Based on Nickel Titanate Nanoparticles, *Ind. Eng. Chem. Res.*, 2008, **47**, 4750-4753.

[39] X. Lin, Y. Xi, D. L. Phillips and W. Guo, The effect of a silica support: a density functional theory study of the C-H bond activation of ethane on a nickel oxide cluster, *J. Phys. Org. Chem.*, 2016, **29**, 134-144.

[40] Y. Wang, Q. Chen and J. Wang, Enhancing Stability and Photocatalytic Activity of ZnO Nanoparticles by Surface Modification of Graphene Oxide, *J. Nanosci. Nanotechnol*, 2014, **12** 3896-3902.

[41] A. Erlebach, C. Hunhn, R. Jana and M. Sierka, Structure and magnetic properties of $(Fe_2O_3)_n$ clusters $n = 1 - 5$, *Phys. Chem. Chem. Phys.*, 2014, **16** 26421-26426.

[42] N. M. Reilly, J. U. Reveles, G. E. Johnson, S. N. Khanna and A. W. Castelman Jr., Experimental and Theoretical Study of the Structure and Reactivity of $Fe_{1-2}O^-_{\leq 6}$ Clusters with CO, *J. Phys. Chem. A*, 2007. **111**, 4158-4166.

[43] N. M. Reilly, J. U. Reveles, G. E. Johnson, S. N. Khanna A. M. Koser and A. W. Castelman Jr., Experimental and Theoretical Study of the Structure and Reactivity of $Fe_mO_n^+$ $(m = 1, 2; n = 1 - 5)$ with CO, *J. Phys. Chem. A*, 2007, **111**, 19086-19097.

[44] K. Ota, K. Koyasu, K. Ohshimo and F. Misaizu, Structures of cobalt oxide cluster cations studied by ion mobility mass spectrometry, *Chem. Phys. Lett.*, 2013, **588** 63-67.

[45] N. T. Tung, N. M. Tam, M. T. Nguyen, P. Lievens and E. Janssens, Influence of Cr doping on the stability and structure of small cobalt oxide clusters, *J. Chem. Phys*, 2014, **141** 044311.

[46] G. E. Johnson, J. U. Reveles, N. M. Reilly, E. C. Tyo, S. N. Khanna and A. W. Castleman Jr, Influence of Stoichiometry and Charge State on the Structure and Reactivity of Cobalt Oxide Clusters with CO, *J. Phys. Chem. A*, 2008, **112** 11330-11340.

[47] S. Yin, W. Xue, X-L. Ding, W-G. Wang, S-G. He and M-F. Ge, Formation, distribution, and structures of oxygen-rich iron and cobalt oxide clusters, *International Journal of Mass Spectrometry*, 2009, **281**, 72-78.

[48] C. J. Dible, S. T. Akin, S. Ard, C. P. Fowler and M. A. Duncan, Photodissociation of Cobalt and Nickel Oxide Cluster Cations, *J. Phys. Chem. A*, 2012, **116**, 5398-5404.

[49] A. Kirilyuk, A. Fielicke, K. Demyk, G. von Helden, G. Meijer and Th. Rasing, Ferrimagnetic cagelike Fe_4O_6 cluster: Structure determination from infrared dissociation spectroscopy, *Phys. Rev. B*, 2010, **82**, 020405(R).

[50] S. Li, H-J. Zhai, L-S. Wang, and D. A. Dixon, Structural and Electronic Properties of Reduced Transition Metal Oxide Clusters, M_4O_{10} and $M_4O_{10}^-$ $(M = Cr, W)$, from Photoelectron Spectroscopy and Quantum Chemical Calculations, *J. Phys. Chem. A,*, 2012, **116**, 5256-5271.

[51] H-Q. Wang and H-F. Li, Probing the structural and electronic properties of small vanadium dioxide clusters by density functional theory and comparison with experimental photoelectron spectroscopy, *J. of Chem. Phys.*, 2012, **137**, 164304.

[52] K. Ohshimo, T. Komukai, R. Moriyama, and F. Misaizu, Isomer Separation of Iron Oxide Cluster Cations by Ion Mobility Mass Spectrometry, *J. Phys. Chem. A*, 2014, **118**, 3899-3905.

[53] R. H. Aguilera-del-Toro, F. Aguilera-Granja, A. Vega and L. C. Balbas, Structure, fragmentation patterns, and magnetic properties of small cobalt oxide clusters, *Phys. Chem. Chem. Phys.*, 2014, **16**, 21732-21741.

[54] R. H. Aguilera-del-Toro, F. Aguilera-Granja, A. Vega and L. C. Balbas, Structure, fragmentation patterns, and magnetic properties of small nickel oxide clusters, *Phys. Chem. Chem. Phys.*, 2017, **19**, 3366-3383.

[55] T.B. Massalki, H. Okamoto and P.R. Subramanian, *Binary Alloy Phase Diagrams*, 2nd ed,; ASM International: Metals Park OH, 1990.

[56] F. Ducastelle, in *Order and Phase Stability in Alloys*, edited by R. de Boer and D.G. Pettifor, North Holland, Amsterdam, 1991.

[57] G. Mpourmpakis, G.E. Froudakis, A.N. Andriotis, and M. Menon, Role of Co in enhancing the magnetism of small Fe clusters, *Phys. Rev. B*, 2005, **72**, 104417-104417-7.

[58] Anna N. Popova, Yuriy A. Zaharov and Valeri M. Pugachev, Chemical synthesis, structure and magnetic properties of nanocrystalline Fe-Co alloys, *Materials Letters*, 2012, **74**, 173-175.

[59] Andreas Hütten, Daniela Sudfeld, Inga Ennen, Günter Reiss, Klaus Wojczykowski, and Peter Jutzi, Ferromagnetic FeCo nanoparticles for biotechnology. *J. Magn. Magn. Mater.*, 2005, **293**, 93-101.

[60] R. Ferrando, Julius Jellinek and R. L. Johnston, Nanoalloys: From theory to applications of alloy clusters and nanoparticles, *Chem. Rev.*, 2008, **108**, 845-910.

[61] Maria F. Casula, Erika Conca, Ioanna Bakaimi, Ayyappan Sathya, Maria Elena Materia, Alberto Casu, Andrea Falqui, Elisa Sogne, Teresa Pellegrino and Antonios G. Kanaras, Manganese doped-iron oxide nanoparticle clusters and their potential as agents for magnetic resonance imaging and hyperthermia, *Phys. Chem. Chem. Phys.*, 2016, **18**, 16848-16855.

[62] Wojciech Szczerba, Jan Zukrowski, Marek Przybylski, Marcin Sikora, Olga Safonova, Aleksey Shmeliov, Valeria Nicolosi, Michael Schneider, Tim Granath, Maximilian Oppmann, Marion Strabere and Karl Mandel, Pushing up the magnetisation values for iron oxide nanoparticles via zinc doping: X-ray studies on the particle's sub-nano structure of different synthesis routes, *Phys. Chem. Chem. Phys.*, 2016, **18**, 25221-25229.

[63] J. M. Soler, E. Artacho, J. D. Gale, A. Garcia, J. Junquera, P. Ordejón and D. Sánchez-Portal, The SIESTA method for ab initio order-N materials simulation, *J. Phys.: C. M.*, 2002, **14**, 2745.

[64] N. Troullier and J. L. Martins, Efficient pseudopotentials for plane-wave calculations, *Phys. Rev. B*, 1991, **43**, 1993-2006.

[65] L. Kleinman and D. M. Bylander, Efficacious Form for Model Pseudopotentials, *Phys. Rev. Lett.*, 1982, **48**, 1425-1428.

[66] G. Kresse and J. Hafner, Ab initio molecular dynamics for liquid metals *Phys. Rev. B*, 1993, **47**, 558 (1993); ibid. 1994, **49**, 14251

[67] G. Kresse and J. Furthmüller, Efficiency of ab-initio total energy calculations for metals and semiconductors using a plane-wave basis set, *Comput. Mat. Sci.*, 1996, **6**, 15.

[68] G. Kresse and J. Furthmüller, Efficient iterative schemes for ab initio total-energy calculations using a plane-wave basis set, *Phys. Rev. B*, 1996, **54**, 11169.

[69] G. Kresse and D. Joubert, From ultrasoft pseudopotentials to the projector augmented-wave method, *Phys. Rev. B*, 1999, **59**, 1758 (1999).

[70] P. E. Blochl, Projector augmented-wave method, *Phys. Rev. B*, 1994, **50**, 17953.

[71] C. Rostgaard, The Projector Augmented-wave Method, Cond-Mat (2009)

[72] J. P. Perdew, K. Burke, and M. Ernzerhof, Generalized gradient approximation made simple, *Phys. Rev. Lett.*, 1996, **77**, 3865-3868.

[73] S. G. Louie, S. Froyen, and M. L. Cohen, Non linear ionic pseudopotentials in spin-density-functional calculations, *Phys. Rev. B*, 1982, **26**, 1738-1742.

[74] P. Geerlings, F. De Proft and W. Langenaeker, Conceptual density functional theory, *Chem. Rev.*, 2003, **103** 1793-1873.

[75] R.G. Parr, L. von Szentpaly and S. Liu, Electrophilicity index, *J. Am. Chem. Soc.*, 1991, **121**, 1922-1924.

[76] R.G. Pearson, Absolute electronegativity and hardness: application to inorganic chemistry, *Inorg. Chem.*, 1988, **27**, 734-740.

[77] P.K. Chattaraj and S. Duley, Electron affinity, electronegativity, and electrophilicity of atoms and ions, *J. Chem. Eng. Data*, 2010, **55**, 1882-1886.

[78] P. Fuentealba, P. Pérez, R. Contreras, DFT Calculations for Corrosion Inhibition of Ferrous Alloys by Pyrazolopyrimidine Derivatives, *J. Chem.Phys.*, 2000, **113** 2544-2551.

[79] W. Yang, R.G. Parr and Hardness, Hardness, softness, and the fukui function in the electronic theory of metals and catalysis, *Proc. Natl. Acad. Sci. U. S. A.*, 1985, **82**, 6723-6726.

[80] P. Geerlings, F. De Proft and W. Langenaeker, Conceptual Density Functional Theory, *Chem. Rev.*, 2003, **103** 1793-1873.

[81] J.P. Perdew, R.G. Parr, M. Levy, J.L. Balduz, Density functional theory for fractional particle number: derivative discontinuities of the energy, *Phys. Rev. Lett.*, 1982, **49**, 1691-1694.

[82] C. J. Dible, S. T. Akin, S. Ard, C. P. Fowler and M. A. Duncan, Photodissociation of Cobalt and Nickel Oxide Cluster Cations, *J. Phys. Chem. A*, 2012, **116**, 5398-5404.

[83] K. Ohshimo, A. Azuma, T. Komukai, R. Moriyama and F. Misaizu, Structures and CO-Adsorption Reactivities of Nickel Oxide Cluster Cations Studied by Ion Mobility Mass Spectrometry, *J. Phys. Chem. C*, 2015, **119**, 11014

[84] C. N. van Dijk, D. B. Roy, A. Fielicke, T. Rasing, A. C. Reber, S. N. Khanna and A. Kirilyuk, Eur. Phys. J. D, 2014, 68, 357.

[85] K. Sakuma, K. Miyajina and F. Mafune, Oxidation of CO by Nickel Oxide Clusters Revealed by Post Heating, *Phys. Chem. A*, 2013, **117**, 3260-3265.

[86] S. Goel and A. Masunov, Density functional theory study of small nickel clusters,*J. mol. model*, 2011, **18**, 783-790.

[87] D. Schooss, M.N. Blom, J.H. Parks, B. v. Issendorf, H. Haberland, and M.M. Kappes, The structures of Ag_{55}^{+} and Ag_{55}^{-}: Trapped ion electron difraction and Density Functional Theory, *NanoLett.*, 2005, **5**, 1972-1977.

[88] T. Rapps, R. Ahlrichs, E. Waldt, M. M. Kappes and D. Schooss, On the structures of 55-atom transition-metal clusters and their relationship to the crystalline bulk. *Angew. Chem. Int. Ed.*, 2013, **52**, 6102-6105.

[89] Mauricio J. Piotrowski, Crina G. Ungureanu, Polina Tereshchuk, Krys E. A. Batista, Anderson S. Chaves, Diego Guedes-Sobrinho, and Juarez L. F. Da Silva, Theoretical study of the structural, energetic and electronic

properties of 55-atom metal nanoclusters: A DFT investigation within van der Waals corrections, spin-orbit coupling, and PBE+U or 42 metal systems, *J. Phys. Chem. C*, 2016, **120**, 28844-28856.

[90] M. Pereiro, D. Baldomir, and J.E. Arias, Unexpected magnetism of small silver clusters, *Phys. Rev. A*, 2007, **75**, 063204-063204-4.

[91] Eva M. Fernández, José M. Soler, Ignacio L. Garzón, and Luis. C. Balbás, Trends in the structure and bonding of noble metal clusters, *Phys. Rev. B*, 2004, **70**, 165403-165403-14.

[92] G. Rossi, A. Rapallo, C. Mottet, A. Fortunelli, F. Balleto and R. Ferrando, Magic polyicosahedral core-shell structures, *Phys. Rev. Lett.*, 2004, **93**, 105503.

[93] D. Bochicchio and R. Ferrando, Size-Dependent Transition to High-Symmetry Chiral Structures in AgCu, AgCo, AgNi, and AuNi Nanoalloys, *Nano Letters*, 2010, **10**, 4211-4216.

[94] D. Bochicchio and R. Ferrando, Morphological instability of core-shell metallic nanoparticles, *Phys. Rev. B*, 2013, **87**, 165435-1-13.

[95] K. Laasonen, E. Panizon, D. Bochicchio, and R. Ferrando, Competition between Icosahedral Motifs in AgCu, AgNi, and AgCo Nanoalloys: A combined atomistic-DFT study, *J. Phys. Chem. C*, 2013, **117**, 26405-26413.

[96] M. Harb, F. Rabilloud and D. Simon, Structural, electronic, magnetic and optical properties of icosahedral silver-nickel nanoclusters, *Phys. Chem. Chem. Phys.*, 2010, **12**, 4246-4254.

[97] Bader, R. F. W. *Atoms in Molecules. A Quantum Theory*; John Wiley and Sons, Ltd, Clarendon, Oxford, 1990.

[98] H. Henkelman, G.; Arnaldsson, A.; Jónsson, A fast and robust algorithm for Bader decomposition of charge density, *Comput. Mater. Sci.*, 2006, **36**, 354-360.

[99] H. Portales, L. Saviot, E. Duval, M. Gaudry, E. Cottancin, M. Pellarin, J. Lermé and M. Broyer, Resonant Raman scattering by quadrupolar vibrations of Ni-Ag core-shell nanoparticles, *Phys. Rev. B*, 2002, **65** 165422-165422-16.

[100] M. Gaudry, E. Cottancin, M. Pellarin, J. Lermé, L. Arnaud, J.R. Huntzinger, J.-L Vialle, M. Broyer, J.L. Rousset, M. Treilleux and P. Mélinon, Size and composition dependence in the optical properties of mixed (transition metal/noble metal) embedded clusters, *Phys. Rev. B*, 2003, **67**, 155409-155419.

[101] A. Rapallo, G. Rossi, R. Ferrando, A. Fortunelli, B.C. Curley, L.D. Lloyd, M. Tarbuck and R.L. Jonhston, Global optimization of bimetallic cluster structures.I. Size-mismatched Ag-Cu, Ag-Ni and Au-Cu systems, *J. Chem. Phys.*, 2005, **122**, 194308-194321.

[102] M. Harb, F. Rabilloud and D. Simon, Density functional study of structural and electronic properties of small bimetallic silver-nickel clusters, *J. Phys. Chem. A*, 2007, **111**, 7726-7731.

[103] C. Mottet, G. Rossi, F. Baletto, and R. Ferrando, Magic Polyicosahedral Core-Shell Clusters, *Phys. Rev. Lett*, 2005, **95**, 035501-1-4.

[104] F. Luis, F. Bartolomé, F. Petroff, J. Bartolomé, L.M. García, C. Deranholt, H. Jaffres, M.J. Martínez, P. Bencok, F. Wilhelm, A. Rogalev and N.B. Brookes, Tunning the magnetic anisotropy of Co nanoparticles by metal capping, *Europhys. Lett.*, 2006, **76**(1), 142-148.

[105] A. Fortunelli and A. M. Velasco, Structural and electronic properties of Pt/Fe nanoclusters from EHT calculations, *J. Mol. Struc.(THEOCHEM)*, 1999, **487**, 251-266.

[106] K. S. Molek, C. Anfuso-Cleaty, and M. A. Duncan, *J. Phys. Chem. A*, 2008, **112**, 9238-9247.

[107] S. Yin, W. Xue, X.-L. Ding, W.-G. Wang, S.-G. He and M.-F. Ge, *Chem. Phys. Lett.*, 2009, **281**, 72.

[108] M. B. Torres, A. Aguado, F. Aguilera-Granja, A. Vega and L. C. Balbas, *J. Phys. Chem. C*, 2015, **119**, 20, 11200-11209.

[109] K. S. Molok, C. Anfuso-Cleaty, and M. A. Duncan, *J. Phys. Chem. A*, 2008, **112**, 9238-9247.

[110] Q. Zheng-Wang and K. Geert-Jan, Theoretical study of stable, defect-free $(TiO_2)_n$ nanoparticles with $n = 10 - 16$, *Jour. Phys. Chem. B*, 2007, **111**, 16808-16817.

[111] F. Aguilera-Granja, A. Vega and L.C. Balbas, New structural and electronic properties of $(TiO_2)_10$, *Jour. Chem. Phys. C*, 2016, **144**, 234312-234320.

[112] M. Salazar-Villanueva, A. Cruz-Lopez, A.A. Zaldivar-Cadena, A. Tovar-Corona, M.L. Guevara-Romero and O. Vazquez-Cuchillo, Effect of the electronic state of Ti on Mdoped (TiO_2) nanoparticles $(M = Zn, GaorGe)$ with high photocatalytic activities: a experimental and DFT molecular study, *Materials Science in Semiconductor Processing*, 2017, **58**, 8-14.

[113] O. Lamiel-Garcia, A. Cuko, M. Calatayud, F. Illas and Stefan T. Bromley, Predicting sizedependent emergence of crystallinity in nanomaterials: titania nanoclusters versus nanocrystal, *Nanoscale*, 2017, **9**,1049-1058.

[114] S.-G. Park, B. Magyari-Köpe and Y. Nishi, *Phys. Rev. B*, 2010, **82**, 115109-115118.

[115] H. Chen, X. Li, R. Wan, S. Kao-Walter and Y. Lei, *Chemical Physics*, 2018, **501**, 60-67.

[116] A. Janotti, J. B. Varley, P. Rinke, N. Umezawa, G. Kresse and C. G. Van de Walle, *Phys. Rev. B*, 2010, **81**, 085212-085219.

[117] H.-Ch. Wu, S.-H. Li and S.-W. Lin, *Int. Jour. of Photoenergy*, 2012, **2012**, 823498-823504.

[118] X. Li, J. Shi, H. Chen, R. Wan, Ch. Leng, S. Chen and Y. Lei, *Comp. Mat. Sci.*, 2017, **129**,295-303.

[119] A. Fakhim Lamrani, M. Ouchri, M. Belaiche, A. El Kenz, M. Loulidi and A. Benyoussef, *Jour. Mag. Mag. Mat.*, 2016, **401**, 977-981.

[120] A. Fakhim Lamrani, M. Ouchri, M. Belaiche, A. El Kenz, M. Loulidi and A. Benyoussef, *Thin Solid Films*, 2014, **570**, 45-48.

[121] D. Çakir and O. Gülseren, *J. Phys.: C.M. Matter*, 2012, **24**, 305301-305314.

[122] K. Chul–Ko, O. Lamiel–García, J. Yong–Lee and F. Illas, *Phys. Chem. Chem. Phys.*, 2016, **18**, 12357-12367.

[123] J.P. Perdew, K. Burke, and M. Ernzerhof, Generalized Gradient Approximation Made Simple, *Phys. Rev. Lett.*, 1996, **77**, 3865-3868.

[124] T. Umebayashi, T. Yamaki, H. Itoh, and K. Asai, *Jour. of Phys. and Chem. of Solids*, 2002, **63**, 1909-1920.

[125] Y. Wang, R. Zhang, J. Li, L. Li and S. Lin, *Nanoscale Res. Lett.*, 2014. **9** 46-54.

[126] H. Xing Gang, H. Mei Dong, W. Xiao Ling, L. An Dong and Sci China Ser, *G-Phys Mech. Astron.*, 2009, **52**, 838-842.

[127] V. E. Henrich, G. Dresselhaus and H. J. Zeiger, *Phys. Rev. Lett.*, 1976, **36**, 1335-1339.

[128] M. Nolan, S. D. Elliott, J. S. Mulley, R. A. Bennett, M. Basham and P. Mulheran, *Phys. Rev. B*, 2008, **77**, 235424.

[129] A. M. Knight, B. Bandyopadhyay, C. L. Anfuso, K. S. Molek, M. A. Duncan MA, *IJMS*, 2011, **304**, 29-35.

[130] S. Mukhopadhyay, S. Gowtham, R. Pandey, A. Costales, *J. Mol. Struct-THEOCHEM*, 2010, **948**, 31-35.

[131] E. Janssens, S. Neukermans, F. Vanhoutte, R. E. Silverans, P. Lievens, A. Navarro-Vazquez and P. V. R. Schleyer, *J Chem Phys*, 2003, **118**, 5862-5871.

[132] M. Gausa, G. Ganteför, H. O. Lutz and K. H. Meiwes-Broer, *Int J of Mass Spectr and Ion Processes*, 1990, **101**, 227-237.

[133] S. F. Boys and f. Bernardy, The calculation of small molecular interactions by the differences of separate total energies. Some procedures with reduced errors, *Mol Phys*, 1970, 19, 553-566.

[134] J. L. Bredas, Mind the gap!, *Mater Horiz*, 2014, **1**, 17-19.